

University of St Andrews



Full metadata for this thesis is available in
St Andrews Research Repository
at:

<http://research-repository.st-andrews.ac.uk/>

This thesis is protected by original copyright

A

MICROELECTRODE

IMPEDANCE SPECTROSCOPY

STUDY OF

INTERFACIAL ELECTRON

TRANSFER

A thesis presented for the degree of

Doctor of Philosophy

in the Faculty of Science of the University of St. Andrews

by Douglas Stewart.

August 1998



TR
D134

DECLARATION

- (i) I, Douglas Stewart, hereby certify that this thesis, which is approximately 50,000 words in length, has been written by me, that it is the record of work carried out by me and that it has not been submitted in any previous application for a higher degree.

Date: 31/8/98 Signature of Candidate:

- (ii) I was admitted as a research student in January 1994 and as a candidate for the degree of Doctor of Philosophy in January 1995; the higher study for which this is a record was carried out in St. Andrews between January 1994 and August 1998 but was suspended between January 1997 and December 1997 to allow me to pursue business interests.

Date: 31/8/98 Signature of Candidate:

- (iii) I hereby certify that the candidate has fulfilled the conditions of the Resolution and Regulations appropriate for the degree of Doctor of Philosophy in the University of St. Andrews and that the candidate is qualified to submit this thesis in application for that degree.

Date: 31. 8. 98 Signature of Supervisor:

LIBRARY DECLARATION

In submitting this thesis to the University of St. Andrews I understand that I am giving permission for it to be made available for use in accordance with the regulations of the University Library for the time being in force, subject to any copyright vested in the work not being affected thereby. I understand that the title and abstract will be published, and that a copy of the work may be made and supplied to any bona fide library or research work.

Date: 2/10/98

Signature of Candidate:

Acknowledgements

I would like to express my gratitude to my supervisor, Professor Colin Vincent for his guidance during my work, his open door when I needed to discuss anything, and for giving me the encouragement I needed, after a year out, to complete my thesis.

I would also like to thank Professor Peter Bruce for technical discussions relating to my work and Dr. P. Los for telling me many interesting stories, not always related to chemistry, and introducing me to practical methods in impedance spectroscopy and the methods by which the key equations are derived here for microelectrode impedance spectroscopy.

My thanks are also due to Dr's Ali and Lynn Christie for their practical help in the laboratory and making the time for technical discussions with me, and to Dr Joe Crayston for allowing me to use his group's equipment to make many cyclic voltammetry measurements and to the EPSRC for funding.

Last but most certainly not least I would like to give a big thank you to my wife Audrey for all her support during my work, our four year old daughter Amanda who, particularly in the last few hectic weeks has had much less attention than usual because of "Daddy's pee aitch dee!", and my parents for their encouragement and financial support both when I was at school and when I was an undergraduate.

ABSTRACT

Microelectrode impedance spectroscopy was used to study the electrode kinetics of ferrocene in tetraethyleneglycol dimethylether (tetraglyme), a liquid oligomer of ethylene oxide, and in solid poly(ethylene oxide). Despite complications owing to ion-pairing in the liquid, and adsorption in the solid, it was found that both the heterogeneous electron transfer rate constant and diffusion coefficient varied by one order of magnitude between the liquid and solid, consistent with outer sphere solvent dynamic control in both phases.

Equations were derived to permit analysis of microelectrode impedance data from an EC reaction. Computer simulations and experimental trials indicated that it is not necessary to obtain impedance data at sufficiently high frequencies that a semi-circle is obtained in impedance plots. Provided the kinetics are not too fast, reliable values of the double-layer capacitance, the diffusion coefficient, the heterogeneous rate constant, and the microdisc radius can be obtained from least squares analysis of lower frequency data.

Studies of the electrode kinetics of 7,7,8,8-tetracyanoquinodimethane (TCNQ) in tetraglyme and buckminsterfullerene (C_{60}) in dichloromethane, 1,2 dichlorobenzene and benzonitrile were complicated by ion-pairing and double-layer effects. It was established, contrary to predictions in the literature, that where the supporting electrolyte cation is tetrabutylammonium (TBA^+), C_{60} reduction exhibits a strong Frumkin effect whereby the value of the heterogeneous rate constant increases markedly with (TBA^+) concentration. This indicates that the location of the reacting molecules is at the outer Helmholtz plane (OHP) and not, as had been proposed, outside it. When lithium, Li^+ , is the supporting electrolyte cation no Frumkin effect is observed, indicating that C_{60} is located outside the OHP. Shifts in half-wave potential with changing supporting electrolyte concentration were consistent with Li^+ cations associating with neutral C_{60} in preference to anionic C_{60}^- .

TABLE OF CONTENTS

CHAPTER 1

INTRODUCTION.....	1
-------------------	---

CHAPTER 2

EXPERIMENTAL PROCEDURES

2.1	Preparation And Purification Of Salts.....	7
2.1.1	General.....	7
2.1.2	Tetracyanoquinodimethane.....	7
2.1.3	Lithium Tetracyanoquinodimethane.....	7
2.1.4	Potassium and Lithium Chlorides.....	8
2.1.5	Potassium Hexacyanoferrate (II) Trihydrate.....	8
2.1.6	Potassium Hexacyanoferrate (III)	8
2.1.7	Ferrocenecarboxylic Acid.....	9
2.1.8	Tetrabutylammonium Tetrafluoroborate	9
2.1.9	Lithium Perchlorate.....	9
2.1.10	Buckminsterfullerene.....	9
2.1.11	Ferrocene.....	9
2.1.12	Tetrabutylammonium Perchlorate.....	9

2.2	Solvent Purification.....	10
2.2.1	Tetraethyleneglycol dimethyl ether.....	10
2.2.2	Poly(ethylene oxide)	10
2.2.3	Dichloromethane, 1,2 Dichlorobenzene, and Benzonitrile.....	10
2.2.4	Water.....	12
2.3	Preparation of Electrolytes.....	12
2.3.1	General.....	12
2.3.2	Liquid Electrolytes.....	12
2.3.3	Preparation of Polymer Films via Solvent Casting.....	12
2.4	Instrumentation.....	14
2.4.1	Cell Design – General.....	14
2.4.2	Microelectrode Preparation.....	14
2.4.3	Counter/Quasi-Reference Electrode Preparation.....	15
2.4.4	Impedance Spectroscopy.....	17
2.4.5	Cyclic Voltammetry.....	17
2.4.6	Conductivity.....	19
2.5	References.....	20

CHAPTER 3

ELECTROCHEMICAL THEORY AND MICROELECTRODE METHODS

3.1	An Introduction to Double-Layer Theory and the Faradaic and Non-Faradaic Impedances.....	21
3.1.1	Equations for the Faradaic Impedance.....	24
3.1.2	The Charge Transfer Impedance in a System at Equilibrium.....	28
3.1.3	The Diffusion Impedance in a System at Equilibrium.....	29
3.2	Electrochemical Impedance Spectroscopy.....	34
3.2.1	Impedance Spectroscopy and Electric Circuits.....	34
3.2.2	The Resistor in an ac Circuit.....	35
3.2.3	The Capacitor in an ac Circuit.....	36
3.2.4	The Capacitor and Resistor in Series in an ac Circuit.....	38
3.2.5	Impedance and how it may best be described.....	39
3.2.6	The Complex Plane Plot.....	40
3.3	Comparison of Properties of Microelectrodes and Normal Electrodes and Derivation of the Exact Solution for Diffusion to a Microdisc.....	45
3.3.1	General.....	45
3.3.2	Two-electrode and Three-electrode Cells.....	46
3.3.3	Impedance at Normal and Microelectrodes.....	48
3.3.4	The Exact Solution for Diffusion to a Microdisc Electrode.....	55
3.4	The Hemispherical Approximation for Diffusion to a Microdisc for an E Mechanism.....	63

3.5	The Advantages of Microelectrodes.....	66
3.5.1	General.....	66
3.5.2	The Potential Drop (iR) Over the Electrolyte.....	66
3.5.3	Non-linear Diffusion at the Microelectrode.....	68
3.6	Influence of a Chemical Step in the Impedance Response at a Microdisc. Derivation of the Hemispherical Approximation for Diffusion to the Microdisc for an EC mechanism.....	69
3.7	Cyclic Voltammetry at Microelectrodes.....	79
3.8	Conclusions.....	84
3.9	References.....	85
	Appendix A Values of Functions Arising from Analysis of the Diffusion Impedance of a Disc Shaped Microelectrode.....	87
	Appendix B FORTRAN Subroutine for the Exact Solution to the Microdisc for an E mechanism.....	88
	Appendix C FORTRAN Subroutine for the Hemispherical Approximation to the Microdisc for an E Mechanism.....	90
	Appendix D FORTRAN Subroutine for the Hemispherical Approximation to the Microdisc for an EC Mechanism where only one of the Redox Species is Present in the Bulk Solution..	92

CHAPTER 4

A MICROELECTRODE IMPEDANCE STUDY OF THE $\text{Fe}^{2+} / \text{Fe}^{3+}$ REDOX COUPLE IN AQUEOUS SOLUTION

Introduction.....	95
4.1 Impedance Spectroscopy of Dummy Cells.....	95
4.2 The Aqueous Electrochemical Cell.....	101
4.2.1 Preparation.....	101
4.2.2 Aqueous KCl - Impedance Results and Discussion.....	102
4.2.3 Aqueous LiCl - Impedance Results and Discussion.....	111
4.3 Refinement of Models with a CPE.....	115
4.4 How Could the Experimental Method Be Improved?.....	121
4.5 Conclusions.....	126
4.6 References.....	127

CHAPTER 5

A MICROELECTRODE IMPEDANCE STUDY OF THE HETEROGENEOUS KINETICS OF FERROCENE IN TETRAGLYME

Introduction.....	128
5.1 Electrochemical Impedance Study of the Ferrocene/Ferrocenium Couple.....	129

5.1.1	Preliminary Impedance and Voltammetry Measurements.....	129
5.1.2	The Dummy Cell.....	137
5.1.3	Effect of Ferrocene Concentration.....	140
5.1.4	Effect of Temperature.....	153
5.1.5	Effect of Background Electrolyte Concentration.....	165
5.2	CNLS Analysis of Impedance Data using the Hemispherical Approximation for Diffusion to the Microdisc for an EC Mechanism.....	173
5.3	Alternative Mechanisms.....	181
5.4	Conclusions.....	185
5.5	References.....	188

CHAPTER 6

A MICROELECTRODE IMPEDANCE STUDY OF THE HETEROGENEOUS KINETICS OF TCNQ IN TETRAGLYME

	Introduction.....	189
6.1	Cyclic Voltammetry Measurements.....	190
6.2	Conductivity Measurements.....	196
6.3	Impedance Measurements.....	198
6.3.1	The Effect of Potential on Impedance Data.....	198
6.3.2	The Effect of Temperature on Impedance Data.....	198

6.3.3	The Effect of Redox Couple Concentration on Impedance Data.....	201
6.3.4	CNLS Analysis of the Impedance Data.....	202
6.3.5	The Effect of Supporting Electrolyte.....	218
6.4	Conclusions.....	236
6.5	References.....	238

CHAPTER 7

A MICROELECTRODE IMPEDANCE STUDY OF THE HETEROGENEOUS KINETICS OF FERROCENE AND FERROCENE CARBOXYLIC ACID IN NEAR-SOLID PEO.

	Introduction.....	239
7.1	Impedance Measurements.....	240
7.1.1	Effect of Potential on Impedance.....	240
7.1.2	Effect of Time on Impedance.....	243
7.1.3	Effect of Temperature on Impedance.....	246
7.1.4	CNLS Fitting Of Impedance Data.....	251
7.2	Conclusions.....	256
7.3	References.....	258

CHAPTER 8

A MICROELECTRODE IMPEDANCE STUDY OF THE HETEROGENEOUS KINETICS OF BUCKMINSTERFULLERENE IN APROTIC ORGANIC SOLVENTS

	Introduction.....	259
8.1	Cyclic Voltammetry.....	261
8.2	8.2.1 The Effect of Time on Impedance Data.....	274
	8.2.2 The Effect of Potential on Impedance Data.....	277
	8.2.3 Simulations of Impedance Data.....	279
	8.2.4 CNLS Analysis of Impedance Data.....	291
	8.2.5 Discussion of Results for TBAP and TBABF ₄ Supporting Electrolytes.....	302
	8.2.6 Discussion of Results for LiClO ₄ Supporting Electrolyte.....	312
8.3	Conclusions.....	314
8.4	References.....	316

CHAPTER 9

	CONCLUDING REMARKS.....	318
--	-------------------------	-----

CHAPTER 1

INTRODUCTION

Electron transfer between an electrode and a molecule is one of the most fundamental of the solution phase reactions because chemical bonds are neither created nor destroyed. The lack of complications owing to bond formation or breaking indicates that electron transfer should be the most readily understood of reactions in solution. Although bonds are neither made nor broken the bond lengths and bond angles within the molecule undergoing electron transfer do change owing to electron redistribution. If significant structural changes are required before a molecule can achieve the transition-state for the rate-determining electron transfer step, there will be a significant energy requirement. The energy associated with intra-molecular rearrangement is termed the inner sphere rearrangement energy. If only slight changes in molecular structure result from the electron gain or loss, the inner sphere rearrangement energy will be low and the majority of energy associated with the change will be that of rearrangement of solvent molecules around the reacting species, termed the outer sphere rearrangement energy. The fastest processes are those in which the internal rearrangement is minimal. The kinetics of such processes are described as being controlled by outer sphere solvent dynamics. Molecules expected to exhibit outer sphere solvent dynamic control are large, symmetrical species with delocalised electronic structure, the best example of which is buckminsterfullerene, C_{60} .

The faster a reaction is, the more difficult it is to measure the reaction rate. This is because, generally, processes other than the reaction rate itself become rate limiting. In solution chemistry the fastest reactions are diffusion controlled, i.e. the reaction is so fast that the overall rate of reaction is determined by the diffusion rate of reactants and not by the rate of the chemical reaction. An analogous problem exists in electrochemistry where fast heterogeneous electron transfers are difficult to measure because the overall rate becomes limited by the rate of diffusion of reactants to and from the electrode surface. The result of this has been to make it more difficult to measure the rates of fast electrode reactions and hence more difficult to compare experiment with different interpretations and theories of heterogeneous electron transfer.

Improved understanding of electron transfer is not only of theoretical interest, however, since everywhere around us and indeed within our bodies interfaces abound, the majority of which are charged. Improving our understanding of interfacial electron transfer, and improved electrochemical techniques generally have significance in biological and physical environments.

There are a variety of electrochemical methods which may be used to gather information about heterogeneous electron transfer rates, all relying on the established principal that the measured current can indicate the rate of electrochemical reaction. Cyclic voltammetry and ac voltammetry are commonly used. Impedance spectroscopy offers one of the best methods for characterising interfacial processes because, in addition to measuring the magnitude of the current response to a voltage perturbation, it also measures the phase angle between the

current and the voltage. The phase sensitivity enables the technique simultaneously to evaluate the faradaic current, resulting from interfacial charge transfer, and non-faradaic current caused by rearrangements of polar solvent molecules and ions at the metal/solution interface. This was first exploited experimentally by Randles in 1947 who presented preliminary results and discussed the combined effect of the faradaic and non-faradaic processes on the impedance of an aqueous electrochemical cell. At its simplest, the metal/solution interface consists of a metal in contact with solvent molecules whose dipoles, owing to their proximity to the metal, are aligned differently to their disposition in the bulk solution. The interfacial region is termed the double layer. The structure of the double layer can have a crucial effect on electrode kinetics. Molecules undergoing electron transfer are generally supposed to lie in a plane just outside the solvent layer surrounding the electrode at a location termed the outer Helmholtz plane, in honour of Helmholtz who produced the first coherent description of the interfacial zone in the nineteenth century.

Practical studies of electrode kinetics have been assisted greatly by the development of microelectrodes, beginning with Fleischmann et al. Microelectrodes typically have at least one dimension of the order of about 1-10 μm . One of their benefits is to promote radial diffusion rather than the linear diffusion associated with larger electrodes. Radial diffusion draws on a more rapidly increasing volume profile than linear diffusion and therefore results in faster diffusion of electroactive species to the electrode surface. The faster the diffusion rate, the greater is the likelihood that an electrochemical reaction rate will become limited by electron transfer rather than diffusion, enabling the determination of fast electron transfer rates.

The use of microelectrodes for impedance spectroscopy was hampered initially because for the most easily made microelectrode, a circular disc inlaid in glass, it proved very difficult to model the current/potential profile at the join between the metal disc and the glass. Fleischmann and Pons published a numerical integration solution based on the properties of Bessel functions enabling the use of disc shaped microelectrodes in impedance studies. The complexity of the integrals employed by Fleischmann and Pons, however, often necessitates a knowledge of, for example, diffusion coefficients before their model can be applied to a cell and also renders the development of the model to analyse more complicated reactions more difficult. Bruce, Lisowska-Oleksiak, Los and Vincent published an approximation to the diffusion profile at the disc shaped microelectrode based on the principle that at very high frequencies diffusion is linear and at low frequencies it is approximately hemispherical. In theory, using this model enables all of the important electrochemical parameters, i.e. heterogeneous rate constant for electron transfer, diffusion coefficient, electrochemical radius of the microelectrode, and double layer capacitance to be obtained in a single experiment. The relative simplicity of the hemispherical approximation, so named by Bruce et al., also renders it more flexible for further derivation to analyse cells in which the electrochemistry is more complicated.

The objective of the work reported here was to verify that the hemispherical approximation produced realistic values for electrochemical parameters for cells whose properties are well known. Once this had been accomplished, it was planned to use the technique to study systems in which microelectrodes offer advantages

over normal sized electrodes, such as systems in which the reactant is expected to exhibit rapid electron transfer and also systems in which the resistance of the bulk is high.

Ferrocene, for example, is a symmetrical molecule with a highly delocalised electronic structure for which fast heterogeneous kinetics have been measured in a range of aprotic organic solvents. Its kinetics had not, however, been measured in solid poly(ethylene oxide), PEO. PEO is capable of dissolving suitable salts and in this form is a polymer electrolyte. Solid polymer electrolytes are technologically important because of their applications in modern devices. All-solid-state batteries, for example, may be fabricated which do not suffer from the leakage problems associated with liquid electrolytes and do not have electrode contact problems associated with ceramics. Furthermore, as plastics, polymer electrolytes can readily be made into thin films and hence be incorporated into various devices such as smart cards, for example. Determining the kinetics of ferrocene in solid or near-solid PEO is of theoretical interest since in these materials the dipole motions are constrained relative to liquids. If electron transfer from or to ferrocene is controlled by outer sphere solvent dynamics, as it is believed to be, the time taken to adjust the structure of the polymer solvent around the ferrocene molecule to accommodate the electronic change will be slower than in the liquid. Tetraethyleneglycol dimethylether (tetraglyme) is a liquid oligomer of ethylene oxide and hence has a chemical structure identical to PEO. It was hoped that microelectrode impedance spectroscopy could be used to study differences between the heterogeneous kinetics of ferrocene in the chemically alike solid PEO and liquid tetraglyme.

The electrochemistry of buckminsterfullerene, C_{60} , a molecule of current theoretical and practical interest, was also studied by impedance spectroscopy at a microelectrode. Kinetic data had been published for C_{60} in a variety of organic solvents. It was desired to compare the kinetic data from microelectrode impedance spectroscopy with recently published data acquired using other modern electrochemical techniques. It had also been predicted that because C_{60} is a large molecule it would lie outside the outer Helmholtz plane. It was hoped that data from microelectrode impedance spectroscopy could be used to verify this claim.

CHAPTER 2

EXPERIMENTAL PROCEDURES

2.1 Preparation And Purification Of Salts

2.1.1 *General*

All salts were dried before electrochemical use, the particular methods are described below. The dried salts were transferred to an MBraun glove-box (Mbraun mb 150B) and stored under Argon with moisture and oxygen levels maintained below 0.2 ppm.

2.1.2 *Tetracyanoquinodimethane*

7,7,8,8-Tetracyanoquinodimethane (TCNQ) (Fluka purum grade 98%+) was purified for electrochemical experiments by recrystallisation from acetonitrile.⁽¹⁾

2.1.3 *Lithium Tetracyanoquinodimethane*

Lithium tetracyanoquinodimethane (LiTCNQ) was prepared by reaction of lithium iodide (Aldrich 99%) with tetracyanoquinodimethane (Fluka purum grade 98%+) in acetonitrile as described by Melby et al.⁽²⁾



The resulting salt was analysed by C-H-N microanalysis. The results are shown in Table 2.1.

Table 2.1
C-H-N analysis of synthesised LiTCNQ

	Carbon (%)	Hydrogen (%)	Nitrogen (%)
Theoretical Composition	68.26	1.91	26.54
Result Of Analysis	67.95	2.04	26.30

2.1.4 Potassium and Lithium Chlorides

Potassium and lithium chlorides (Fisons Analytical Reagents) were used as received.

2.1.5 Potassium Hexacyanoferrate (II) Trihydrate

Potassium hexacyanoferrate (II) trihydrate $K_4Fe(CN)_6 \cdot 3H_2O$ (Fluka microselect 99.5%+) was used as received.

2.1.6 Potassium Hexacyanoferrate (III)

Potassium hexacyanoferrate (III) $K_3Fe(CN)_6$ (Fluka microselect 99%+) was used as received.

2.1.7 *Ferrocenecarboxylic Acid*

Ferrocenecarboxylic acid (Fluka, purum grade, 97%+) was dried at 50°C under dynamic vacuum for 48 hours.

2.1.8 *Tetrabutylammonium Tetrafluoroborate*

Tetrabutylammonium tetrafluoroborate (TBABF₄) (Fluka puriss. electrochemical grade 99%+) was dried under dynamic vacuum for 72 hours at 120°C.

2.1.9 *Lithium Perchlorate*

Lithium perchlorate (Fluka purum 98%+) was dried under dynamic vacuum for 72 hours at 100°C.

2.1.10 *Buckminsterfullerene*

Buckminsterfullerene (C₆₀, Aldrich reagent grade) was used as received.

2.1.11 *Ferrocene*

Ferrocene was sublimed under vacuum at 45°C and the resulting crystals ground using a mortar and pestle.

2.1.12 *Tetrabutylammonium Perchlorate*

Tetrabutylammonium Perchlorate (TBAP) (99%+ puriss. electrochemical grade) was dried under dynamic vacuum for 72 hours at 120°C.

2.2 Solvent Purification

2.2.1 *Tetraethyleneglycol dimethyl ether*

Tetraethyleneglycol dimethyl ether $[\text{CH}_3(\text{OCH}_2\text{CH}_2)_4\text{OCH}_3]$ (Aldrich 99%), abbreviated henceforth as *tetraglyme*, was purified by vacuum distillation at 10^{-6} bar. The first and last 20% of distillate by volume were discarded to leave the middle cut for use in experiments. This middle cut was stored in darkness in a dry box as described for salts in section 2.1.1. Distillations were performed using a Fischer HMS 500C apparatus (Figure 2.1) with 90 theoretical plate column. The column was maintained at 90°C and the oil bath at 147°C .

2.2.2 *Poly(ethylene oxide)*

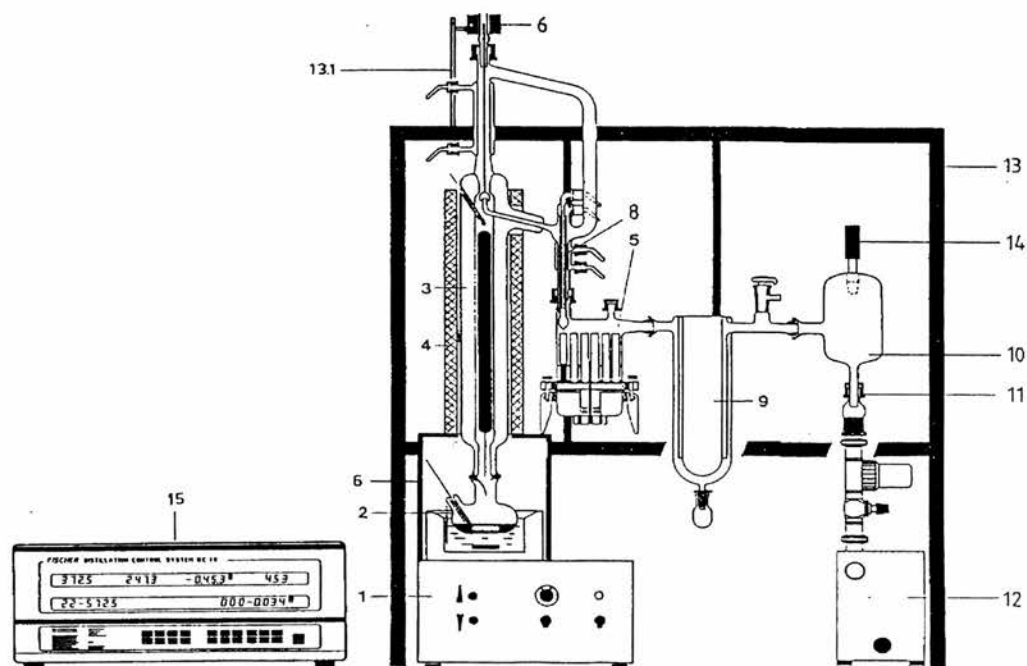
The polymer (Aldrich, $(-\text{CH}_2\text{CH}_2\text{O}-)_n$ average molar mass M_n 100,000) was dried under vacuum at 50°C for 48 hours then transferred to the glove-box.

2.2.3 *Dichloromethane, 1,2-Dichlorobenzene, Benzonitrile and Acetonitrile*

These solvents were purchased (Aldrich) as anhydrous grades and used as received. Microelectrode cyclic voltammetry was used to establish that the solvents were not electrochemically active at potentials of interest in experiments.

Figure 2.1

The Fischer HMS 500C distillation apparatus



Legend for Figure 2.1

- | | |
|-----------------------|---------------------------------|
| 1. Oil bath | 10. Buffer vessel |
| 2. Distillation flask | 11. Vacuum line |
| 3. SPAHLTROHR™ column | 12. Vacuum pump |
| 4. Heating mantle | 13. Mounting frame |
| 5. Fraction collector | 13.1. Support rod |
| 6. Solenoid coil | 14. Vacuum sensor |
| 8. Distillate cooler | 15. Distillation control device |
| 9. Cold trap | |

2.2.4 *Water*

Water for electrochemical experiments was triply distilled under Argon. Tap-water was distilled initially to remove salts. The second distillation was carried out over potassium hydroxide and potassium permanganate in order that organic contaminants were removed. Finally a third distillation was carried out to yield water of conductivity $0.2 \mu\text{S cm}^{-1}$.

2.3 **Preparation of Electrolytes**

2.3.1 *General*

Other than in aqueous experiments, all procedures were carried out in the glove-box (section 2.1.1.)

2.3.2 *Liquid Electrolytes*

All solutions were prepared by dissolving a known mass of the electroactive reactant and the supporting electrolyte into a known mass of liquid or to make up a known volume of liquid. Solutions were stirred to ensure homogeneity.

2.3.3 *Preparation of Polymer Films via Solvent Casting*

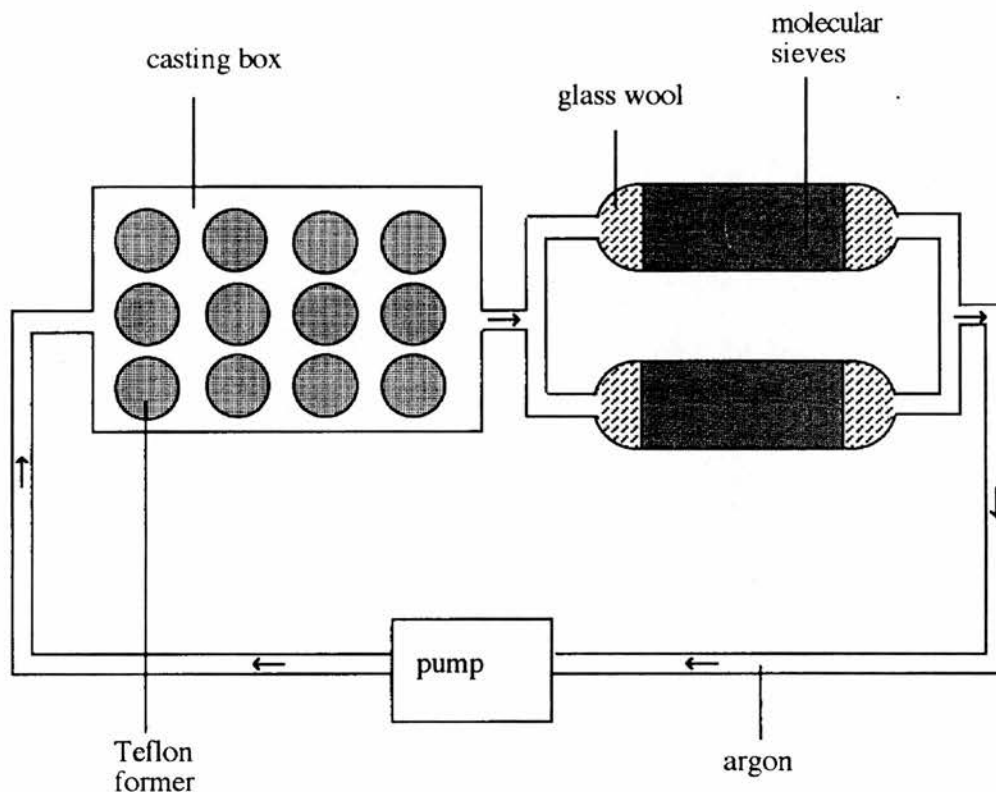
Known masses of poly(ethylene oxide), the electroactive reactant and the supporting electrolyte were dissolved in anhydrous acetonitrile and stirred overnight to ensure homogeneity. These solutions were poured into Teflon formers and

placed in a stream of argon to assist solvent evaporation. The apparatus for argon assisted drying is shown in Figure 2.2.

After a few days, all visible traces of acetonitrile were gone and the bases were removed from the Teflon formers. At this stage, traces of solvent in the films made them tacky to touch. The films were then heated in a drying tube to 50°C under dynamic vacuum for several more days to remove the residual acetonitrile, leaving a dry polymer film. The films were usually about 0.2 to 0.5 mm thick.

Figure 2.2.

Apparatus for evaporation of solvent from polymer electrolyte solutions.



2.4 Instrumentation

2.4.1 Cell Design - General

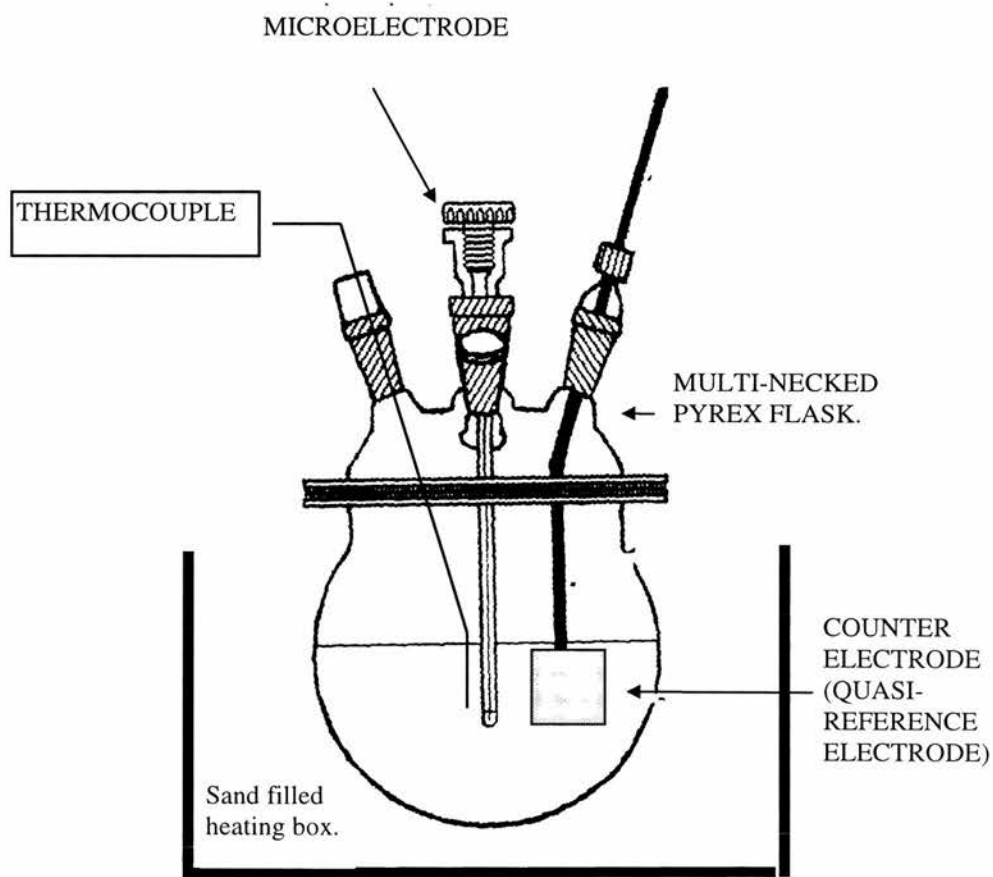
Electrochemical measurements were carried out using two-electrode cells, the design of which was determined by whether a liquid or solid electrolyte was to be studied. (Figures 2.3, 2.4 and 2.5.) In aqueous experiments, argon was bubbled through the water for 15 minutes in order to de-gas it prior to electrochemical measurements. The working electrode was a platinum microdisc of radius 5, 10 or 12.5 μm . The microelectrodes were supplied by Projekt, Warsaw, Poland. The counter electrode was a platinum gauze of approximate surface area 1 cm^2 or a lithium disc of similar surface area. The need for a third (reference) electrode was obviated by the low currents flowing in the cell. Such low currents (less than 10 nA) cause minimal potential changes at the relatively large counter electrode which thus acts as a quasi-reference electrode. All experiments were carried out within a Faraday cage.

2.4.2 Microelectrode Polishing

Microelectrodes were polished successively with 1.0, 0.3 and 0.05 μm alumina slurries prior to use. Slurries were prepared from the alumina and the electrolyte solvent. The alumina and polishing cloths were obtained from Buehler. After polishing, the electrodes were washed with the electrolyte solvent to remove the alumina and examined by optical microscope (400x magnification) to verify a smooth, clean surface. Immediately prior to immersion in the experimental cell, the electrodes were washed with a sample of the electrolyte solution.

Figure 2.3

Schematic of cell for liquid measurements



2.4.3 Counter/Quasi-Reference Electrode Preparation

Counter/quasi-reference electrodes of area around 1 cm^2 were made of platinum gauze or lithium. Prior to immersion in cells the platinum gauze was washed and heated to red heat in a blue Bunsen flame to remove impurities.

Figure 2.4

Schematic of cell for solid measurements

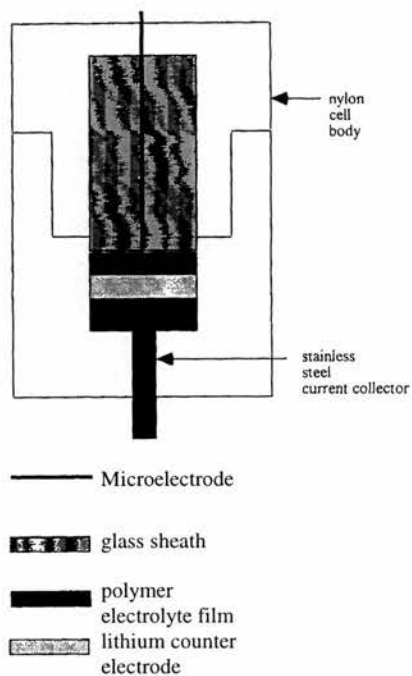
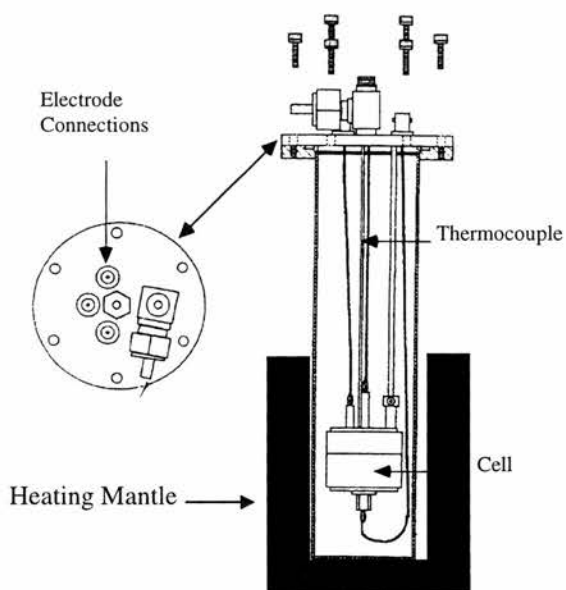


Figure 2.5

Schematic of faraday cage / heating mantle for solids cell



2.4.4 *Impedance Spectroscopy*

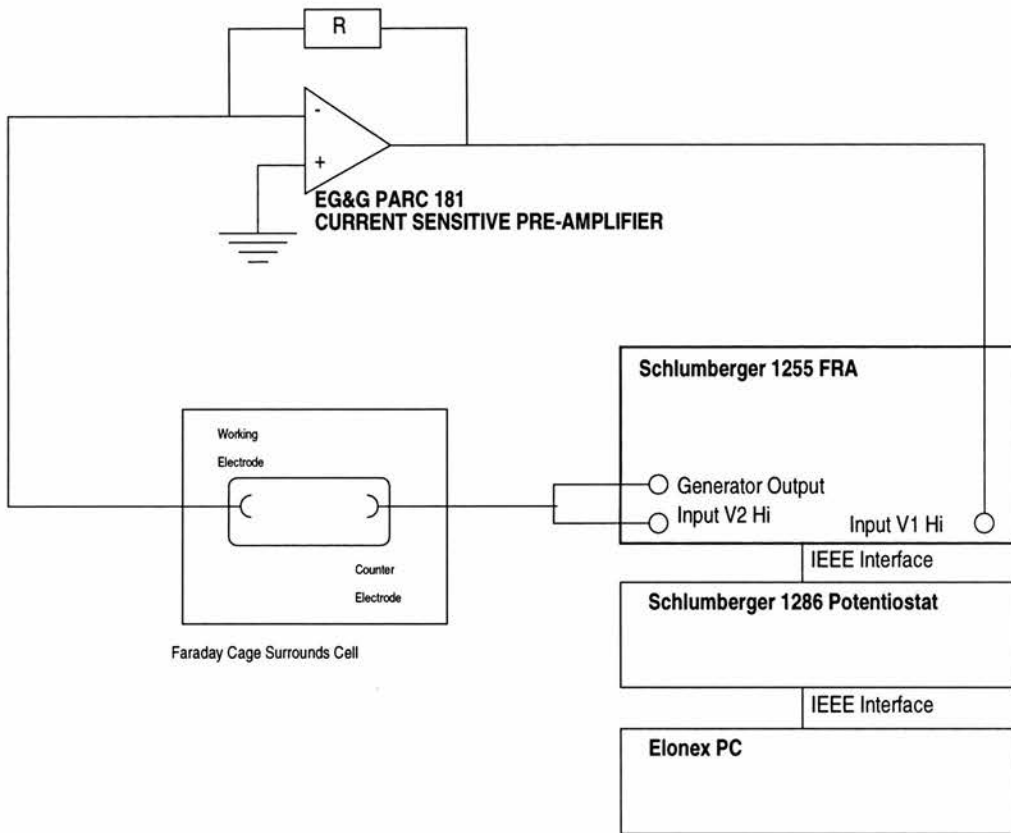
Impedance measurements were performed using the equipment shown in Figure 2.6. A low amplitude sinusoidal alternating potential (typically 10 mV r.m.s or less) was applied to the counter electrode by the generator output of a Solartron 1255 frequency response analyser (FRA). Depending on the experiment, a d.c. potential was also sometimes imposed on the ac signal using the 1255. The current at the microelectrode was amplified by an EG&G PAR preamplifier 181 before being fed to the input of the 1255. Coaxial BNC cables were used to connect the cell to the instruments. The instruments were driven by Z-plot software (Scribner Associates.) Frequency ranges between 500 kHz and 0.01 Hz were employed. Data were analysed using modified versions of the LEVM complex non-linear least squares (CNLS) fitting program written by Macdonald et al. ⁽³⁾

2.4.5 *Cyclic Voltammetry*

Voltammetric measurements were performed using an EG&G PAR Potentiostat / Galvanostat 273A driven by EG&G PAR echem software.

Figure 2.6

Apparatus for impedance spectroscopy at a microelectrode

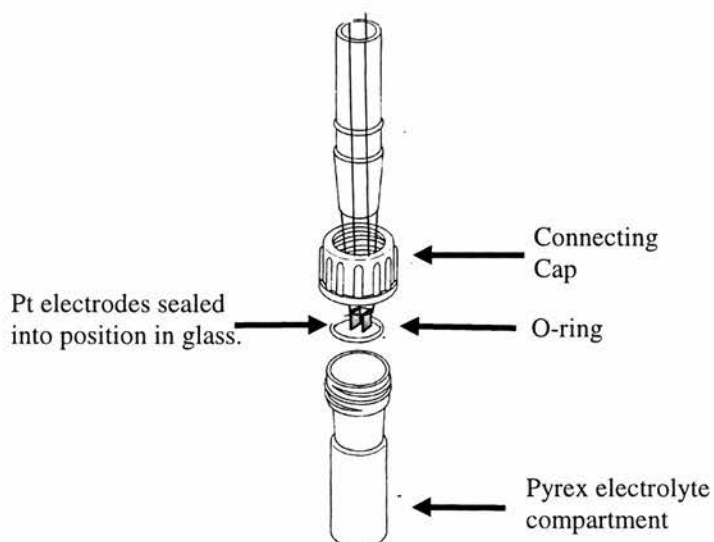


2.4.6 Conductivity

Conductivities were determined by impedance measurements using a Solartron 1255 FRA coupled to a Solartron 1286 potentiostat, driven, once again, by Z-plot software. The frequency response was monitored over the range 1 MHz - 1 Hz. Cells (Orion) were allowed to equilibrate in a thermostatically controlled water-bath at 25°C for one hour before measurements were made. A schematic of a conductivity cell is shown in Figure 2.7. The platinum electrodes were sealed into glass such that only one face of each electrode was in contact with the solution. The cell compartment was also made of glass into which the connecting cap with the electrodes was inserted. The cell had been factory calibrated with a cell constant of 1.0 cm⁻¹.

Figure 2.7

Schematic Of Glass Conductivity Cell



2.5 REFERENCES

1. D.D. Perrin and W.L.F. Armarego, Purification Of Laboratory Chemicals 3rd Edition, (1988), Pergamon Press.
2. L.R. Melby, R.J. Harder, W.R. Hertler, W. Mahler, R.E. Benson and W.E. Mochel, *J. Am. Chem. Soc.*, (1962), 84, p3374.
3. J.R. Macdonald LEVM Software Version 5 Manual, 1990.

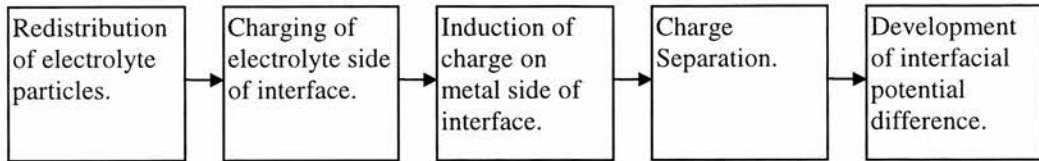
CHAPTER 3

ELECTROCHEMICAL THEORY AND MICROELECTRODE METHODS

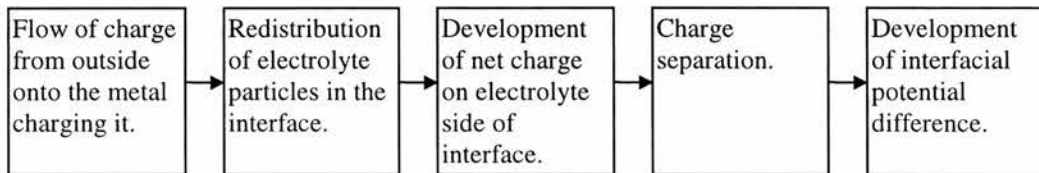
The importance of heterogeneous electron transfer was introduced briefly in Chapter 1. In this chapter, theories of the double-layer region and interfacial electron transfer will be introduced in more detail. Then the means by which impedance measurements and cyclic voltammetry at microelectrodes can elucidate mechanisms of interfacial electron transfer will be discussed.

3.1 An Introduction to Double-Layer Theory and the Faradaic and Non-Faradaic Impedances

If a metal electrode is placed into a liquid solvent, the solvent molecules nearest the metal interact with the metal's surface electrons, resulting in an ordering of dipoles or an accumulation of ionic charge in the solvent at the interface. Any accumulation of charge on the solvent side of the interface induces an equal and opposite charge on the metal, forming a double charged layer and hence an interfacial potential difference. The following schematic from Bockris and Reddy is a good summary of the process⁽¹⁾.



Alternatively, if the metal is connected to an external source of charge:

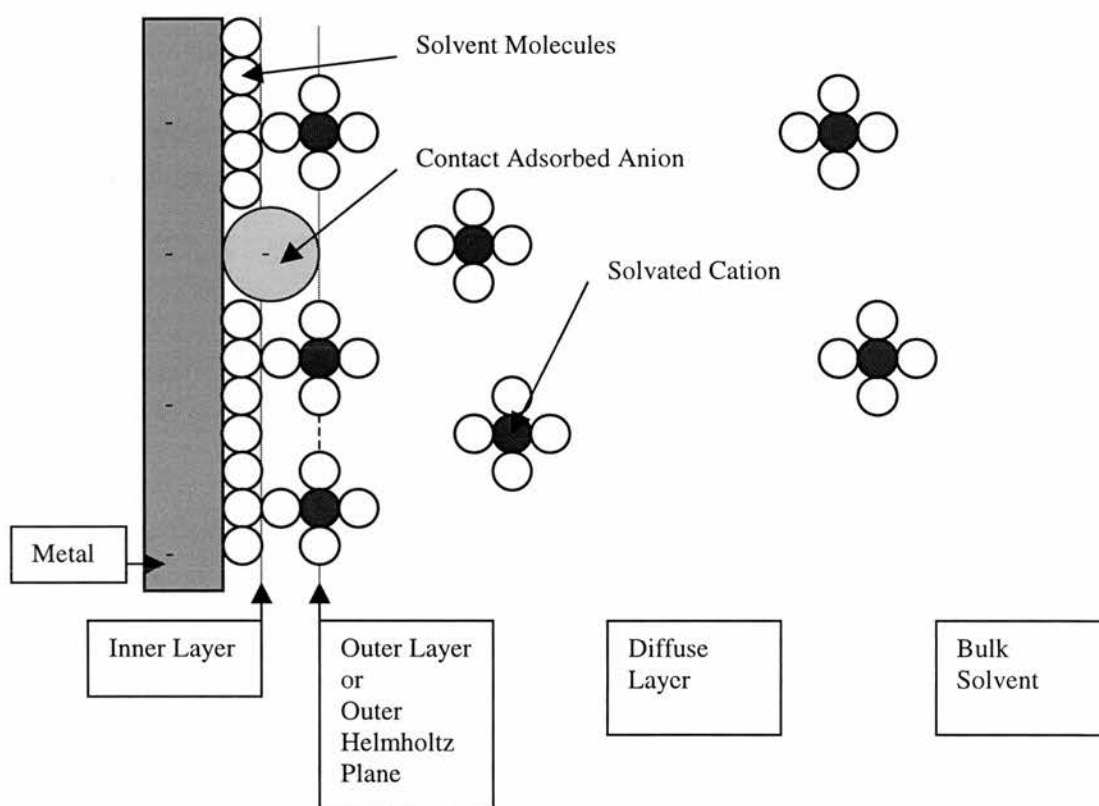


Helmholtz studied the region of the electrode/solution interface in the second half of the nineteenth century and modelled it as two rigid layers of opposite charge, hence the name *double layer*. Early in the twentieth century Gouy and Chapman produced independent models of the double layer. Each recognized that although the charge on an electrode is confined to the surface, the equal and opposite charge in solution will occupy a volume whose thickness is determined by the balance of electrostatic attraction and thermal agitation. They proposed a *diffuse layer* of charge in the solution. Figure 3.1 illustrates the concept of the double layer in which the greater the distance from the electrode, the more similar is the solution to bulk electrolyte. The closer to the electrode one looks, the more concentrated is the charge accumulation within the electrolyte until it reaches a peak at the outer layer or *outer Helmholtz plane* (OHP) where, in general, there is a layer of solvated ions whose charge is opposite to that on the electrode. The outer layer is separated from the opposing charge on the electrode by the electrode's own solvation layer and by

contact adsorbed species, if any. (Contact adsorption is caused by chemical interaction rather than simple electrostatic attraction of point charges. It is thus possible for a negatively charged metal to specifically adsorb negatively charged ions.)

Figure 3.1

2-Dimensional schematic of the double layer region



It is evident that the charge separation at the double layer resembles a parallel plate capacitor. Any flow of electrons which does not bring about oxidation or reduction but instead results in charge differentiation at the interface is said to be charging or discharging the double layer capacitor. Such current is termed *non-faradaic*. Current causing or resulting from redox reactions is termed *faradaic*.

By measuring the faradaic current the rates of electrochemical reactions can be determined. To characterise an electrochemical cell, it is necessary to employ experimental methods capable of identifying that proportion of the current which is faradaic and that which is non-faradaic. As will be shown in Chapter 4, for example, it is one of the inherent advantages of impedance methods that non-faradaic current is accounted for by placing an appropriate element in the equivalent circuit (see section 3.2.1.) In other methods the non-faradaic current may interfere with measurement of the faradaic current.

3.1.1 Equations for the Faradaic Impedance

The faradaic current is dependent on the number of electrons taking part in a reaction, the rate constant for electron transfer, the concentration of the redox species and the potential driving the electron transfer. Equation [3.1], the absolute rate equation, relates the faradaic current to the electrochemical properties of a system ⁽²⁾.

$$i_f = nFk_s \left\{ C_R \exp\left[\frac{\alpha nF}{RT}(E - E^o)\right] - C_o \exp\left[\frac{-\beta nF}{RT}(E - E^o)\right] \right\} \quad [3.1]$$

The symbols used in equation [3.1] are defined as follows. i_f is the faradaic current density (i.e. faradaic current divided by electrode area), k_s is the standard

heterogeneous rate constant for electron transfer (units cm s^{-1})[#], E is the electrode potential, E° is the formal standard electrode potential, C is the concentration of the redox species (O or R) at the electrode surface, n is the number of electrons transferred and F is the Faraday constant. α and β are the anodic and cathodic transfer coefficients. It is believed that the size of each transfer coefficient indicates the fraction of interfacial potential driving the electron-transfer reaction through its transition state to oxidation or reduction. The sum of α and β is unity, i.e. $\beta = 1 - \alpha$. Often α and β values are close to 0.5 and the equality of α and β was assumed for the systems studied in this thesis. This is justified on the basis of published values for the transfer coefficients for electrochemical cells similar or identical to the ones used here. For example, reference 7 to Chapter 5 and reference 7 to chapter 8.

It is possible, starting with the absolute rate equation, to derive an expression for the faradaic impedance which can be used in impedance spectroscopy. The outline of the derivation given here follows the approach in papers published by Sluyters-Rehbach, Sluyters and Timmer^{(2), (3)}.

If it is assumed that the faradaic current has both ac and dc components, i_{ac} and i_{dc} associated with potentials E_{ac} and E_{dc} but that these components do not influence one another then equation [3.1] can be rewritten as;

[#] Strictly speaking, k_s should be described as the *apparent* standard heterogeneous rate constant. The true standard heterogeneous rate constant is defined with respect to activities.

$$i_f = i_{dc} + i_{ac} = nFk_s \left\{ \begin{array}{l} (C_{Rdc} + C_{Rac}) \exp\left[\frac{\alpha nF}{RT} (E_{dc} + E_{ac} - E^o)\right] \\ - (C_{Odc} + C_{Oac}) \exp\left[\frac{-\beta nF}{RT} (E_{dc} + E_{ac} - E^o)\right] \end{array} \right\} \quad [3.2]$$

Restricting E_{ac} to small amplitudes and expanding the ac components of the exponential functions as a Maclaurin series of the first power yields:

$$i_f = i_{dc} + i_{ac} = nFk_s \left\{ \begin{array}{l} (C_{Rdc} + C_{Rac}) \left(1 + \frac{\alpha nF}{RT} E_{ac}\right) \exp(\alpha\varphi) \\ - (C_{Odc} + C_{Oac}) \left(1 - \frac{\beta nF}{RT} E_{ac}\right) \exp(-\beta\varphi) \end{array} \right\} \quad [3.3]$$

$$\text{where } \varphi = \frac{nF}{RT} (E_{dc} - E^o).$$

Expressing the equation now as the ac component of the faradaic current and multiplying out the brackets in [3.3] gives:

$$i_{ac} = i_f - i_{dc} = i_f - nFk_s [C_{Rdc} \exp(\alpha\varphi) - C_{Odc} \exp(-\beta\varphi)] \quad [3.4]$$

$$i_{ac} = nFk_s \left(C_{Rdc} \frac{\alpha nF}{RT} E_{ac} \exp(\alpha\varphi) + C_{Rac} \frac{\alpha nF}{RT} E_{ac} \exp(\alpha\varphi) + C_{Rac} \exp(\alpha\varphi) \right) \quad [3.5]$$

$$- nFk_s \left(- C_{Odc} \frac{\beta nF}{RT} E_{ac} \exp(-\beta\varphi) - C_{Oac} \frac{\beta nF}{RT} E_{ac} \exp(-\beta\varphi) + C_{Oac} \exp(-\beta\varphi) \right)$$

All terms containing the product of C_{ac} and E_{ac} are negligible compared to the others and can be removed, yielding;

$$i_{\max} \sin \omega t = nFk_s \left(\frac{nFE_{ac}}{RT} [\alpha C_{Rdc} \exp(\alpha\phi) + \beta C_{Odc} \exp(-\beta\phi)] + [C_{Rac} \exp(\alpha\phi) - C_{Oac} \exp(-\beta\phi)] \right) \quad [3.6]$$

Equation [3.6] now explicitly recognises the alternating current as sinusoidal with angular frequency ω . (See Section 3.2.2.) Re-arranging [3.6] as a function of E_{ac} gives:

$$E_{ac} = \frac{RTi_{\max} \sin \omega t}{n^2 F^2 k_s (\alpha C_{Rdc} \exp(\alpha\phi) + \beta C_{Odc} \exp(-\beta\phi))} + \frac{RT}{nF} \frac{C_{Oac} \exp(-\beta\phi) - C_{Rac} \exp(\alpha\phi)}{(\alpha C_{Rdc} \exp(\alpha\phi) + \beta C_{Odc} \exp(-\beta\phi))} \quad [3.7]$$

The *ac* voltage is now separated into the series sum of a charge transfer component, containing the standard heterogenous rate constant, and a mass transfer component. Both of these processes have impedances, therefore we can write for the faradaic *ac* impedance:

$$Z_f = Z_{ct} + Z_{mt} \quad [3.8]$$

Indeed, to find the impedance to charge transfer, Z_{ct} , the relevant portion of [3.7] requires now only to be divided by current to give a pure resistance. To find the mass transport impedance, or more precisely the diffusion impedance, a little

further mathematics is required. These impedances are considered in the following sections.

3.1.2 The Charge Transfer Impedance in a System at Equilibrium

Equating Z_{ct} from [3.8] with the charge transfer component of E_{ac} in [3.7] and dividing by current density yields the charge transfer resistance, Θ_{ct} , (dimensions $\Omega \text{ cm}^2$);

$$\Theta_{ct} = \frac{RT}{n^2 F^2 k_s [\alpha C_{Rdc} \exp(\alpha\varphi) + \beta C_{Odc} \exp(-\beta\varphi)]} \quad [3.9]$$

This equation describes the impedance to charge-transfer but, because it contains expressions relating to the (generally) unknown surface concentrations of the redox species, it is difficult to use in practice. It is desirable to replace the surface concentrations with (known) bulk concentrations. This is straightforward for a system in equilibrium, as the Nernst equation^(3b) applies and:

$$\exp(\varphi) = C_{Obulk}/C_{Rbulk} \quad (= C_{Odc}/C_{Rdc}) \quad [3.10]$$

A little algebra yields:

$$\Theta_{ct eq} = \frac{RT}{n^2 F^2 k_s (C_{Obulk})^\alpha (C_{Rbulk})^\beta} \quad [3.11]$$

If it is more convenient both sides of [3.11] can be divided by the electrode area, A, to give R_{ct} in Ohms.

$$R_{ct} = \frac{RT}{n^2 F^2 k_s A (C_{O_{bulk}})^\alpha (C_{R_{bulk}})^\beta} \quad [3.12]$$

Expressions [3.11] and [3.12] can be used practically for systems in equilibrium. Provided the bulk concentrations of the redox species are known R_{ct} can be determined using impedance spectroscopy (Section 3.2) and the apparent standard rate constant for an electron transfer process deduced.

3.1.3 The Diffusion Impedance in a System at Equilibrium

There are three mechanisms of mass transport in electrolytes - *diffusion, migration and convection*^(4a). The rate of mass-transport to an electrode is a function of these three mechanisms and is described in the Nernst-Planck equation, written here for mass transport in one dimension;

$$J = -D \frac{\delta C}{\delta x} - \frac{zF}{RT} DC \frac{\delta \phi}{\delta x} + C v \quad [3.13]$$

where (for the electroactive species); J is the flux, D is the diffusion coefficient, ϕ is the potential, z is the charge, C the concentration and v is the velocity of a volume element with respect to the electrode. It is well known that methods are available which make negligible the mass transported by convection and migration. Unstirred systems (i.e. those neither mechanically agitated nor with flow resulting from density gradients) and solid systems can be assumed to exhibit negligible convection. Migration can be made negligible by means of a *supporting or background electrolyte*. The supporting/background electrolyte is an ionic species that takes no part in the reaction at the electrode. It is present in excess concentration (often about 100 times greater than the electroactive species) to ensure that the potential drop over any given ion of the electroactive species is greatly reduced and migration of electroactive species is made negligible.

If it is assumed that all of the material at the electrode arrives by diffusion then Fick's laws can be used to derive the solution for mass transport in an alternating field. Fick's 2nd Law for linear diffusion may be written as:

$$\frac{\partial C_{ac}(x,t)}{\partial t} = D \frac{\partial^2 C_{ac}(x,t)}{\partial x^2} \quad [3.14]$$

where x is displacement from the electrode surface and t is time. To solve [3.14] the initial condition is that the concentration at the electrode surface is equal to that in the bulk and the boundary conditions used are;

$$i_{ac} = -nFD_O \left(\frac{\partial C_{Oac}}{\partial x} \right)_{x=0} = nFD_R \left(\frac{\partial C_{Rac}}{\partial x} \right)_{x=0} \quad [3.15]$$

and

$$(C_{Oac})_{x=\infty} = (C_{Rac})_{x=\infty} = 0 \quad [3.16]$$

Equation [3.15] states that the current owing to diffusion is dependent on the concentration gradient and the diffusion coefficient, D . The magnitude of D is dependent on how quickly the diffusing molecule moves through the medium surrounding it. It is thus dependent on the molecule's size and the medium's viscosity.

Equation [3.16] is the semi-infinite boundary condition and requires that at infinite distance from the electrode the concentrations of redox species resulting from the ac perturbation are zero and hence are equal to those in the bulk. (The justification for this condition is that it takes a relatively long time for a concentration gradient to spread throughout an electrochemical cell. Since the signal frequencies used in an impedance experiment are typically in the range of 10^5 Hz to 10^{-1} Hz, the concentration gradient never gets enough time to spread throughout the cell.) The solution of [3.14] with the above conditions yields an equation in x . By setting x equal to zero one finds that:

$$C_{ac} = \frac{i_{\max} (\sin \alpha x - \cos \alpha x)}{nF(2\alpha D)^{1/2}} \quad [3.17]$$

This equation is in fact valid for combined ac and dc current provided that the time dependence of the dc component is small and that the concentration gradient due to the dc current is linear. The equations above describe *semi-infinite linear diffusion*.

Substituting [3.17] into [3.7] yields:

$$E_{ac} = \left\{ \begin{array}{l} \frac{RTi_{\max} \sin \alpha}{n^2 F^2 k_s [\alpha C_{Rdc} \exp(\alpha\varphi) + \beta C_{Odc} \exp(-\beta\varphi)]} \\ + \frac{RTi_{\max} (\sin \alpha - \cos \alpha)}{\sqrt{2\omega} n^2 F^2} \left(\frac{D_R^{-1/2} \exp(\alpha\varphi) + D_O^{-1/2} \exp(-\beta\varphi)}{\alpha C_{Rdc} \exp(\alpha\varphi) + \beta C_{Odc} \exp(-\beta\varphi)} \right) \end{array} \right\} \quad [3.18]$$

Equating Z_{mt} from [3.8] with the appropriate voltage in [3.18] and dividing by current density yields the mass transport impedance, Θ_{mt} , (dimensions $\Omega \text{ cm}^2$);

$$\Theta_{mt} = \frac{(1-j)RT}{\sqrt{2\omega} n^2 F^2} \left(\frac{D_R^{-1/2} \exp(\alpha\varphi) + D_O^{-1/2} \exp(-\beta\varphi)}{\alpha C_{Rdc} \exp(\alpha\varphi) + \beta C_{Odc} \exp(-\beta\varphi)} \right) \quad [3.19]$$

Equation [3.19] was obtained by substituting equation [3.17] into [3.7]. Any constraints on the use of equation [3.17] also apply to [3.19] and this equation, therefore, is applicable to situations in which there is semi-infinite linear diffusion. In other words equation [3.19] is valid for situations in which the size of the cell is large enough that the diffusion layer may extend unimpaird by physical boundaries and that the concentration profile of the diffusion layer is linear. i.e. the electrode is large compared with the size of the diffusion layer and planar.

Like equation [3.9], equation [3.19] contains expressions relating to the unknown surface concentrations of the redox species. By assuming, once again, that the system is in equilibrium and $\exp(\varphi) = C_{O_{bulk}}/C_{R_{bulk}}$ ($= C_{O_{dc}}/C_{R_{dc}}$) equation [3.20] describing the *Warburg Impedance*, Z_w , which has both real and imaginary components (see Sections 3.2.5 and 3.2.6) is found;

$$Z'_w = Z''_w = (\sigma_o + \sigma_R)\omega^{-1/2} \quad [3.20]$$

$$\Theta_{mt\ eq} = Z_w = \sigma_{eq} \left(\frac{1-j}{\omega^{1/2}} \right)$$

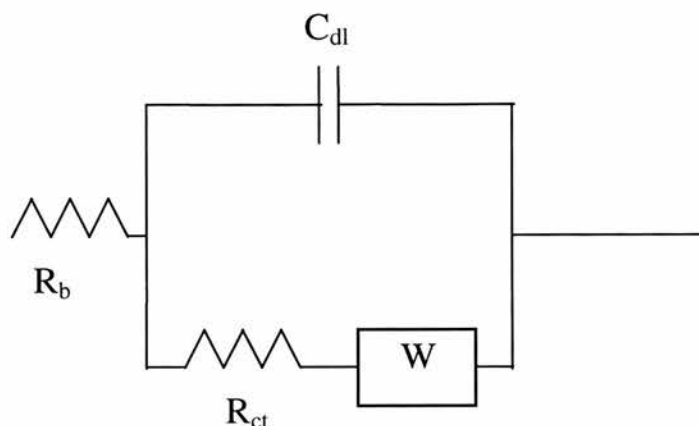
$$\sigma_{eq} = \frac{RT}{\sqrt{2}n^2F^2} \left(\frac{1}{C_{O_{bulk}}D_O^{1/2}} + \frac{1}{C_{R_{bulk}}D_R^{1/2}} \right)$$

The imaginary component of the Warburg impedance in [3.20] is indicated by the appearance of j , the square root of minus one. The reasons why it is preferable to make use of complex numbers in describing impedance are discussed in Section 3.2.5.

The equivalent circuit (see Section 3.2.1) used to describe an electrochemical system with charge transfer impedance, R_{ct} , and Warburg impedance, W , is known as the Randles equivalent circuit (Figure 3.2). This circuit also contains elements representing the double-layer capacitance, C_{dl} , and the electrolyte or bulk resistance R_b . The separation of faradaic and non-faradaic elements in the Randles circuit suggests that these elements may be readily separated using impedance spectroscopy.

Figure 3.2

The Randles equivalent circuit



3.2 Electrochemical Impedance Spectroscopy

3.2.1 Impedance Spectroscopy and Electric Circuits

The fundamental premise of impedance spectroscopy is that the response of an electrochemical cell to ac perturbations of different frequencies could also have been obtained by applying the signal to an electric circuit, the *equivalent circuit*, consisting of electric circuit elements such as resistors and capacitors. From the configuration of elements making up a cell's equivalent circuit the electrochemist can draw inferences about the cell's electrochemical properties while from the numerical values of the equivalent circuit elements, numerical values can be placed on the electrochemical properties. In much of the work reported here impedance spectroscopy is used to study the electrode/electrolyte interface of electrochemical cells. Although in practice no equivalent circuit behaves exactly like an interface,

sufficient theory has been accumulated this century to make satisfactory comparisons possible, leading to increased understanding of electrical and chemical processes at the interface. A more extensive general introduction to impedance spectroscopy is given by Bruce⁽⁵⁾.

3.2.2 *The Resistor in an AC Circuit*

When a sinusoidally varying potential is applied to a resistor, at any time t , the voltage v across the resistor is given by;

$$v = v_0 \sin \omega t \quad [3.21]$$

where v_0 is the voltage amplitude and ω is the angular frequency of the sine wave.

The current passing through the resistor is given by Ohm's law, $v = iR$, hence;

$$i = \frac{v_0 \sin \omega t}{R} \quad [3.22]$$

$$\Rightarrow i = i_0 \sin \omega t \quad [3.23]$$

where i_0 is the current amplitude. The current i reaches maximal and minimal values at the same time as does v ; thus current and voltage are in phase with one another.

3.2.3 The Capacitor in an AC Circuit

The charge q stored by a capacitor is;

$$q = Cv \quad [3.24]$$

where C is the capacitance. The effect of applying a sinusoidally varying voltage at a capacitor is given by substituting equation [3.21] in [3.24];

$$q = C v_0 \sin \omega t \quad [3.25]$$

$$\text{but} \quad i = dq/dt \quad [3.26]$$

$$\text{hence} \quad i = \omega C v_0 \cos \omega t \quad [3.27]$$

$$= \omega C v_0 \sin (\omega t + \pi/2) \quad [3.28]$$

$$\Rightarrow \quad i = i_0 \sin (\omega t + \pi/2) \quad [3.29]$$

Dimensional analysis of equation [3.28] shows that $1/\omega C$ has dimensions of Ω and thus is similar to electrical resistance. Unlike resistance, however, $1/\omega C$ depends on the frequency of the applied signal. The term *impedance* is used to encompass processes whose dimensions are Ohms but whose properties may otherwise differ.

$1/\omega C$ is often called *reactance*. It is apparent that reactance is lowest at high frequencies. To characterise an electric circuit's impedance behaviour with respect to a signal varying with time, analysis of the current and voltage phases is required. Comparison of equations [3.23] and [3.29] shows that, for a capacitor, the voltage and current are out of phase by $\pi/2$ radians - the current is said to lead the voltage by $\pi/2$ radians. This is illustrated in Figure 3.3.

Figure 3.3
Current leading voltage by $\pi/2$.

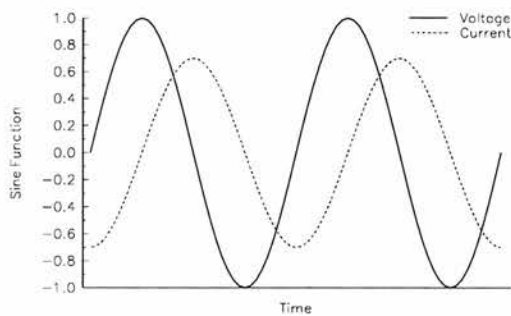
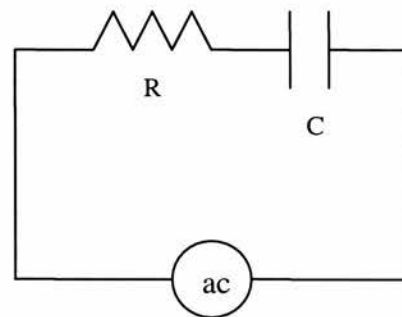


Figure 3.4
The capacitor and resistor in series in an ac circuit.



3.2.4 The Capacitor and Resistor in Series in an AC Circuit

It was established in the previous sections that v and i are in phase in a resistor but out of phase by $\pi/2$ in a capacitor. In any series circuit all elements must carry the same current; hence in a series RC circuit, such as that shown in Figure 3.4, the voltage across the capacitor lags that across the resistor by $\pi/2$. This is shown on the voltage vector diagram in Figure 3.5 where the voltage across the resistor is drawn on the x-axis and that across the capacitor on the y-axis. By tradition, electrochemists draw $-v_c$ on the positive part of the y-axis so that plots lie in the first rather than the fourth quadrant.

Figure 3.5
Vector diagram of voltages
in an RC series circuit

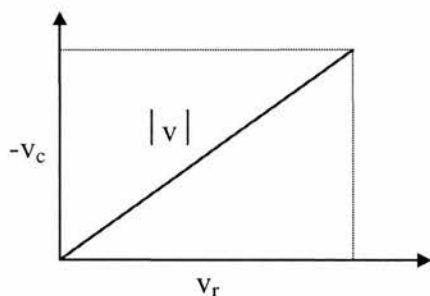
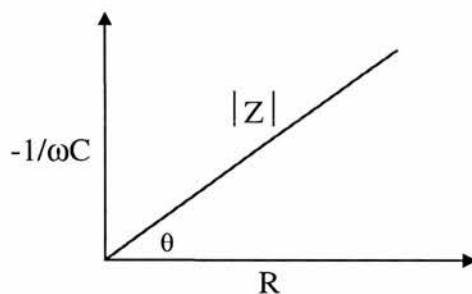


Figure 3.6
The impedance diagram



Since $v_c = i/\omega C$ and $v_r = iR$, dividing the voltage axes in Figure 3.5 by i results in an *impedance diagram* (Figure 3.6) in which the axes have units of Ohms. The angle θ in Figure 3.6 describes the phase angle between the impedance of the circuit and the pure resistance; thus low values of θ indicate mainly resistive impedance while high phase angles indicate mainly reactive impedance.

3.2.5 Impedance and how it may best be described

Impedance, \mathbf{Z} , is a vector of magnitude $|\mathbf{Z}|$ and phase-angle Θ . There are different vector approaches that could be taken to manipulate impedance data. For example, the polar co-ordinate system (r, Θ) could be used as shown in Figure 3.7 where $|\mathbf{Z}| \cos\Theta$ is plotted on the x-axis and $|\mathbf{Z}| \sin\Theta$ on the y-axis.

Figure 3.7
Polar co-ordinate diagram
of impedance

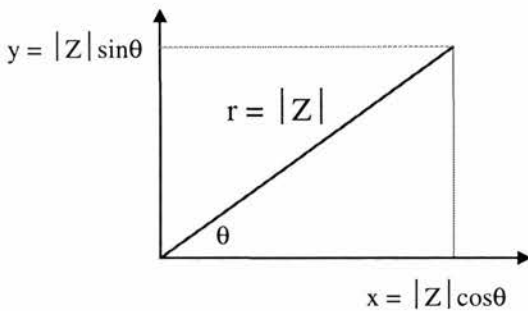
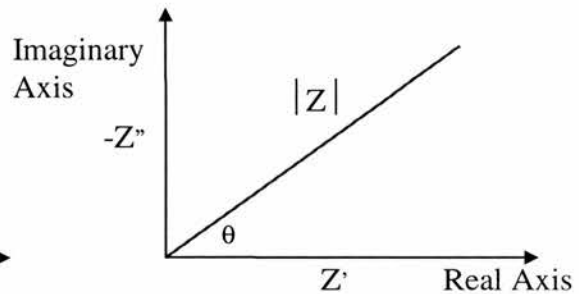


Figure 3.8
Complex plane plot
of the impedance vector \mathbf{Z}^*



The polar co-ordinate system is in fact very similar to the complex number co-ordinate system, in which the impedance vector $(|\mathbf{Z}|, \Theta)$ is given by;

$$\mathbf{Z}^* = |\mathbf{Z}| (\cos \Theta + j \sin \Theta) \quad [3.30]$$

where j is $\sqrt{-1}$. The x and y axes are described as the real (Z') and imaginary (Z'') axes respectively. \mathbf{Z}^* can be expressed simply in the *complex plane*, shown in Figure 3.8. The advantage of using complex-numbers is that manipulation of trigonometric functions in the polar co-ordinate system can be dispensed with in

favour of the straightforward rules of complex-number algebra. For example, expressing [3.30] in terms of the complex plane one finds;

$$\mathbf{Z}^* = \mathbf{Z}' - j\mathbf{Z}'' \quad [3.31]$$

Since \mathbf{Z}' describes the resistive part of a circuit and $-\mathbf{Z}''$ the capacitive reactance part it is apparent that the impedance of a resistor and capacitor in series is;

$$\mathbf{Z}^* = R - j/\omega C \quad [3.32]$$

3.2.6 *The Complex Plane Plot*

In order to interpret the shapes of complex plane plots, there are two key circuits whose spectra must be understood; the series RC circuit and the parallel RC circuit.

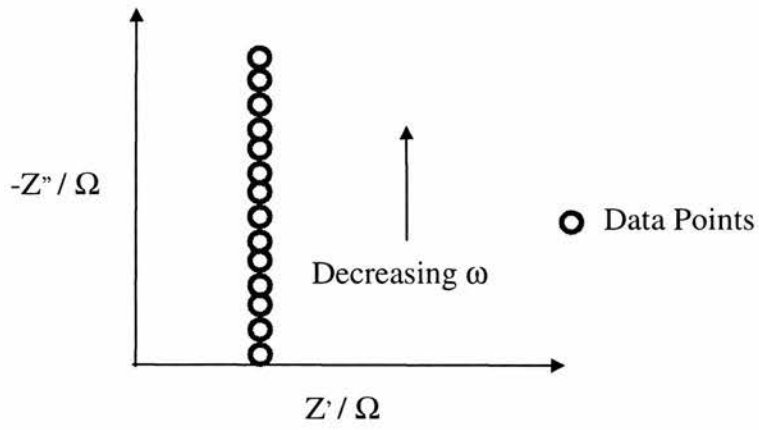
(a) *The Series RC Circuit*

Consider the effect of changing the frequency of the sine wave signal in a series RC circuit. Equation [3.32] shows that the resistance is constant while the reactance is inversely proportional to frequency, falling to zero in the limit of infinite frequency. If the impedance \mathbf{Z}^* was measured at a series of different frequencies the complex plane plot which would result is shown schematically in Figure 3.9. The magnitude of the resistance is calculated from the intersection of the data with the \mathbf{Z}' axis and

the magnitude of the reactance and hence capacitance may be calculated from any data point.

Figure 3.9

The complex plane plot of a series RC circuit



(b) The Parallel RC Circuit

The parallel RC circuit, shown in Figure 3.10, yields the complex plane plot in Figure 3.11.

Figure 3.10
The parallel RC circuit

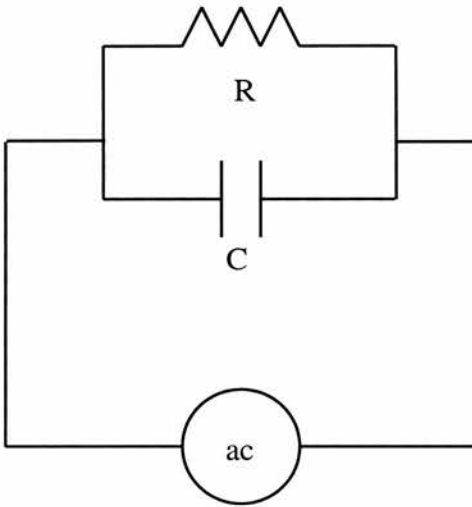
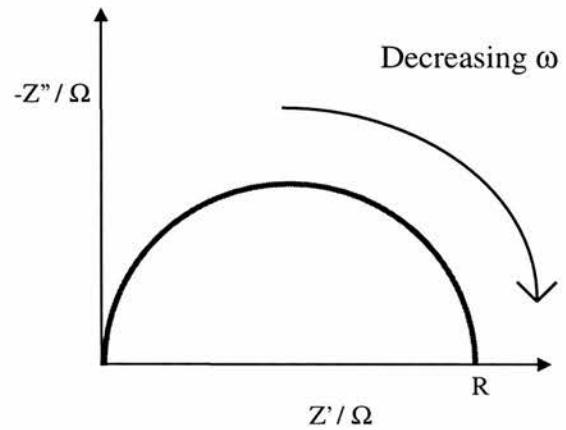


Figure 3.11
The complex plane plot of
the parallel RC circuit.



The complex plane plot of the parallel RC circuit is a semi-circle. The reason for this is apparent from the impedance equation for the circuit. In a parallel circuit the reciprocal of total impedance is the sum of the reciprocals of the individual impedances:

$$\frac{1}{Z^*} = \frac{1}{R} + j\omega C \quad [3.33]$$

By taking reciprocals of both sides of equation [3.33] an expression for Z^* is found;

$$Z^* = \frac{R}{(1 + j\omega CR)} \quad [3.34]$$

Multiplying the numerator and denominator of [3.34] by the complex conjugate, $(1 - j\omega CR)$ removes j from the denominator, yielding;

$$Z^* = \frac{R - j\omega CR^2}{1 + (\omega CR)^2} \quad [3.35]$$

Finally this expression is split into its real and imaginary parts which are equal to Z' and Z'' , (i.e., $Z^* = Z' - jZ''$), therefore;

$$Z' = \frac{R}{1 + (\omega CR)^2} \quad [3.36]$$

$$Z'' = \frac{\omega CR^2}{1 + (\omega CR)^2} \quad [3.37]$$

When these expressions for Z' and Z'' are plotted in the complex plane the characteristic semi-circle associated with the parallel RC circuit is obtained. Using equations [3.36] and [3.37] the values of the circuit elements may be obtained readily from the plot. In the low frequency limit $Z' = R$ and $Z'' = 0$, i.e. the low frequency intercept of the semi-circle with the Z' axis yields the resistance of the

resistor R. When $Z' = Z''$ it is clear by equating the right hand sides of equations [3.36] and [3.37] that $\omega CR = 1$. This condition is satisfied uniquely at the highest point on the semi-circle. Thus;

$$\omega_{(z'=z'')} CR = 1 \quad [3.38]$$

or

$$\omega_{(z'=z'')} = \frac{1}{RC} \left(= \frac{1}{\tau} \right) \quad [3.39]$$

It is evident from equation 3.39 that semi-circles appear at different frequencies in impedance spectra depending on the value of the time-constant, τ .

This brief introduction has endeavoured to show that impedance plots can be a valuable method for characterizing simple electric circuits. It is possible to extrapolate from this and show that a spectrum with two semi-circles indicates a circuit composed of the series arrangement of two parallel RC circuits, etc. In order to use impedance methods to study an electrochemical cell, the electrochemist must begin by proposing an equivalent circuit for the cell. The response of the actual cell may then be compared with the theoretical circuit over a range of conditions. Indeed it is now well established that spectra can be related to the chemical and electrical process within the cell at the molecular level ^{(5) to (8)}. In the study reported here, correct interpretation of impedance data is the means by which it is hoped interfacial processes will be identified and quantified.

3.3 Comparison Of Properties Of Microelectrodes and Normal Electrodes and Derivation of The Exact Solution for Diffusion to a Microdisc

3.3.1 General

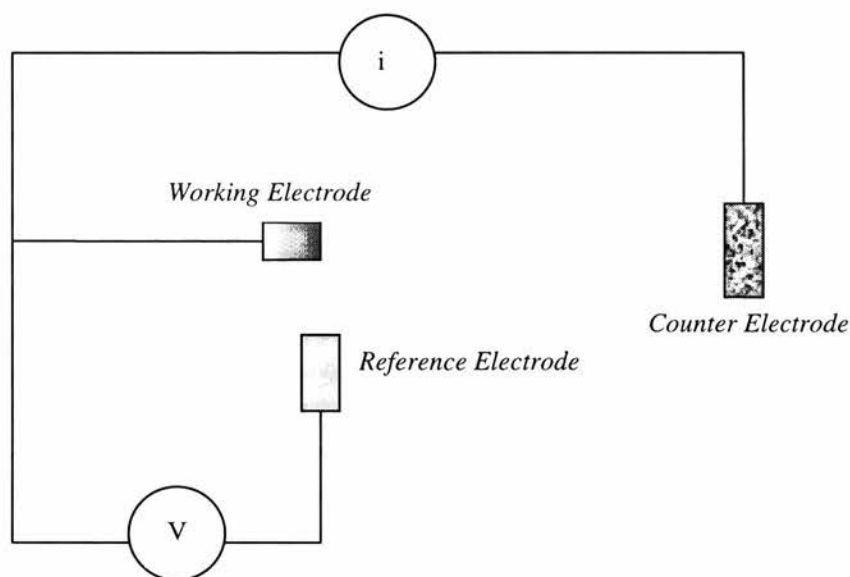
The objective of much of the work reported in this thesis is to quantitatively model the electrochemical processes at the electrode-electrolyte interface. Very small electrodes provide an excellent means of achieving this. In order to see why, the advantages of the microelectrode over the normal electrode are demonstrated and discussed in this section. A microelectrode is defined here as one with at least one dimension small enough so that under the prevailing experimental conditions the diffusion flux to the electrode surface is greater than would be obtained if there were linear diffusion. Only disc shaped microelectrodes were employed in this work. The geometry of this type of electrode is reflected in its nomenclature and the term *microdisc* appears often in this thesis. Ribes and Osteryoung have discussed microelectrode definitions and nomenclature ⁽⁹⁾.

3.3.2 Two-electrode and Three-electrode Cells

When normal sized electrodes are employed in electrochemical cells, it is traditional to configure a three-electrode cell consisting of working, counter and reference electrode as shown in Figure 3.12.

Figure 3.12

Schematic diagram of a three electrode cell.



A variety of different electrodes are employed as references. One commonly employed is the calomel electrode ^(1c). The critical property of a reference electrode is that its potential should stay constant during experiments, hence the use of *non-polarisable* electrodes such as the calomel electrode. (An ideal non-polarisable electrode is one whose potential does not change when current flows.) The non-polarisable reference electrode is used in conjunction with a high impedance voltmeter that renders the current flow through the reference electrode negligible.

Thus, by minimising both current and the potential response to the current, the reference electrode provides a constant potential relative to which changes in potential at the working electrode may be measured. The counter electrode is an inert material that passes current. Measurements are made of the current flowing through the working electrode versus the potential difference between the working and reference electrodes.

When the working electrode is a microelectrode and the counter electrode is of normal size the necessity of a reference electrode is often obviated. This is because the difference in surface areas between the working microelectrode and the counter electrode is many orders of magnitude. In the experiments reported in this thesis, the surface areas differ typically by a factor of one million. The result of this is that the current density and resulting potential change at the counter electrode is negligible in comparison to potential changes at the working microelectrode. For all practical purposes the counter electrode has become a reference electrode. In two-electrode microelectrode experiments the counter electrode is described as a *quasi reference electrode*.

3.3.3 Impedance at Normal and Microelectrodes

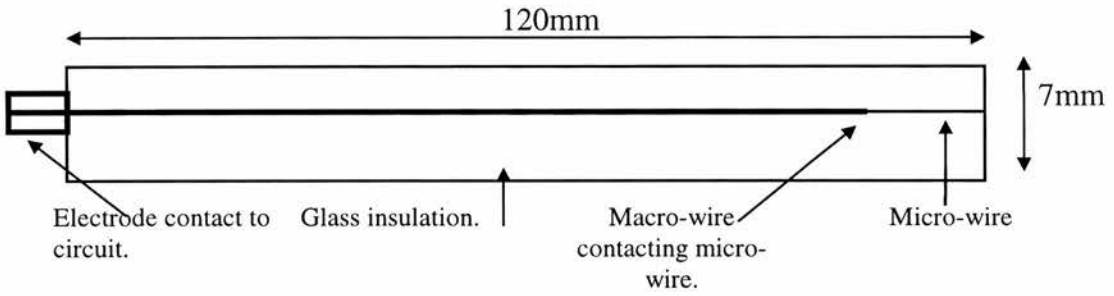
Equations [3.8], [3.11] and [3.20] provide the means of quantitatively describing the faradaic impedance for an electrochemical cell at equilibrium. The applicability of the equations is determined by the boundary conditions used to derive them. No boundary conditions were used to derive the charge transfer resistance equation. It can therefore be applied with equal validity at micro and normal sized electrodes. In the case of the Warburg diffusion impedance the boundary conditions used were in linear (Cartesian co-ordinate) form and apply only at infinite, planar electrodes. Thus the equations for the Warburg impedance are valid only for electrodes which are large in comparison to the width of the diffusion layer. (The absolute value of the concentration gradient falls as displacement from the electrode increases. The diffusion layer extends from the electrode until the gradient tends to zero. Of course, the gradient becomes zero when the concentration of species becomes identical to that of the bulk electrolyte.) The graph of Z' against Z'' for the Warburg impedance is a straight line of unit slope; hence an impedance spectrum consisting simply of a straight line of unit slope is indicative of an electrochemical cell where the current flowing to a *normal sized planar electrode* is under diffusion control.

In order to describe the diffusion impedance to a microelectrode, Fick's laws must be solved with appropriate boundary conditions. Cartesian co-ordinates, as mentioned above, are convenient to describe planar diffusion to an infinite plane. A microelectrode, however, is not an infinite plane but a very small surface area, which may be flat, or curved. Various views of a microdisc are shown schematically in Figure 3.13.

Figure 3.13

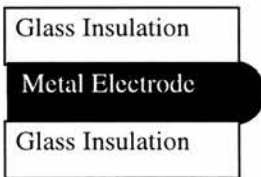
Schematics of a typical microdisc

a. Side view of a microdisc

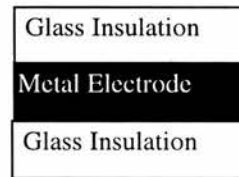


b. Side view of a microdisc magnified for comparison with a microhemisphere

The microhemisphere

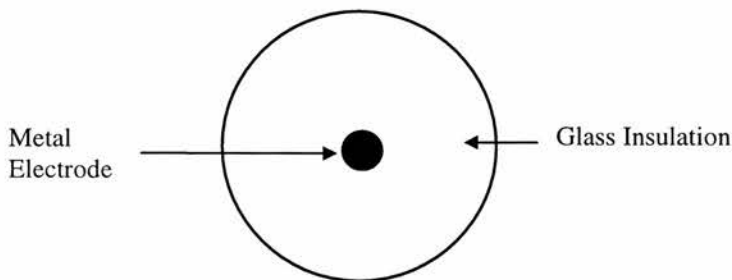


The microdisc



c. End view of the microdisc

(Diameter of the metal disc enlarged for clarity.)



While relatively simple equations may be derived to describe diffusion to spherical or hemispherical microelectrodes, derivation of equations for the microdisc is complicated by discontinuities in the diffusion field where the electrically conducting disc meets the electrically insulating glass sheath around the disc.

Despite the difficulties, since microdiscs are easy to make and, other than in the case of mercury, micro-hemispheres are not, diffusion equations have been derived for the microdisc. The outline of the derivation below follows that of Fleischmann and Pons^{(10), (11)}.

Firstly, to describe diffusion to the microdisc, Fick's 2nd Law is written in cylindrical co-ordinates;

$$\frac{\partial^2 C}{\partial r^2} + \frac{1}{r} \frac{\partial C}{\partial r} + \frac{\partial^2 C}{\partial z^2} = 0 \quad [3.40]$$

where r is the radial distance from the centre of the disc and z is the distance normal to the disc. For a reversible reaction at the surface of a microdisc, boundary conditions can be set as:

$$C = C_{surface} = C_{bulk} - \Delta C, \quad 0 < r < a, \quad z = 0 \quad [3.41]$$

$$\frac{\partial C}{\partial z} = 0 \quad r > a, \quad z = 0 \quad [3.42]$$

where ΔC is the difference between the bulk and surface concentrations and a is the radius of the metal disc. The boundary conditions [3.41] and [3.42] indicate a discontinuity at $r = a$ (i.e. where the metal meets the glass) which is tackled mathematically using discontinuous Bessel functions with the result that the total flux, F , to the surface of the disc can be shown to be;

$$F = 4D(C_{bulk} - C_{surface})a \quad [3.43]$$

and that the mass-transfer coefficient for constant concentration conditions at the surface of a microdisc is:

$$(k_m)_C = \frac{4D}{\pi a} \quad [3.44]$$

For an irreversible reaction at the surface of a microdisc, boundary conditions can be set by again using [3.42] but this time in conjunction with;

$$D\left(\frac{\partial C}{\partial z}\right) = Q \quad 0 < r < a, \quad z = 0 \quad [3.45]$$

where Q is a constant flux ($\text{mol cm}^{-2} \text{s}^{-1}$) to the surface of the disc.

By setting the average concentration at the surface of the disc equal to zero, it is possible to define a mass transfer coefficient for constant flux conditions;

$$(k_m)_Q = \frac{3\pi D}{8a} \quad [3.46]$$

Provided the reactions are first order or pseudo-first order, Fleischmann and Pons showed that the theory may be applied to impedance experiments. The starting point is to note that the differential equation representing Fick's 1st Law must be modified to incorporate an ac component, the sine function;

$$D \left(\frac{\delta C}{\delta z} \right) = -Q \sin \omega t, \quad 0 < r < a, \quad z = 0, \quad t > 0$$

$$\frac{\delta C}{\delta z} = 0, \quad r > a, \quad z = 0, \quad t > 0$$
[3.47]

By taking Laplace transforms, a concentration function can then be derived, i.e.;

$$C_{av} = \frac{2Q}{D^{1/2} \omega^{1/2}} \int_0^\infty \left[J_1 \left(\frac{\beta a}{l} \right) \right]^2 \frac{\sin(\omega t - \theta / 2) d\beta}{\beta(1 + \beta^4)^4} \quad [3.48]$$

where J_1 (and J_0) are Bessel functions of the discontinuous integral;

$$\int_0^\infty J_0(\alpha r) J_1(\alpha a) d\alpha = \begin{cases} 0 & r > a \\ 1/2a & r = a \\ 1/a & r < a \end{cases} \quad [3.49]$$

and

$$\theta = \tan^{-1} 1 / \beta^2$$

$$l^2 = D / \omega$$

$$\beta = \alpha l$$

C_{av} is then be substituted into the linearized absolute rate equation to yield the following expressions for the real and imaginary components of diffusion impedance;

$$Z'(\Omega) = \left(\frac{4RT}{\pi n^2 F^2 D^{1/2} \omega^{1/2} a^2 C} \right) \int_0^\infty \left[J_1 \left(\beta \frac{a}{l} \right) \right]^2 \frac{\cos(\theta/2) d\beta}{\beta(1+\beta^4)^{1/4}}$$

$$= \left(\frac{4RT}{\pi n^2 F^2 D^{1/2} \omega^{1/2} a^2 C} \right) \Phi_a \left(\frac{a^2 \omega}{D} \right) \quad [3.50]$$

$$Z''(\Omega) = \left(\frac{4RT}{\pi n^2 F^2 D^{1/2} \omega^{1/2} a^2 C} \right) \int_0^\infty \left[J_1 \left(\beta \frac{a}{l} \right) \right]^2 \frac{\sin(\theta/2) d\beta}{\beta(1+\beta^4)^{1/4}}$$

$$= \left(\frac{4RT}{\pi n^2 F^2 D^{1/2} \omega^{1/2} a^2 C} \right) \Phi_b \left(\frac{a^2 \omega}{D} \right) \quad [3.51]$$

Thus Z' and Z'' in equations [3.50] and [3.51] are the real and imaginary diffusion impedances for a disc shaped microelectrode. It is interesting to compare these expressions for Z' and Z'' with those for semi-infinite linear diffusion to a normal electrode. By arranging the equations such that dimensions cancel, the comparison can be carried out via non-dimensional impedances. For example taking the Z' value for linear diffusion from [3.20] and assuming, as Fleischmann and Pons did in the above derivation, that $C_R = C_O$ and that $D_R = D_O$;

$$Z' = \frac{\sqrt{2}RT}{\pi n^2 F^2 D^{1/2} a^2 \omega^{1/2} C} \quad [3.52]$$

where both the LHS and RHS of the equation have dimensions of Ω . Re-arranging the equation, we can arrive at;

$$\frac{\pi n^2 F^2 DaCZ'}{\sqrt{2}RT} = \left(\frac{D}{\omega a^2} \right)^{1/2} \quad [3.53]$$

where both the LHS and RHS are dimensionless. Thus, the dimensionless impedances are;

a. For the normal electrode;

$$\frac{\pi n^2 F^2 DaC}{\sqrt{2}RT} Z' = \left(\frac{D}{\omega a^2} \right)^{1/2} \quad [3.54]$$

$$\frac{\pi n^2 F^2 DaC}{\sqrt{2}RT} Z'' = \left(\frac{D}{\omega a^2} \right)^{1/2} \quad [3.55]$$

b. For the disc microelectrode;

$$\frac{\pi n^2 F^2 DaC}{4RT} Z' = \left(\frac{D}{\omega a^2} \right)^{1/2} \Phi_a \left(\frac{a^2 \omega}{D} \right) \quad [3.56]$$

$$\frac{\pi n^2 F^2 DaC}{4RT} Z'' = \left(\frac{D}{\omega a^2} \right)^{1/2} \Phi_b \left(\frac{a^2 \omega}{D} \right) \quad [3.57]$$

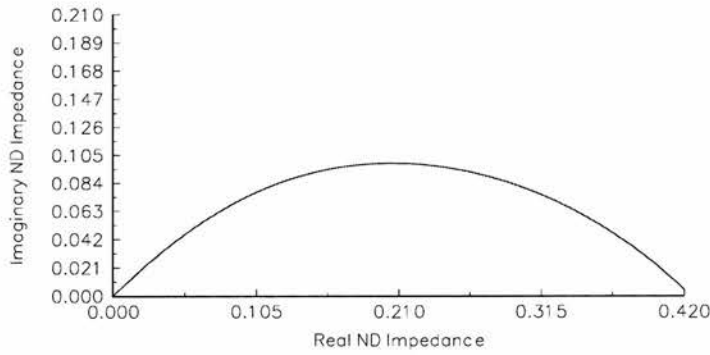
It is striking that if the value of the Φ integrals in [3.56] and [3.57] is $1/\sqrt{8}$ then the equations [3.54] - [3.57] are identical and the diffusion at the microdisc is identical to linear Warburg diffusion at the normal electrode. We shall return to this 'coincidence' in Section 3.4.

3.3.4 *The Exact Solution for Diffusion to a Microdisc Electrode.*

In the previous section, the exact equations for diffusion to a microdisc were presented and re-arranged into a non-dimensional form [#]. Unfortunately the integrals in these equations are not analytic and numerical integration is required to evaluate them. The results of the integration were given by Fleischmann and Pons and are shown in Appendix A to this chapter. Using these results, a plot of the real versus imaginary part of the non-dimensional impedance to a microdisc can be constructed. The resulting graph (Figure 3.14) is a quarter circle.

[#] These equations are not truly exact in that their derivation requires assumptions which, although a good representation of physical reality, will not describe that physical reality with total accuracy. The term *exact equations* has evolved to distinguish it from the *approximation* to the exact equations which will be described later.

Figure 3.14
Non dimensional diffusion impedances for a microdisc



It is interesting to compare this graph with that for semi-infinite linear diffusion to a normal electrode which can be drawn from the non-dimensional impedances in equations [3.54] and [3.55]. Figure 3.15 shows the diffusion impedances to the microelectrode and normal electrode together. The non-dimensional impedance to the microelectrode is so small in comparison to the normal electrode that it can barely be seen on the same scale. Figure 3.16 shows part of Figure 3.15 magnified greatly in order that the microelectrode impedance curve can be seen.

Figure 3.15
Comparison of non dimensional diffusion impedances
to micro and normal electrodes

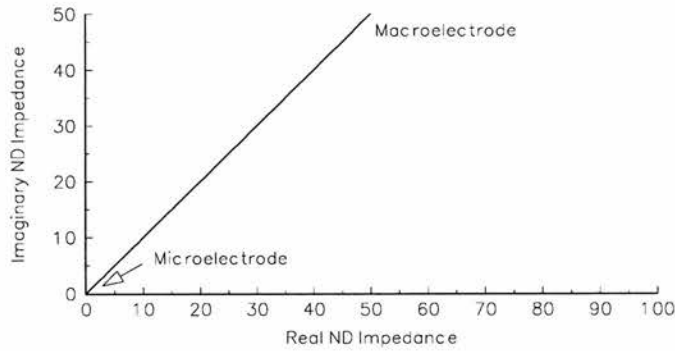
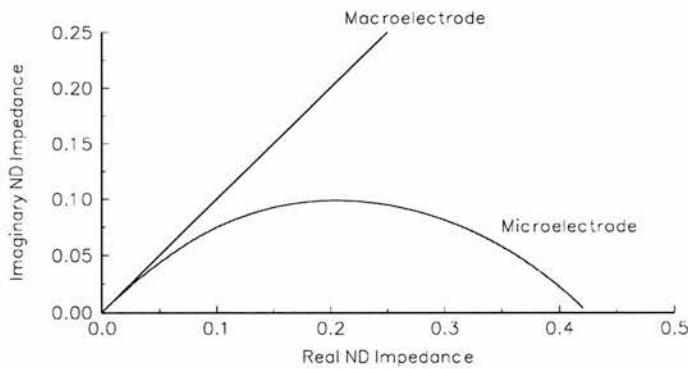


Figure 3.16
Enlarged comparison of non dimensional diffusion
impedances to micro and normal electrodes



In the complex plane the shapes and magnitudes of the non-dimensional diffusion impedance graphs are very different for the normal and microelectrodes. In the case of the normal electrode, as the frequency decreases both the real and imaginary impedances increase at the same rate without apparent limit. (In fact a limitless *linear* increase is possible only in an infinitely large system.) For the microdisc,

however, as the frequency decreases the imaginary impedance reaches a maximum at the top of its quarter circle and then falls to reach zero in the limit of the non-dimensional frequency, $(a^2\omega/D)$, tending to zero. For all but the highest frequencies the diffusion impedance to the microdisc is very much lower than to the normal electrode.

In order to apply the information in this and the preceding section to impedance experiments it will first be necessary to formulate equations upon which an equivalent circuit can be based. Since the Φ integrals are not analytic, in order to model the microdisc behaviour they represent, it is appropriate to find an equation or equations which *are* analytic representations of the integrals. The values of Φ_a and Φ_b from numerical integration are graphed as the data points in Figures 3.17 and 3.18 respectively.

Looking at the graphs of the Φ functions it is apparent that it may be difficult to find a single function to describe the whole domain of either Φ_a or Φ_b . It is sensible to split each of them into two parts - at the $(a^2\omega/D)$ value of say 1.69 (from Appendix A) and to find analytic functions which describe the data for $(a^2\omega/D) < 1.69$ and $(a^2\omega/D) \geq 1.69$. This was done by starting with polynomial functions based on those used by Baranski ⁽¹²⁾ to describe the steady-state a.c. current at a microelectrode in a.c. voltammetry experiments and using the Graftit™ least-squares fitting program ⁽¹³⁾ to minimise the least-squares error in the equations. The following equations were derived for Φ_a and Φ_b .

1) For $x < 1.69$ (where $x = (a^2\omega/D)$)

$$\Phi_{a1}(x) = 0.4243x^{0.5} - 0.1763x^{0.9996} + 0.02582x^{1.9898} - 0.007360x^{2.4721} \quad [3.58]$$

$$\Phi_{b1}(x) = 0.1770x^{1.0005} - 0.1145x^{1.5035} + 0.03260x^{2.0169} - 0.0038x^{2.559} \quad [3.59]$$

2) For $x \geq 1.69$:

$$\Phi_{a2}(x) = 0.3697 - 0.1155x^{-1.4005} - 0.0408 \exp(-0.9785) \quad [3.60]$$

$$\Phi_{b2}(x) = 0.3991 - 0.2353x^{-0.2402} - 0.0940 \exp(-0.2267x) - 0.0010 \exp(-0.0032x) \quad [3.61]$$

These equations give an excellent fit to the data, as shown in the Φ equation fits in Figures 3.17 and 3.18 and also in Figures 3.19 and 3.20, where the axes have been magnified in the critical area to show the smoothness of the join between the 'vertical' function and the 'horizontal' function. These equations shall henceforth be termed the *exact solution* for diffusion to the microdisc for simple electron (or *E mechanism*) transfer. (More complicated reactions in which a homogeneous chemical reaction precedes or follows the heterogeneous electron transfer are described as *CE mechanisms* and *EC mechanisms* respectively. Equations describing impedance at a microelectrode in the case of an EC mechanism are derived later in this chapter.)

Figure 3.17
The Φ_a function

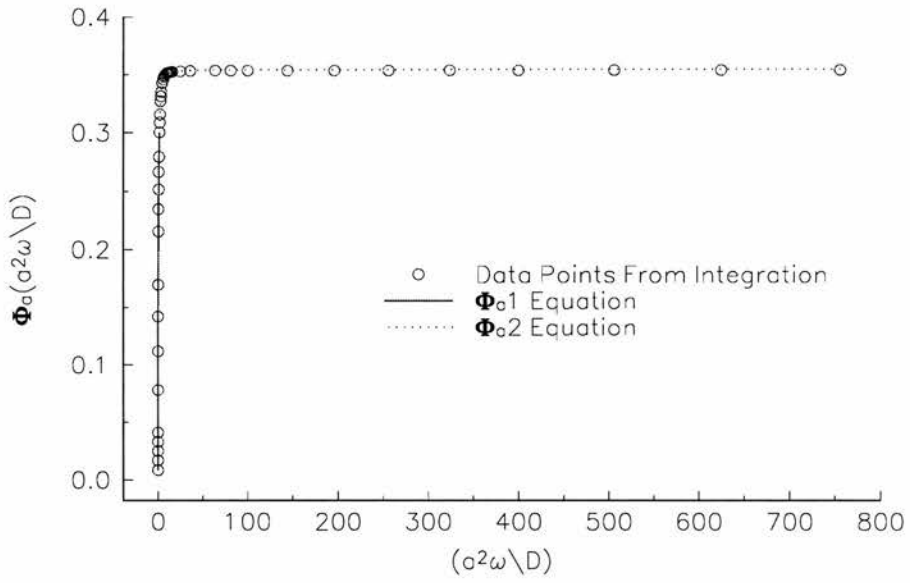


Figure 3.18
The Φ_b function

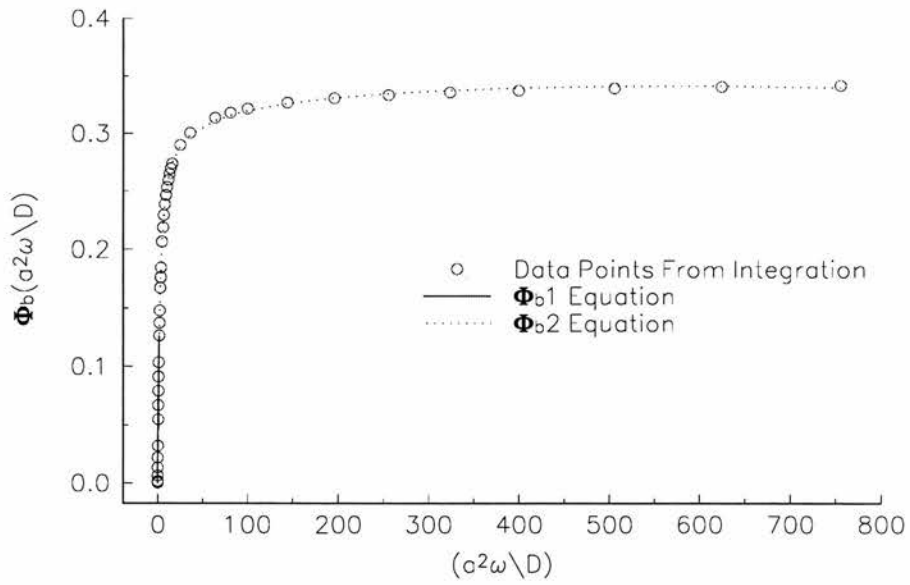


Figure 3.19
Enlarged plot of the Φ_a function

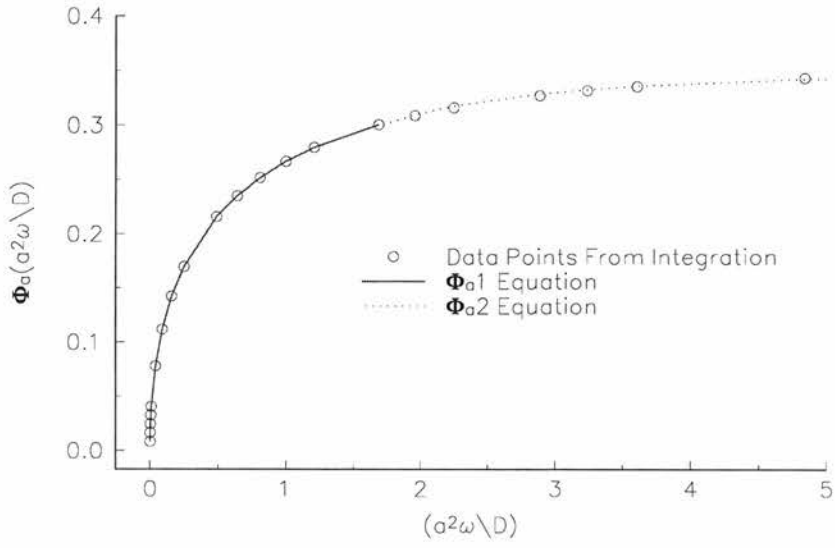
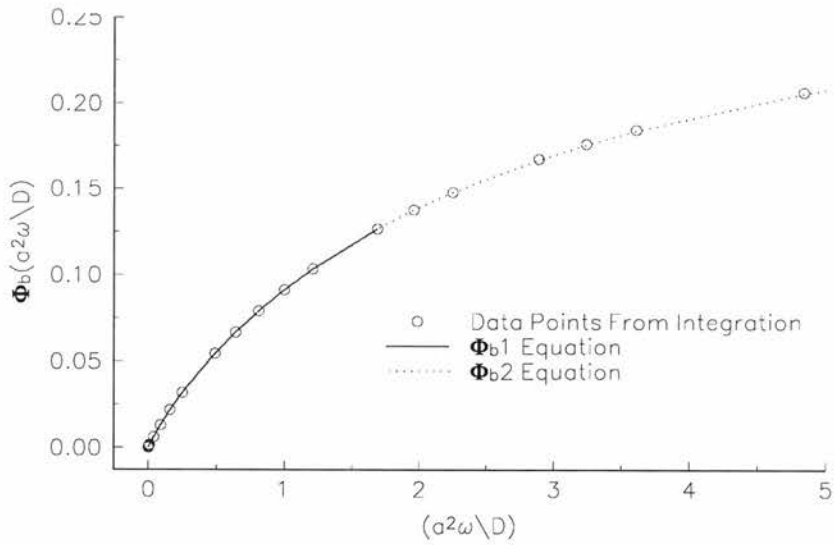


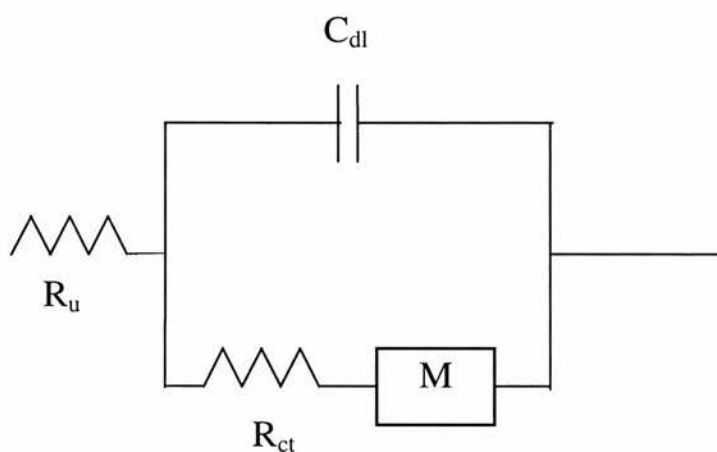
Figure 3.20
Enlarged plot of the Φ_b function



Fleischmann and Pons proposed that the equivalent circuit shown in Figure 3.21 was appropriate for their model. This circuit differs from the Randles circuit of Figure 3.2 in that the Warburg Impedance is replaced by the impedance element M corresponding to the diffusion described by the Φ integrals. This circuit shall be used to analyse impedance data in Chapter 4 and shall be referred to as the *equivalent circuit for the exact solution to the microdisc for E mechanisms*. A FORTRAN subroutine for this circuit, which can be added to the Macdonald LEVM program for CNLS analysis of impedance data ⁽¹⁴⁾, is shown in Appendix B to this chapter.

Figure 3.21

The equivalent circuit for the exact solution to the microdisc for E mechanisms



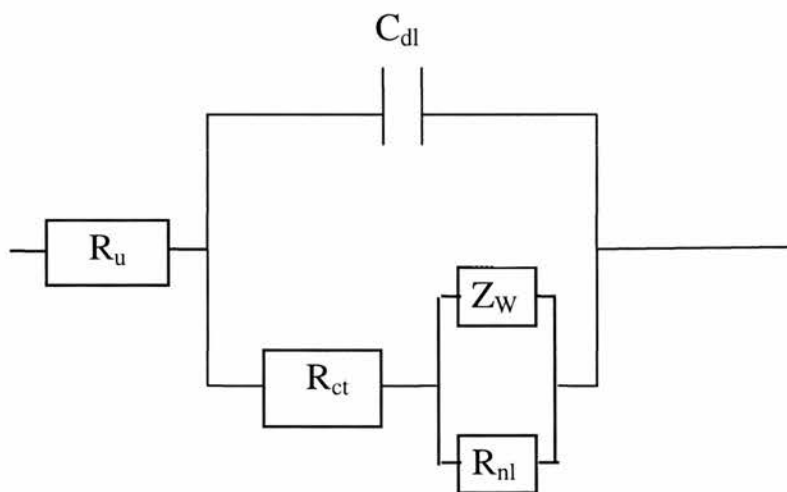
Now that the exact solution for diffusion to the microdisc has been outlined, it is appropriate to return to the ‘coincidence’ that diffusion to the microdisc and normal electrode are identical (equations [3.54] to [3.57]) provided the value of the integrals is $1/\sqrt{8}$.

3.4 The Hemispherical Approximation for Diffusion to a Microdisc Electrode for an E Mechanism

The circuit shown in Figure 3.22 has been used in a.c. voltammetry studies to analyse the impedance of a micro-hemisphere ⁽¹⁵⁾. Bruce, Lisowska-Oleksiak, Los and Vincent ⁽¹⁶⁾ proposed that this circuit could be used as an *approximation* for the microdisc, believing that it should be particularly valid for high and low frequency perturbations but less good at intermediate frequencies.

Figure 3.22

The equivalent circuit for the hemispherical approximation to the disc microelectrode for E mechanisms



In order to derive the hemispherical approximation it is necessary to return once more to the Φ integrals, this time to look at their high and low frequency limits. It is apparent from the numerical values of Φ_a and Φ_b in Appendix A that in the high frequency limit, as $(a^2\omega/D) \rightarrow \infty$, the values of $\Phi_a(a^2\omega/D)$ and $\Phi_b(a^2\omega/D)$ tend to

$1/\sqrt{8}$. ($1/\sqrt{8} = 0.35355$ to 5 sig. figs.) Thus at high frequencies, linear diffusion is dominant at the microdisc and the equations for Warburg impedance apply; i.e. the Warburg impedance can be used as a high frequency approximation for the impedance of the microdisc;

$$Z_w(\Omega) = \frac{(1-j)\sqrt{2}RT}{\pi n^2 F^2 D^{1/2} a^2 C \omega^{1/2}} \quad [3.62]$$

Analysing the behaviour at the low frequency extremity, i.e. as the non-dimensional frequency ($a^2\omega/D$) $\rightarrow 0$, Appendix A shows that;

$$\left(\frac{D}{a\omega^2}\right)^{1/2} \Phi_a\left(\frac{a^2\omega}{D}\right) \cong 0.425 \quad [3.63]$$

and

$$\left(\frac{D}{a\omega^2}\right)^{1/2} \Phi_b\left(\frac{a^2\omega}{D}\right) = 0 \quad [3.64]$$

Substituting these values back into equations [3.56] and [3.57] respectively, the low frequency values for the hemispherical approximation to the microdisc are given by;

$$Z' = R_{nl} \cong \frac{4RT}{\pi n^2 F^2 DaC} \times 0.425 \quad [3.65]$$

$$\Rightarrow Z'(\Omega) = R_{nl} \cong \frac{0.54RT}{n^2 F^2 DaC} \quad [3.66]$$

$$\text{and} \quad Z'' = 0 \quad [3.67]$$

Thus values for linear (high frequency limit) and non-linear (low frequency limit) diffusion impedance have been derived which allow the circuit in Figure 3.22 to be used as an equivalent circuit in the analysis of impedance data from a microelectrode experiment. Obviously the approximation will be best at high and low frequencies and poorest at intermediate frequencies. A FORTRAN subroutine for the hemispherical approximation to the microdisc for E mechanisms, which can be added to the Macdonald LEVM program for complex non-linear least squares (CNLS) analysis of impedance data, is shown in Appendix C to this chapter.

3.5 The Advantages of Microelectrodes

3.5.1 General

There are two features which distinguish microelectrodes from normal electrodes in impedance spectroscopy experiments; the reduced potential drop over the electrolyte and the establishment of non-linear diffusion fields.

3.5.2 The Potential Drop (iR) Over the Electrolyte

The iR drop, often referred to as ohmic loss, is the product of the faradaic current and the resistance of the bulk electrolyte. The iR drop at a microelectrode is smaller than at larger electrodes because a microelectrode's smaller diameter allows less current to pass than a normal electrode.

In fact;

$$i \propto a^2 \quad [3.68]$$

and the electrolyte or bulk resistance in Ohms is given by ⁽¹⁷⁾;

$$R_b = \frac{\rho}{4a} \quad [3.69]$$

where ρ is the specific resistivity of the solution in Ω cm. Combining equations [3.68] and [3.69] yields;

$$iR_b \propto a \quad [3.70]$$

Thus the potential drop over the electrolyte ($V = iR_b$) decreases with electrode radius. The use of microelectrodes therefore ensures low migrational ohmic losses and thus ensures the validity of the assumption that the migration component of the Nernst-Planck equation [3.13] is negligible, an assumption necessary for the earlier derivation of the mass-transport impedance. Traditionally migration of the electroactive species has been minimised via the supporting electrolyte. Unfortunately, however, the charge transfer process at the electrode can be affected by the supporting electrolyte[#]. If one wanted to measure the true heterogeneous electron transfer rate-constant for an electroactive species one conceivable option is to work without supporting electrolyte. The method by which this could be achieved is to render the potential drop over the electrolyte so low that even without supporting electrolyte the migration of electroactive species would be negligible. This can be made possible using microelectrodes⁽¹⁸⁾.

[#] This is shown in Chapter 4 for example where the electron transfer rate-constant changes significantly when the supporting electrolyte is changed from KCl to LiCl and in Chapter 5, 6 and 8 where interactions between the supporting electrolyte and the electroactive species complicate the situation.

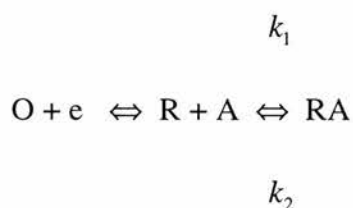
3.5.3 *Non-linear Diffusion at the Microelectrode*

The objective of this work is to generate clear values for R_{ct} and hence k_s . In order to achieve this it is a general condition that the impedance owing to other sources (i.e. diffusion) is minimized.

Equations [3.54] - [3.57] show that in all circumstances, other than in the limit of infinite frequency, non-linear impedance is lower than linear impedance and the likelihood of clear resolution of R_{ct} is increased by experiments in which there is significant non-linear diffusion. Equations [3.62] - [3.67] show that when the value of the non-dimensional frequency ($a^2\omega/D$) tends to infinity, diffusion is linear and only for small values of ($a^2\omega/D$) is diffusion non-linear. Thus the type of diffusion depends not only on the size of the electrode but also the diffusion coefficient of the electroactive species and the frequency of the applied signal. For a given species in an electrochemical cell at any given frequency, the smaller the microelectrode radius becomes, the smaller will be the non-dimensional frequency and the more dominant will be non-linear diffusion. This is illustrated in real experiments by, for example, Figures 4.6 and 4.7 in Chapter 4 where the $R_{ct}C_{dl}$ semi-circle in the low impedance region of the plots is difficult to distinguish when a microdisc of radius 16 μm is employed. It is more clearly seen when a 6.4 μm radius disc is employed. The greater the enhancement of the diffusion rate, the greater is the chance that R_{ct} will become rate limiting and be clearly seen.

3.6 Influence of a Chemical Step on the Impedance Response at a Microdisc. Derivation of the Hemispherical Approximation for Diffusion to the Microdisc for an EC Mechanism.

If, as has been touched on previously in this chapter, the product of electron transfer undergoes a further, homogeneous, reaction in solution (such as ion-pairing), the equations derived for the simple E mechanism will no longer suffice to describe the situation. This is because the diffusion profile of the redox species in the solution around the electrode will be affected by the homogeneous reaction of diffusing species within the diffusion layer. This is often described as coupling between the diffusion and chemical reaction. The following reaction scheme was considered by Sluyters-Rehbach and Sluyters in their treatment of impedance of coupled homogeneous reactions at normal sized electrodes ⁽¹⁹⁾:



Only O is present in the bulk solution. R is generated by heterogeneous reduction of O at the cathode. R subsequently undergoes a homogeneous chemical reaction with species A. Experiments on such a system are discussed in Chapter 8, for example, which is concerned with the reduction of buckminsterfullerene in organic solvents in the presence of a background electrolyte. The equations derived for the EC reduction, however, are interchangeable in CNLS analysis with EC oxidation

and one derivation is sufficient to analyse both situations. The derivation here follows that of Sluyters-Rehbach and Sluyters and considers the reduction.

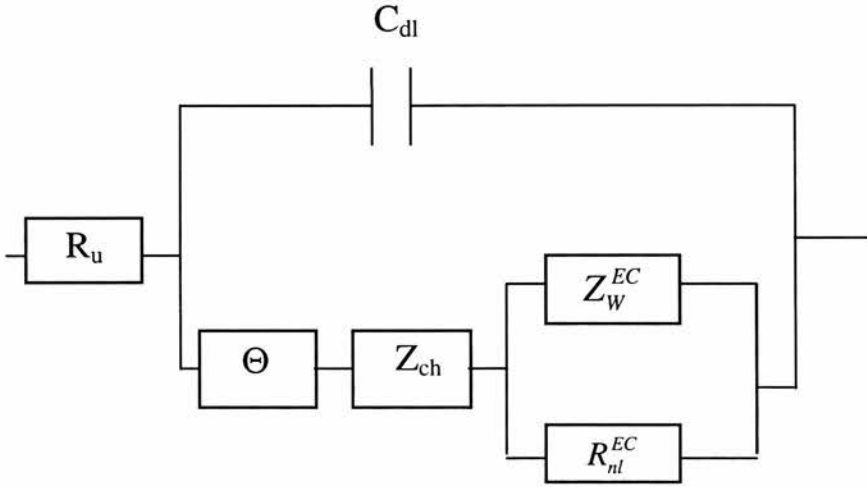
The chemical reaction is assumed to be in equilibrium with forward rate constant k_1 , backward rate constant k_2 and equilibrium constant $K=k_1/k_2$. Sluyters-Rehbach and Sluyters, basing their analysis on diffusion layer theory⁽²⁰⁾, presented equations describing how the coupled chemical and diffusion mass transport process differs from uncoupled diffusion in a simple E reaction. The modification of these equations for CNLS analysis at the microdisc electrode is presented here.

Sluyters produced equations based on the Nernst equation for dc reversible systems, and based on the partly linearized current-voltage equation for dc irreversible systems. While it is possible to adapt both sets of equations for CNLS analysis, the equations for the dc reversible case are more readily manipulated. It is sufficient to concentrate on the solution of the dc reversible case here because the systems studied in this thesis are essentially nernstian.

The faradaic impedance of a cell undergoing an electron transfer with a coupled homogeneous chemical reaction may be represented as the series sum of a charge transfer resistance, a mass transport impedance and a chemical reaction impedance. For a microelectrode an equivalent circuit for the hemispherical approximation to such a system can be defined as shown in Figure 3.23.

Figure 3.23

The equivalent circuit for the hemispherical approximation to the microdisc with an EC process



In order to analyse impedance data from a microdisc, equations for each circuit element are required to quantitatively define the faradaic impedance, i.e.

$$Z_f = \Theta + Z_{ch} + Z_D^{EC} \quad [3.71]$$

Z_f is the faradaic impedance, Θ the charge transfer impedance, Z_{ch} the impedance associated with the homogeneous chemical reaction and Z_D^{EC} the impedance of the diffusion process coupled to the homogeneous chemical reaction. In order to derive these terms, it is convenient to begin by finding the surface concentrations of the reactants at the electrode. These are:

$$\bar{C}_R = C_R^* - \frac{i\delta_R L}{nFD_R} \quad [3.72a]$$

$$\bar{C}_o = C_o^* + \frac{i\delta_o}{nFD_o} \quad [3.72b]$$

δ is the thickness of the diffusion layer, \bar{C} the surface concentration and C^* the bulk concentration of the electroactive species. L is greater than zero and less than one and its value reflects the influence of the chemical reaction. The lower the value of L , the greater the influence of the chemical reaction. More precisely, L is given by:

$$L = \frac{KF(\lambda)+1}{(K+1)F(\lambda)} \quad [3.73]$$

where

$$F(\lambda) = \pi^{1/2} \frac{\Gamma[1 + (\lambda^2/\pi)]}{\Gamma[1/2 + (\lambda^2/\pi)]} \quad [3.74]$$

and Γ is the gamma function. A very good approximation for $F(\lambda)$ is:

$$F(\lambda) = \lambda \coth \lambda \quad [3.75]$$

In general, the value of the kinetic parameter λ at any electrode is given by:

$$\lambda = \delta \left(\frac{k}{D} \right)^{1/2} \quad [3.76]$$

At the microdisc the diffusion layer thickness for constant flux is given by:

$$\delta = \frac{D}{k_m} = \frac{8a}{3\pi} \quad [3.77]$$

Hence at the microdisc, the value of λ is given by:

$$\lambda = \frac{8a}{3\pi} \left(\frac{k_m}{D} \right)^{1/2} \quad [3.78]$$

This value of λ may be used to find a value of L. L may then be substituted in equation [3.72] to render the equations suitable for analysis of microdisc electrode experiments.

In order to express the surface concentrations as functions of potential the assumption is made that the electrode reaction is dc reversible and [3.72a and b] are substituted into the Nernst equation, i.e.

$$\text{into} \quad \bar{C}_O D_O^{1/2} = \bar{C}_R D_R^{1/2} \exp \bar{j} \quad [3.79]$$

$$\text{where} \quad \bar{j} = \left(\frac{nF}{RT} \right) (E - E^O) + \ln \left(\frac{D_O}{D_R} \right)^{1/2} = \left(\frac{nF}{RT} \right) (E - E'_{1/2}) \quad [3.80]$$

and $E'_{1/2}$ is the reversible half-wave potential.

The surface concentrations are thus:

$$\bar{C}_R = \frac{\left[C_R^* + C_O^* L \left(\frac{D_O}{D_R} \right)^{1/2} \right]}{L \exp \bar{j} + 1} \quad [3.81a]$$

$$\bar{C}_O = \frac{\left[C_R^* \left(\frac{D_R}{D_O} \right)^{1/2} + C_O^* L \right] \exp \bar{j}}{L \exp \bar{j} + 1} \quad [3.81b]$$

These equations describe how the surface concentrations of R and O are determined by the chemical reaction within the diffusion layer and by the cell potential. It is important to note that the only assumptions required to formulate the equations are that the reaction is dc reversible and that it is appropriate to apply diffusion-layer theory to derive surface concentrations. Armed with these expressions for surface concentrations, the mass transport equations for the EC reaction can now be addressed.

The Coupled Non-Linear Resistance, R_{nl}^{EC}

The non-linear resistance has been given previously [3.66] in the case of an E reaction where $C_O^* = C_R^* = \bar{C}_O = \bar{C}_R$.

Expressing R_{nl} in units of $\Omega \text{ cm}^2$ yields:

$$R_{nl} = \frac{0.54RT\pi a}{n^2 F^2 DC} \quad [3.82]$$

The concentration here is a surface concentration.

The Coupled Warburg Impedance, Z_w^{EC}

The Warburg coefficients for the EC reaction were given by Sluyters-Rehbach and Sluyters as:

$$\sigma_a = \sigma_o + \sigma_R \frac{K}{K+1} \quad [3.83a]$$

$$\sigma = \sigma_R + \sigma_o \quad [3.83b]$$

$$\sigma_R = \frac{RT}{n^2 F^2 \bar{C}_R (2D)^{1/2}} \quad [3.83c]$$

$$\sigma_o = \frac{RT}{n^2 F^2 \bar{C}_o (2D)^{1/2}} \quad [3.83d]$$

Since we are using the hemispherical approximation to the microdisc, the Warburg impedance derived for the normal sized electrode may also be used for the microdisc. The Warburg coefficients are therefore:

$$\sigma_R = \frac{RT}{F^2 2^{1/2} (C_R^* D_R^{1/2} + C_o^* L D_o^{1/2})} [L \exp \bar{j} + 1] \quad [3.84a]$$

$$\sigma_o = \frac{RT}{F^2 2^{1/2} (C_R^* D_R^{1/2} + C_O^* L D_O^{1/2})} [L + \exp - \bar{j}] \quad [3.84b]$$

It is clear that the diffusion parameters σ_R and σ_o now contain a potential dependent term (i.e. \bar{j}) and terms dependent upon the homogeneous chemical reaction (i.e. K and $F(\lambda)$.) Thus expressions appropriate for Z_W^{EC} in Figure 3.23 are now defined. Unfortunately the potential dependent \bar{j} term is expressed as a function of E and E^o which is inappropriate for CNLS analysis of impedance data. In order to reformulate \bar{j} it is useful to consider equation [3.71] for the total faradaic impedance of the circuit in Figure 3.23. Sluyters-Rehbach and Sluyters found that:

$$Z_f = \Theta + Z_D + \frac{\sigma_R}{K+1} \left[\frac{(\omega^2 + k^2)^{1/2} + k}{\omega^2 + k^2} \right]^{1/2} - \frac{(-1)^{1/2} \sigma_R}{K+1} \left[\frac{(\omega^2 + k^2)^{1/2} - k}{\omega^2 + k^2} \right]^{1/2} \quad [3.85]$$

where the third and fourth terms correspond to the chemical reaction impedance Z_{ch} . For convenience of notation, $k = k_1 + k_2$.

In order to reformulate \bar{j} the potential dependence of all three parts of the faradaic impedance is required. Of special interest is the potential at which the minimal value of impedance is obtained. Finding an expression is made straightforward by looking at the situation where $\omega \rightarrow 0$. If we allow $\omega \rightarrow 0$ in equation [3.85], then in this low frequency limit, Z_{ch} is given by the expression:

$$Z_{ch} = \frac{\sigma_R}{K+1} \left(\frac{2}{k} \right)^{1/2} \quad [3.86]$$

In this low frequency region, the changes of Θ as a function of the dc potential are negligible in comparison with Z_D and Z_{ch} . The minimum of the faradaic impedance as a function of dc potential is found by differentiating Z'_f with respect to \bar{j} . There is no need to include Z_w in the expression for Z'_f since it was established earlier that as $\omega \rightarrow 0$, $Z_w \rightarrow 0$. Hence an expression for the real faradaic impedance is obtained ⁽²¹⁾:

$$\begin{aligned} Z'_f &= R_{nl} + Z_{ch} \\ &= \frac{0.54\pi a}{(2D)^{1/2}} \left(\sigma_o + \sigma_R \frac{K}{K+1} \right) + \frac{\sigma_R}{K+1} \left(\frac{2}{k} \right)^{1/2} \end{aligned} \quad [3.87]$$

$$\frac{dZ'_f}{d\bar{j}} = \frac{d(R_{nl} + Z_{ch})}{d\bar{j}} = 0 \quad [3.88]$$

To differentiate with respect to \bar{j} , a potential dependent function, it is convenient to separate R_{nl} and Z_{ch} into potential and non-potential dependent parts.

The terms A , A_1 and A_2 are independent of potential and are defined as follows:

$$A = \frac{RT}{F^2 C (2D)^{1/2}} \quad \left(\text{so that } \sigma_R = \frac{A}{1+L} (L \exp \bar{j} + 1) \right) \quad [3.89]$$

(and so that $\sigma_o = \frac{A}{1+L}(L + \exp(-j))$)

$$A_1 = \frac{0.54\pi a}{(2D)^{1/2}} \quad [3.90]$$

$$A_2 = \left(\frac{2}{k}\right)^{1/2} \frac{1}{K+1} \quad [3.91]$$

Hence, writing the faradaic impedance in the A terms defined above:

$$Z_f = A_1 \left(\frac{A(L + \exp(-\bar{j}))}{(1+L)} + \frac{A(L \exp \bar{j} + 1)K}{(1+L)(K+1)} \right) + \frac{A_2 A}{1+L} (L \exp \bar{j} + 1) \quad [3.92]$$

Setting the first derivative of the faradaic impedance with respect to \bar{j} equal to zero yields the minimum of the faradaic impedance.

$$\frac{dZ_f}{d\bar{j}} = -\frac{A_1 A}{(1+L)} \exp(-\bar{j}) + \frac{A_1 A K L}{(K+1)(1+L)} \exp(\bar{j}) + \frac{A_2 A L}{(1+L)} \exp \bar{j} = 0 \quad [3.93]$$

$$\Rightarrow \exp(2\bar{j}) = \frac{A_1}{\frac{A_1 K L}{(K+1)} + A_2 L} \quad [3.94]$$

$$\Rightarrow \bar{j} = 0.5 \ln \left(\frac{A_1 (K+1)}{K L (A_1 + A_2) + A_2 L} \right) \quad [3.95]$$

This is in fact the value of \bar{j} which yields the minimum low-frequency real-axis intercept on a complex-plane plot. Since the minimum value of the faradaic impedance as the frequency tends to zero is also the minimum impedance at all other frequencies, the value of \bar{j} derived above is applicable over the complete frequency range.

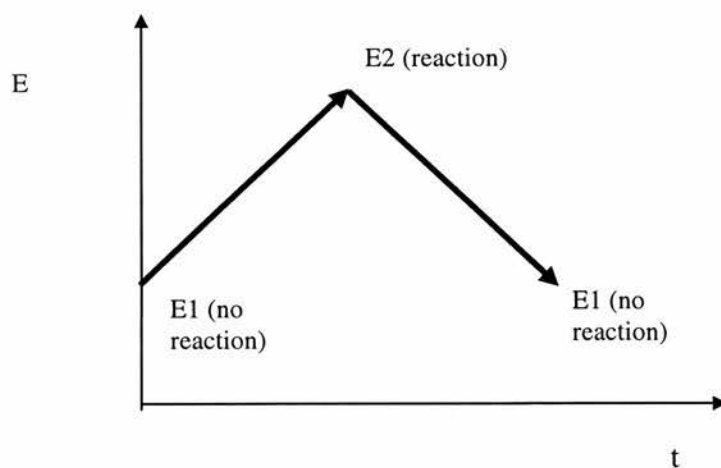
Now that appropriate impedance equations have been derived for the EC mechanism at a microdisc it is appropriate to write the FORTRAN subroutine to enable these equations to be used to fit data from impedance experiments to the EC model. This is shown in Appendix D to this chapter.

3.7 Cyclic Voltammetry at Microelectrodes

While impedance techniques form the principal basis of the majority of the results produced for this thesis, cyclic voltammetry was also frequently employed. A cyclic voltammetry experiment consists of sweeping the potential applied to a cell linearly with time from a starting potential to another potential and then back again to the starting potential while measuring the resulting current. Generally the experiment begins and ends at a potential at which there is no electrode reaction and sweeps through a potential range where reaction(s) is (are) observed. The variation of potential with time for a typical cyclic voltammetry sweep is shown in Figure 3.24.

Figure 3.24

Variation in potential with time in a typical cyclic voltammetry experiment



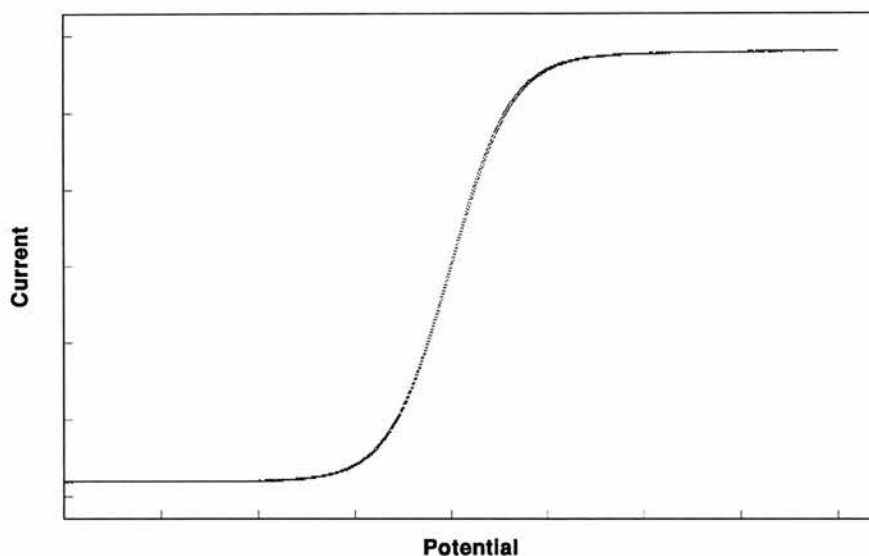
If cyclic voltammetry is performed at a microelectrode using experimental time scales of seconds the dimensions of the electrode are much smaller than the diffusion distance for molecules in solution. These conditions result in non-linear diffusion and a steady-state response. The diffusion limited steady state current for a microdisc is given by ⁽¹⁷⁾ :

$$i_d = 4nFDC_{\text{bulk}} a \quad [3.96]$$

A typical voltammogram for a reversible process is shown in Figure 3.25. The voltammogram shape is described as sigmoidal and is characteristic of reversible electron transfer at a microelectrode with spherical diffusion.

Figure 3.25

Typical cyclic voltammogram for a reversible electron transfer.



In the plateau regions of the cyclic voltammogram the system is in a diffusion-controlled steady state and it is by measuring the plateau or diffusion-controlled current that voltammetry yields a value for the diffusion coefficient D via equation [3.96]. Of course, application of this equation relies on the assumption, true for nearly all cases, that the diffusion coefficients of the oxidised and reduced electroactive species are equal or very nearly equal ^(4b).

The potential at which the current is the arithmetic mean of the oxidation and reduction diffusion controlled currents is termed the half-wave potential, $E_{1/2}$, and is the point of inflexion in the cyclic voltammogram. Provided the reaction is described by a simple E mechanism, the half wave potential is given by:

$$E_{1/2} = E_o' + \frac{RT}{nF} \ln \frac{D_R^{1/2}}{D_O^{1/2}} \quad [3.97]$$

where E_o' is the standard formal potential. Clearly, provided once again that $D_R = D_O$, measurement of the half wave potential is in fact equivalent to measuring the standard formal potential for the redox couple. If the reaction mechanism is EC or CE, the surface concentrations of electroactive species are modified and both the formal and half wave potentials are shifted to new values. If the electrode reaction is kinetically fast, the modified formal potential will be given by the Nernst equation.

The electron-transfers studied in this thesis are in fact all reversible or nearly reversible at the relatively slow voltammetric sweep rates employed - i.e. the observed reaction rate (current) is determined by the rate of diffusion of electroactive species to and from the electrode. Surface concentrations are determined by thermodynamic rather than kinetic factors.

In the experimental work described in the following chapters cyclic voltammetry was used to:

- a. Determine the presence or absence of reactions in any given electrochemical window.

- b. Establish that the microelectrode was behaving correctly and yielding sigmoidally shaped voltammograms consistent with radial diffusion and with $|E_{3/4} - E_{1/4}| = 56.4$ mV at 25°C consistent with reversible electron transfer.
- c. Establish the half-wave potential at which electron transfer took place.
- d. Calculate diffusion coefficients for comparison with those obtained from impedance experiments.

3.8 Conclusions

The relationship between equations describing impedance at normal and microelectrodes has been explored. The equations describing microelectrode impedance have been stated for an electron transfer with an E mechanism and FORTRAN subroutines permitting their use with Macdonald's LEVM least-squares analysis program written. New equations have been derived to allow analysis of microelectrode impedance data as an EC mechanism.

3.9 References

- 1a. J. O'.M. Bockris, A.K.N. Reddy, Modern Electrochemistry, Macdonald & Co., London, (1970), 2, p640.
- 1b. J. O'.M. Bockris, A.K.N. Reddy, Modern Electrochemistry, Macdonald & Co., London, (1970), 2, p897.
- 1c. J. O'.M. Bockris, A.K.N. Reddy, Modern Electrochemistry, Macdonald & Co., London, (1970), 2, p654.
2. M. Sluyters-Rehbach, J.H. Sluyters, Electroanalytical Chemistry (A.J. Bard, Ed.), Marcel Dekker, New York, (1970), Volume 4, p1.
3. B. Timmer, M. Sluyters-Rehbach, J.H. Sluyters, J. Electroanal. Chem., (1967), 14, p169.
- 4a. A.J. Bard, L.R. Faulkner, Electrochemical Methods Fundamentals and Applications, John Wiley & Sons Inc., (1980), p27.
- 4b. A.J. Bard, L.R. Faulkner, Electrochemical Methods Fundamentals and Applications, John Wiley & Sons Inc., (1980), p160.
5. P.G. Bruce, Polymer Electrolyte Reviews, (J.R. MacCallum and C.A. Vincent, Eds.), Elsevier, London, (1987), Volume 1, p237.
6. J.E.B. Randles, Disc. Farad. Soc., (1947), 1, p11.
7. J.R Macdonald (Ed.), Impedance Spectroscopy Emphasizing Solid Materials And Systems, John Wiley And Sons, (1987).

8. R.D. Armstrong, M.F. Bell, A.A Metcalfe, *Electrochemistry*, Chemical Society Specialist Periodical Reports, (1978), 6, p98.
9. A.J. Ribes, J. Osteryoung, *Microelectrodes: Theory and Applications*, (M.I. Montenegro, M.A. Queiros and J.L. Daschbach (Eds.), NATO ASI Series, Series E, Applied Sciences, Kluwer Academic Publishers, Dordrecht. (1991), 197, p259.
10. M. Fleischmann, S. Pons, D.R. Rolinson and P.P. Schmidt (Eds.), *Ultramicroelectrodes*, Datatech Systems, Inc., Morganton, NC, (1987).
11. M. Fleischmann, S. Pons, *J. Electroanal. Chem.*, (1988), 250, p277.
12. A.S. Baranski, *J. Electrochem Soc.*, (1986), 133, p93.
13. Erithacus Software Limited, 1989 - 1990, Staines, Middlesex, UK.
14. J.R. Macdonald LEVM Software Version 5 Manual, 1990.
15. A.S. Baranski, *J. Electroanal. Chem.*, (1991), 300, p309.
16. P.G. Bruce, A. Lisowska-Oleksiak, P. Los, C.A. Vincent, *J. Electroanal. Chem.*, (1994), 367, p279.
17. R.M. Wightman, D.O. Wipf, *Electroanalytical Chemistry*, (A.J. Bard Ed.), Marcel Dekker, New York, (1988), 15, p267.
18. A.M. Bond, M. Fleischmann, J. Robinson, *J. Electroanal. Chem.*, (1984), 168, p299.
19. M. Sluyters-Rehbach, J.H. Sluyters, *J. Electroanal. Chem.*, (1970), 26, p237.
20. J. Jacq, *Electrochimica Acta*, (1967), 12, p1.
21. P. Los, P.G. Bruce, *Polish J. Chem.*, (1997), 71, p1151.

Appendix A

Values of Functions Arising From Analysis of the Diffusion Impedance of a Disc
Shaped Microelectrode.

$(a^2\omega/D)$	$(D/a^2\omega)^{1/2}$	$\Phi_a(a^2\omega/D)$	$\Phi_b(a^2\omega/D)$	$(D/a^2\omega)^{1/2}\Phi_a(a^2\omega/D)$	$(D/a^2\omega)^{1/2}\Phi_b(a^2\omega/D)$
0.00040	50.000000	0.00841	0.000070	0.420500	0.003500
0.00160	25.000000	0.01669	0.000276	0.417250	0.006900
0.00360	16.666666	0.02483	0.000612	0.413833	0.010200
0.00640	12.500000	0.03282	0.001075	0.410250	0.013437
0.01000	10.000000	0.04068	0.001658	0.406800	0.016580
0.04000	5.000000	0.07786	0.006213	0.389300	0.031065
0.09000	3.333333	0.1116	0.013090	0.372000	0.043633
0.1600	2.500000	0.1421	0.021790	0.355250	0.054475
0.2500	2.000000	0.1695	0.031860	0.339000	0.063720
0.4900	1.428571	0.2156	0.054650	0.308000	0.078071
0.6400	1.250000	0.2348	0.066770	0.293500	0.083462
0.8100	1.111111	0.2517	0.079050	0.279667	0.087833
1.000	1.000000	0.2665	0.091310	0.266500	0.091310
1.210	0.909091	0.2794	0.103400	0.254000	0.094000
1.690	0.769231	0.3002	0.126600	0.230923	0.097385
1.960	0.714286	0.3086	0.137600	0.220429	0.098286
2.250	0.666667	0.3157	0.148000	0.210467	0.098667
2.890	0.588235	0.3269	0.167400	0.192294	0.098471
3.240	0.555556	0.3312	0.176200	0.184000	0.097889
3.610	0.526316	0.3349	0.184500	0.176263	0.097105
4.840	0.454545	0.3427	0.206400	0.155773	0.093818
5.760	0.416667	0.3460	0.218600	0.144167	0.091083
6.760	0.384615	0.3482	0.229200	0.133923	0.088154
7.840	0.357143	0.3496	0.238400	0.124857	0.085143
9.000	0.333333	0.3506	0.246400	0.116867	0.082133
10.24	0.312500	0.3513	0.253400	0.109781	0.079187
11.56	0.294118	0.3517	0.259500	0.103441	0.076324
12.96	0.277778	0.3520	0.264900	0.097778	0.073583
14.44	0.263158	0.3522	0.269600	0.092684	0.070947
16.00	0.250000	0.3524	0.273900	0.088100	0.068475
25.00	0.200000	0.3529	0.289900	0.070580	0.057980
36.00	0.166667	0.3532	0.300500	0.058867	0.050083
64.00	0.125000	0.3534	0.313800	0.044175	0.039225
81.00	0.111111	0.3534	0.318200	0.039267	0.035356
100.0	0.100000	0.3535	0.321700	0.035350	0.032170
144.0	0.083333	0.3535	0.327000	0.029458	0.027250
196.0	0.071429	0.3535	0.330800	0.025250	0.023629
256.0	0.062500	0.3535	0.333600	0.022094	0.020850
324.0	0.055556	0.3535	0.335900	0.019639	0.018661
400.0	0.050000	0.3535	0.337600	0.017675	0.016880
506.2	0.044447	0.3535	0.339400	0.015712	0.015085
625.0	0.040000	0.3535	0.340800	0.014140	0.013632
756.2	0.036365	0.3535	0.342000	0.012855	0.012437

Appendix B

FORTRAN Subroutine for the Exact Solution to the Microdisc for an E Mechanism.

C *ADDED PART OF CNLS PROGRAM TO RUN ON MICROSOFT FORTRAN, V4.00*

C

C *Exact Solution to the microdisc for E mechanisms.*

C

SUBROUTINE KSUB(M,FREQ,P,F)

*IMPLICIT REAL*8(A-H,O-Z)*

DOUBLE PRECISION P(),F(*),FREQ(*),X,F14,F14A,F15,F15A,RE,IM*

*COMPLEX*16 ZT,IOMEGA,YB,ZW,ZI*

ST=P(1)

TE=P(2)

CDL=P(3)

DY=P(4)

RA=P(5)

RKS=P(6)

RS=P(7)

TDE=P(8)

DO 100 I=1,M

OMEGA=FREQ(I)

IOMEGA=DCMPLX(0.,OMEGA)

*RCT=(2.8429367E-10)*TE/(RKS*ST*RA*RA)*

*A=(2.8429367E-10)*TE/(SQRT(DY)*SQRT(OMEGA))*

*AA=4*A/(ST*RA*RA)*

*X=(RA**2)*OMEGA/DY*

```

IF (X.LT. 1.690000) THEN
  FI4A=0.42432*X**(0.5)-0.17627*X**(0.9996)+0.02582*X**(1.9898)
  FI4=FI4A-0.00736*X**(2.4721)
  FI5A=0.177*X**(1.0005)-0.1145*X**(1.5035)+0.0326*X**(2.0169)
  FI5=FI5A-0.0038*X**(2.559)
ELSE
  FI4A=0.3697-0.1155*X**(-1.4005)
  FI4=FI4A-0.0408*EXP(-0.9785)
  FI5A=0.3991-0.2353*X**(-0.2402)-0.0940*EXP(-X*0.2267)
  FI5=FI5A-0.0010*EXP(-0.0032*X)
END IF

RE=AA*FI4
IM=AA*FI5
ZW=RE-DCMPLX(0.D0,1.D0)*IM
ZI=RCT+ZW
YB=IOMEGA*CDL+1.D0/ZI
ZT=RS+1.D0/YB
F(I)=-DREAL(ZT)/TDE
F(I+M)=DIMAG(ZT)/TDE
00 CONTINUE

RETURN

END

```

Appendix C

FORTRAN Subroutine for the Hemispherical Approximation to the Microdisc for
an E Mechanism.

C ADDED PART OF CNLS PROGRAM TO RUN ON MICROSOFT FORTRAN, V4.00

C

C Hemispherical Approximation to the microdisc for E mechanisms.

C

SUBROUTINE KSUB(M,FREQ,P,F)

*IMPLICIT REAL*8(A-H,O-Z)*

DOUBLE PRECISION P(),F(*),FREQ(*),AA,RNL,A,TDE,RF,RCT*

*COMPLEX*16 ZT,IOMEGA,YB,ZW,ZI,YI*

C

ST=P(1)

TE=P(2)

CDL=P(3)

DY=P(4)

RA=P(5)

RKS=P(6)

RS=P(7)

TDE=P(8)

RF=P(12)

C Zw=A/SQRT(OMEGA)-jA/SQRT(OMEGA)

DO 100 I=1,M

OMEGA=FREQ(I)

IOMEGA=DCMPLX(0.,OMEGA)

RCT=2.D0(2.8429367D-10)*TE/(RKS*ST*RA*RA)*

*A=(2.8429367D-10)*TE/(SQRT(DY)*SQRT(OMEGA))*

*AA=2.D0*SQRT(2.0)*A/(ST*RA*RA)*

$RNL=2.D0*(8.9313489D-10)*0.5386*TE/(ST*DY*RA)$

$ZW=AA-DCMPLX(0.D0,1.D0)*AA$

$YI=1.D0/ZW+1.D0/RNL$

$ZI=RCT+1.D0/YI$

$YB=(IOMEGA)**RF*CDL+1/ZI$

$ZT=RS+1.D0/YB$

$F(I)=DREAL(ZT)/TDE$

$F(I+M)=DIMAG(ZT)/TDE$

100 CONTINUE

C

RETURN

END

Appendix D

FORTRAN Subroutine for the Hemispherical Approximation to the Microdisc for
an EC Mechanism where only one of the Redox Species is Present in the Bulk
Solution

```
C  ADDED PART OF CNLS PROGRAM TO RUN ON MICROSOFT FORTRAN, V4.00
C
C  EC Mechanism, Ox or RED present in the solution, Edc=E(sigma,min)
C
SUBROUTINE KSUB(M,FREQ,P,F)
IMPLICIT REAL*8(A-H,O-Z)
DOUBLE PRECISION P(*),F(*),FREQ(*),AA,RNL,A,TDE,RF,RCT,K0,L0,
$      REA,CRS,COXS,JOT,KONST,REA1,FLAMB,
$      KM,LAMB,SIGMAR,QA1,QA2,QA3
COMPLEX*16 ZT,IOMEGA,YB,ZW,ZI,Y1,REAC
OPEN (UNIT=7, FILE= 'AAA')

      ST=P(1)
      TE=P(2)
      CDL=P(3)
      DY=P(4)
      RA=P(5)
      RKS=P(6)
      RS=P(7)
      TDE=P(8)
      KONST=P(10)
      RF=P(12)
      K0=P(13)

DO 100 I=1,M
```

```

OMEGA=FREQ(I)

IOMEGA=DCMPLX(0.,OMEGA)

KM=3.D0*3.1415927/(8.D0*RA)

LAMB=(1.D0/KM)*(SQRT(KONST/DY))

FLAMB=LAMB*(1.D0/DTANH(LAMB))

QA1=0.54*3.1415927*RA/(SQRT(2.D0*DY))

QA2=(SQRT(2.D0/KONST))*(1.D0/(K0+1.D0))

L0=(K0*FLAMB+1.D0)/((K0+1.D0)*FLAMB)

JOT=Dlog(SQRT(QA1*(K0+1.D0)/(L0*K0*(QA1+QA2)+QA2*L0)))

CRS=ST*L0/(L0*exp(JOT)+1.D0)

COXS=ST*L0*(exp(JOT))/(L0*exp(JOT)+1.D0)

SIGMAR=(2.842937D-10)*TE*(L0*exp(JOT)+1.D0)

£    /(ST*L0*SQRT(2.D0*DY))

SIGMAR=SIGMAR/(RA*RA)

REA=(SIGMAR/(K0+1.D0))*(SQRT(
& (KONST+SQRT(OMEGA*OMEGA+KONST*KONST))/
$ (OMEGA*OMEGA+KONST*KONST)))

REAI=(SIGMAR/(K0+1.D0))*(SQRT(
*(-KONST+SQRT(OMEGA*OMEGA+KONST*KONST))/
$ (OMEGA*OMEGA+KONST*KONST)))

REAC=REA-DCMPLX(0.D0,1.D0)*REAI

RCT=(2.8429367D-10)*TE/(RKS*RA*RA)

RCT=RCT*(1.D0/(0.5*CRS*EXP(0.5*JOT)+0.5*COXS*EXP(-0.5*JOT)))

A=(2.8429367D-10)*TE/(RA*RA*SQRT(2.D0*DY))

AA=(A/ST)*(1.D0 + 1.D0/(L0*exp(JOT)) + (K0/(K0+1)))*

```

```

      £ exp(JOT) + 1.D0/L0))
RNL=0.54*3.1415927*AA*RA/(SQRT(2.D0*DY))
ZW=AA/(SQRT(OMEGA))-(DCMPLX(0.D0,1.D0)*AA)/(SQRT(OMEGA))
YI=1.D0/ZW+1.D0/RNL
ZI=RCT+1.D0/YI+REAC
YB=(IOMEGA)**RF*CDL+1.D0/ZI
ZT=RS+1.D0/YB

F(I)=-DREAL(ZT)/TDE
F(I+M)=DIMAG(ZT)/TDE
100 CONTINUE

RETURN
END

```

CHAPTER 4

A MICROELECTRODE IMPEDANCE STUDY OF THE $\text{Fe}^{2+} / \text{Fe}^{3+}$ REDOX COUPLE IN AQUEOUS SOLUTION

Introduction

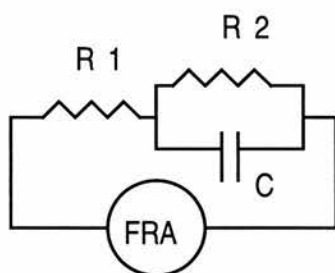
Very few published data were available from impedance spectroscopy at a microelectrode in non-aqueous environments with which to compare experimental results. The first practical study undertaken for the thesis, therefore, was a control experiment in aqueous solution, for which results were already available using different techniques, and for which results had recently been obtained using microelectrode impedance spectroscopy at St. Andrews University.

4.1 Impedance Spectroscopy of Dummy Cells.

Prior to carrying out impedance experiments in aqueous solution, the LEVM program's ability to output accurate data for each element within a circuit was tested using a *dummy cell* made up of standard electric circuit elements. The values of the circuit elements obtained by CNLS analysis of data from the whole circuit were compared with those obtained for the individual elements using a Wayne Kerr

B641 Universal Bridge. The dummy cell circuit is shown in Figure 4.1 and was chosen on the basis that it is similar to the model of the aqueous electrochemical cell to be tested.

Figure 4.1
The dummy cell



A variety of conditions were tested in the dummy-cell study to see which would lead to the most reliable results. Different aspects of a typical spectrum are shown in Figures 4.2, 4.3 and 4.4. The calculated values of R1, R2 and C from CNLS are shown in Table 4.1 where they are compared with the values individually and accurately determined for R1, R2 and C using the bridge.

Table 4.1

Dummy cell results.

Frequency Range / s ⁻¹	Amp	R1 / Ω		R2 / MΩ		C / pF	
		<+1>	<-2>	<+1>	<-2>	<+1>	<-2>
100,000 - 1,000	10 ⁴	92,892	58,455	10.15	10.12	122	115
6,000 - 100	10 ⁵						
400 - 0.2	10 ⁷						
10,000 - 0.2	10 ⁶	120,470	65,668	10.16	10.14	123	116
70,000 - 0.2	10 ⁶	109,810	62,161	10.18	10.16	123	115
Wayne Kerr B641 Universal Bridge		50,994		10.216		116.1	

Figure 4.2
The complete impedance plot of the dummy cell

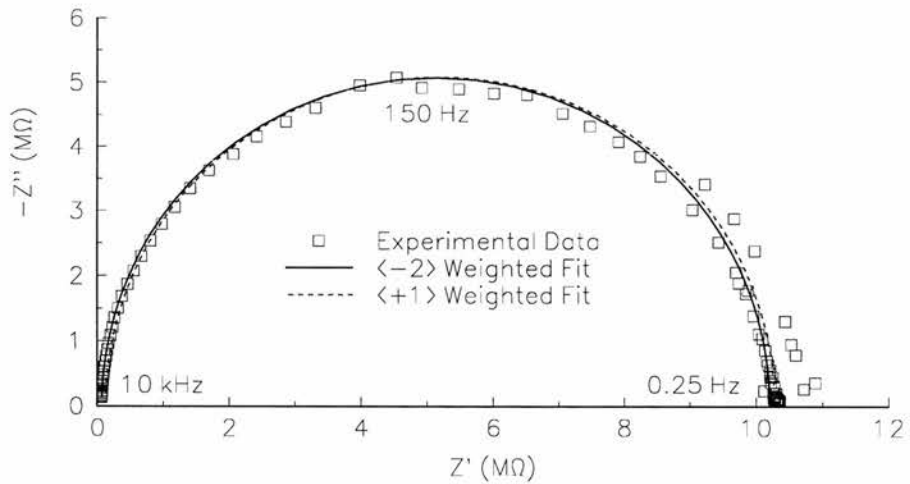


Figure 4.3
The high frequency part of the
dummy cell impedance plot

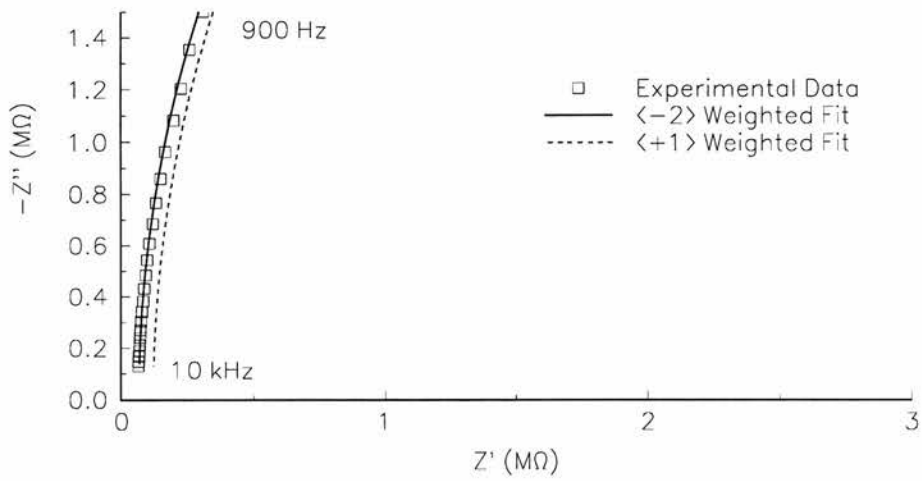
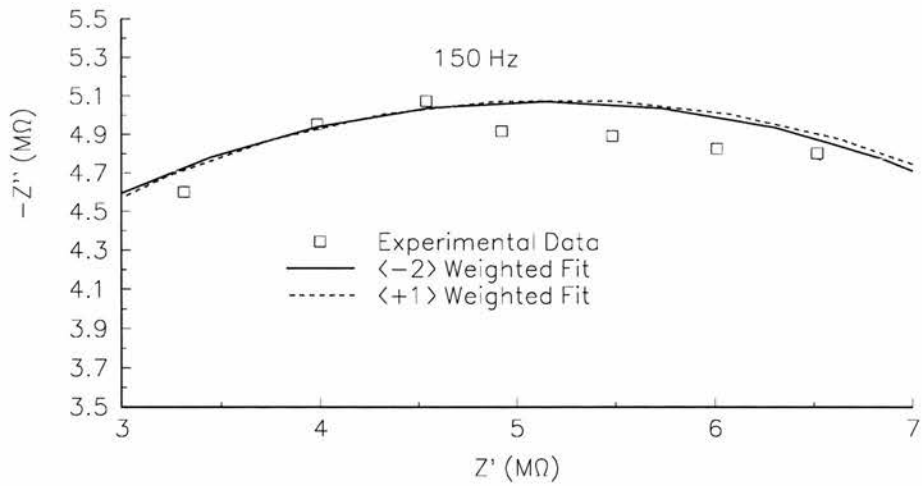


Figure 4.4
The dummy cell complex plane plot
in the region of the R2C time constant



The best match between the true values of circuit elements and the CNLS predicted values was achieved when a weighting factor of $\langle -2 \rangle$ was used in the LEVM program. The LEVM program can be run using different least-squares weighting

factors, of which the two most commonly employed are $< +1 >$ and $< -2 >$. A $< +1 >$ fit leads to each data point being weighted by a factor of one (effectively no weighting.) With $< -2 >$ fitting, instead of weighting the experimental data, data points arising from the least-squares model are weighted such that the uncertainty in the real and imaginary components is proportional to their respective magnitudes. The practical effect this has is to give more weight to the highest frequency points because these are the points associated with the lowest impedances. The $< -2 >$ factor is the one recommended by Macdonald in the notes accompanying the LEVM-5 software. The dummy cell results demonstrate that the recommendation is appropriate.

The impedance spectrum from the dummy cell is shown in its totality in Figure 4.2, while Figure 4.3 shows the high frequency part magnified and Figure 4.4 the R2C time-constant part magnified. The semi-circular shape of the spectrum is characteristic of a parallel resistance and capacitance. It is evident that the $< -2 >$ weighted fit is a better fit to the data than the $< +1 >$ fit, particularly at high frequencies. In addition to confirming the superiority of the $< -2 >$ fit, results from the dummy cell measurements led to the following conclusions:

- (a) The accuracy of the R1 value increases when higher frequencies are swept. This is logical because the value of R1 is given by the high frequency intercept of the data and the real axis. Furthermore this intercept is best found by the $< -2 >$ weighting factor.
- (b) The value for R1 is given less accurately than R2 or C. This is because R1's impedance (in $k\Omega$) is so very much lower than the other elements that it is

very difficult to separate its contribution to impedance from the $M\Omega$ contributions. In other words it is difficult to read differences of a few thousand Ohms when you are looking at a scale measured in millions of Ohms. Thus measurements on the aqueous system reported later in this chapter and the systems reported in later chapters are unlikely to yield very accurate values for solution resistance. This is not of great importance as the experiments are primarily concerned with probing the charge-transfer process.

- (c) The values of both R_2 and C are very accurate, indicating the CNLS technique's suitability for measurement of charge-transfer impedances and double-layer capacitances.

4.2 The Aqueous Electrochemical Cell.

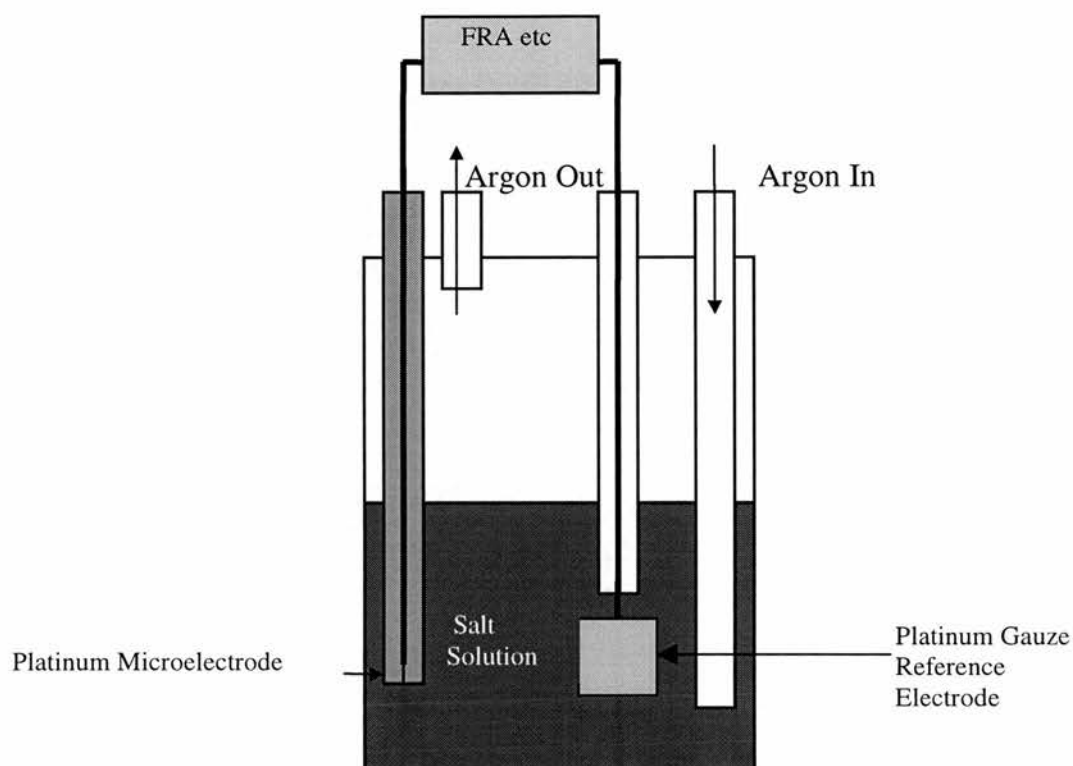
4.2.1 Preparation

The two-electrode cell shown in Figure 4.5 was employed. Prior to use, glassware was cleaned by immersion for several hours in a solution of potassium permanganate in concentrated sulphuric acid then rinsed thoroughly, firstly with distilled water, and then with the experimental solution. All solutions were prepared using triply distilled water. The salts used were potassium chloride, KCl; lithium chloride, LiCl; potassium ferricyanide, $\text{K}_3\text{Fe}(\text{CN})_6$; and potassium ferrocyanide, $\text{K}_4\text{Fe}(\text{CN})_6 \cdot 3\text{H}_2\text{O}$. KCl and LiCl were used at 1.0 M, i.e. 1.0 mol dm^{-3} (supporting electrolyte) while $\text{K}_3\text{Fe}(\text{CN})_6$ and $\text{K}_4\text{Fe}(\text{CN})_6$ - (i.e. the $\text{Fe}^{2+} / \text{Fe}^{3+}$ redox couple) were both used at 1 mM, i.e. $0.001 \text{ mol dm}^{-3}$.

Platinum microdiscs of nominal radii $5\mu\text{m}$, $10\mu\text{m}$ or $12.5\mu\text{m}$ were used. Following receipt the microelectrodes were prepared as outlined in Section 2.4.2. When the cell was fully prepared it was de-gassed by blowing high purity argon (BOC, 99.998% min) through the salt solution for thirty minutes. The argon flow was turned off shortly before making each measurement.

Figure 4.5

Two electrode cell used in study of aqueous $\text{Fe}^{2+} / \text{Fe}^{3+}$ system



4.2.2 Results In Aqueous KCl and Discussion

Frequency sweeps from 10,000 - 0.1 Hz were carried out at 10 mV r.m.s amplitude at room temperature ($21 \pm 1^\circ\text{C}$). Data were collected at the reversible potential of the redox couple in a number of different aqueous solutions each of which were 1.0 M in KCl supporting electrolyte and 1mM in $\text{Fe}^{2+}/\text{Fe}^{3+}$ redox couple. Figures 4.6 and 4.7 show complex plane impedance plots of data obtained using (nominally) $5\mu\text{m}$, $10\mu\text{m}$ and $12.5\mu\text{m}$ radius microelectrodes. (The radii quoted in the plots are those obtained from CNLS analysis.)

Figure 4.6.
Complex plane impedance plots using
microdiscs of different radii. Ω axes

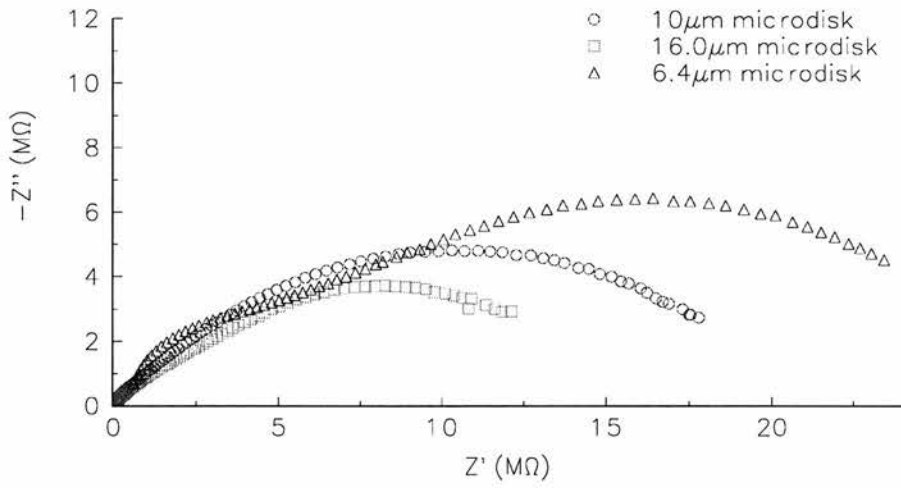
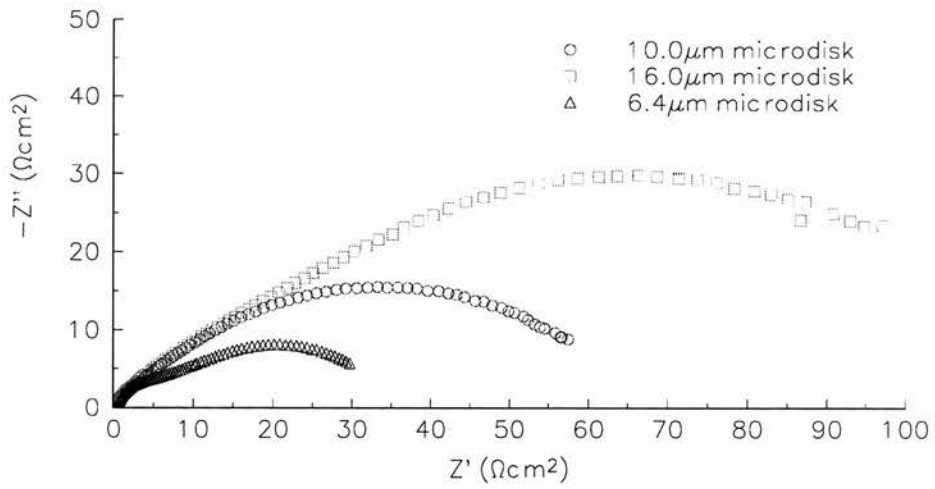


Figure 4.7.
Impedance plots from
electrodes of different radii. $\Omega \text{ cm}^2$ axes



It is apparent from Figure 4.6 that the highest overall impedance is exhibited by the microelectrode with the lowest surface area and vice-versa. Figure 4.7 shows the data plotted on axes of dimension $\Omega \text{ cm}^2$ rather than Ω . On these axes, the smallest microelectrode shows the lowest impedance. To see why this is so, consider Ohm's law written for current density; i.e. $R\pi a^2 = V/I$. ($R\pi a^2$ is represented by the symbol Θ in equation [3.11], for charge transfer and in equation [3.19] for diffusion.) Current density expresses the measured current per unit of electrode area and hence permits a true comparison between different sized electrodes to be made because if identical processes take place at different sized electrodes the *current densities* will be identical. (Different *currents* will be measured because more current can pass through the larger electrode.) Thus Θ depends only on electrochemical processes. It has previously been established that the diffusion rate increases with decreasing disc size and thus it is not surprising that in Figure 4.7 Θ is lowest at the smallest electrode. Since Θ_{ct} is identical for all three electrodes the advantage of the smallest electrode is clear - only at the smallest electrode is the diffusion impedance sufficiently low that the $R_{ct}C_{dl}$ semi-circle is seen clearly.

The data were analysed using both $< +1 >$ and $< -2 >$ weights. The $< -2 >$ fits were again superior. Both of the models discussed in Chapter 3, i.e. the exact model and the hemispherical approximation for an E mechanism, were applied to the data, yielding values for the disc radius a , the diffusion coefficient D , the double layer capacitance C_{dl} and the standard heterogeneous rate constant k_s . These are shown in Table 4.2. The averages of the values in Table 4.2 are shown in Table 4.3 and compared the values obtained by other researchers.

Values from the exact and hemispherical models are in reasonably good agreement with values found by previous workers at normal sized electrodes ^{(1), (2)} and microelectrodes ^{(3), (4)} #. The merits of the exact and hemispherical models are discussed below with respect to each parameter.

a) *The Radius*

In general, both the hemispherical and exact models yielded values of radii higher than the geometric value. If this is attributed to the fact that a rough surface has a greater surface area for reaction than a smooth surface then the roughness factors here would lie between 1 and 1.4 ^{##}. Such values are well within the expected values of roughness reported previously ⁽⁵⁾.

b) *The Diffusion Coefficient*

The majority of D values cluster around $6 \text{ to } 8 \times 10^{-6} \text{ cm}^2 \text{ s}^{-1}$, in good agreement with values determined by other workers.

Note that the results in Tables 4.2 and 4.3 for the hemispherical model derive from the same experimental procedure and CNLS analysis as the hemispherical results from reference 3 and hence should be very similar. Good agreement is indeed found, indicating that averaged results from impedance spectroscopy at a microelectrode seem to be of reasonably good reproducibility.

^{##} The roughness factor is given by (True Surface Area) ÷ (Geometric Surface Area). The geometric surface area is given by πa^2 where a is the geometric radius of the disk.

Table 4.2

Electrochemical parameters from CNLS fitting of impedance data

Calculated Radius / μm		Diffusion Coefficient / $10^6 \text{ cm}^2 \text{ s}^{-1}$		Double-layer Capacitance / $\mu\text{F cm}^{-2}$		Heterogeneous Rate Constant / cm s^{-1}	
Exact	Hemi	Exact	Hemi	Exact	Hemi	Exact	Hemi
5.94	5.47	6.7	6.7	56.8*	59.5*	0.0873	0.124
6.15	5.56	7.4	7.4	27.0	31.3	0.0982	0.125
7.00	6.36	8.1	8.2	29.1	34.3	0.0453	0.062
11.0	10.0	6.4	6.6	36.7	41.6	0.126	0.190
11.0	10.1	6.5	6.6	32.9	35.9	0.0837	0.141
11.8	10.9	13*	13*	31.6	36.2	0.101	0.138
16.7	16.0	5.5	5.3	31.4	33.8	0.0907	0.120

* These abnormal values are excluded from calculations of mean values.

(In Table 4.2 CNLS fitting of data using the exact model is denoted 'Exact' and fitting using the hemispherical approximation is denoted 'Hemi'.)

Table 4.3

Averages of electrochemical parameters from exact and hemispherical models compared with values found by previous workers

Experiment	Diffusion Coefficient / $10^6 \text{ cm}^2 \text{ s}^{-1}$	Double-layer Capacitance / $\mu\text{F cm}^{-2}$	Standard Rate Constant / cm s^{-1}
Exact Model	6.8	31.5	0.0903
Hemispherical Model	6.8	35.5	0.129
Exact ⁽³⁾	6.0	50.3	0.100
Hemispherical ⁽³⁾	6.6	28.3	0.129
Iwasita ⁽¹⁾	7.14	-	0.09
Abrantes ⁽⁴⁾	7.0	-	0.03

c) *The Double Layer Capacitance*

In the absence of adsorption on the electrode one would expect double layer capacitance values in the region of 10-40 μ F^{(6), (7)}. The values found here are certainly at the high end of this range but are not unusually high. The advantage of the CNLS impedance experiment is evident in this experiment where a value for C_{dl} has been produced in addition to values of the other electrochemical variables. The experiments carried out by Iwasita et al. and Abrantes et al. did not yield capacitance values^{(1), (4)}.

d) *The Standard Heterogeneous Rate Constant*

It is in their predictions for the value of the heterogeneous rate constant that the hemispherical and exact models differ most. The difference between the values obtained using the different models is, however, certainly within the precision that could reasonably be claimed for a heterogeneous rate constant. (It is common for values of k_s found in the literature to differ by orders of magnitude, particularly when comparing results from microelectrodes with normal sized electrodes^{(8), (9)}.) Obviously one would like to know which values for k_s are most reliable. One could study the model fits to the data shown in Figures 4.8 to 4.13 in order to try to decide which model was the best fit to the data or study the CNLS output parameters. Whether this would enable one to decide on the "true" value of k_s , however, is debatable. Since, in general, it is common for k_s values to be measured as part of a data set under different experimental conditions, rather than as a single isolated

value, the most important point to be made is that, if at all possible, one single model should be used throughout to yield self-consistent data. In general, the hemispherical approximation is used in this thesis. This is because, when new models required to be derived, e.g. for an EC mechanism, these were more readily derived using the hemispherical approximation as a starting point.

Figure 4.8
Comparison of exact and hemispherical models
at a $5\mu\text{m}$ microelectrode

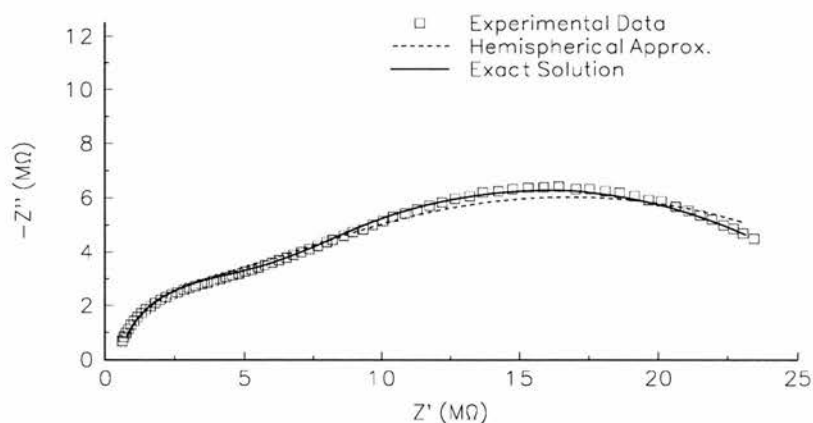


Figure 4.9
Comparison of exact and hemispherical models
at a $5\mu\text{m}$ microelectrode - high frequencies

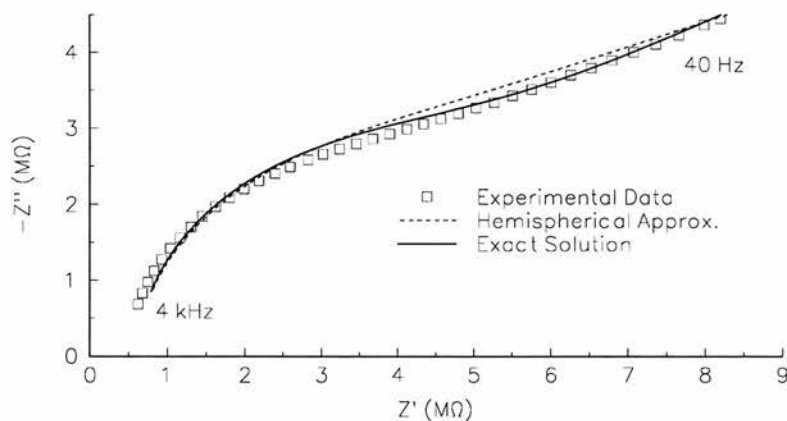


Figure 4.10
Comparison of exact and hemispherical models
at a 10 μ m microelectrode

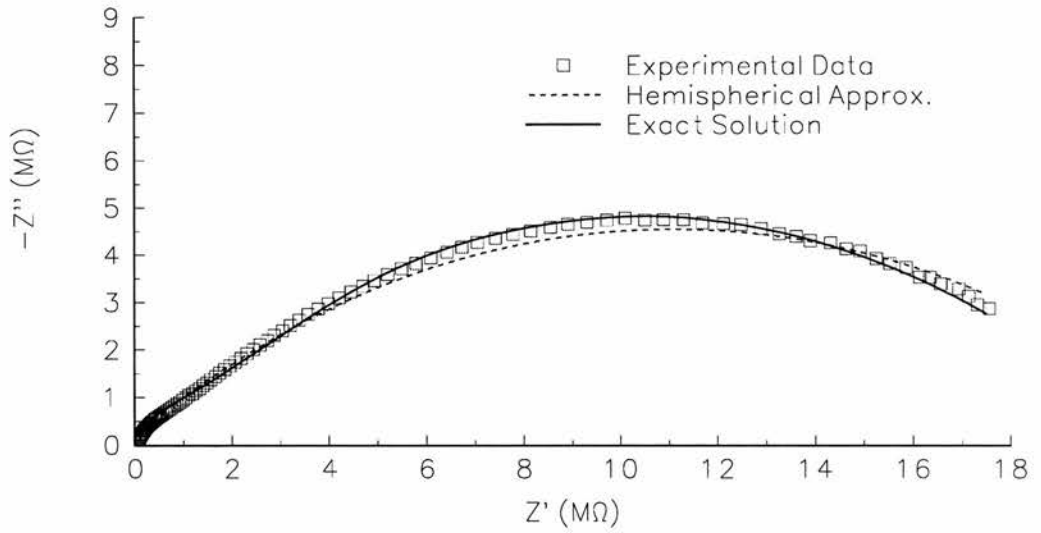


Figure 4.11
Comparison of exact and hemispherical models
at a 10 μ m microelectrode - high frequencies

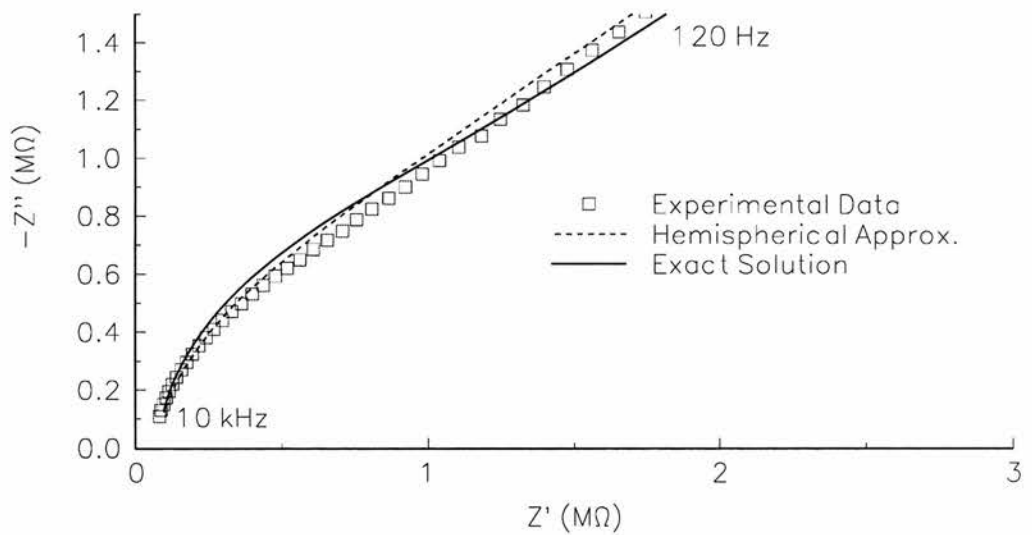


Figure 4.12
Comparison of exact and hemispherical models
at a 12.5 μm microelectrode

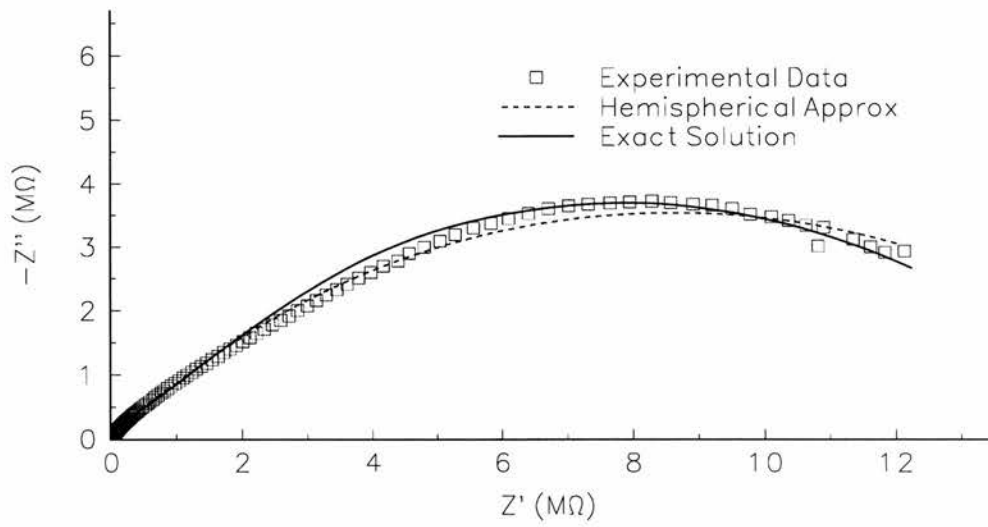
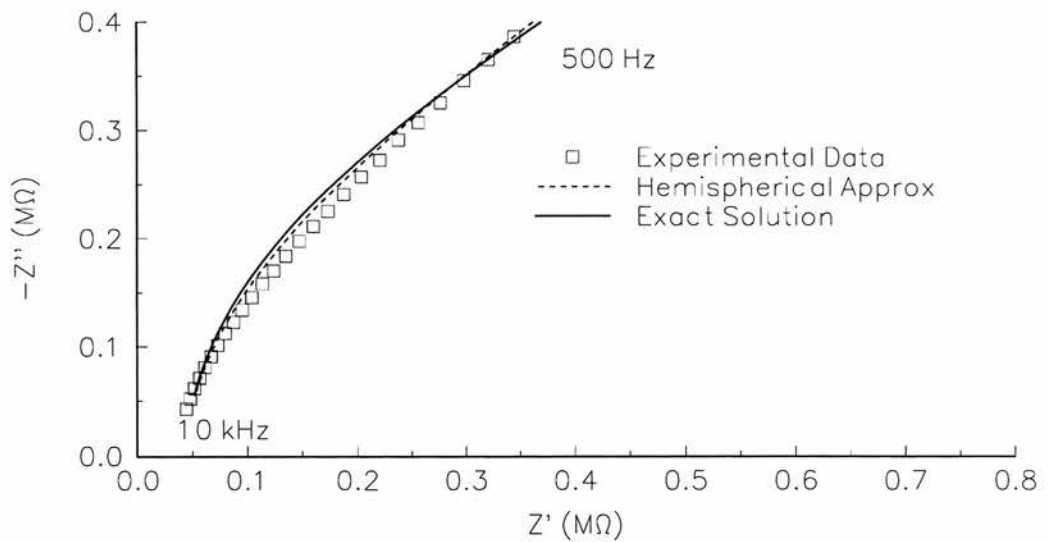


Figure 4.13
Comparison of exact and hemispherical models
at a 12.5 μm microelectrode - high frequencies



4.2.3 Aqueous LiCl - Impedance Results and Discussion

Identical experiments to those reported above were carried out using LiCl instead of KCl as the supporting electrolyte. The complex plane plots shown in Figures 4.14 to 4.17 resulted. The electrochemical parameters resulting from the CNLS analysis are shown in Table 4.4.

Table 4.4

Electrochemical parameters from CNLS fitting of impedance data in LiCl.

Fitted Radius μm		Diffusion Coefficient $/ 10^6 \text{ cm}^2 \text{ s}^{-1}$		Double-layer Capacitance $/ \mu\text{F cm}^{-2}$		Standard Rate Constant $/ \text{ cm s}^{-1}$	
Exact	Hemi	Exact	Hemi	Exact	Hemi	Exact	Hemi
4.9	4.0	5.1	5.9	36.8	55.3	0.0114	0.0186
4.8	3.9	5.1	6.0	38.5	58.4	0.0126	0.0207
13.0	12.0	5.0	5.1	28.3	33.0	0.0290	0.0373
13.9	12.8	4.6	4.7	26.3	31.0	0.0196	0.0249

Figure 4.14
 Comparison of exact and hemispherical models
 at a $5\mu\text{m}$ microelectrode

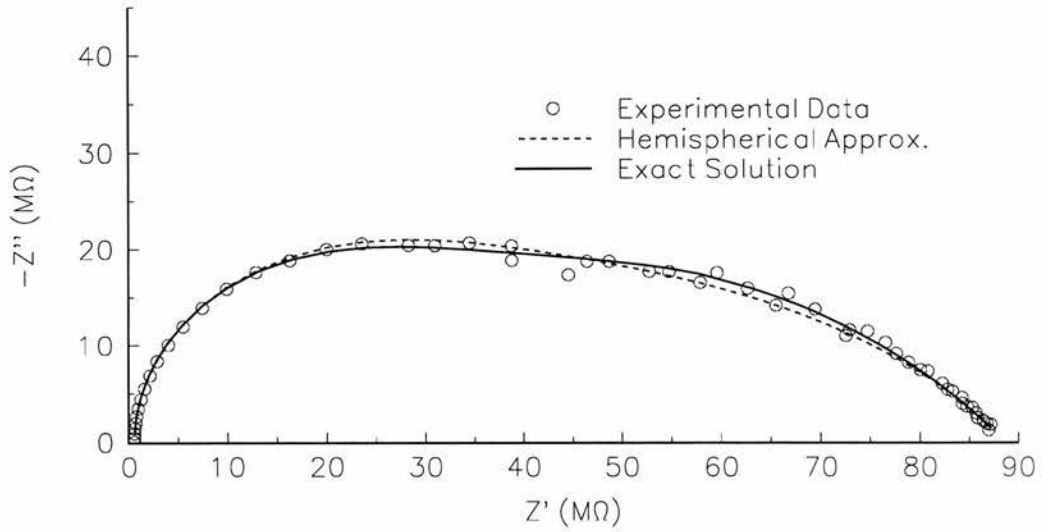


Figure 4.15
 Comparison of exact and hemispherical models
 at a $5\mu\text{m}$ microelectrode - high frequencies

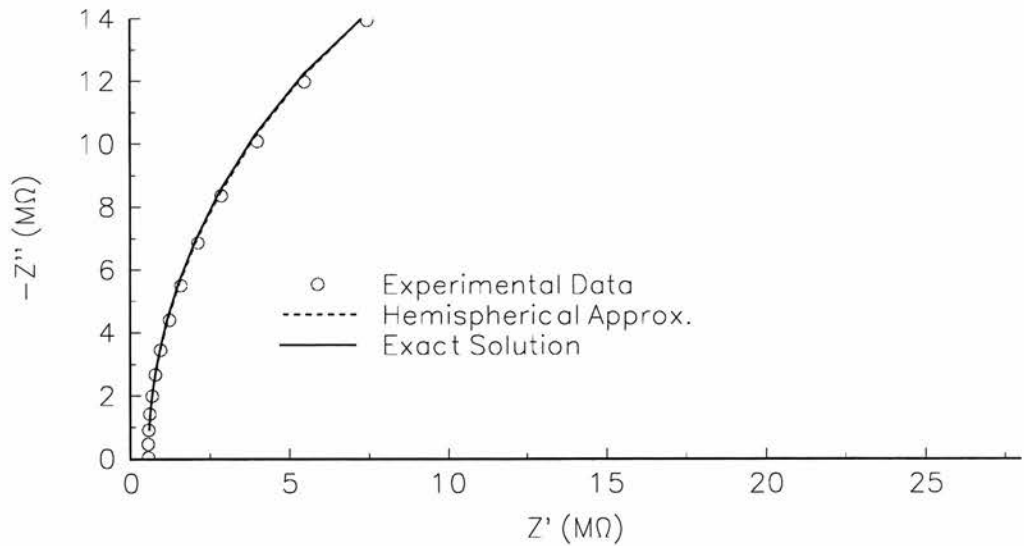


Figure 4.16
Comparison of exact and hemispherical models
at a 12.5 μm microelectrode

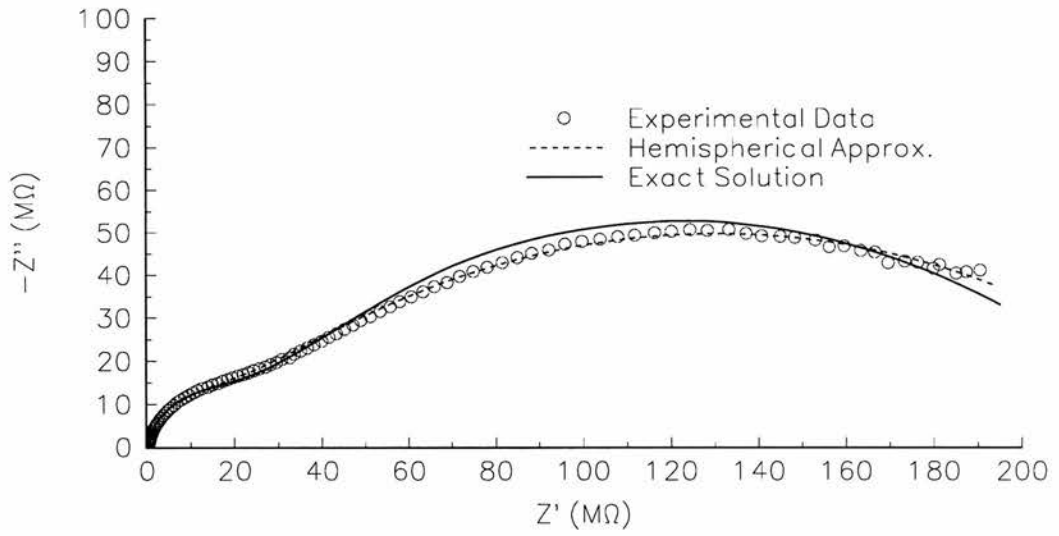
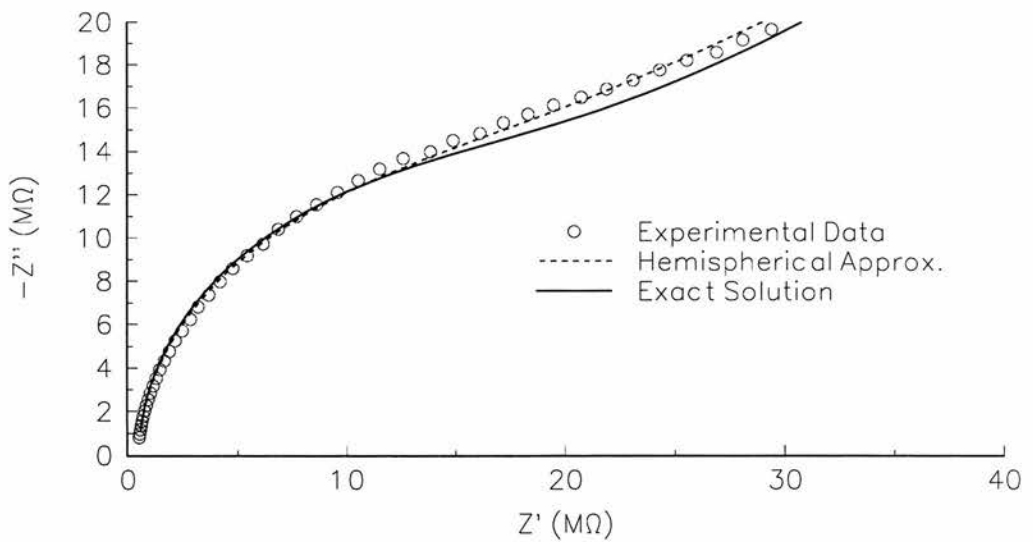


Figure 4.17
Comparison of exact and hemispherical models
at a 12.5 μm microelectrode - high frequencies



Mean values from Table 4.4 are compared with those obtained previously by Los (private communication) in Table 4.5.

Table 4.5
Averages of electrochemical parameters from exact and hemispherical models compared with values found by previous workers.

Experiment	Diffusion Coefficient / $10^6 \text{ cm}^2 \text{ s}^{-1}$	Double-layer Capacitance $\mu\text{F cm}^{-2}$	Standard Rate Constant / cm s^{-1}
Exact Model	5.0	32.5	0.0181
Hemispherical Model	5.4	44.4	0.0254
Los Exact	5.3	46.5	0.010
Los Hemispherical	5.3	47.8	0.010

Again good agreement is observed for diffusion coefficients but somewhat higher values for the rate constant emerged in the work carried out for this thesis. The reasons for this are unknown. The other feature of the data worth commenting upon is the difference in the rate constants for electron transfer when the supporting electrolyte is changed from KCl to LiCl. Higher rate constants are observed in KCl solutions. It is believed that this is because smaller (solvated) alkali metal cations form stronger ion pairs with $\text{Fe}(\text{CN})_6^{3-}$ and $\text{Fe}(\text{CN})_6^{4-}$ and that these ion pairs, such as $\text{M}_{n+1}\text{Fe}(\text{II})(\text{CN})_6^{(3-n)-}$, act to reduce the barrier for electron transfer. Thus the magnitude of k_s decreases with the following supporting cations, $\text{Cs}^+ > \text{K}^+ > \text{Na}^+ > \text{Li}^+$ ⁽¹⁰⁾. In subsequent chapters, the effects of ion-pairing in non-aqueous systems will be explored in more detail than here.

4.3 Refinement of the Models with a CPE.

Instead of representing the capacitance element in the equivalent circuit as an ideal capacitor of impedance $(j\omega C)^{-1}$, it can be represented instead by an element of impedance $X^{-1}(j\omega)^{-\Phi}$, known as a constant phase element or CPE, where X is a constant and $0.5 \leq \Phi \leq 1$ ⁽¹¹⁾. In the case where $\Phi = 1$ the CPE behaves as an ideal capacitor and X is equivalent to the capacitance C . The CPE is an empirical concept introduced in order to fit impedance data in systems where the value of C is frequency dependent - i.e. the capacitance is not ideal. Electrode surface roughness is one of the most studied causes of CPE behaviour from which it is proposed that microscopic grooves and imperfections on the metal surface cause inhomogeneities in the electric field and current density at the electrode leading to frequency dependent capacitance. Given the discussion in Section 4.2.2 where the values of electrode radii from CNLS were bigger than the geometric radii and given simple physical constraints on the likelihood of producing a microscopically smooth electrode it is sensible to assume that the microelectrodes used in these experiments were rough. It is interesting to see whether using a CPE in the CNLS fitting leads to a better fit than the simple capacitance previously employed. The exact and hemispherical models were modified by substituting a CPE for the capacitor in the equations and the new Exact CPE and Hemispherical CPE equations were used to model the data for three microelectrodes. The impedance spectra in Figures 4.18 - 4.19 compare the best fit previously obtained without a CPE with the best fit obtained with a CPE. Table 4.6 below compares the standard deviations of the fits obtained with and without a CPE and shows, for the CPE model, the Φ values of the CPE resulting from the analysis.

Table 4.6

CPE Φ values and comparison of standard deviations of fits from CPE vs Non CPE models.

Geometric Radius (μm)	Standard Deviation Of Fit		CPE Φ value
	Non CPE Model	CPE Model	
5	1.706×10^{-3}	1.075×10^{-3}	1.13
10	3.566×10^{-3}	9.296×10^{-4}	1.15
12.5	2.045×10^{-3}	1.900×10^{-3}	1.15

Figure 4.18
Comparison of exact and exact-CPE models at a $5\mu\text{m}$ microelectrode

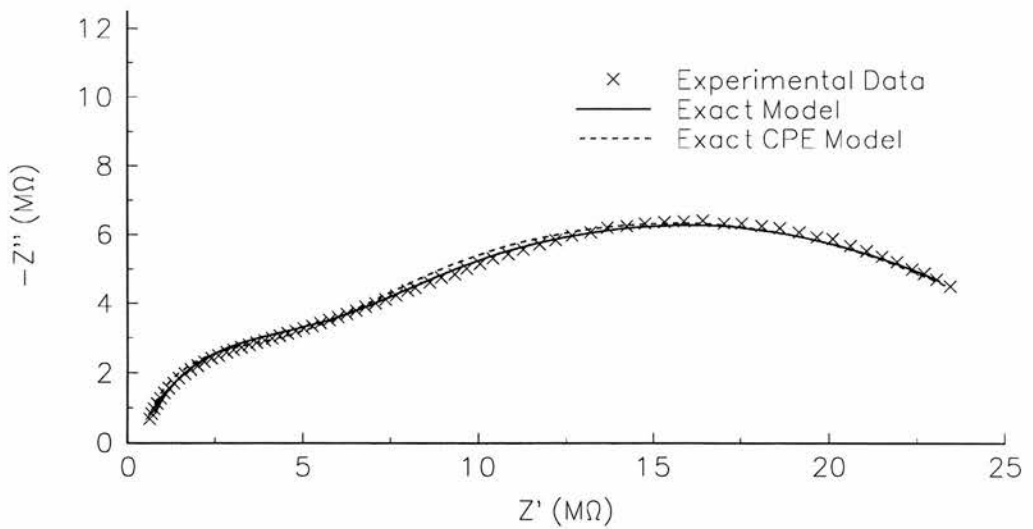


Figure 4.19
Comparison of exact and exact-CPE models
at a 5 μm microelectrode - high frequencies

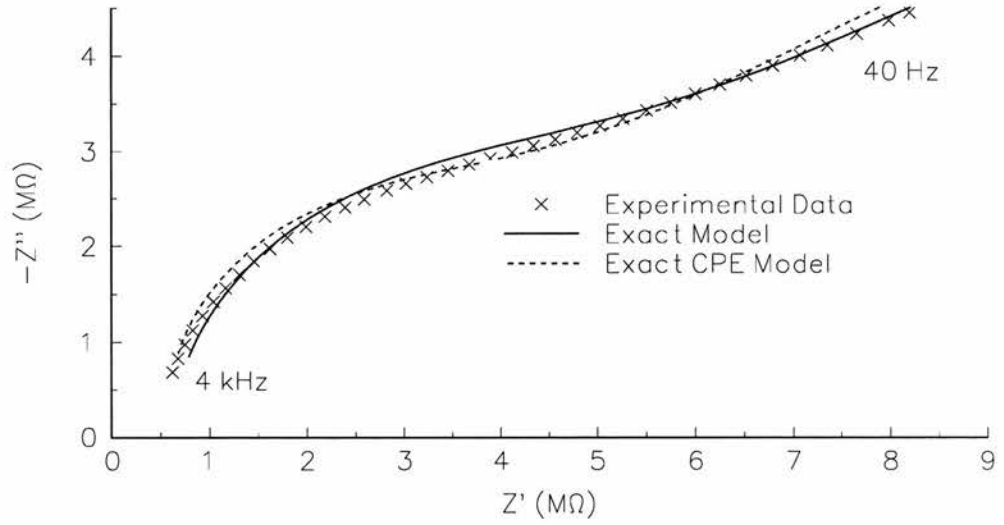


Figure 4.20
Comparison of exact and exact-CPE models
at a 10 μm microelectrode

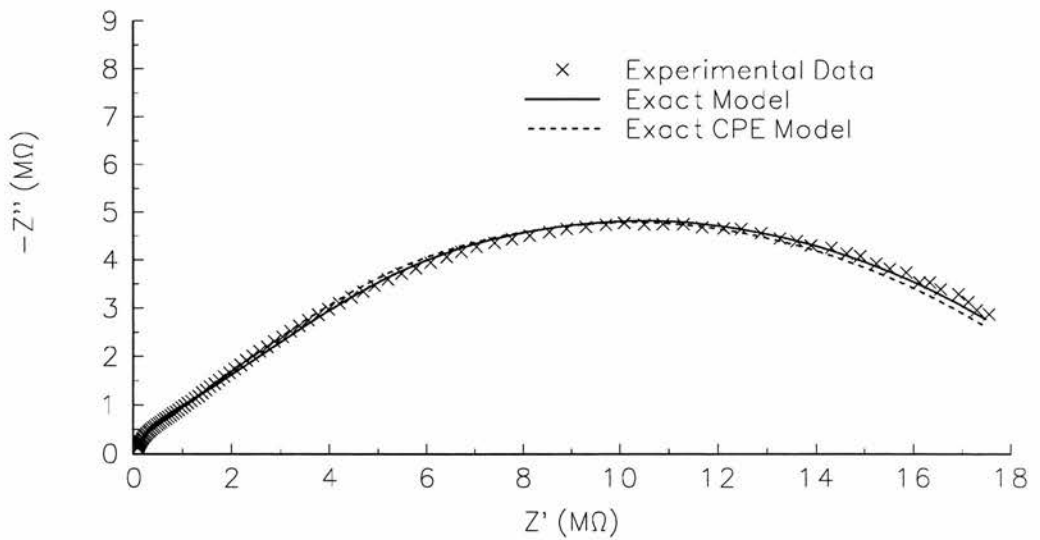


Figure 4.21
Comparison of exact and exact-CPE models
at a $10\mu\text{m}$ microelectrode - high frequencies

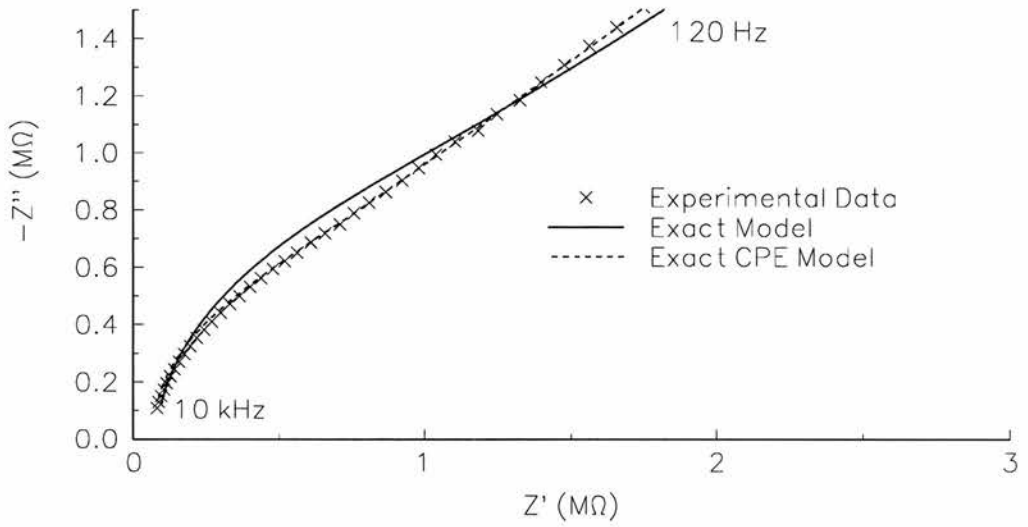


Figure 4.22
Comparison of exact and exact-CPE models
at a $12.5\mu\text{m}$ microelectrode

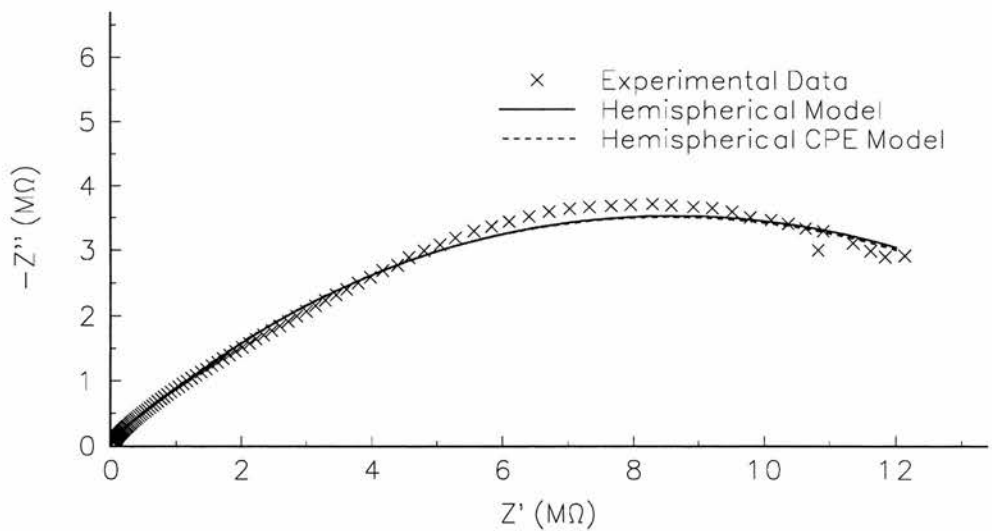
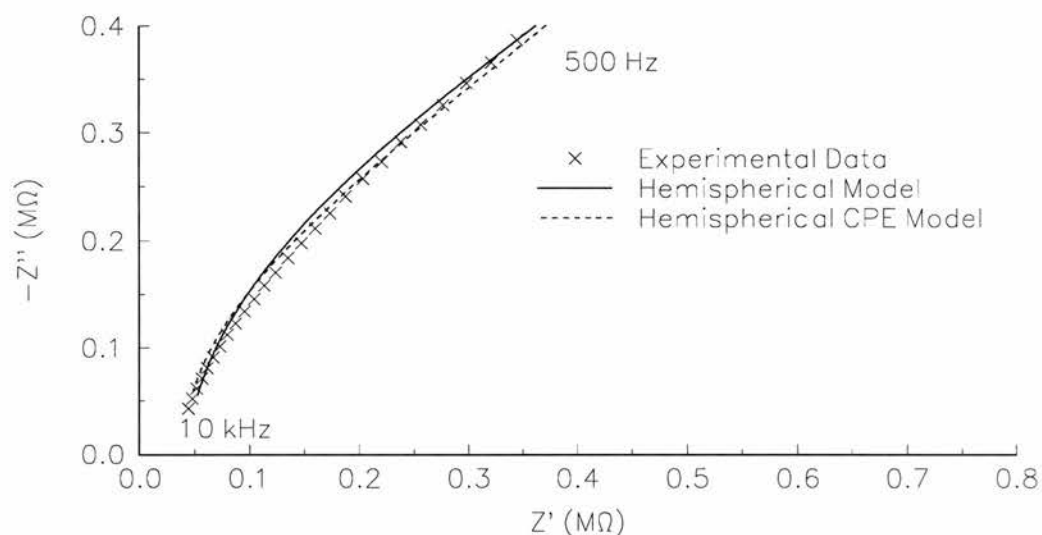


Figure 4.23
 Comparison of exact and exact-CPE models
 at a 12.5 μm microelectrode - high frequencies



The data show that inclusion of the CPE as a free parameter improves the fits. So what effect does inclusion of a CPE have on the other calculated values? Table 4.7 compares the values resulting for each electrode from the best fitting non-CPE model (exact or hemispherical) with the best fitting CPE model (exact or hemispherical.)

The most noticeable feature in the results is the very significant increase in rate constants when the CPE model is used compared with the non-CPE model. Since the model is apparently improved by inclusion of a CPE, it is interesting to see what values of Φ lead to the improvement and to try to relate this to electrode roughness. The values of Φ found by CNLS were 1.13, 1.15 and 1.15 for the 5 μm , 10 μm and 12.5 μm electrodes respectively. These values, lying as they do outside the expected 0.5 - 1.0 range, can have no physical meaning in terms of the frequency

Table 4.7

Comparison of electrochemical parameters from CPE vs non-CPE models

Geometric Radius / μm	CNLS Radius / μm		Diffusion Coefficient / $\text{cm}^2 \text{s}^{-1}$		Standard Rate Constant. / cm s^{-1}	
	Non CPE Model	CPE Model	Non CPE Model	CPE Model	Non CPE Model	CPE Model
5	7.0	6.6	8.1	8.3	0.0453	0.0724
10	10.1	10.5	6.6	6.7	0.141	0.239
12.5	16.0	15.7	5.3	5.4	0.120	0.377

dependence of capacitance. They are simply the numbers that the LEVM program produced when given Φ as a free parameter to manipulate for the best fit. It is interesting to speculate whether it is coincidental that the values of Φ should be so similar to one another if they are simply the empirical numbers found by LEVM to improve the fit most. The fact that the fit has been improved using a Φ value with no apparent physical meaning may indicate that there is still significant room for optimisation of the experimental method. More often than not, however, the LEVM program could not fit the data at all when the Φ parameter was present. The values shown in Table 4.7 are from the data sets that *could* be fitted with acceptable least-squares fitting errors for all parameters - i.e. less than 8%.

4.4 How Could The Experimental Method Be Improved?

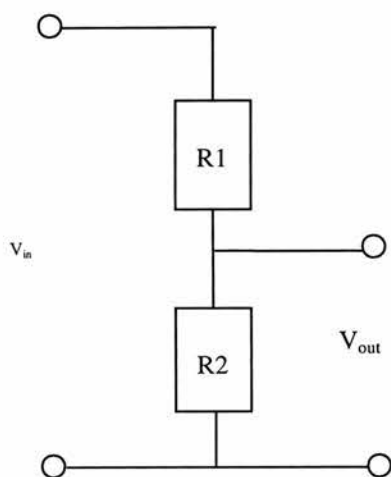
In their derivation of equations for diffusion impedance to a microdisc, Fleischmann and Pons emphasised that the equations are valid only for small signal perturbations. In their subsequent experimental application of the equations they used an excitation signal of 2 mV r.m.s.⁽⁴⁾ Kooyman, Sluyters-Rehbach and Sluyters looked at how large the amplitude of a perturbation signal could be in order to maintain deviation from linearity at less than 1%⁽¹²⁾. Their conclusions indicated that provided the symmetry coefficient α was equal to 0.5 then, dependent on the balance between charge-transfer and diffusion control of the current, a maximum signal of 6 - 8.5 mV r.m.s could be used. If, however the value of α deviated from 0.5 there were serious implications for the size of perturbation allowable. For example, for $\alpha = 0.4$ amplitudes of less than 2 mV r.m.s would be necessary to ensure linear behaviour. In the aqueous experiments reported by Bruce et al. with which this work is being compared a perturbation signal of 10 mV r.m.s was employed⁽³⁾. Obviously such a signal is outside the linear conditions discussed above. It was an interesting possibility that this alone might account for the observed CPE values greater than unity. There was also a possibility, of course, that application of an excessively large perturbation signal had resulted in other inaccuracies, particularly in the values of k_s , which in Table 4.7 are quite variable.

Why was a signal of 10 mV r.m.s employed when the available literature all pointed to the fact that smaller perturbations are obligatory? The reason is that signal to noise ratio was often a significant problem in the impedance experiments and that unless a larger input signal - i.e. 10 mV r.m.s - was used, the output could

be swamped by noise, preventing a complete spectrum from being obtained. In order to improve the signal to noise ratio the following actions were taken. The ultimate aim was to enable the size of the perturbation signal to be reduced.

Action Taken	Result
<p>The current amplifier was mounted within the Faraday cage, adjacent to the experimental cell instead of outside the cage on top of the FRA. The objective of this action was to reduce stray capacitance and prevent amplification of any noise picked up by a long length of cable.</p>	<p>A much cleaner output signal was obtained with the amplifier OUTSIDE the FRA.</p>
<p>A formal connection to earth was provided to the Faraday cage.</p>	<p>No effect was observed.</p>
<p>The 10 mV r.m.s perturbation signal produced by the FRA is rather noisy. The noise increases unacceptably at the lower amplitudes. To enable the FRA to produce a cleaner signal, the use of a voltage divider was adopted. (The voltage divider enables the FRA to produce a very clean signal of, say, 1V amplitude, most of which is dropped over a large resistor leaving a small, clean signal to go to the test cell. (Figure 4.24.)</p>	<p>This method was highly effective. Very clean input signals were produced, observed using an oscilloscope, at 2,3,5 and 10 mV r.m.s resulting in much cleaner outputs for analysis.</p>

Figure 4.24
The voltage divider



$$i_{in} = \frac{V_{in}}{R1 + R2}$$

$$V_{out} = V_{in} \frac{R2}{R1 + R2}$$

Now that a method had been found enabling smaller signals to be employed, impedance experiments using a variety of voltage signals were carried out on freshly prepared solutions. The impedance data are shown in Figures 4.25 and 4.26. These data were analysed using the hemispherical approximation. The resulting values are recorded in Table 4.8 where it is clear that only at an input signal of 40 mV r.m.s did values deviate from those obtained at low amplitude signals.

Thus it was concluded, despite theoretical reservations regarding the use of excitation signals as large as 10 mV r.m.s, that such signals produced results virtually identical to smaller signals. Hence, the data generated using a 10 mV signal should be entirely reliable.

Figure 4.25

Effect of signal amplitude on impedance data - all frequencies

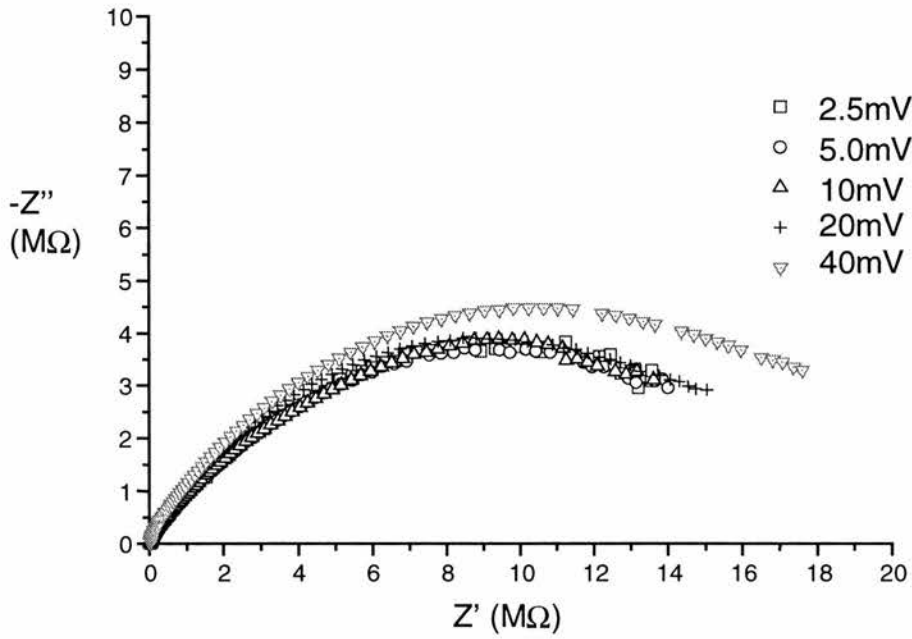


Figure 4.26

Effect of signal amplitude on impedance data - high frequencies

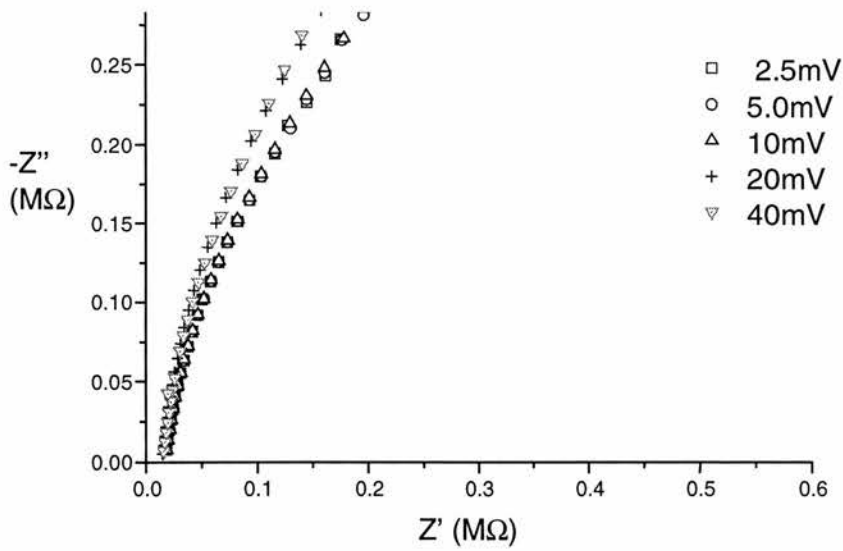


Table 4.8

CNLS analysis using the hemispherical approximation with different excitation voltages

Signal / mV	Double-layer Capacitance / $\mu\text{F cm}^{-2}$	Diffusion Coefficient / $10^6 \text{ cm}^2 \text{ s}^{-1}$	Predicted Electrode Radius / μm	Standard Rate Constant / cm s^{-1}
2.5	24.8	7.53	11.0	0.143
5	25.0	7.68	10.9	0.139
10	25.7	8.03	10.8	0.148
20	32.2	7.46	10.2	0.131
40	34.8	6.99	9.56	0.253

4.5 Conclusions

Impedance data at microelectrodes were similar to those recently obtained by other researchers at St. Andrews University. Sufficient confidence was therefore generated to study other electrochemical cells.

A voltage divider can be employed to produce cleaner output signals from a FRA if undistorted low amplitude signals are required.

Despite theoretical arguments against using excitation amplitudes as large as 10 mV r.m.s, in practice, impedance data at 10 mV were identical to those obtained using smaller excitations.

4.6 References

1. T. Iwasita, W. Schmickler, J. Hermann and U. Vogel, *J. Electrochem. Soc.*, (1983), 130, p2026.
2. R.V. Bucur, A. Bartes, V. Mecea, *Electrochim. Acta*, (1978), 23, p641 - 646.
3. P.G. Bruce, A. Lisowska-Oleksiak, P. Los, C.A. Vincent, *J. Electroanal. Chem.*, (1994), 367, p279.
4. L.M. Abrantes, M. Fleischmann, L.M. Peter, S. Pons, B.R. Scharifker, *J. Electroanal. Chem.*, (1988), 256, p229.
5. R. De Levie, *Electrochimica Acta.*, (1965), 10, p113.
6. T.T. Wooster, M.L. Longmire, M. Watanabe, R.W. Murray, *J. Phys. Chem.*, (1990), 95, p5315.
7. A.J. Bard, L.R. Faulkner, *Electrochemical Methods Fundamentals and Applications*, John Wiley & Sons Inc., (1980), p8.
8. A.P. Abbott, C.L. Miaw, J.F. Rusling, *J. Electroanal. Chem.*, (1992), 327, p31.
9. W.R. Fawcett, M. Opallo, *Angew. Chem. Int. Ed. Engl.*, (1994), 33, p2131.
10. K. Niwa, K. Doblhofer, *Electrochimica Acta*. (1986), 31, p439.
11. J.R. Macdonald *LEVM Software Version 5 Manual*, 1990.
12. D.J. Kooyman, M. Sluyters-Rehbach, J.H. Sluyters, *Electrochim. Acta*, (1966), 11, p1197.

CHAPTER 5

A MICROELECTRODE IMPEDANCE STUDY OF THE HETEROGENEOUS KINETICS OF FERROCENE IN TETRAGLYME

Introduction

It is well established that ferrocene, (often designated $\text{Fe}(\text{Cp})_2$ or simply Fc), may be oxidised to yield the ferrocenium cation, ($\text{Fe}(\text{Cp})_2^+$ or Fc^+). Ferrocene oxidations have been carried out in a wide range of solvents and background electrolytes. The reaction has been shown to be reversible and ferrocene/ferrocenium is recommended by IUPAC as a reference couple for reporting electrode potentials in non-aqueous solvents ⁽¹⁾. To date the electrochemistry of ferrocene has not been studied in tetraglyme nor has CNLS analysis of microelectrode impedance data been used in such a study - these were the principal objectives of the work reported in this chapter. The consequence of acquiring this data, it was hoped, would be a legitimate comparison of kinetic data in the liquid and solid phases. (See Chapter 7.)

5.1 Electrochemical Impedance Study of the Ferrocene / Ferrocenium Couple.

5.1.1 Preliminary Impedance and Voltammetry Measurements

All materials were prepared as described in Chapter 2. The cells were formulated as follows:

Pt (microdisc) / tetraglyme, Fe(Cp)₂, LiClO₄ / Li (s)

or

Pt (microdisc) / tetraglyme, Fe(Cp)₂, LiClO₄ / Pt (gauze)

Typical cyclic voltammograms obtained at a scan rate of 20 mV s⁻¹ using a platinum microdisc of radius 10 μm at a temperature of 22 ± 1°C are shown in Figures 5.1 to 5.4.

It is known that for the reversible transfer of an electron ^(2a), $|E_{3/4} - E_{1/4}| = 56.4$ mV at 25°C. (The potentials $E_{3/4}$ and $E_{1/4}$ are those for which $i = 3i_d/4$ and $i = i_d/4$ where i_d is the diffusion limited current.) In this study, analyses of the current/voltage profiles of all ferrocene/ferrocenium voltammograms yielded $|E_{3/4} - E_{1/4}|$ values of 54 mV to 60 mV. It is concluded, therefore, that the cells investigated here are reversible.

In impedance experiments the ferrocene/ferrocenium couple was generated at the microelectrode surface (Figure 2.3) by applying the dc potential at which impedance was minimised. For an E mechanism this coincides with the condition of the standard equilibrium potential in which the concentrations of the reduced and oxidised species at the surface of the electrode are equal. In this condition no net current flows; this is clear from the absolute rate equation [3.1]. Although there is no net current, the exchange current flows, i.e. equal and opposite faradaic current corresponding to the reduction and oxidation reaction currents. The equation for the exchange current density, i_0 , is obtained by writing equation [3.1] equal to zero followed by a little algebraic manipulation to obtain ^(2b):

$$i_0 = nFk_s C \quad [5.1]$$

where $C = C_O = C_R$. From this equation it is clear that working at the equilibrium potential offers the simplest means of calculating the value of k_s .

Typical complex-plane plots from impedance measurements on the cells at room temperature are shown in Figures 5.5 to 5.9 while Figures 5.10 and 5.11 show spectroscopic plots in which, respectively, the real part of impedance and the imaginary part of impedance are plotted against frequency. The hemispherical approximation CNLS fit is also shown on the plots for comparison with the data.

Figure 5.1
3.7 mM ferrocene
0.5 M LiClO₄

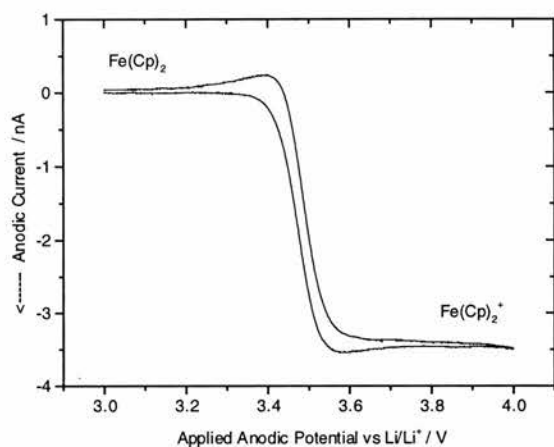


Figure 5.2
6.4 mM ferrocene
0.5 M LiClO₄

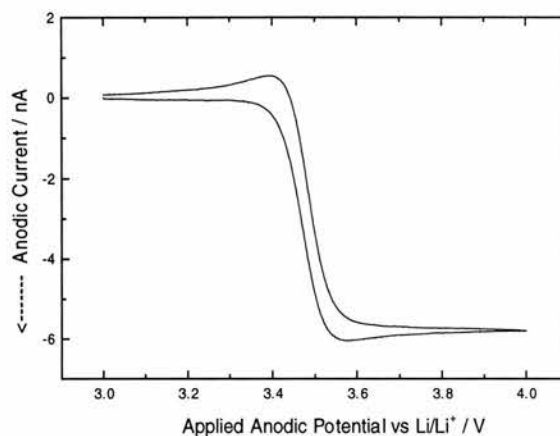


Figure 5.3
13.1 mM ferrocene
0.5 M LiClO₄

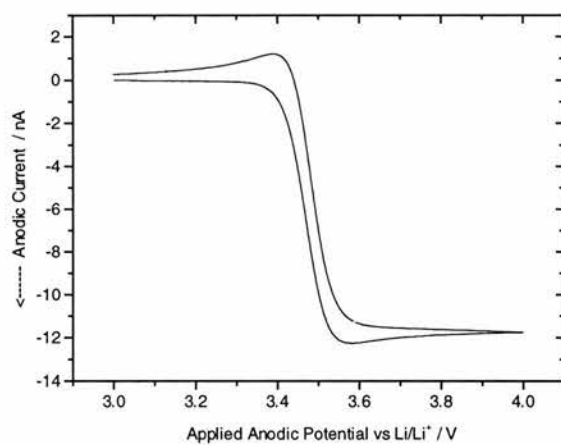


Figure 5.4
21.9 mM ferrocene
0.5 M LiClO₄

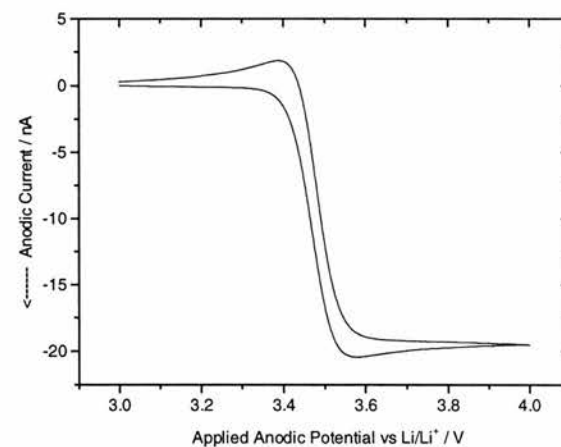


Figure 5.5

Pt ($a = 5 \mu\text{m}$) / tetraglyme, 4 mM ferrocene, 0.5 M LiClO_4 / Pt gauze

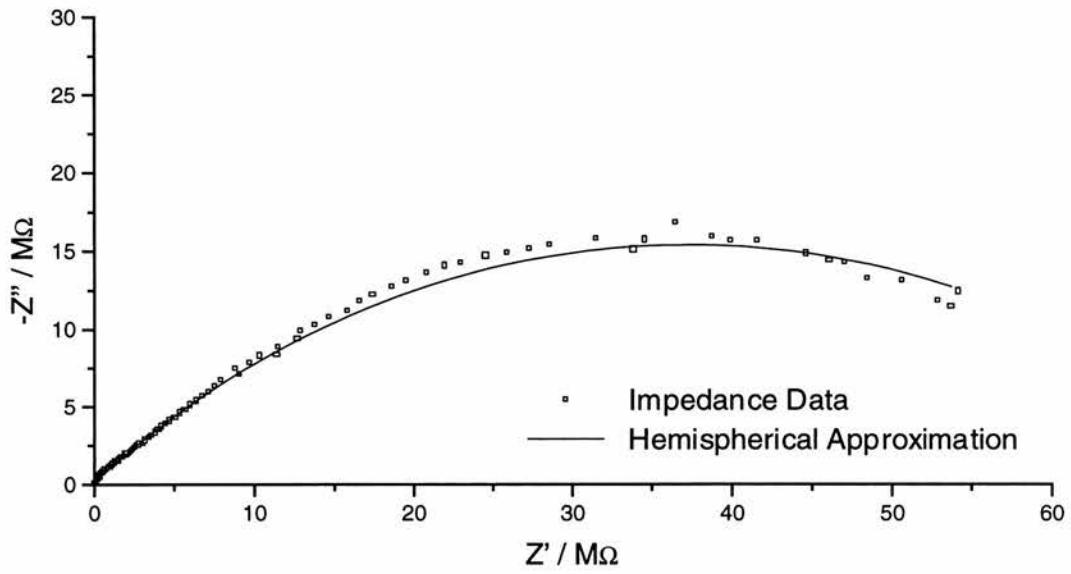


Figure 5.6

Pt ($a = 5 \mu\text{m}$) / tetraglyme, 16 mM ferrocene, 0.5 M LiClO_4 / Pt gauze

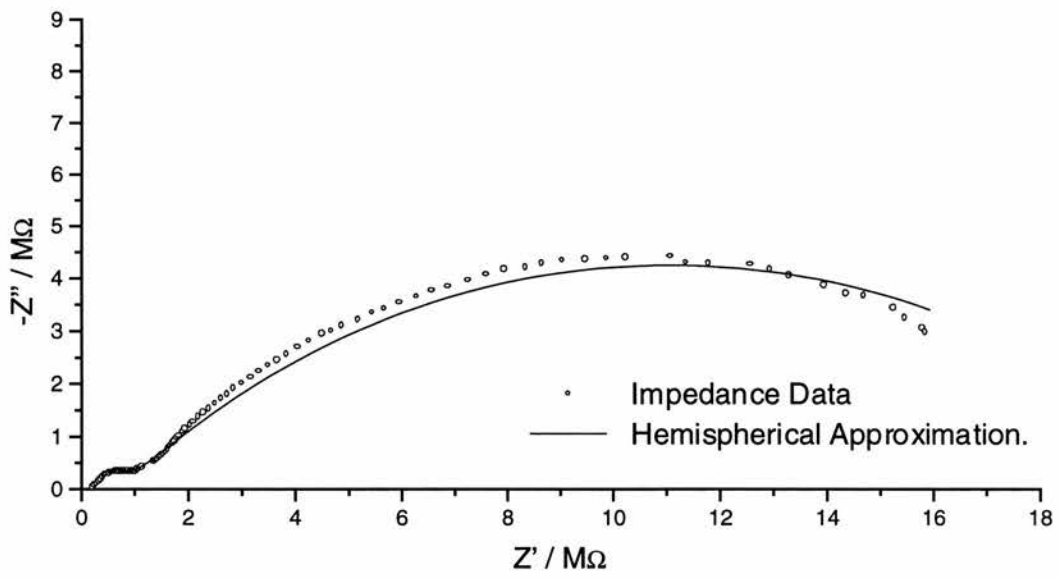


Figure 5.7

Pt ($a = 5 \mu\text{m}$) / tetraglyme, 30 mM ferrocene, 0.5 M LiClO₄ / Pt gauze

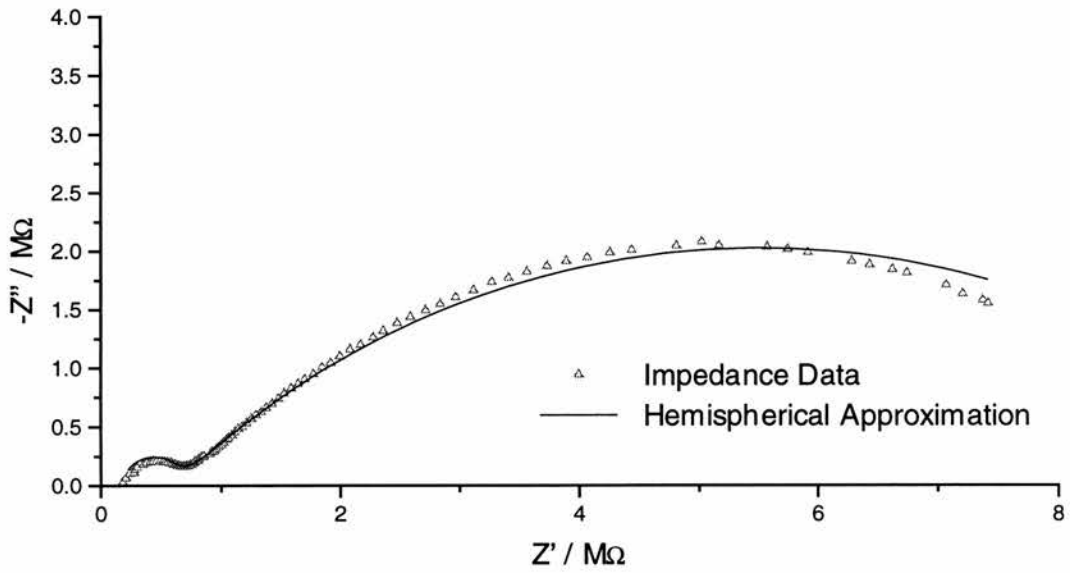


Figure 5.8

Pt ($a = 5 \mu\text{m}$) / tetraglyme, 60 mM ferrocene, 0.5 M LiClO₄ / Pt gauze

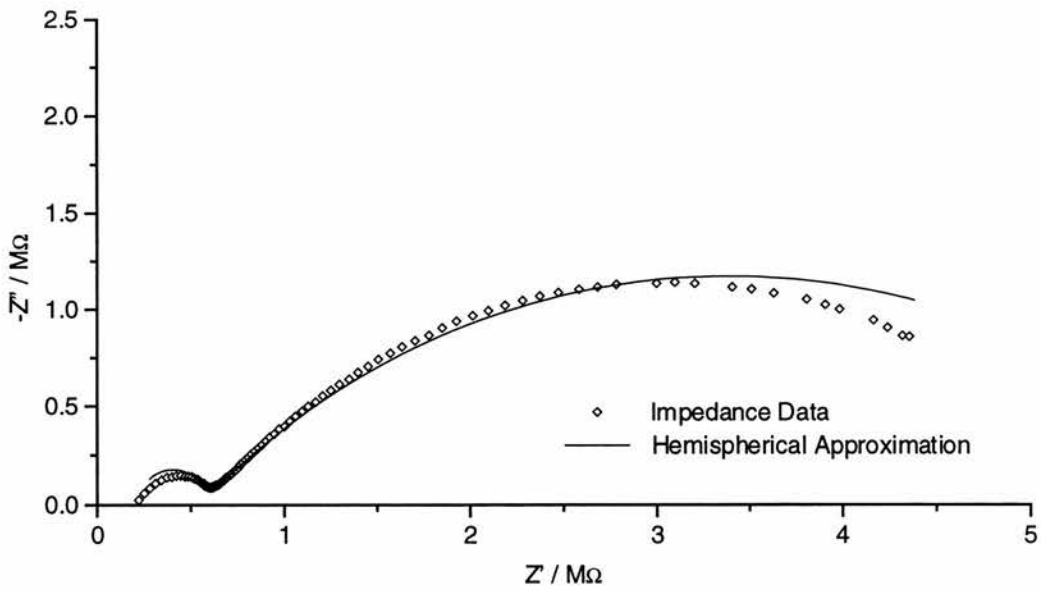


Figure 5.9

Relative impedances with varying ferrocene concentration.

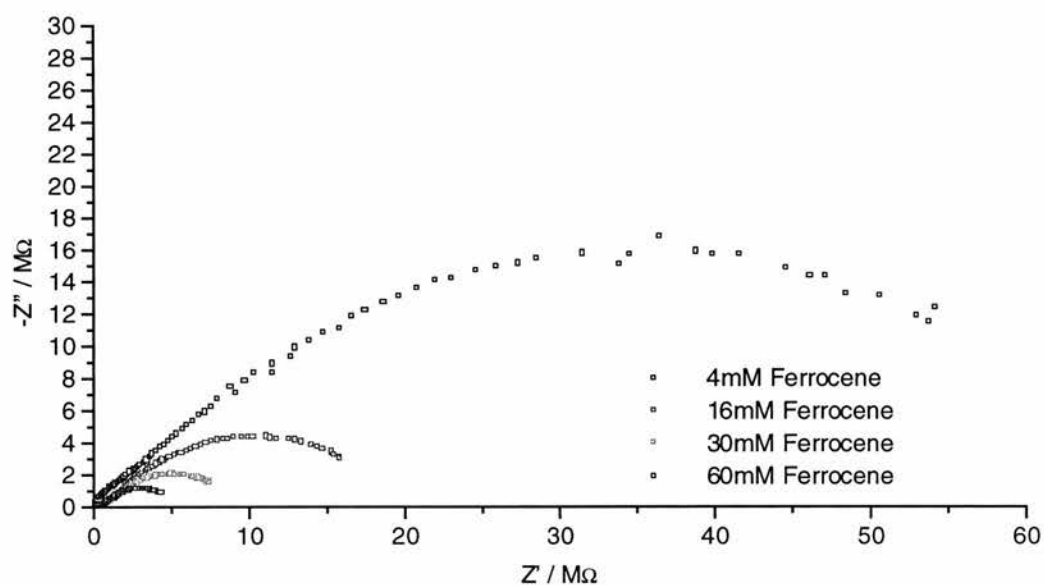


Figure 5.10

Pt ($a = 5 \mu\text{m}$) / tetraglyme, 4 mM ferrocene, 0.5 M LiClO_4 / Pt gauze

Spectroscopic plot of real impedance

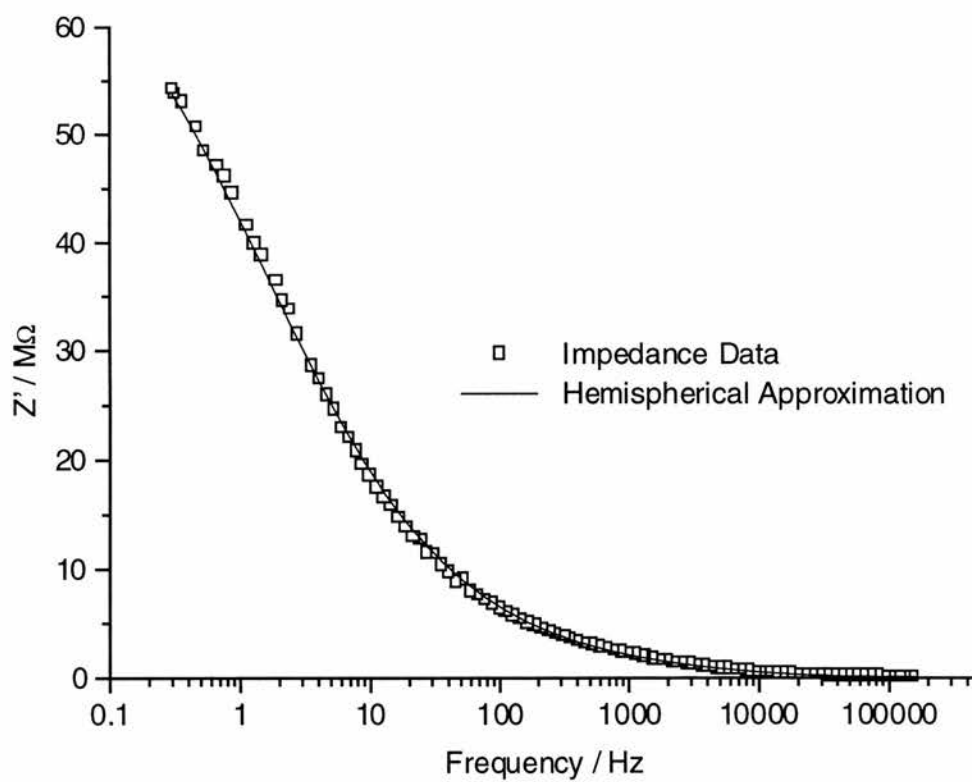
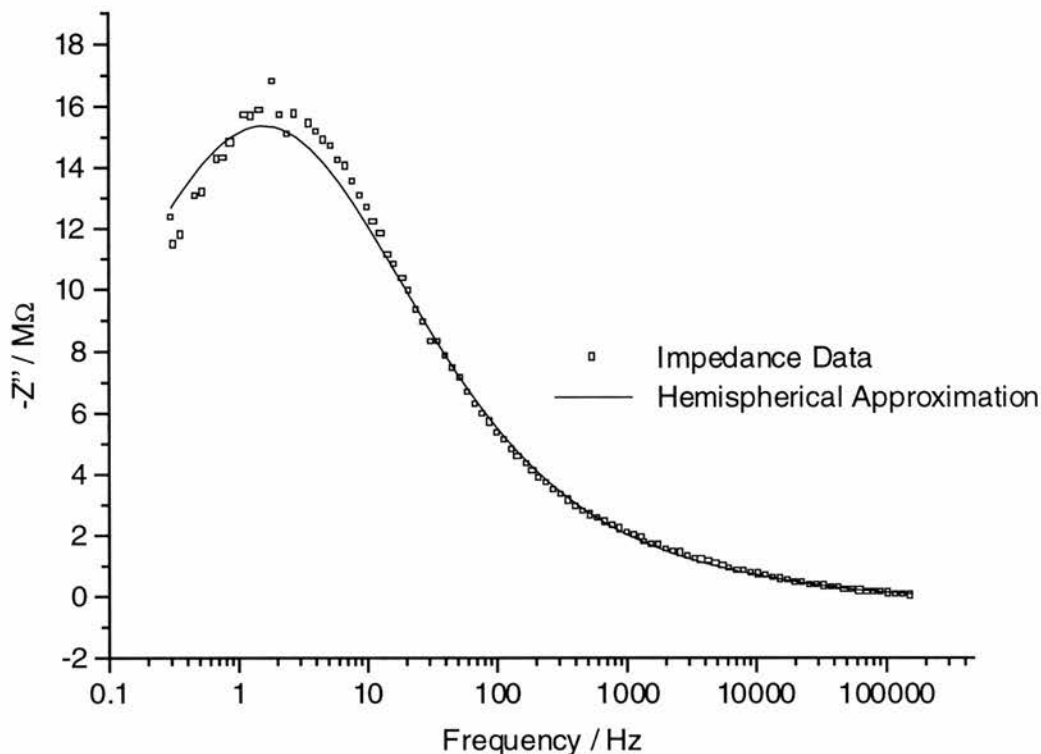


Figure 5.11

Pt ($a = 5 \mu\text{m}$) / tetraglyme, 4 mM ferrocene, 0.5 M LiClO_4 / Pt gauze

Spectroscopic plot of imaginary impedance



Figures 5.12 and 5.13 show the effect of potential on the impedance data, obtained at $(22 \pm 1^\circ\text{C})$ for 6.5 mM ferrocene with a platinum microelectrode and a platinum quasi-reference electrode. The potential of minimum impedance was found to be +0.095 V. With a lithium counter electrode the potential of minimum impedance was +3.48 V. In Figure 5.12 two features are apparent in the complex plane plot at +95 mV, i.e. an RC semi-circle at high frequencies and, at lower frequencies, a diffusion quarter circle, as discussed in Chapter 3. The high frequency semi-circles are shown at greater magnification in Figure 5.13. Figures 5.12 and 5.13 illustrate how, as would be expected, the impedance increases when the potential is varied from the potential of minimum impedance.

Figure 5.12

Effect of potential on the impedance of the ferrocene/ferrocenium couple.

Pt ($a = 10 \mu\text{m}$) / tetraglyme, 6.5 mM ferrocene, 0.5 M LiClO_4 / Pt gauze

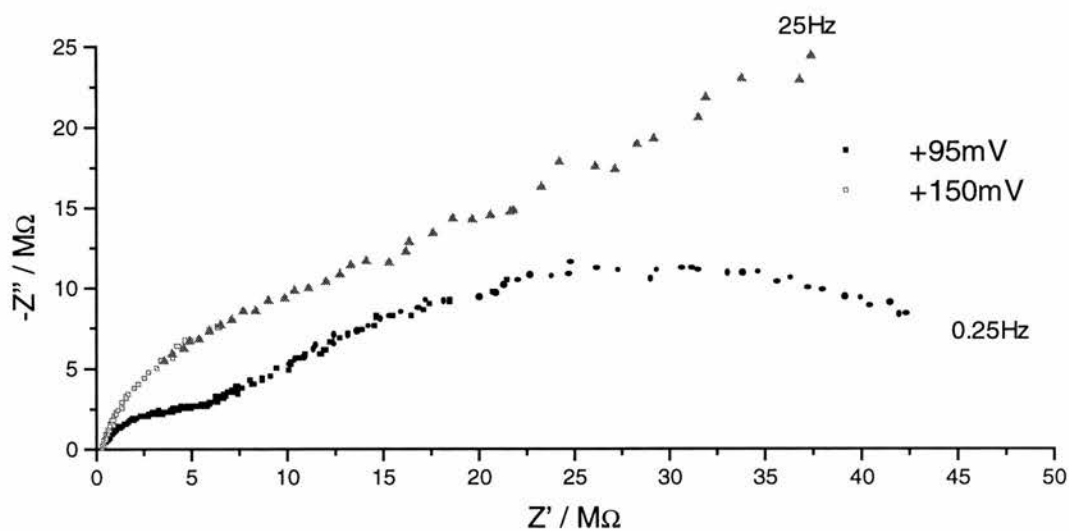
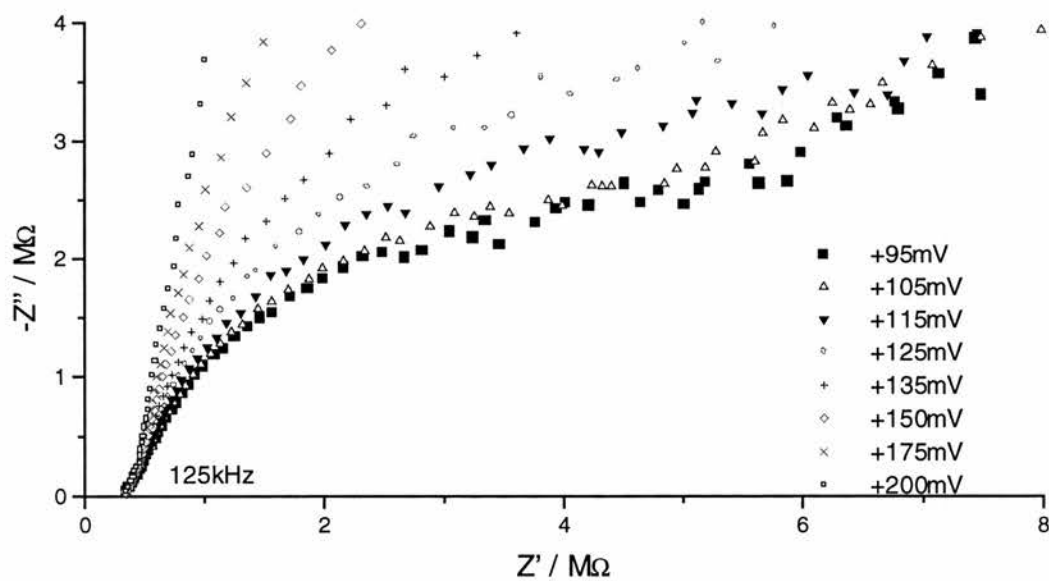


Figure 5.13

Effect of potential on the impedance of the ferrocene/ferrocenium couple at high frequencies.

Pt ($a = 10 \mu\text{m}$) / tetraglyme, 6.5 mM ferrocene, 0.5 M LiClO_4 / Pt gauze



Three series of experiments were carried out to determine the dependence of electrochemical parameters on:

- a. Ferrocene concentration.
- b. Temperature.
- c. Background electrolyte concentration.

CNLS analysis was carried out using the hemispherical approximation with a $< -2 >$ statistical parameter. Use of a $< +1 >$ parameter changed the values slightly but did not affect any of the observed trends significantly. Data were accepted only when the standard deviation between the CNLS fit and the data were less than 8%. Generally, standard deviations were lower than 5%.

5.1.2 *The Dummy Cell*

When the impedance data were analysed using the hemispherical approximation, it was observed that (see Figures 5.7 and 5.8 for example) the high frequency semi-circle was somewhat flattened relative to a true semi-circle. A dummy cell comprised of resistors and a capacitor as shown in Figure 5.14 was used to investigate this flattening. The values of the resistors and the capacitor in the dummy cell were chosen so that they produced a semi-circle of similar size to that observed in the experimental cells. The impedance plot arising from the dummy cell is shown in Figure 5.15.

Figure 5.14

Schematic of the circuit elements in the dummy cell

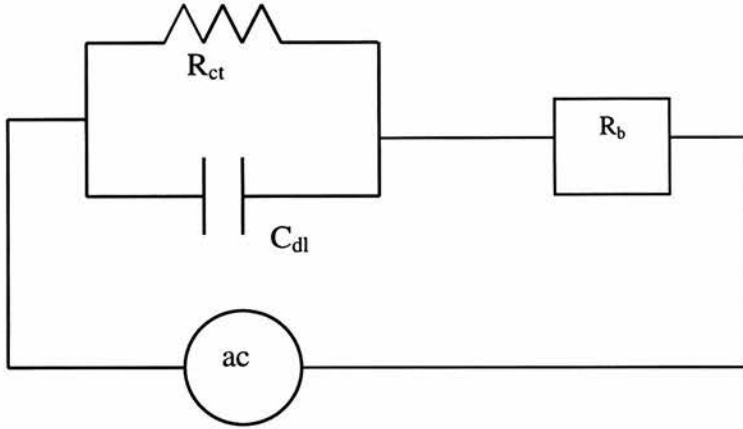
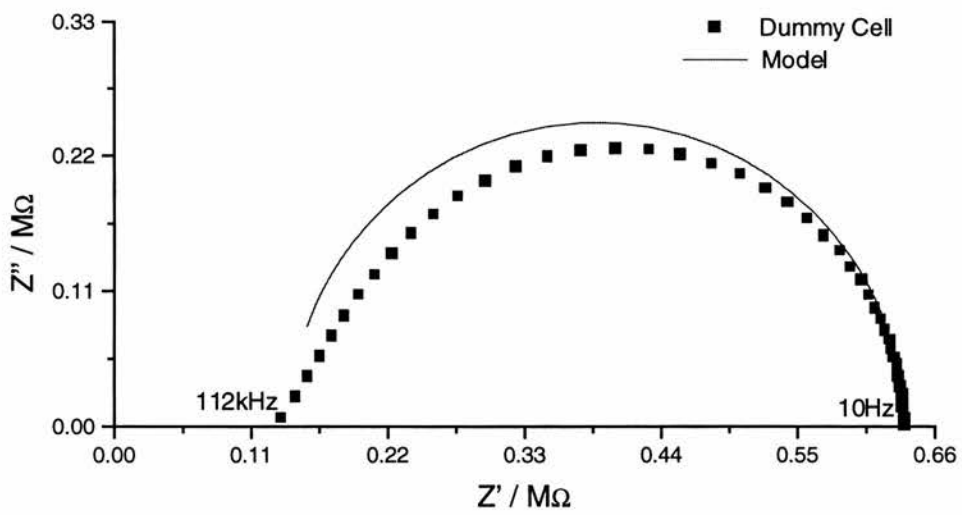


Figure 5.15

Impedance plot of the dummy cell



Clearly the dummy cell exhibits similar flattening of the RC semi-circle observed in the real electrochemical cells. This makes it likely that the distortion of the semi-circle is an artefact of the measuring instruments and equipment and is completely unconnected with processes in the experimental cells. This flattening seems to affect smaller semi-circles, (i.e. diameter $\leq 1 \text{ M}\Omega$), much more so than large ones, (i.e. diameter $> 1 \text{ M}\Omega$), e.g. see Figures 4.2 and 6.12.

In order to determine whether, despite the flattening, the CNLS method yields accurate values for the circuit elements, each individual element in the dummy cell was measured accurately using a Wayne Kerr ac bridge. Values from the bridge were compared with values obtained from CNLS fitting of the impedance spectrum of the whole cell measured by the FRA. The values obtained using both techniques are shown in Table 5.1.

Table 5.1

Comparison of values of circuit elements given by bridge and CNLS methods

Technique	$R_b / \text{k}\Omega$	$R_{ct} / \text{M}\Omega$	C_{dl} / pF
ac Bridge	150.1	0.4837	15.4
FRA/CNLS	141	0.491	15.1

Thus despite the flattening of the semi-circle, the CNLS method returns very similar values for the circuit elements to those returned by ac bridge method. It is concluded that the flattening of the data does not seriously affect the reliability of the results.

Having established the reliability of the CNLS analysis, it was applied to data from the ferrocene cells.

5.1.3 *Effect of Ferrocene Concentration*

Electrochemical cells containing 0.5 M lithium perchlorate and ferrocene concentrations varying from 2 mM to 60 mM were prepared and impedance spectra measured at $22 \pm 1^\circ\text{C}$. Tables 5.2 and 5.3 and Figures 5.16 to 5.21 below illustrate the relationship that was found between ferrocene concentration and electrochemical parameters determined by CNLS analysis using the hemispherical approximation for E mechanisms. All data were obtained with the CPE value fixed at one because generally CPE values were found to be 0.95 to 1.05 and leaving CPE as a free parameter made little difference to the results obtained for the other parameters.

Figure 5.16 shows that the calculated microelectrode radii are slightly larger than the geometric value, owing probably to unevenness on the microdisc surface increasing the effective surface area, as discussed in the previous chapter. The calculated radii were essentially independent of ferrocene concentration. Figure 5.17 shows the double-layer capacitances varying between 5 and $10 \mu\text{F cm}^{-2}$. This is in good agreement with differential capacitance measurements for lithium perchlorate in tetraglyme on mercury made by Bruce, Lisowska-Oleksiak and Vincent which were typically around $10 \mu\text{F cm}^{-2}$ ⁽³⁾.

Figure 5.18 is a plot of ferrocene diffusion coefficient versus ferrocene concentration. The calculated diffusion coefficients are $1.6 \pm 0.3 \times 10^{-6} \text{ cm}^2 \text{ s}^{-1}$ and are independent of ferrocene concentration. No literature data were available for direct comparison with this figure. It is, however, an order of magnitude higher than the $3.4 \times 10^{-7} \text{ cm}^2 \text{ s}^{-1}$ measured by Pyati and Murray for the $[\text{Co}(\text{bpy})_3]^{2+/3+}$ couple in tetraglyme ⁽⁴⁾. Murray et al. measured diffusion coefficients for the ferrocene/ferrocenium couple and the $[\text{Co}(\text{bpy})_3]^{2+/3+}$ couple in polyethylene glycol dimethyl ether (average molecular weight 400) and found that the $[\text{Co}(\text{bpy})_3]^{2+/3+}$ diffused an order of magnitude more slowly than the ferrocene/ferrocenium ⁽⁵⁾. Hence the data from these two studies is consistent with the diffusion coefficient measurements reported from this study.

In contrast to Figures 5.16 to 5.18, the data in Figure 5.19 are somewhat surprising in that there appears to be a dependence of the heterogeneous rate constant on the ferrocene concentration. Figures 5.20 and 5.21 show that if the calculated values of the rate constant are plotted against reciprocal of concentration a straight line, possibly passing through the origin, is obtained. In general, the heterogeneous rate constant is expected to be independent of the concentration of the electroactive species and so this is a curious observation. To ascertain whether this trend of k_s increasing as ferrocene concentration decreases is a quirk of the CNLS analysis or is genuine, the impedance data were re-examined. For example, see Figures 5.22 and 5.23.

Table 5.2
 CNLS analysis results for
 Pt (a = 5 μm) / tetraglyme, ferrocene, 0.5 M $\text{LiClO}_4 / \text{Li}_{(\text{s})}$

Ferrocene Concentration / mM	a_{calc} / μm	C_{dl} / $\mu\text{F cm}^{-2}$	D / $10^6 \text{ cm}^2 \text{ s}^{-1}$	k_{s} / cm s^{-1}
2	5.4	33.7*	1.36	9.06*
4	5.2	12.2	1.86	0.262
4	5.5	9.8	1.67	0.289
6	5.2	7.67	1.51	0.167
6	5.3	7.88	1.29	0.165
9	4.7	9.55	1.85	0.136
9	5.4	8.24	1.61	0.109
12	5.0	8.60	1.52	0.084
12	5.0	8.27	1.53	0.082
16	4.8	8.27	1.81	0.075
30	5.6	7.44	1.74	0.040
30	5.7	6.54	1.67	0.039
60	5.6	8.00	1.51	0.028
60	5.6	7.35	1.49	0.026

* The standard deviation between the CNLS fit and the data is unacceptable for solutions containing 2 mM ferrocene. It is 40% in the case of C_{dl} and greater than 2,500% in the case of k_{s} . Simulations of the impedance data, of the type discussed in Chapter 8, indicate that the value of k_{s} here is greater than 1 cm s^{-1} .

Table 5.3
 CNLS analysis results for
 Pt (a = 10 μm) / tetraglyme, ferrocene, 0.5 M LiClO₄ / Li_(s)

Ferrocene Concentration / mM	a_{calc} / μm	C_{dl} / $\mu\text{F cm}^{-2}$	D / $10^6 \text{ cm}^2 \text{ s}^{-1}$	k_s / cm s^{-1}
2	10.9	3.40*	1.52	4.72*
4	11.8	3.66	1.76	0.148
4	11.8	4.34	1.70	0.147
6	11.5	6.14	1.38	0.101
6	11.6	5.09	1.36	0.115
9	12.1	4.88	1.38	0.082
9	12.1	4.89	1.36	0.082
12	11.7	6.22	1.25	0.065
16	12.3	5.84	1.35	0.054
30	12.5	5.43	1.51	0.037

* The standard deviation between the CNLS fit and the data is unacceptable for solutions containing 2 mM ferrocene. It is 30% in the case of C_{dl} and 350% in the case of k_s . Like the previous results table, simulations indicate that the true value of k_s is greater than 1 cm s^{-1} .

Figure 5.16

Effect of ferrocene concentration on calculated disc radius.

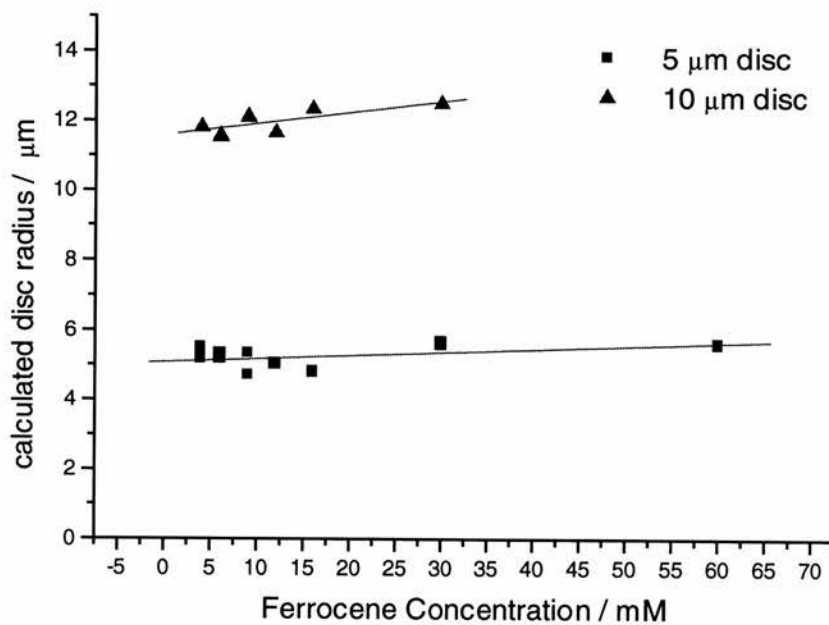


Figure 5.17

Effect of ferrocene concentration on calculated double layer capacitance.

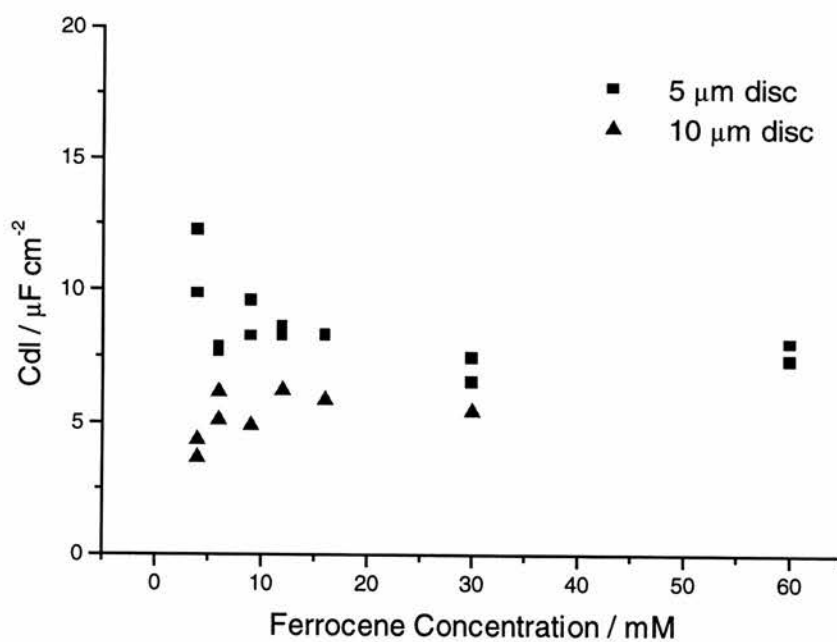


Figure 5.18

Effect of ferrocene concentration on calculated diffusion coefficient.

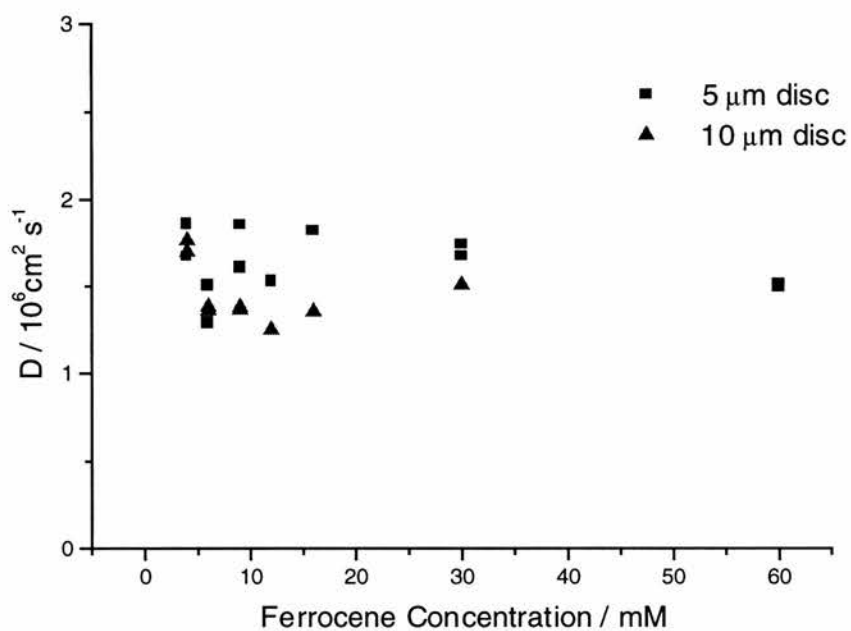


Figure 5.19

Effect of ferrocene concentration on calculated heterogeneous rate constant.

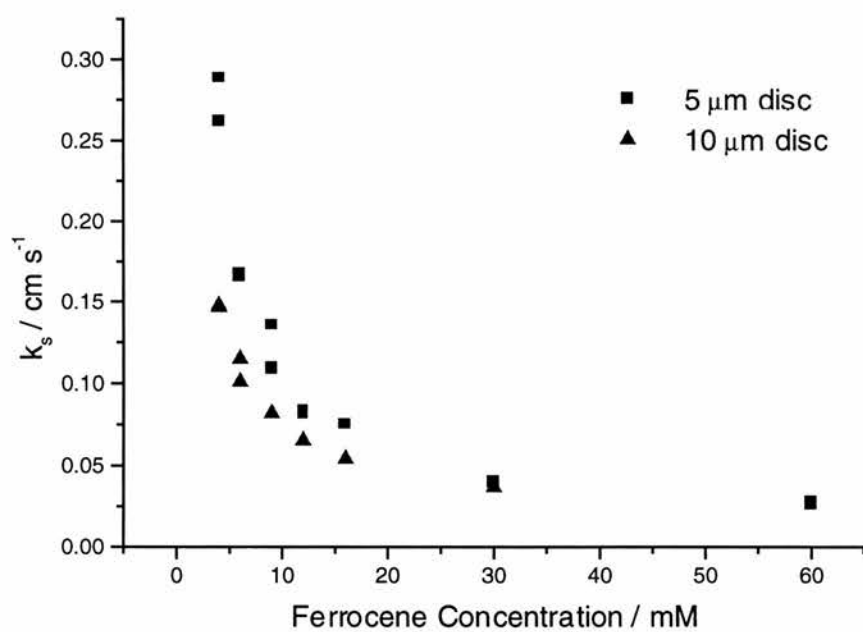


Figure 5.20

Dependence of heterogeneous rate constant on reciprocal ferrocene concentration.
5 μm microdisc.

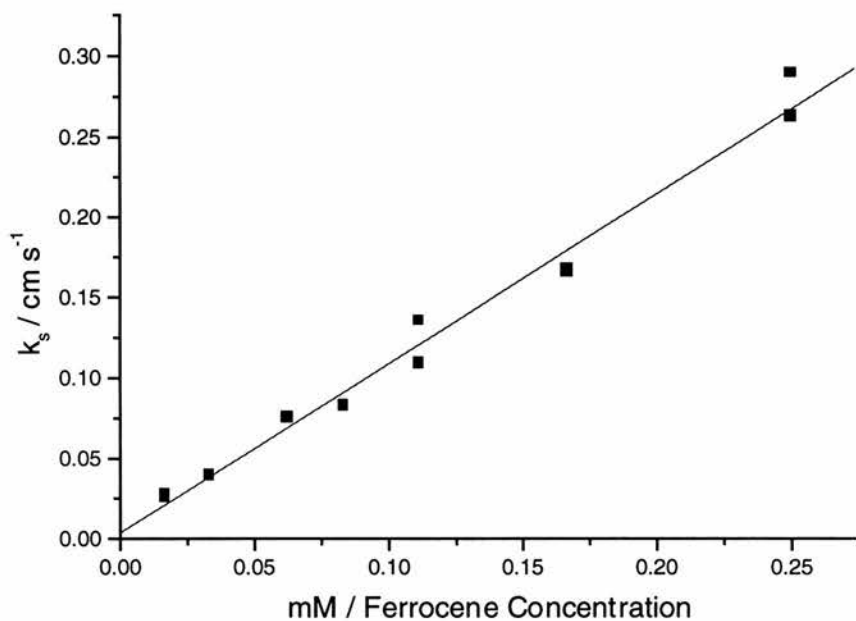


Figure 5.21

Dependence of heterogeneous rate constant on reciprocal ferrocene concentration.

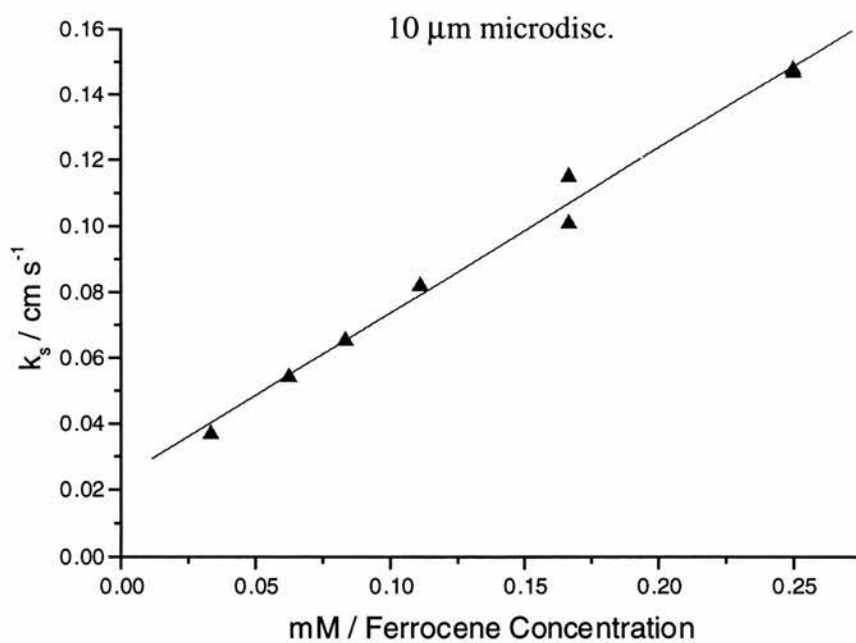


Figure 5.22

Impedance plots of ferrocene cells from 140 kHz - 0.3 Hz, $a = 5 \mu\text{m}$

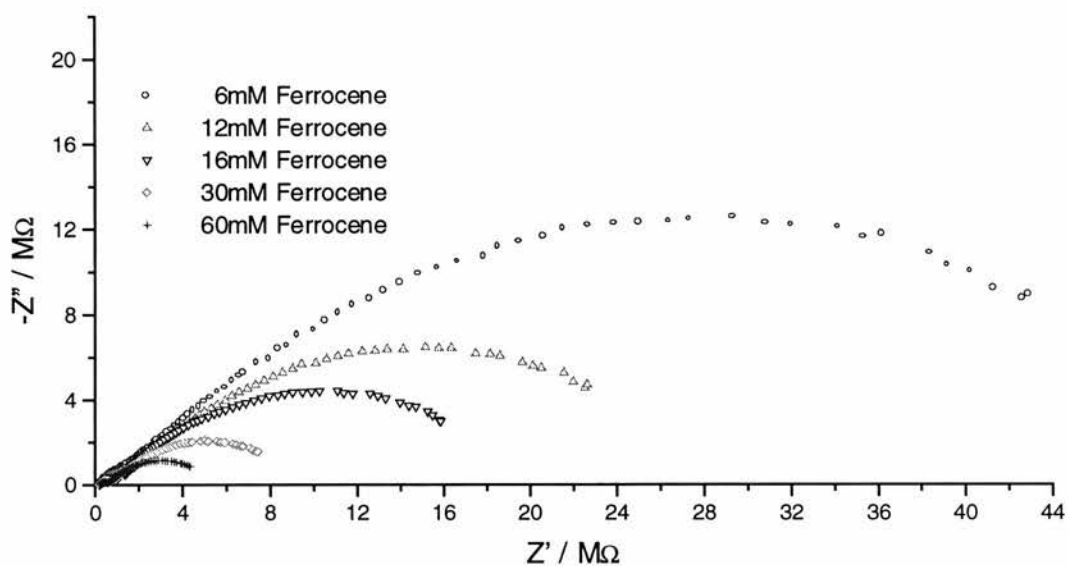
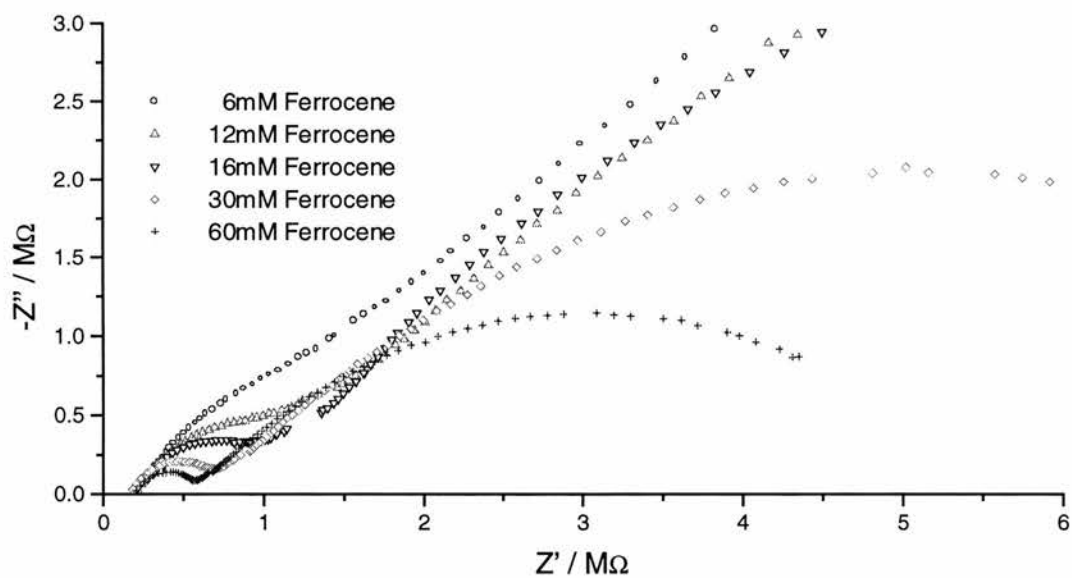


Figure 5.23

Impedance plots of ferrocene cells focussing on lower impedance / high frequency features



Manual analysis of the high frequency semi-circles (semi-circle diameter is equal to charge transfer resistance) is also possible. For example, in the case of 60mM ferrocene, the diameter of the high frequency semi-circle is $0.33\text{M}\Omega$ and thus (see [3.11]) k_s is calculated as follows:

$$\begin{aligned}
 k_s &= \frac{R \times T}{F^2 \times R_{CT} \times \left[\frac{Fc}{2} \right] \times \pi a^2} \\
 &= \frac{2.843 \times 10^{-10} \times 295}{0.33 \times 10^6 \times 30 \times 10^{-6} \times (5 \times 10^{-4})^2} \\
 &= 0.030 \text{ cm s}^{-1}
 \end{aligned}$$

This is in good agreement with the value of 0.0278 cm s^{-1} from CNLS analysis. Similar calculations at other ferrocene concentrations and with the $10 \mu\text{m}$ electrode yield the values shown in Tables 5.4 and 5.5. It is likely that the manual figures at high concentrations are more accurate than at lower concentrations because the semi-circle is more clearly defined at high concentrations. This may go some way to explaining the very good agreement at high concentrations which weakens somewhat at lower concentrations. Regardless of any small discrepancies, the conclusion from the data in the tables is that the trend produced by CNLS analysis of k_s values increasing with decreasing ferrocene concentration is verified by crude manual analysis of the high frequency semi-circle.

Table 5.4

Comparison of k_s values obtained by CNLS and manual analysis at a 5 μm microdisc.

Ferrocene Concentration / mM	k_s from CNLS analysis / cm s^{-1}	k_s from manual analysis / cm s^{-1}
4	0.26	Semi-circle difficult to isolate
6	0.17	0.08
9	0.14	0.06
12	0.083	0.05
16	0.075	0.05
30	0.039	0.04
60	0.028	0.03

Table 5.5

Comparison of k_s values obtained by CNLS and manual analysis at a 10 μm microdisc.

Ferrocene Concentration / mM	k_s from CNLS analysis / cm s^{-1}	k_s from manual analysis / cm s^{-1}
4	0.15	Semi-circle difficult to isolate
6	0.10	0.06
9	0.082	0.06
12	0.065	0.05
16	0.054	0.05
30	0.037	0.04

Although it was useful to calculate k_s values manually, confirming the trends from CNLS analysis, it is those values obtained from CNLS analysis that will be used further in this thesis. These values will be more reliable because they are calculated over a much wider frequency range.

Another means of illustrating that the values of the heterogeneous rate constant in the above tables are truly different for different ferrocene concentrations is through simulations. Simulations were carried out by fixing the microdisc radius at its geometric value and fixing D and C_{dl} at the appropriate values obtained by CNLS fitting. The value of k_s was then varied to see the effect on the predicted impedance plot. In Figure 5.24, for example, simulations at two different values of k_s are shown for comparison with impedance data from the 6 mM ferrocene solution. Clearly the data are much better suited to a rate constant of 0.167 cm s^{-1} than they are to a rate constant of 0.026 cm s^{-1} , indicating the validity of the results in Table 5.2. Similarly Figure 5.25 shows that the data for 60 mM ferrocene are much better interpreted by a rate constant of 0.026 cm s^{-1} than they are by 0.167 cm s^{-1} .

Figure 5.24

Impedance data for 6 mM ferrocene cell compared with simulated data for two different standard heterogeneous rate constants

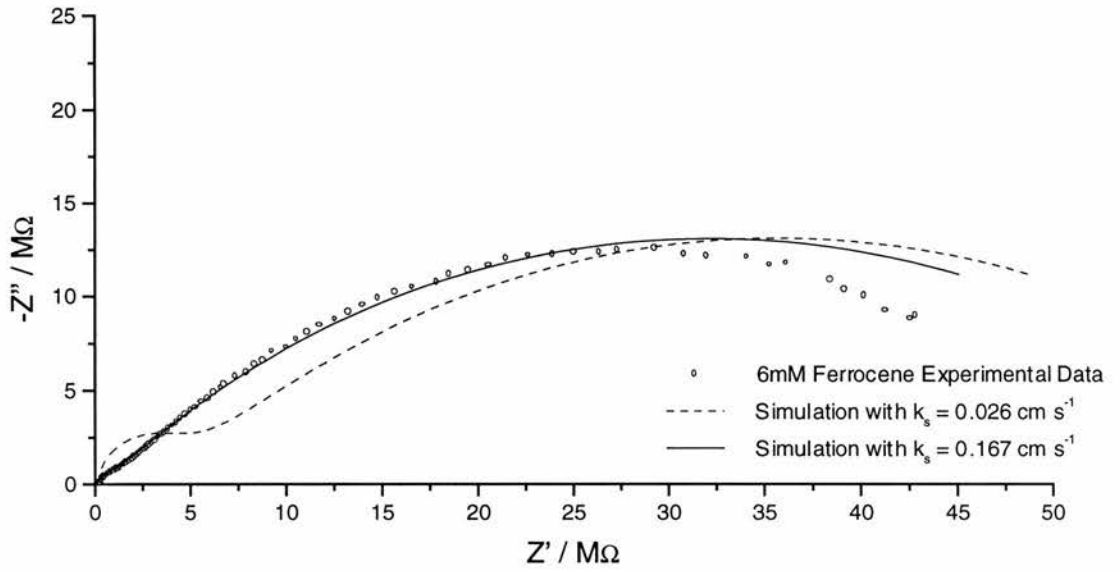
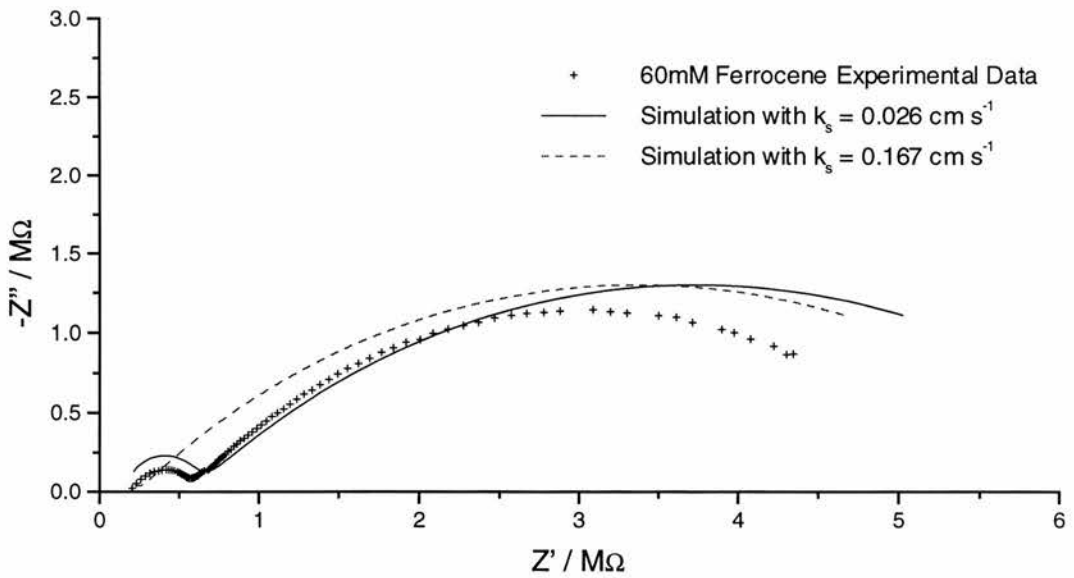


Figure 5.25

Impedance data for 60 mM ferrocene cell compared with simulated data for two different standard heterogeneous rate constants

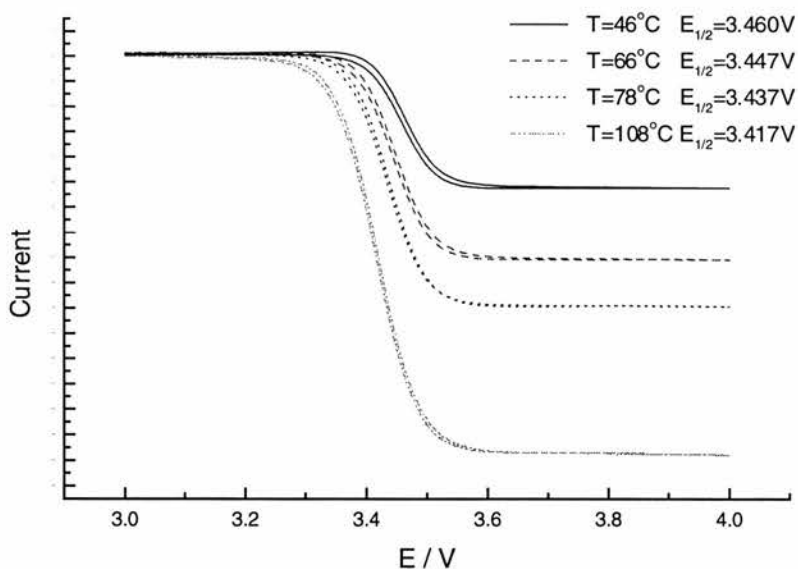


Since manual calculations and simulations have confirmed the decrease in the observed value of k_s as the ferrocene concentration is increased, an explanation for the phenomenon is required. One possibility is that adding increasing concentrations of ferrocene to tetraglyme results in ion-association of the ferrocene, lowering the active concentration of ferrocene in solution. Given that the dielectric constant of tetraglyme is, at 9.16⁽⁶⁾, rather low it is entirely feasible that ion-association may occur. This possibility will be explored further in the following sections.

5.1.4 Effect of Temperature.

Ferrocene cells were studied by impedance spectroscopy and cyclic voltammetry. Impedance measurements were recorded at various temperatures between 20°C and 90°C and voltammetry measurements between 20°C and 110°C. Typical voltammograms at elevated temperatures are shown in Figure 5.26. Note how $E_{1/2}$ shifts to less positive values as the temperature is increased. (As an aside, plotting $E_{1/2}$ vs temperature gives a reaction entropy of $\Delta S = -67 \text{ J mol}^{-1} \text{ K}^{-1}$ for all the solutions. In order to get standard entropies, however, the reference electrode would have to have been held at 25°C while a half-cell corresponding to the working electrode was measured at different temperatures.)

Figure 5.26
Cyclic voltammograms of 16 mM ferrocene solution
at elevated temperatures.



The results of applying the hemispherical model to impedance experiments at different temperatures are shown in Tables 5.6 to 5.8 and Figures 5.27 to 5.30 below.

Table 5.6

Pt ($a = 5 \mu\text{m}$) / tetraglyme, 9 mM ferrocene, 0.5 M $\text{LiClO}_4 / \text{Li}_{(s)}$

Temp. / K	a_{calc} / μm	Cdl / $\mu\text{F cm}^{-2}$	D / 10^6 $\text{cm}^2 \text{s}^{-1}$	ln (D)	k_s / cm s^{-1}	ln (k_s)
295.2	5.74	6.64	1.21	0.195	0.0854	-2.46
295.1	5.84	6.28	1.15	0.142	0.0918	-2.39
295.0	6.06	5.63	0.854	--	0.0857	-2.46
301.7	5.21	9.04	1.74	0.553	0.148	-1.91
302.6	5.53	8.68	1.52	0.422	0.130	-2.04
302.8	5.61	8.21	1.46	0.377	0.122	-2.10
308.8	5.72	8.07	1.82	0.601	0.137	-1.99
309.7	5.69	8.41	1.87	0.626	0.132	-2.03
309.3	5.61	8.42	1.88	0.633	0.124	-2.08
327.0	5.91	9.11	2.66	0.979	0.248	-1.39
324.0	5.90	9.14	2.64	0.971	0.237	-1.44
338.7	5.71	10.6	3.48	1.25	0.343	-1.07
336.2	5.75	10.1	3.25	1.18	0.309	-1.17
332.7	5.81	9.81	3.02	1.11	0.287	-1.25
328.0	5.57	9.99	3.03	1.11	0.210	-1.56
329.0	5.98	10.5	2.85	1.05	0.346	-1.06

Table 5.7

Pt ($a = 5 \mu\text{m}$) / tetraglyme, 16 mM ferrocene, 0.5 M $\text{LiClO}_4 / \text{Li}_{(s)}$

Temp. / K	a_{calc} / μm	Cdl / $\mu\text{F cm}^{-2}$	D / 10^6 $\text{cm}^2 \text{s}^{-1}$	ln (D)	k_s / cm s^{-1}	ln (k_s)
295.6	5.74	6.89	1.26	0.233	0.0517	-2.96
295.9	5.89	6.67	1.26	0.235	0.0544	-2.91
295.9	5.71	6.92	1.28	0.250	0.0519	-2.96
304.2	5.87	6.75	1.43	0.358	0.0604	-2.81
304.1	5.64	7.51	1.64	0.495	0.0699	-2.66
311.5	5.45	8.41	1.90	0.639	0.0861	-2.45
310.7	5.57	8.13	1.76	0.568	0.0922	-2.38
309.8	5.53	8.03	1.80	0.588	0.0856	-2.46
309.5	5.49	8.13	1.86	0.621	0.0781	-2.55
319.4	5.23	11.1	2.23	0.800	0.129	-2.05
318.1	5.21	11.4	2.22	0.798	0.136	-2.00
331.6	4.86	13.2	2.78	1.024	0.192	-1.65
329.1	5.09	11.9	2.52	0.924	0.156	-1.86
337.0	5.75	12.0	3.55	1.27	0.206	-1.58
336.0	5.81	11.5	3.42	1.23	0.197	-1.63
357.5	5.49	14.7	5.45	1.69	0.321	-1.14
353.0	5.71	13.2	4.81	1.57	0.265	-1.33
342.0	5.70	12.3	3.96	1.38	0.226	-1.49
338.0	5.80	11.5	3.68	1.30	0.190	-1.66
320.0	5.88	10.1	2.31	0.836	0.157	-1.85

Table 5.8

Pt ($a = 5 \mu\text{m}$) / tetraglyme, 60 mM ferrocene, 0.5 M $\text{LiClO}_4 / \text{Li}_{(s)}$

Temp. / K	a_{calc} / μm	Cdl / $\mu\text{F cm}^{-2}$	D / 10^6 $\text{cm}^2 \text{s}^{-1}$	ln (D)	k_s / cm s^{-1}	ln (k_s)
295.75	5.76	7.86	1.24	0.219	0.0193	-3.95
295.7	5.78	7.82	1.23	0.210	0.0189	-3.97
295.6	5.87	7.15	1.18	0.169	0.0183	-4.00
307.9	5.91	8.70	1.68	0.520	0.0289	-3.54
307.3	5.97	8.10	1.63	0.487	0.0284	-3.56
329.6	5.99	12.8	2.93	1.07	0.0561	-2.88
327.8	5.98	12.5	2.73	1.00	0.0508	-2.98
337.0	5.78	14.6	3.55	1.27	0.0656	-2.72
338.0	5.79	14.5	3.58	1.28	0.0670	-2.70
336.0	5.86	14.7	3.36	1.21	0.0668	-2.71
349.0	5.84	16.5	4.36	1.47	0.0824	-2.50
359.0	5.12	15.1	6.79	1.92	0.2093	--
359.0	5.15	14.4	6.48	1.87	0.1874	--
354.0	5.78	17.8	4.75	1.56	0.0873	-2.44
345.0	5.73	15.1	4.28	1.45	0.0657	-2.72
345.0	5.53	18.1	4.54	1.51	0.0768	-2.57
320.8	5.82	11.6	2.40	0.874	0.0472	-3.05
321.3	5.44	13.1	2.78	1.02	0.0535	-2.93

Figure 5.27

Effect of temperature on calculated disc radius for disc of 5 μm geometrical radius.

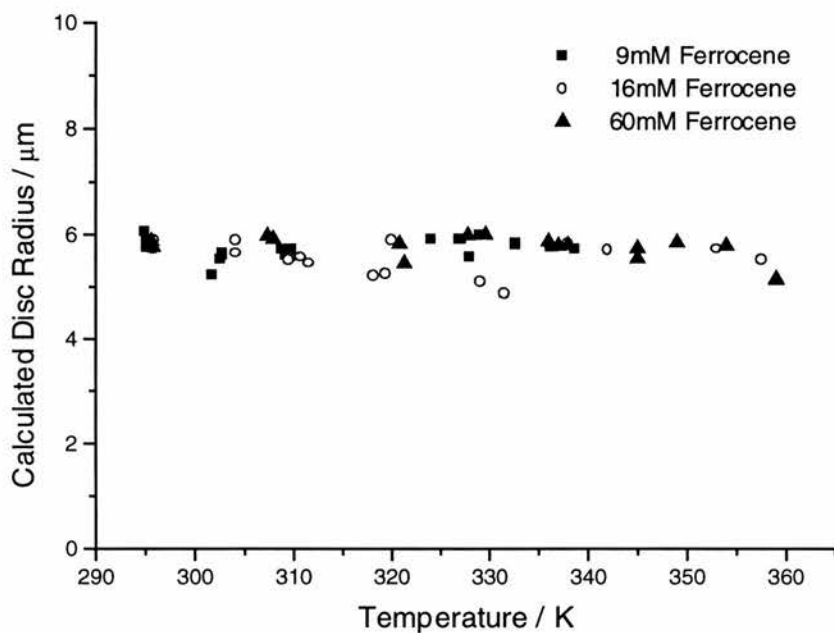


Figure 5.28

Effect of temperature on double-layer capacitance

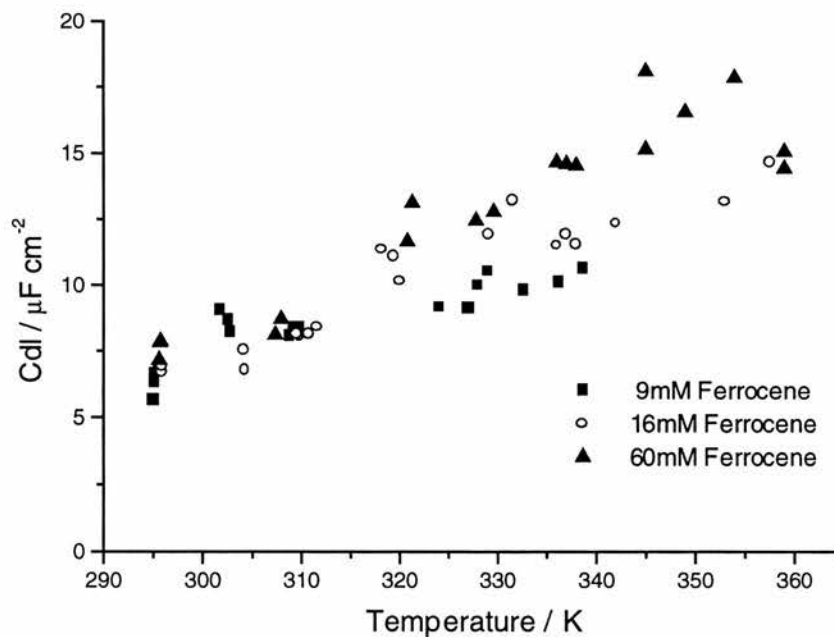


Figure 5.29

Arrhenius plot of diffusion coefficient against temperature

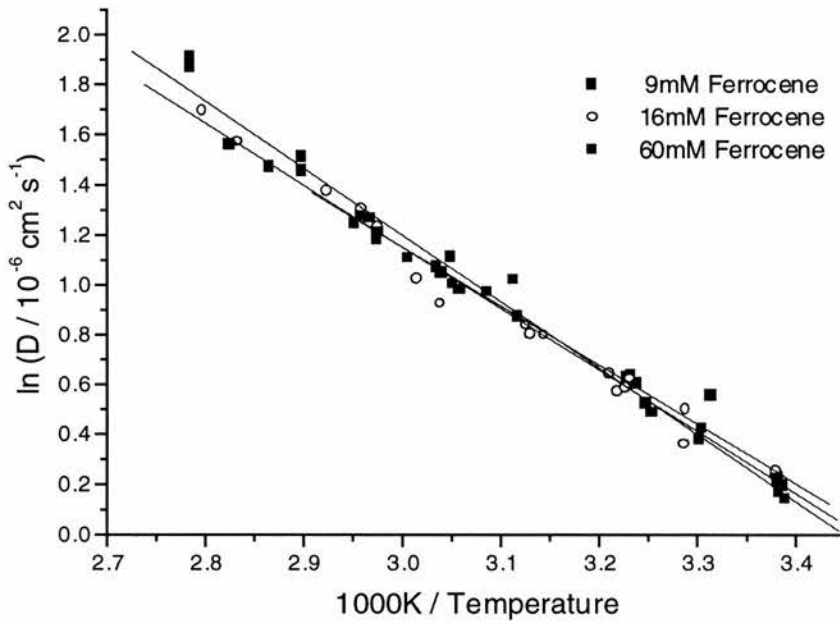


Figure 5.30

Arrhenius plot of k_s against temperature

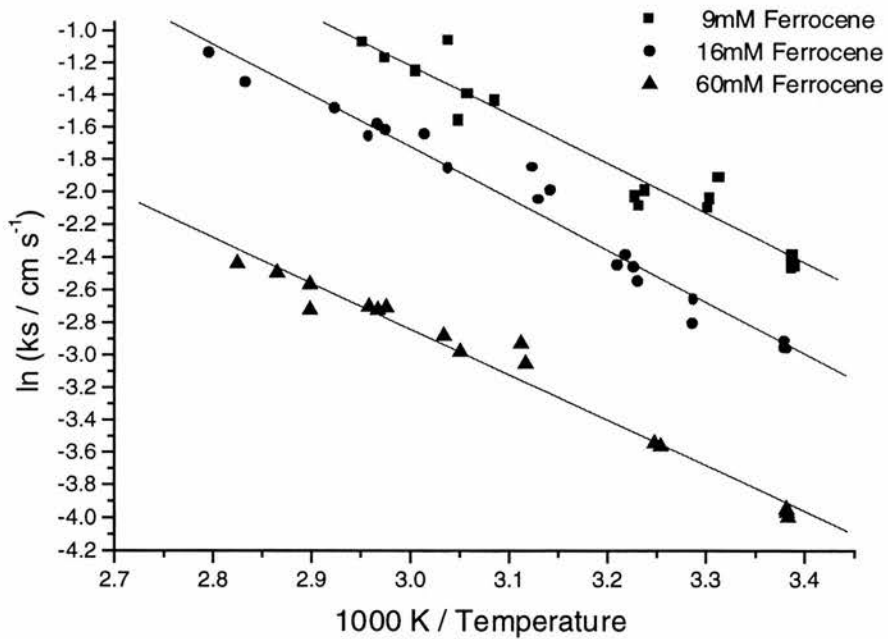


Figure 5.27 shows the calculated values of the microelectrode radius to be independent of ferrocene concentration and independent of temperature. Figure 5.28 shows that, as expected, the double-layer capacitance is independent of ferrocene concentration but unexpectedly appears to increase somewhat with increasing temperature. Figure 5.29 shows that ferrocene's diffusion coefficient is independent of ferrocene concentration and yields an Arrhenius type plot with reciprocal temperature. In Figure 5.30, the Arrhenius type behaviour of k_s is shown but, unlike D , the value of k_s is dependent on ferrocene concentration. In Table 5.9 the activation energies for diffusion and electron transfer, obtained from the Arrhenius plots are shown.

Table 5.9

Activation energies for electron transfer and diffusion for ferrocene in tetraglyme

Ferrocene Concentration / mM	E_a (Diffusion) / kJ mol ⁻¹	E_a (Charge Transfer) / kJ mol ⁻¹
9	19.7 ± 0.9	25.2 ± 1.8
16	20.5 ± 0.6	26.4 ± 1.1
60	22.2 ± 0.7	23.3 ± 1.1

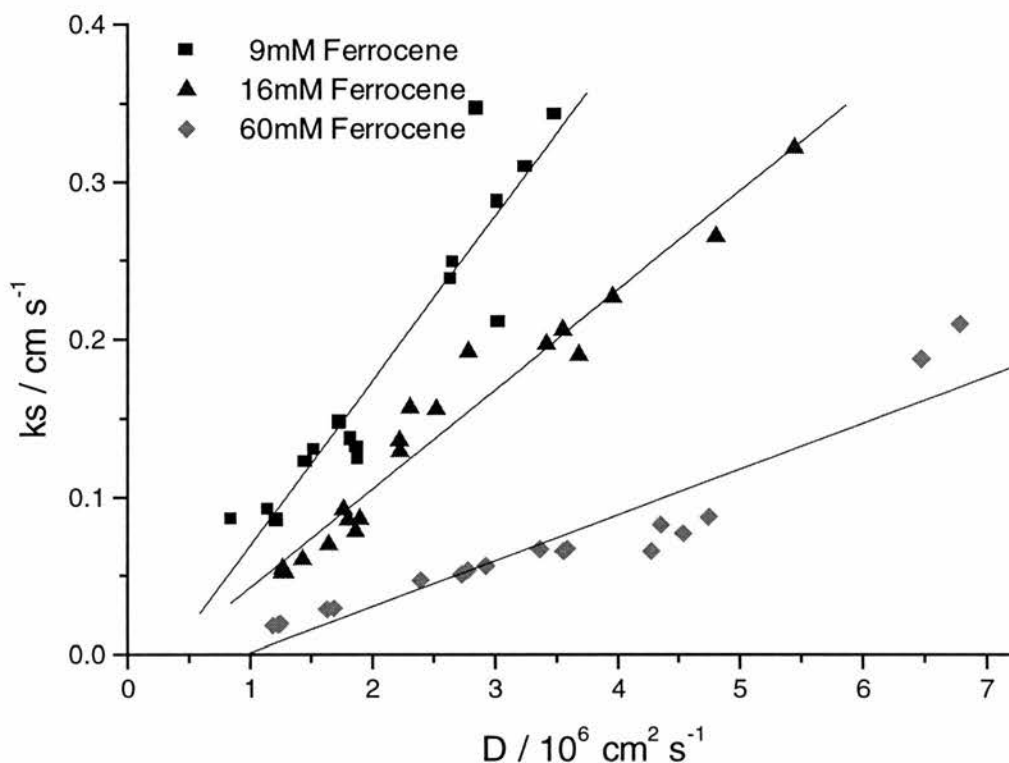
With regard to electron transfer it is clear from Table 5.9 and Figure 5.30 that, although the rate decreases as more ferrocene is added, the activation energy stays the same. In other words the height of the energy barrier to electron transfer remains a constant height but it is crossed relatively less frequently when more ferrocene is present. Such an observation is consistent with lower availability of the electroactive species owing, perhaps, to some sort of association mechanism.

Also of note in Table 5.9 is the similarity of values for activation energy of diffusion and electron transfer, particularly for 60 mM ferrocene. This may indicate that the same solvent dynamic factors which determine diffusion rates and viscosity also (when the effect of association is excluded) primarily determine electron transfer rates.

Figure 5.31 shows a straight-line correlation between k_s and D at different temperatures. A straight line relationship between these parameters was also found by Pyati and Murray, who studied the couple $[\text{Co}(\text{bpy})_3]^{2+/3+}$ (cobalt tris(bipyridine)) in a range of solvents including glymes with LiClO_4 supporting electrolyte ⁽⁴⁾. For each ten-fold change in k_s , a ten-fold change in D was found from which Pyati and Murray concluded that the reaction kinetics respond in a sensitive way to those characteristics of the solvent which determine diffusion. Hence the dynamics of solvent dipolar relaxations influencing the barrier crossing are directly influenced by solvent diffusive characteristics. The straight-line correlation therefore indicates outer sphere solvent dynamic control of the electrode kinetics. Such a conclusion is not inconsistent with the results of the experiments reported here.

Figure 5.31

k_s against D for ferrocene in tetraglyme



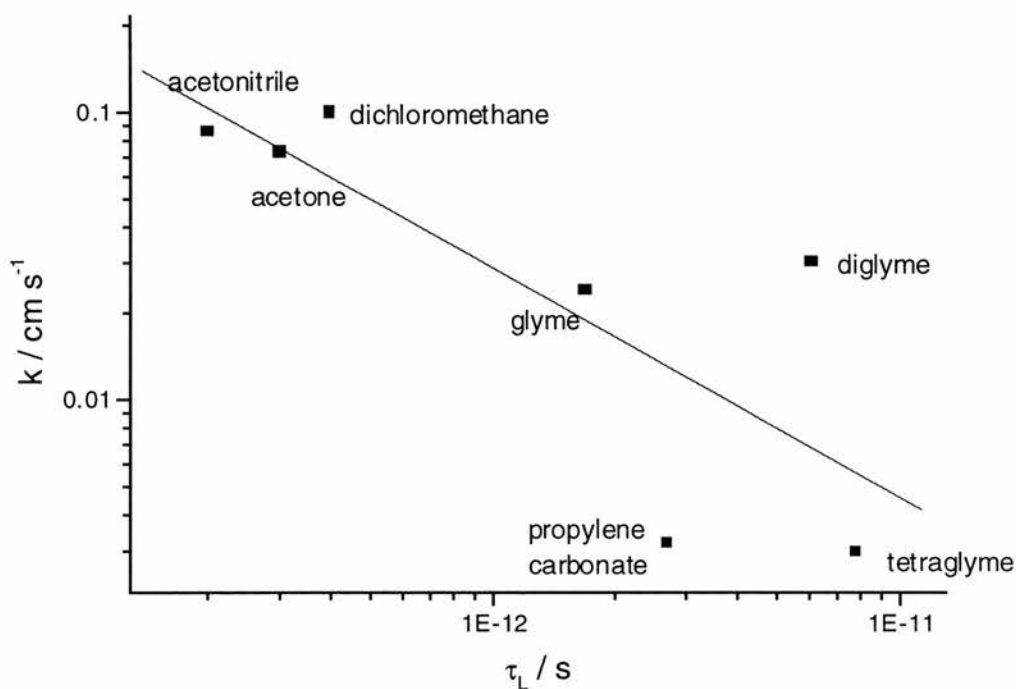
On the basis of viscosity measurements, however, Pyati and Murray also concluded that ion-pairing is probably not a major factor in rate constant changes but indicated that its existence was an unresolved uncertainty in their electrolyte concentration studies, particularly as regards the data presented here in Figure 5.32. In Figure 5.32 rate constants are plotted against τ_L , the longitudinal relaxation time of the solvent. τ_L is a measure of how quickly solvent dipoles relax to their equilibrium state around a solvated species following a perturbation, such as the loss or gain of an electron. The relationship between k_s and τ_L is a measure of the importance of solvent reorientation in electron transfer. A strong relationship indicates a small

internal reorganisation energy of the molecule relative to outer sphere organisation and hence outer sphere control of the electron transfer rate.

Figure 5.32

Heterogeneous rate constant for $[\text{Co}(\text{bpy})_3]^{2+/3+}$ versus longitudinal relaxation time.

Graph prepared from data sourced from reference 4.



Looking at Figure 5.32, however, it seems unlikely that ion-association satisfactorily explains deviations from the straight line. This is because the largest deviations from the fitted straight line are in the opposite direction from that which would be expected if ion association was influencing the observed rate. i.e. diglyme has a low dielectric constant, 5.79, for which significant ion-association would be expected, leading to a rate constant below the fitted line. The measured rate-constant is in fact above the fitted line. Propylene carbonate has a high dielectric constant, 64.79, for which little ion-association would be expected,

leading to a rate constant above the average. The measured rate-constant is in fact below the fitted line.

It is strange that there seems to be no observable affect attributable to ion-association or pairing in Pyati and Murray's paper given that varying the concentration of ferrocene from 2 mM to 60 mM in tetraglyme results in a change in the measured rate constant of greater than an order of magnitude. If such changes in rate are attributable to ion-association, it is reasonable to expect that over the range of solvents employed by Pyati and Murray that an affect would have been apparent.

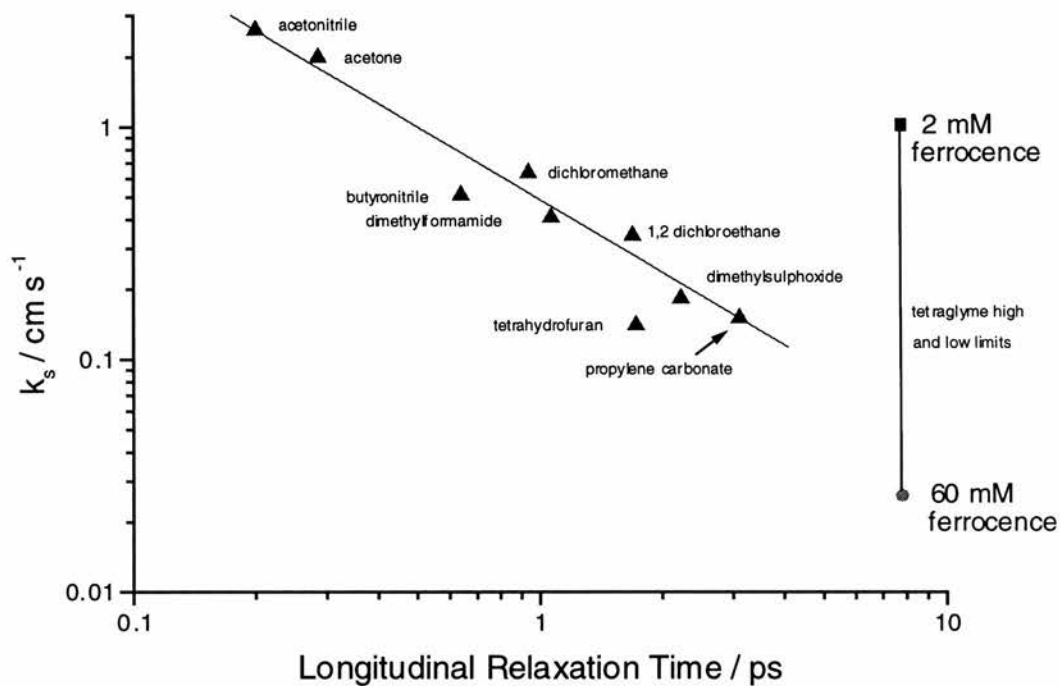
Baranski, Winkler and Fawcett used a.c. admittance and cyclic voltammetry at a platinum microelectrode to obtain rate data for ferrocene in a number of organic solvents with 0.1 M TBAP supporting electrolyte ⁽⁷⁾. These rate constants were plotted against the longitudinal relaxation time of the solvent to yield a fairly good straight-line correlation. These data are plotted in Figure 5.33 below and show neither ion-association effects nor odd behaviour for propylene carbonate. Added to the figure are the extremes of the k_s values for ferrocene in tetraglyme measured in this study. (The longitudinal relaxation time of tetraglyme is 7.8 ps ⁽⁸⁾)

In Baranski's study, ferrocene was employed at a concentration of 1 mM. The tetraglyme points in this study were obtained between 2 and 60 mM. It is clear therefore that for 1 mM ferrocene the rate constant for ferrocene in tetraglyme found by microelectrode impedance spectroscopy will be greatly in excess of that predicted on the basis of the longitudinal relaxation time from Baranski's plot.

Figure 5.33

Standard heterogeneous rate constant for ferrocene vs longitudinal relaxation time.

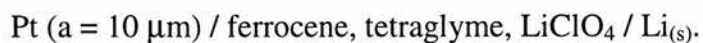
Data from reference 7.



The possibility of ferrocenium ions becoming associated is explored further in the next and following sections where cyclic voltammetry is used as the experimental method.

5.1.5 Effect of Background Electrolyte Concentration

An electrochemical cell was assembled with the following configuration:



The ferrocene concentration was 5 mM. Cyclic voltammetry was carried out on a range of solutions with different lithium perchlorate concentrations. Limiting currents and half-wave potentials were found to be dependent on this concentration. Typical cyclic voltammograms are shown in Figures 5.34 and 5.35. All cyclic voltammograms are shown in Figure 5.36.

Figure 5.34

Cyclic voltammogram of 5 mM ferrocene in tetraglyme with 0.077 M LiClO₄

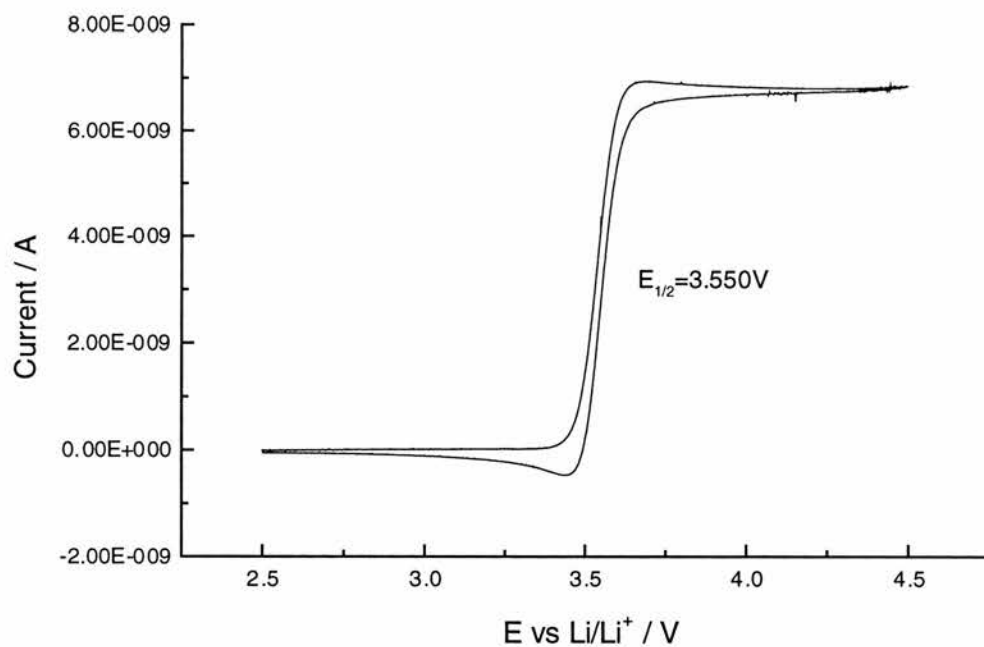


Figure 5.35

Cyclic voltammogram of 5 mM ferrocene in tetraglyme with 0.534 M LiClO₄

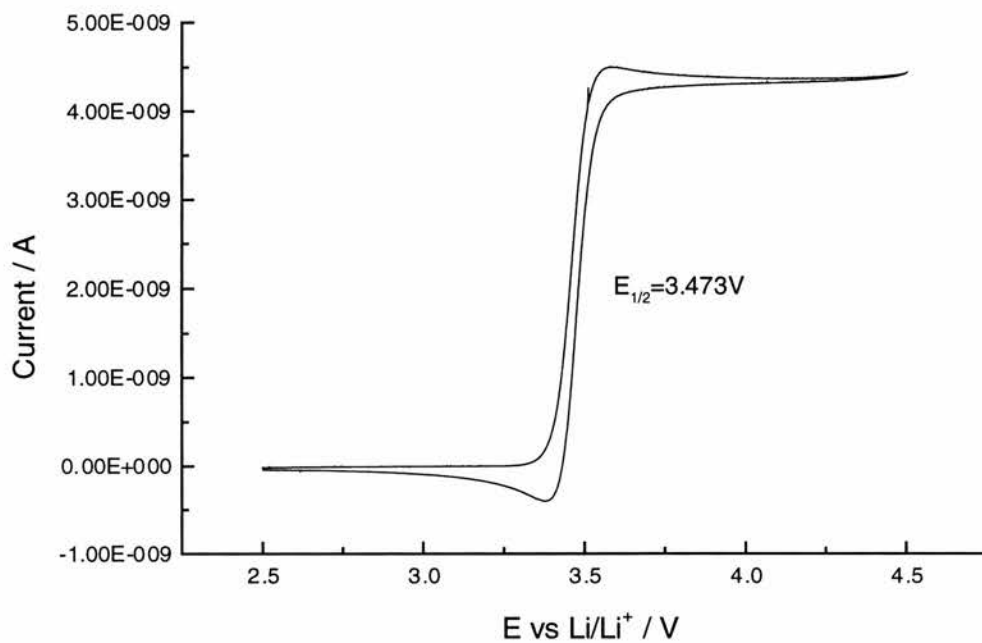
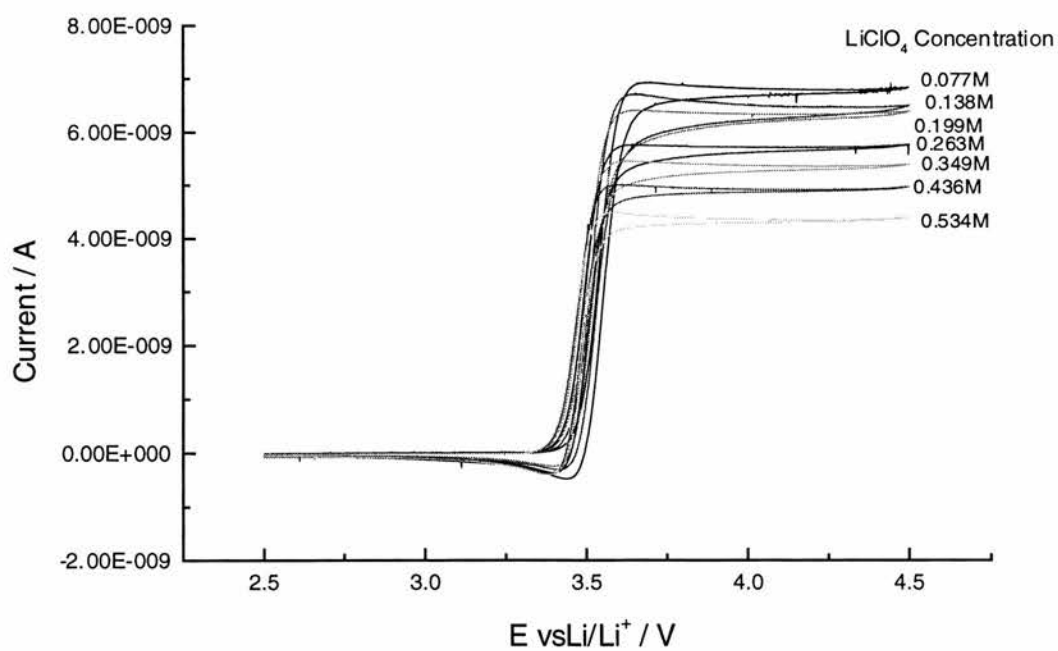


Figure 5.36

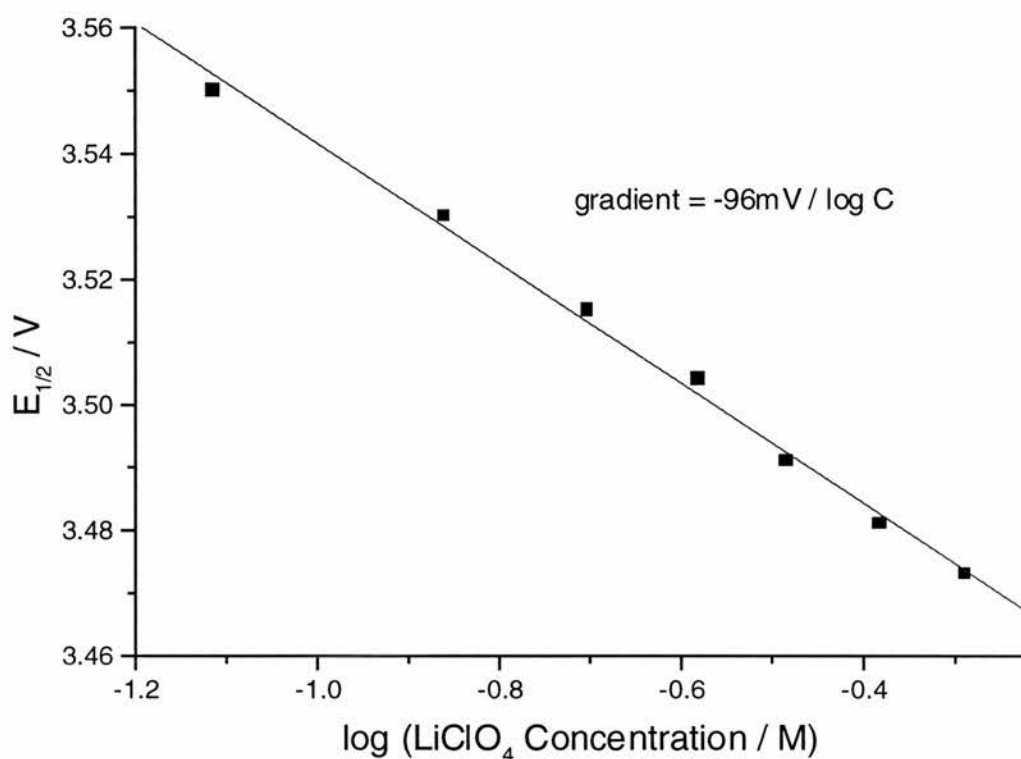
Cyclic voltammogram of 5 mM ferrocene in tetraglyme with different concentrations of LiClO₄ background electrolyte



Half-wave potentials are plotted against lithium perchlorate concentration in Figure 5.37.

Figure 5.37

Half wave potentials of ferrocene in tetraglyme versus concentration of LiClO_4 background electrolyte



There is a clear linear relationship between the logarithm of perchlorate concentration and the half-wave potential. The above graph does not take account of changes in potential at the lithium quasi-reference electrode caused by changes in the lithium ion activity in solution. At these relatively high concentrations of lithium ions there will be a certain divergence between activities and concentrations. Nevertheless, to obtain a rough estimate of the effects of changing lithium-ion concentration on the above graph, the concentrations may be inserted into the Nernst equation to yield a gradient of $-58 \text{ mV} / \log C$ caused by

concentration changes at the quasi-reference electrode. Taking this calculation into account yields a "corrected" gradient of about $-38 \text{ mV} / \log C$. This negative gradient could result from ion-pairing of ferrocenium with perchlorate - i.e. an EC mechanism. A further set of experiments was carried out in which the lithium quasi-reference electrode was replaced by a platinum electrode. It was hoped that by having both electrodes made of platinum any potential changes other than those caused by the proposed ion-pairing step might be minimized. Typical cyclic voltammograms are shown in Figures 5.38 and 5.39. All cyclic voltammograms are shown in Figure 5.40.

Figure 5.38

Cyclic voltammogram with sweep rate 20 mV s^{-1}

Pt ($a = 5 \mu\text{m}$) / tetraglyme, 5.5 mM TCNQ, 0.19 M LiClO_4 , 6.5 mM ferrocene / Pt gauze

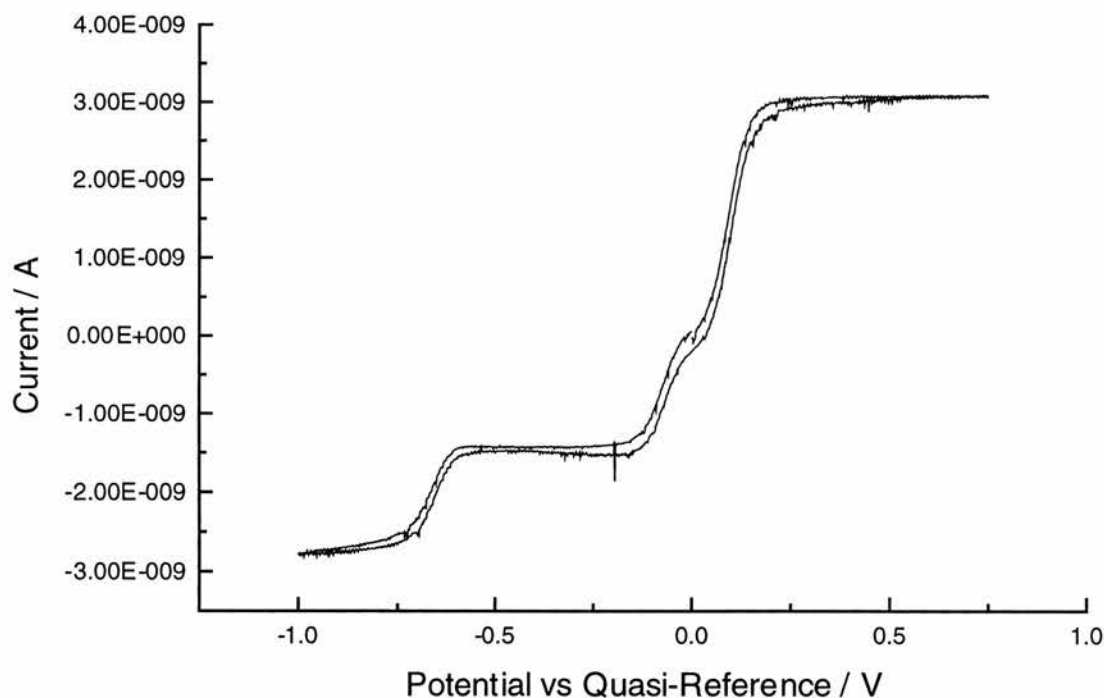


Figure 5.39

Cyclic voltammogram with sweep rate 20 mV s^{-1}

Pt ($a = 5 \mu\text{m}$) / tetraglyme, 5.5 mM TCNQ, 0.49 M LiClO_4 , 6.5 mM Ferrocene / Pt gauze

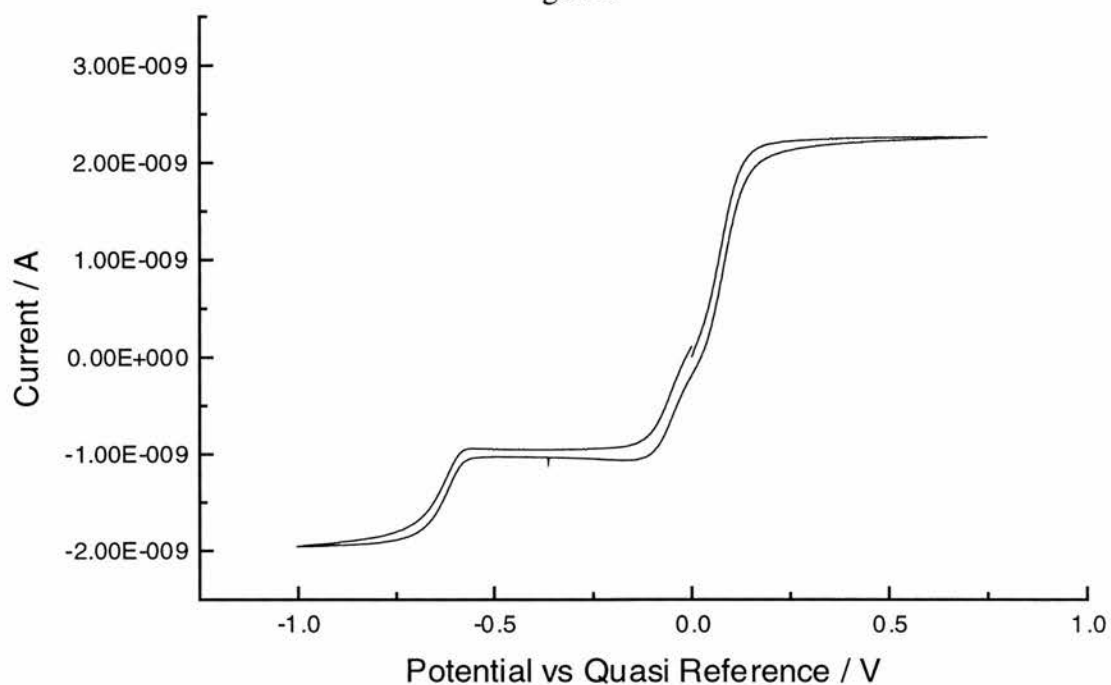
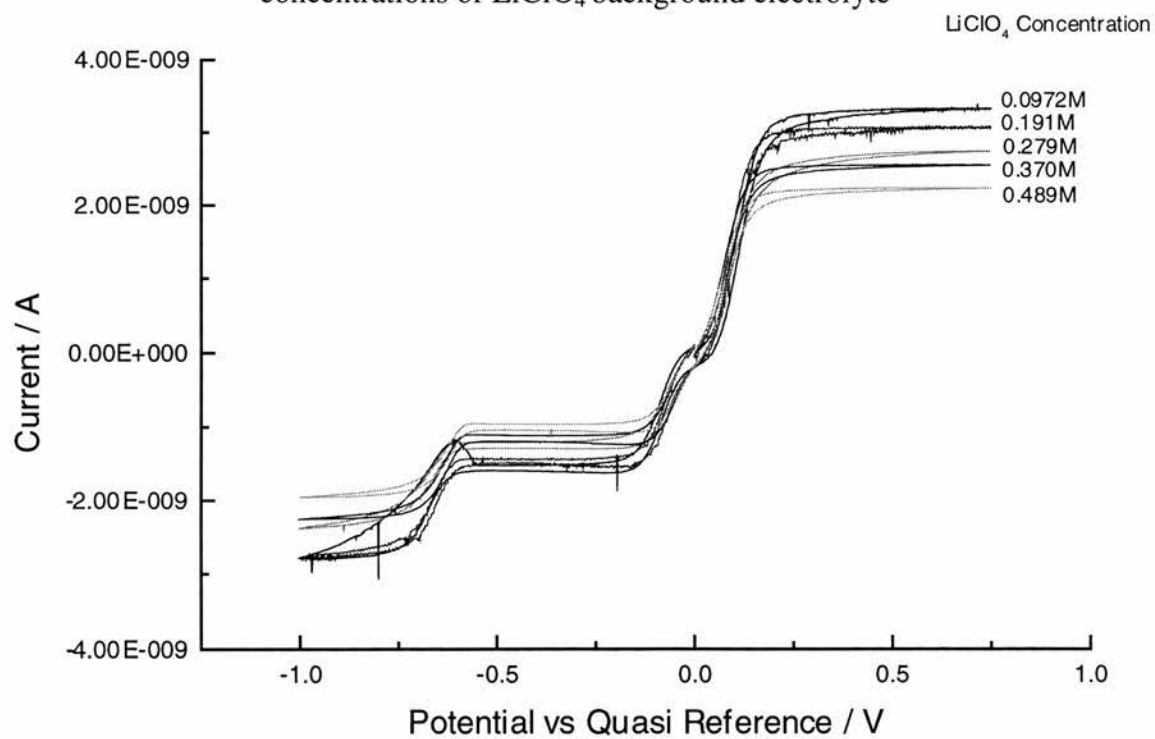


Figure 5.40

Cyclic voltammograms of ferrocene and TCNQ in tetraglyme with different concentrations of LiClO_4 background electrolyte



In these voltammograms, 3 waves are observed - from left to right these waves correspond to transitions between TCNQ^{2-} and TCNQ^- , between TCNQ^- and TCNQ , and between ferrocene and the ferrocenium cation. The TCNQ data will be discussed in Chapter 6.

Half-wave potentials for the ferrocene/ferrocenium transition at each lithium perchlorate concentration are shown in Table 5.10 and plotted in Figure 5.41.

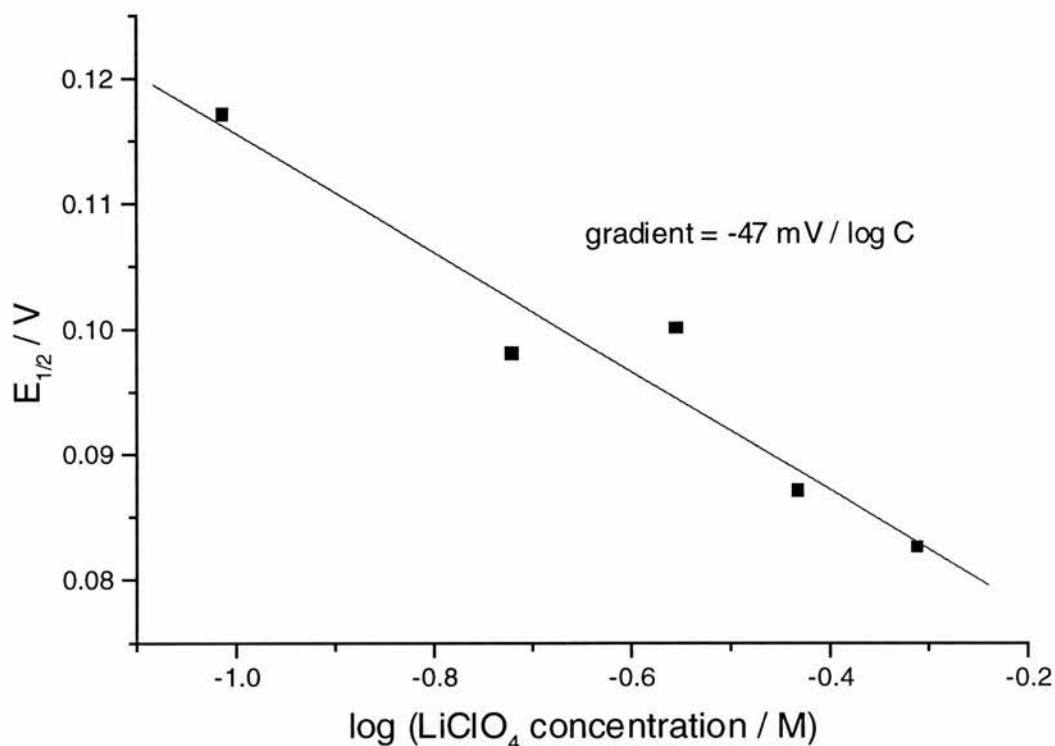
Table 5.10

Half wave potentials for ferrocene oxidation at different LiClO_4 concentrations.

LiClO_4 Concentration / M	$E_{1/2}$ / V
0.0972	0.117
0.191	0.098
0.279	0.1
0.370	0.087
0.489	0.0825

As the concentration of lithium perchlorate is increased, the ferrocene half wave potential shifts with a gradient of $-47 \text{ mV} / \log C$, similar to the corrected $-38 \text{ mV} / \log C$ observed against Li/Li^+ and confirming the direction of potential shift.

Figure 5.41
Half wave potentials of ferrocene in tetraglyme
versus concentration of LiClO_4 background electrolyte



Further confirmation comes from the work of Zhou and Dong ⁽⁹⁾ who, in voltammetry studies, also observed a potential shift for ferrocene oxidation in poly(ethylene glycol) (PEG, average molecular weight = 400) when the lithium perchlorate background electrolyte concentration was changed. From their data a gradient of $-116 \text{ mV} / \log C$ may be calculated. Zhou and Dong noted the possibility that the potential shift may be due to ion-pairing but investigated no further.

A shift to less positive potentials is consistent with pairing of ferrocenium with perchlorate. This is evident from the Lingane equation ⁽¹⁰⁾:

$$E = E^o - \frac{RT}{nF} \ln \beta - \frac{pRT}{F} \ln a_x \quad [5.2]$$

where β is the formation constant for $\text{Fc}^+(\text{X}^-)_p$, a_x is the activity of the counter-anion, p is the number of anions associating with each ferrocenium and E^o is the potential in the absence of ion-pairing. If it is assumed that ferrocene does not pair with the counter-anion and that ferrocenium does and that there exists nearly complete association between ferrocenium and the counter-anion this equation may be used quantitatively to estimate potential shifts. If, however, complete association is not assumed, then a more general equation must be used, i.e.

$$E - E^o = -\frac{RT}{F} \ln(1 + \beta a_x^p) \quad [5.3]$$

In seeking to apply this equation to the half-wave potential data from ferrocene oxidation, it becomes apparent that an estimate is required for one of either β or p and for a_x . The estimates used are that p is unity - i.e. ion pairs form rather than triples or higher associations, and that concentrations may be substituted for activities. By writing [5.3] twice for two different potentials, E_1 and E_2 , obtained at two concentrations, C_1 and C_2 , then subtracting one equation from the other, equation [5.4] is obtained.

$$E_1 - E_2 = \frac{RT}{F} \ln(1 + \beta C_2) - \frac{RT}{F} \ln(1 + \beta C_1) \quad [5.4]$$

Rearranging [5.4] yields:

$$\exp\left(\frac{F}{RT}(E_1 - E_2)\right) = \frac{1 + \beta C_2}{1 + \beta C_1} \quad [5.5]$$

Substituting the values from Table 5.10, for example, into [5.5] results in an average value of the association constant $\beta = 25.7$ for ferrocenium pairing with perchlorate.

The fact that an association constant of 25.7 was obtained from the voltammetry data lends considerable support to the proposal that when ferrocenium is formed in tetraglyme it pairs with perchlorate. The hemispherical model used up to this point to analyse the ferrocene impedance data may therefore have been inappropriate since it is based on an E mechanism. In order to reanalyse the data an EC model appropriate for analysis of impedance data from a microdisc is necessary.

5.2 CNLS Analysis of Impedance Data using the Hemispherical Approximation for Diffusion to the Microdisc for an EC Mechanism.

Applying the hemispherical approximation EC model discussed in Section 3.6 to, for example, impedance data obtained at a 5 μm microdisc yields the results shown in Table 5.11.

These results seem quite credible in that a rather good fit to the data is obtained from the model (see Figure 5.42) and the calculated values for disc radius, double layer capacitance, and diffusion coefficients are very much in accord with expectations.

Figure 5.42

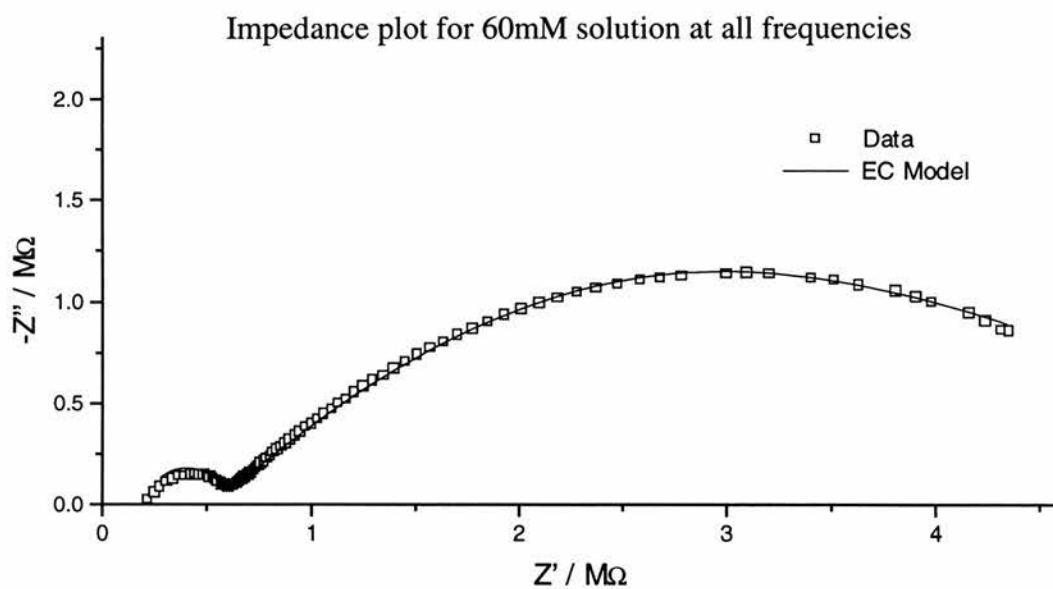


Table 5.11

Pt ($a = 5 \mu\text{m}$) / tetraglyme, ferrocene, 0.5 M $\text{LiClO}_4 / \text{Li(s)}$

Ferrocene Concentration / M	a / μm	C_{dl} / $\mu\text{F cm}^{-2}$	D / $10^6 \text{ cm}^2 \text{ s}^{-1}$	k_s / cm s^{-1}	k_1 / s^{-1}	k_2 / s^{-1}	K
4	5.43	11.9	1.96	0.296	3.24	6.55	0.495
6	5.13	8.24	1.71	0.171	3.34	6.45	0.518
9	5.43	9.53	1.77	0.108	3.74	7.36	0.508
12	4.93	8.54	1.80	0.088	2.32	5.78	0.401
16	5.22	7.61	1.98	0.077	1.94	8.36	0.232
30	5.51	9.32	1.98	0.042	1.65	5.54	0.298
60	5.81	10.0	1.60	0.027	5.00	7.90	0.632

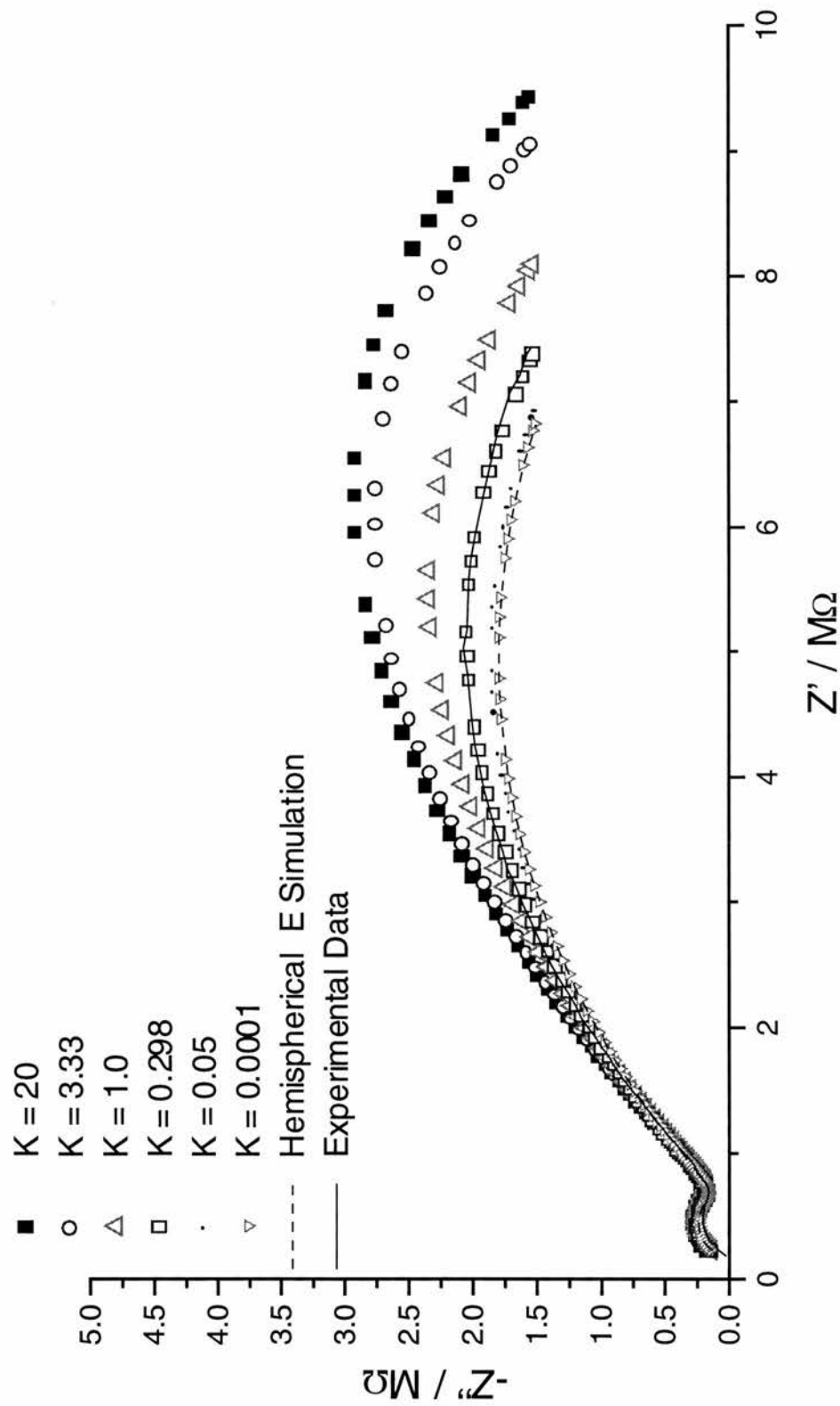
Chemical rate constants for the homogeneous reaction have reasonably stable values over the range of ferrocene concentrations and the degree of association averages about 0.5.

Figure 5.43 shows a variety of simulations for the 30 mM ferrocene solution in which all parameters are held at those shown in Table 5.11 except the value of K which is varied. It is interesting to note in Figure 5.43 that when K is small the impedance plots converge on the hemispherical E simulation. This is logical because one could think of the E reaction as an EC reaction in which the ratio of the forward to backward rate constants, K , is infinitely small.

Clearly in Figure 5.43 the experimental data are much better fitted if $K = 0.298$ than if, for example, $K = 1$ or $K = 0.05$. Thus the impedance method appears able to yield fairly precise values of K , provided K is not so small that the behaviour of the impedance data approaches that of the E mechanism in which $K \rightarrow 0$.

Figure 5.43

Impedance plot for 30 mM solution compared with simulations using different K values and with the hemispherical E simulation.



The values of the heterogeneous rate constant k_s show exactly the same trend with ferrocene concentration as they did for the somewhat simpler E mechanism - i.e. k_s increases when ferrocene concentration is lowered. In order to obtain a "true" k_s value, it is clear that further physical or chemical phenomena must be accounted for. Prior to discussing other possible phenomena, diffusion coefficients for ferrocene/ferrocenium may be obtained from the cyclic voltammetry steady state currents using the well-known equation for diffusion limited current.

$$i_d = 4nFDCa \quad [5.6]$$

Prior to using this equation, it is necessary to check that the voltammetry experiment truly conforms to steady-state conditions. The equation provided by Aoki et al. may be used to this end⁽¹¹⁾. The dimensionless parameter p is given by:

$$p = \left(\frac{nF}{RT} a^2 \nu / D \right)^{1/2} \quad [5.7]$$

where ν is the scan-rate. When $p < 0.33$ the voltammograms deviate from the steady-state by less than 5%. Substituting the values of $a = 10 \mu\text{m}$, $\nu = 20 \text{ mV s}^{-1}$, and $D = 1.79 - 2.66 \times 10^{-6} \text{ cm}^2 \text{ s}^{-1}$ yields p values of 0.54 to 0.66. Thus, the experimental values of D from voltammetry should be in error by no more than 12%.

The values of D obtained are shown in Table 5.12 and are plotted against perchlorate concentration in Figure 5.44 yielding a straight line falling as

concentration increases. These diffusion coefficients are consistent with voltammetry measurements shown in Figures 5.1 to 5.4.

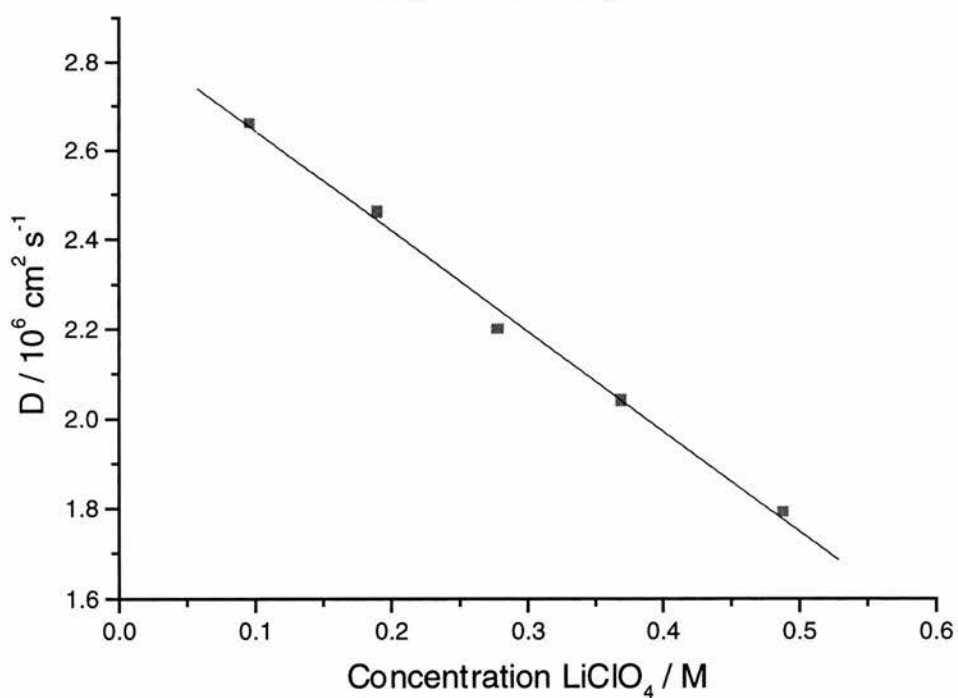
Table 5.12

Ferrocene diffusion coefficients for different lithium perchlorate concentrations

LiClO ₄ Concentration / M	D (Ferrocene) / 10 ⁶ cm ² s ⁻¹
0.0972	2.66
0.191	2.46
0.279	2.20
0.370	2.04
0.489	1.79

Figure 5.44

Ferrocene diffusion coefficients versus concentration of lithium perchlorate background electrolyte



Decreases in D with increasing additions of supporting electrolyte to glymes were also studied by Pyati and Murray⁽⁴⁾ who, by varying the concentrations of different glymes were able to keep the solution viscosity constant while varying the concentration of lithium perchlorate from 0.02 to 1.5 M. Their results show that maintaining the viscosity at a constant value also keeps the value of D and k_s more or less constant. This result appears to indicate that D and k_s are dominated by solution dynamics and that ion-association is unimportant.

In the experiments reported in this thesis, however, k_s is strongly dependent on ferrocene concentration in solutions which are also essentially iso-viscous. (Changes in the ferrocene concentration of a few millimolar units cannot alter the viscosity significantly, as indicated by the fact that D values are invariant with ferrocene concentration.) The results reported here, therefore, obtained by varying not only the background electrolyte concentration but also that of the electroactive species indicate that, in the case of ferrocene/ferrocenium a more complex mechanism than that reported by Pyati and Murray for $[\text{Co}(\text{bpy})_3]^{2+/3+}$ may be an important factor in determining the observed rate of charge transfer.

5.3 Alternative Mechanisms

An alternative mechanism that may help to explain these observations is a surface catalysed reaction of ferrocene/ferrocenium species. As the bulk ferrocene concentration is increased, each electroactive moiety on the electrode surface finds itself increasingly close to others, resulting in increased chemical reactions between them and deactivation with regard to electron transfer reactions. If we accept that a surface catalysed reaction occurs, a chemically reversible pairing between ferrocene and ferrocenium perhaps, then the rate of this reaction on the platinum could reasonably be initially postulated as:

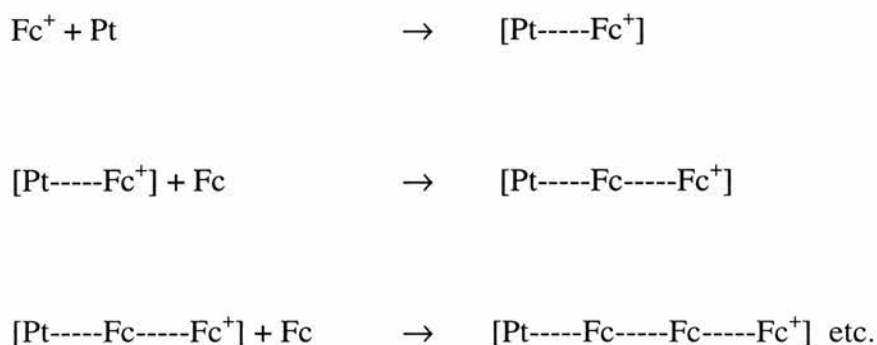
$$Rate = k_{pt}[Fc][Fc^+]$$

where k_{pt} is the rate constant for the surface catalysed reaction. This reaction will, of course, compete for ferrocene/ferrocenium with the heterogeneous electron transfer reaction, lowering the effective concentration of electroactive species at the electrode surface. The current owing to heterogeneous electron transfer, ET, and hence the observed value of k_s will then be decreased by an amount corresponding to the rate of the surface chemical reaction, i.e.:

$$ET\ Rate_{(obs)} = ET\ Rate_{(true)} - Rate\ Surface\ reaction$$

$$ET\ Rate_{(obs)} \propto k_{s(obs)} \propto k_{s(true)}[Fc] - k_{pt}[Fc]^2 / 4 \quad [5.8]$$

Alternatively we could propose a first order reaction with respect to the concentration of ferrocene in the bulk solution. A mechanism that could lead to this behaviour is:



In the case of a first order reaction the observed value of k_s would be related to:

$$ET \text{ Rate}_{(obs)} \propto k_{s(obs)} \propto k_{s(true)}[\text{Fc}] - k_{pol}[\text{Fc}] \quad [5.9]$$

where k_{pol} is the rate constant for the proposed polymerisation.

The mechanism is essentially a cationic polymerisation of ferrocene. Interestingly it results in the removal of mainly Fc from the electrode vicinity while, as previously discussed, pairing with perchlorate may remove Fc^+ .

If there were a polymerisation of ferrocene on the microdisc surface, then some physical evidence of it might reasonably be expected. Examination under an optical microscope of microdisc surfaces sometimes revealed that a layer of dirty material had accumulated on the disc surface during the ferrocene experiments but that other times the microdisc surface was still shiny and clean. It tended to be

solutions with low concentrations of ferrocene which yielded clean surfaces and high concentrations dirtier surfaces. It did not, however, prove practical to remove the "dirt" for analysis. Impedance data were examined for any indication of time dependence caused by polymerisation at the electrode surface. Figure 5.45 shows that at 2 mM ferrocene concentration the impedance did not change with time, while Figure 5.46 shows that at 22 mM ferrocene concentration there was a slight increase in impedance. These plots are consistent with the observation of a dirty coating forming on the electrode surface at higher concentrations which could increase the impedance to electron transfer.

More pronounced increases in impedance with time were found by Mahlendorf and Heinze for ferrocene at just 0.7mM in acetonitrile, tetrahydrofuran, dimethylformamide and propylene carbonate ⁽¹²⁾. These authors attributed the impedance increase to passivation of the electrode by film formation. Formation of films/precipitates during ferrocene electron transfer at platinum microelectrodes has also been reported by Kamau et al., who observed an insoluble precipitate on the electrode surface in acetonitrile solvent ⁽¹³⁾. Spectroscopic analysis of the precipitate indicated the presence of iron and the ferrocenium ion and it was proposed that the film resulted from polymerisation of the electroactive species. Although Kamau et al. did not attribute any significance to it, they also noted that the precipitate formed most readily when TBA(BF₄) was the background electrolyte and least readily for perchlorate salts and not at all for cetyltrimethylammonium bromide. This behaviour is consistent with a cationic polymerisation mechanism in which growth is critically dependent on the nature of the counter ion.

Figure 5.45

Time dependence of impedance plot for 2 mM ferrocene solution

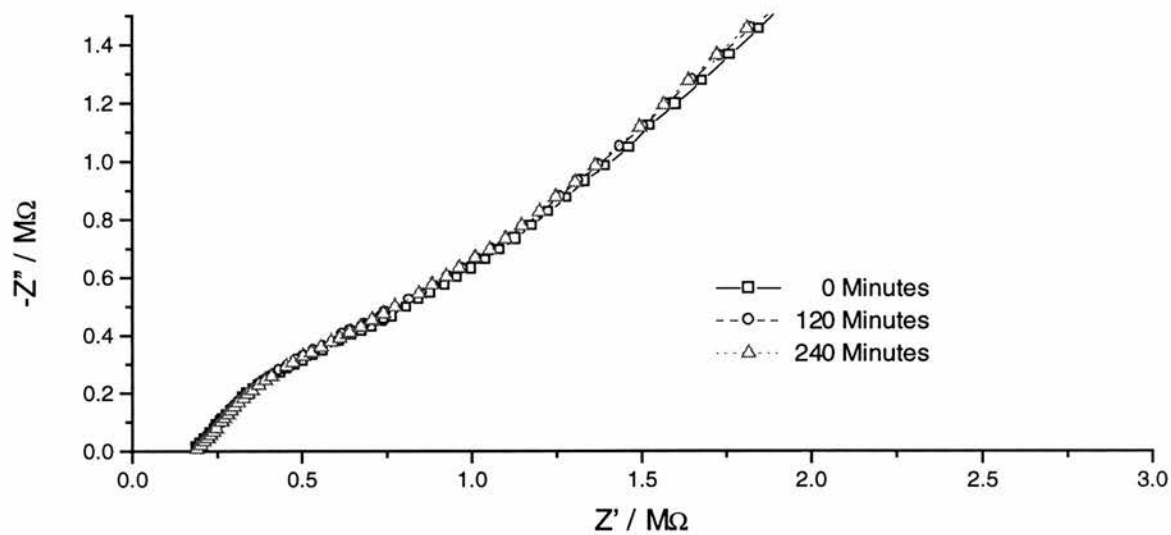
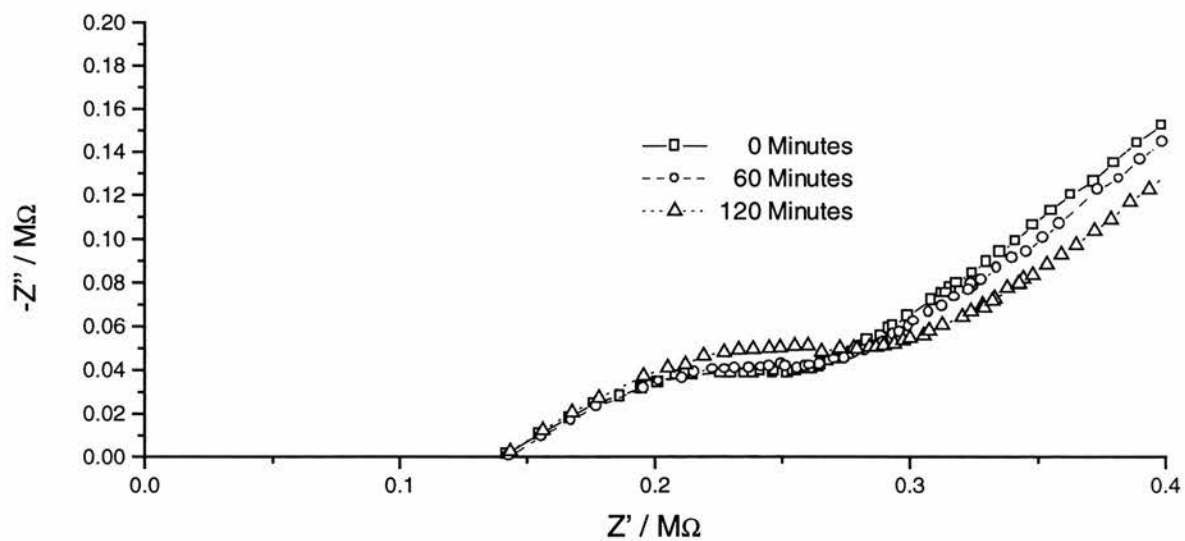


Figure 5.46

Time dependence of impedance plot for 22 mM ferrocene solution



Two equations ([5.8] and [5.9]) above show how the observed value of k_s might be lowered by side reactions. Neither mechanism, however, directly explains the observation that k_s is proportional to reciprocal concentration. If the values of k_{pt} or k_{pol} were not constants, however, but increased with ferrocene concentration then the trend may be more explicable.

5.4 Conclusions

CNLS analysis of impedance data, using the hemispherical approximation for an E mechanism, for the heterogeneous kinetics of ferrocene in tetraglyme with lithium perchlorate supporting electrolyte produced credible values for electrochemical parameters of interest. Calculated values of the microdisc radius were close to the geometric value, double-layer capacitances were in the region of $10 \mu\text{F cm}^{-2}$ and diffusion coefficients were in accord with expectations.

In most electrochemical rate studies, (such as the references cited in this chapter,) factors such as the type and concentration of background electrolyte, temperature and solvent are varied. The concentration of the electroactive species is generally held constant. In this study a clear relationship was found between the observed heterogeneous standard rate constant and the reciprocal of ferrocene concentration. Results from experiments with ferrocene could perhaps be caused by a polymerisation of ferrocene on the electrode surface #.

This conclusion is fair on the basis of data obtained in ferrocene experiments. In the next chapter, however, further data will be presented leading to the conclusion that a different explanation of the dependence of the observed heterogeneous rate constant on the redox couple concentration is more likely.

Heterogeneous rate constants and diffusion coefficients showed Arrhenius type behaviour, enabling Gibbs activation energies for the two process to be extracted. These averaged 25.0 and 20.8 kJ mol⁻¹ respectively.

Cyclic voltammetry experiments in which the half-wave potential shifted to less positive values as the concentration of background electrolyte was increased suggested the possibility of an EC mechanism. New equations had been derived in Chapter 3 to allow analysis of microdisc impedance data as an EC mechanism. Results obtained using the EC model were in broad agreement with those obtained using the E model except that values for the forward and backward homogenous rate constants were also obtained from the EC model. The association constants for ferrocenium and perchlorate obtained by voltammetry and impedance are at variance, the voltammetric value indicating a significant preponderance of paired species whereas the impedance value indicates a slight preponderance of the unpaired species.

The possibility that there may be a number of competing mechanisms operating on the electroactive species (i.e. electron-transfer, ion-pairing, polymerisation) could render it very difficult to produce an impedance model to satisfactorily extract all of the relevant parameters. The true standard rate constant of ferrocene in the system studied here is probably reflected most accurately in the low concentration data and is greater than 1 cm s⁻¹.

The fact that results from this and other studies are consistent with both ion-pairing of ferrocenium and a polymerisation of ferrocene on the surface of platinum give

some pause for thought over whether, under all circumstances, the ferrocene/ferrocenium couple is an appropriate choice as a reference redox system as recommended by IUPAC ⁽¹⁾.

5.5 References

1. G. Gritzner, J. Kuta, J. Heyrovského, *Pure & Appl. Chem.*, (1984), 56, p461.
- 2a. A.J. Bard, L.R. Faulkner, *Electrochemical Methods Fundamentals and Applications*, John Wiley and Sons Inc., (1980), p160.
- 2b. A.J. Bard, L.R. Faulkner, *Electrochemical Methods Fundamentals and Applications*, John Wiley and Sons Inc., (1980), p100.
3. P.G. Bruce, A. Lisowska-Oleksiak, C.A. Vincent, *J. Electroanal. Chem.*, (1994), 364, p163.
4. R. Pyati and R. W. Murray, *J. Am. Chem. Soc.*, (1996), 118, p1743.
5. T.T. Wooster, M.L. Longmire, H. Zhang, M. Watanabe, R.W. Murray, *Anal. Chem.*, (1992), 64, p1132.
6. J.A. Riddick, W.B. Bunger, Eds, *Organic Solvents 4th Edition*, (1986), Wiley Interscience, New York.
7. A.S Baranski, K. Winkler, W.R. Fawcett, *J. Electroanal. Chem.*, (1991), 313, p367.
8. T. Gennett, D.F. Milner, M.J. Weaver, *J. Phys. Chem.*, 1985, 89, p2787.
9. H. Zhou and S. Dong, *Electrochimica Acta*, (1997), 42, p1801.
10. J.T. Hupp, *Inorganic Chemistry*, (1990), 29, p5010.
11. K. Aoki, K. Akimoto, K. Tokuda, H. Matsuda, J.G. Osteryoung, *J. Electroanal. Chem.*, (1984), 171, p219.
12. F. Mahlendorf and J. Heinze, *J. Electroanal. Chem.*, (1993), 352, p119.
13. G.N. Kamau, T.M. Saccucci, G. Gounili, A.F. Nassar, J.F. Rusling, *Anal. Chem.*, (1994), 66, p994.

CHAPTER 6

A MICROELECTRODE IMPEDANCE STUDY OF THE HETEROGENEOUS KINETICS OF TCNQ IN TETRAGLYME

Introduction

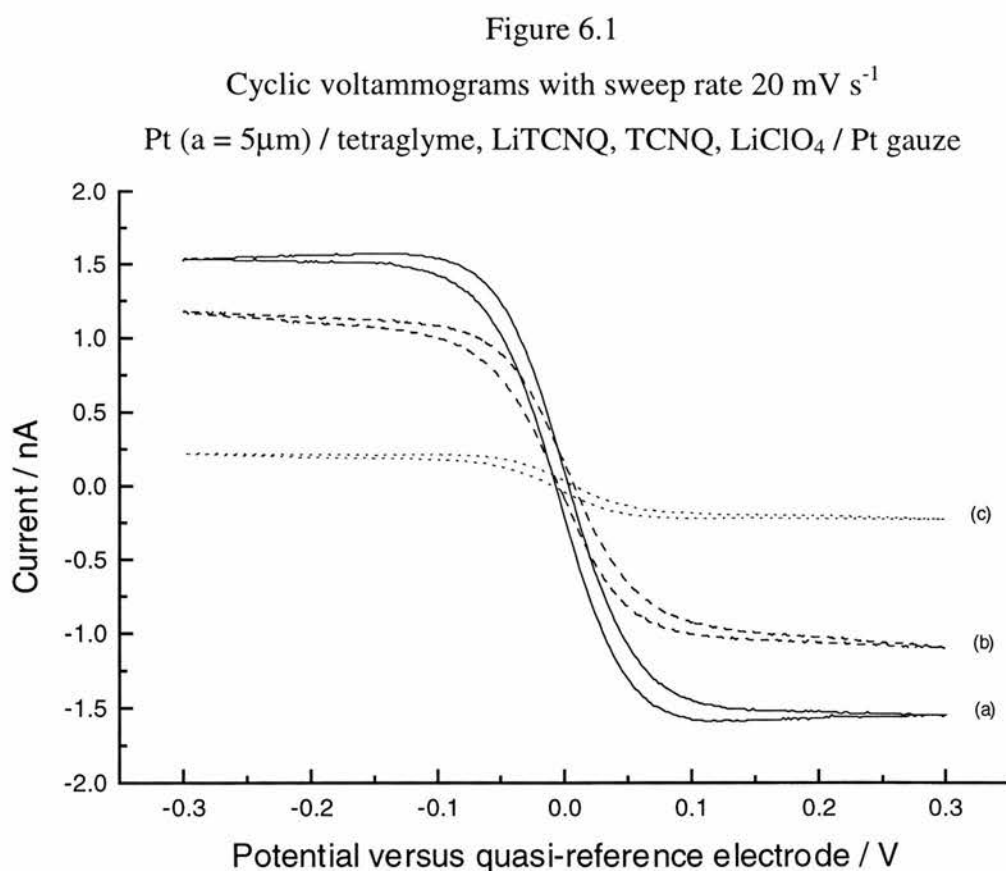
The electrochemistry of tetracyanoquinodimethane (TCNQ) and its radical anion has been reported by a number of authors in both liquid organic solvents and solid polymer electrolytes. Well behaved, reversible electrochemistry has been reported at platinum electrodes in the liquid organic environment ⁽¹⁻⁴⁾. In the solid polymer environment, i.e. poly(ethylene oxide), the electrochemistry is reported to be more complicated, owing principally to homogeneous electron exchange between TCNQ and its anion occurring in addition to heterogeneous electron exchange at the platinum electrode ⁽⁵⁻⁶⁾.

Here the electrochemistry of the TCNQ/TCNQ⁻ couple is investigated in tetraglyme, a liquid, low molecular weight oligomer of poly(ethylene oxide) in which the electrochemistry of the TCNQ/TCNQ⁻ couple has not previously been reported. In comparison with electrochemical studies of ferrocene, the advantage offered by a study of the TCNQ redox couple is that solutions can be prepared containing only the oxidant, TCNQ, or only the reductant, TCNQ⁻, or both species

can be added together in equimolar quantities. As is demonstrated below, this flexibility offers the opportunity to carry out experiments that yield rather more information than could be obtained in the study of ferrocene.

6.1 Cyclic Voltammetry Measurements

The electrochemical cells were assembled as shown in Figure 2.3 with the following constituents; Pt microdisk / tetraglyme, LiTCNQ, TCNQ, LiClO₄ / Pt gauze. This cell is written here as containing both LiTCNQ and TCNQ. Cells were also prepared containing only TCNQ. Figure 6.1 shows typical cyclic voltammograms obtained for cells with different concentrations of equimolar LiTCNQ and TCNQ and different concentrations of the background electrolyte.



For the reversible transfer of a single electron, $|E_{3/4} - E_{1/4}| = 56.4$ mV at 25 °C. For voltammograms (a) - (c) $|E_{3/4} - E_{1/4}|$ values were found to be 57, 58 and 61 mV at 22 °C, 20 °C and 19 °C respectively. It is concluded therefore that the cells investigated here are nernstian reversible. Steady state behaviour was verified with $p < 0.33$. (See equation [5.7].)

Table 6.1 shows that when equimolar TCNQ and LiTCNQ are present in the bulk solution there is no shift in the half-wave potential with varying background electrolyte concentration. When cells were prepared with only TCNQ, reversible transfer was also obtained. Cyclic voltammograms for TCNQ were shown in Figure 5.40. In these cells, shifts in the half-wave potential *were* observed when the concentration of background electrolyte was varied. The variation in half-wave potential with background electrolyte concentration is shown in Tables 6.1 and 6.2 and illustrated in Figure 6.2.

Table 6.2 and Figure 6.2 show that when only TCNQ is present in the bulk solution the half-wave potential shifts to less negative values when the background electrolyte concentration is increased.

The gradient of the graph is expressed in units of mV / log C, where C is the molar concentration of the background electrolyte.

Table 6.1

Diffusion coefficients and $E_{1/2}$ in cells (a) to (c) with both TCNQ and LiTCNQ added:

Cell	[TCNQ] / mM	[LiTCNQ] / mM	[LiClO ₄] / M	D / 10 ⁶ cm ² s ⁻¹	E _{1/2} / mV
(a)	5	5	0.1	1.59	-1.9
(b)	5	5	0.5	1.18	-1.9
(c)	1	1	0.5	1.14	+1.6

Table 6.2

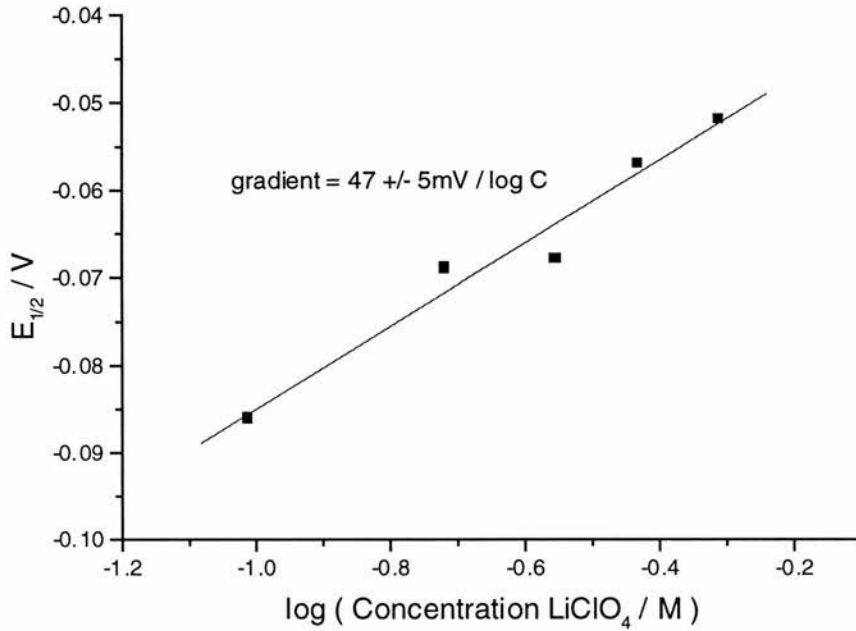
Diffusion coefficients and $E_{1/2}$ in cells with only TCNQ redox species added

[LiClO ₄] / M	D / 10 ⁶ cm ² s ⁻¹	E _{1/2} / mV
0.097	1.47	-86
0.19	1.37	-69
0.28	1.17	-68
0.37	1.13	-57
0.49	0.933	-52

Figure 6.2

Half-wave potential of TCNQ reduction in tetraglyme.

Pt ($a = 5 \mu\text{m}$) / tetraglyme, 5.5 mM TCNQ, LiClO_4 / Pt gauze



The direction of half-wave potential shift, or indeed whether a shift is observed at all, is dependent on which of the redox species was added to the bulk solution. At first sight this situation may appear paradoxical. It is helpful to look at the half-wave potential shifts in energetic terms.

When only TCNQ is present in solution at the quasi-reference electrode and TCNQ^- is generated at the microelectrode there is a potential difference between the two electrodes and the potential at the microelectrode is negative of the quasi-reference electrode. When more background electrolyte is added, the potential difference moves closer to zero. In other words the Gibbs energy of the electron transfer reaction is lowered by the addition of background electrolyte. If, however, equimolar TCNQ and TCNQ^- are present at the quasi-reference electrode then the

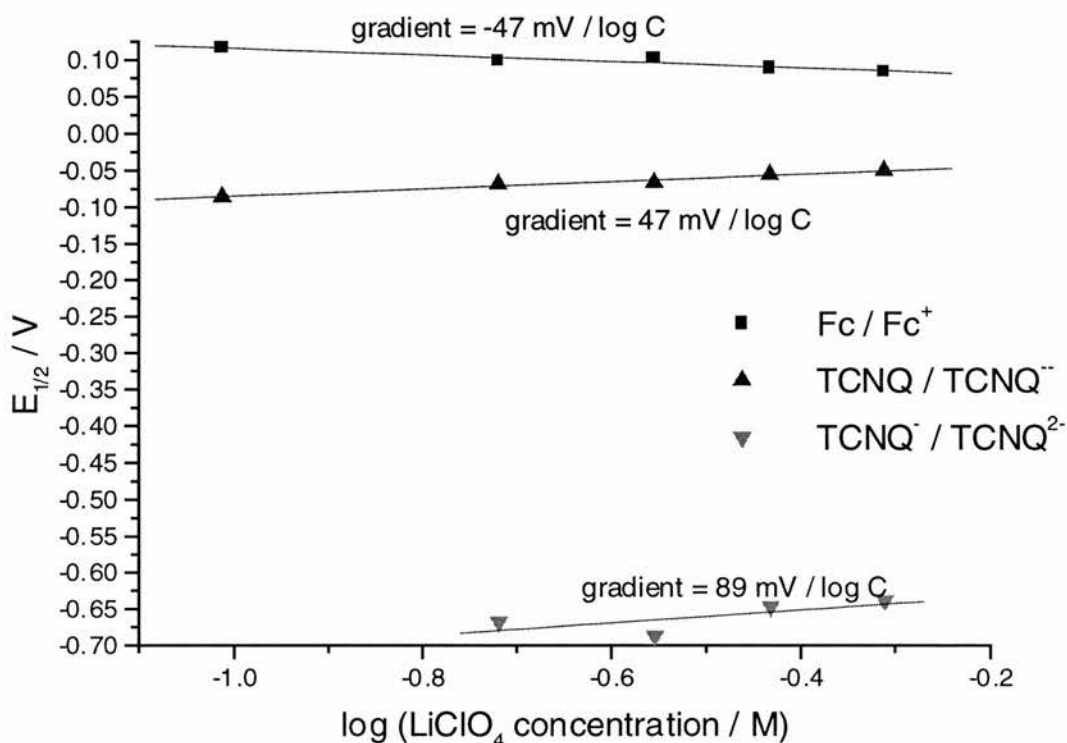
potential difference between the quasi-reference electrode and the microelectrode at half-wave potential (where TCNQ and TCNQ⁻ must also be equimolar) is necessarily zero. Thus the voltammetry results are self-consistent and indicate that the Gibbs energy of electron transfer is lowered by addition of background electrolyte. This is likely to occur because the background electrolyte associates with and stabilises the TCNQ⁻ product of electron transfer.

The half-wave potential shift was also measured for the TCNQ⁻/TCNQ²⁻ couple and is shown below in Figure 6.3 which summarises the half wave potential shifts for ferrocene/ferrocenium as well as for TCNQ/TCNQ⁻ and TCNQ⁻/TCNQ²⁻. The gradient of the second reduction step is higher than for the first step.

This behaviour has also been observed in a study carried out by Kamau and Rusling who used carbon or platinum microdiscs in two or three-electrode cells. In the three electrode cells the reference electrode was Ag/Ag⁺ (0.01M AgNO₃) connected to the cell with a bridge containing the same solvent and electrolyte as in the main cell ⁽⁷⁾. These authors studied TCNQ reductions in 2:1 tetrahydrofuran and acetonitrile with TBABF₄ background electrolyte. They measured half-wave potential shifts in of 41 ± 7 mV / log C for the first reduction and 115 ± 7 mV / log C for the second. These results are rather similar to those obtained here in tetraglyme, i.e. 47 ± 5 mV / log C for the first reduction and 89 ± 69 mV / log C for the second. (If the obvious outlier point in Figure 6.3 is removed from the analysis, the second reduction has a gradient of 71 ± 2 mV / log C.) It is interesting to note that Kamau and Rusling observed that two and three electrode cells were used interchangeably, yielding *identical* results.

Figure 6.3

Comparison of shifts in half-wave potential with increasing lithium perchlorate concentration



A concluding remark on the voltammetry measurements with regard to diffusion coefficients is merited. The diffusion coefficients from the voltammograms appear realistic. In Table 6.1, for example, when the concentration of the redox couple is increased by a factor of five and the concentration of supporting electrolyte is held constant, the diffusion coefficient remains more or less constant. If, however, the concentration of the redox couple is held constant whilst the supporting electrolyte concentration is decreased by a factor of five, the diffusion coefficient increases by about one third. This and the data in Table 6.2 are consistent with observations and discussions in the previous chapter regarding ferrocene diffusion.

6.2 Conductivity Measurements

The voltammetry results have indicated the likelihood of ion association. In order to confirm this, the conductivities of a series of LiTCNQ solutions in tetraglyme were measured using the apparatus described in Section 2.4.6. Only LiTCNQ was added to the solutions. No other species, such as lithium perchlorate, was added. The molar conductivities, denoted Λ , are recorded in Table 6.3 and graphed in Figure 6.4.

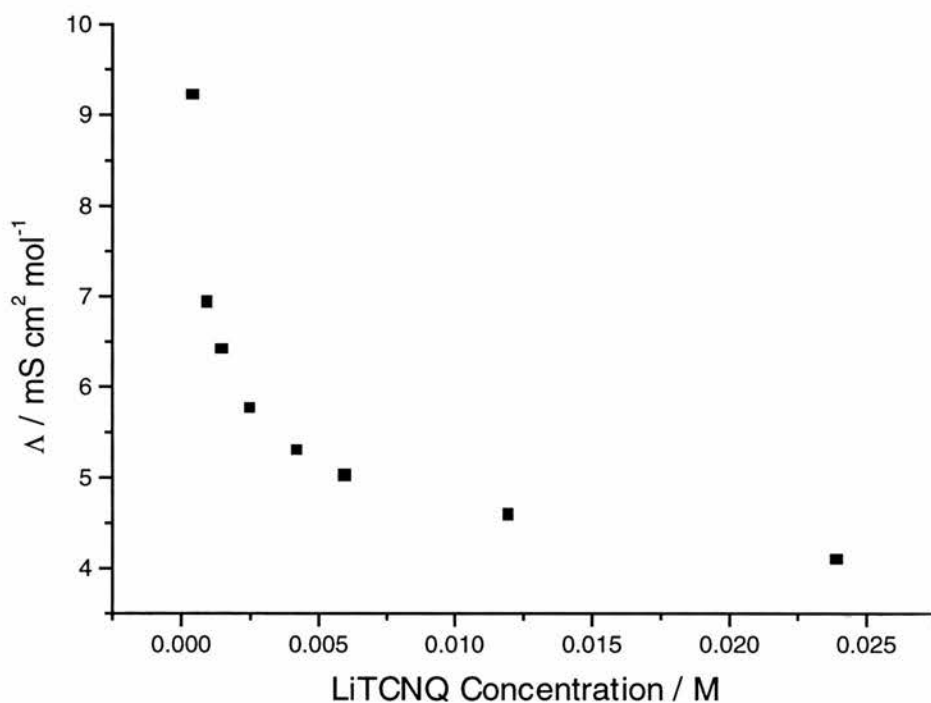
Table 6.3
Conductivities of tetraglyme solutions containing LiTCNQ

LiTCNQ Concentration / mM	Resistance / k Ω	Conductivity / 10^6 S cm $^{-1}$	Λ / mS cm 2 mol $^{-1}$
0.439	247	4.0	9.2
0.972	148	7.0	6.9
1.49	105	10	6.4
2.49	69.8	14	5.8
4.22	44.7	22	5.3
5.96	33.4	30	5.0
12.0	18.2	55	4.6
23.9	10.2	98	4.1

There is a very clear decrease in molar conductivity as concentration is increased. In fact, the shape of the graph is very similar to the classical shape of a molar conductivity plot for a weak electrolyte. For weak electrolytes the equilibrium

$MA \rightleftharpoons M^+ + A^-$ between the non-ionised and ionised species shifts to the right as the dilution is increased resulting in more ions per mole of MA added and hence higher molar conductivity ⁽⁸⁾. Strong electrolytes, i.e. those in which there is minimal ion-pairing, show a much less pronounced increase in molar conductivity when their concentration is decreased.

Figure 6.4
Molar conductivity of LiTCNQ in tetraglyme at 25°C.



The conductivity measurements have thus provided unequivocal evidence that LiTCNQ behaves as a weak electrolyte in tetraglyme and hence for substantial ion-association between TCNQ⁻ and Li⁺. It is clear therefore that the change in half wave potentials discussed in the previous section results from ion association.

6.3 Impedance Measurements

A series of impedance experiments was performed, sweeping frequencies from about 380 kHz to 1 Hz, with the objective of determining the effect of temperature and electrolyte concentration on the cells' electrochemical properties.

6.3.1 *The Effect of Potential on Impedance Data*

The complex plane plots in Figures 6.5 and 6.6 show how, as expected, the impedance increases when the potential is varied from that of minimum impedance. Potentials in Figures 6.5 and 6.6 are quoted versus the quasi-reference electrode. When determining k_s all measurements were made at the potential of minimum impedance.

6.3.2 *The Effect of Temperature on Impedance Data*

Figures 6.7 and 6.8 show the effect of changing the cell temperature at constant electrolyte concentration. As would be expected higher temperatures result in an increase in the rate of charge transfer, marked by the diminishing size of the charge-transfer semi-circle, and an increase in the rate of diffusion, marked by the diminishing size of the lower frequency quarter circle.

Figure 6.5

Effect of potential on impedance - full frequency sweep

Pt (a = 5 μm) / tetraglyme, 10 mM TCNQ, 0.1 M LiClO₄ / Pt gauze

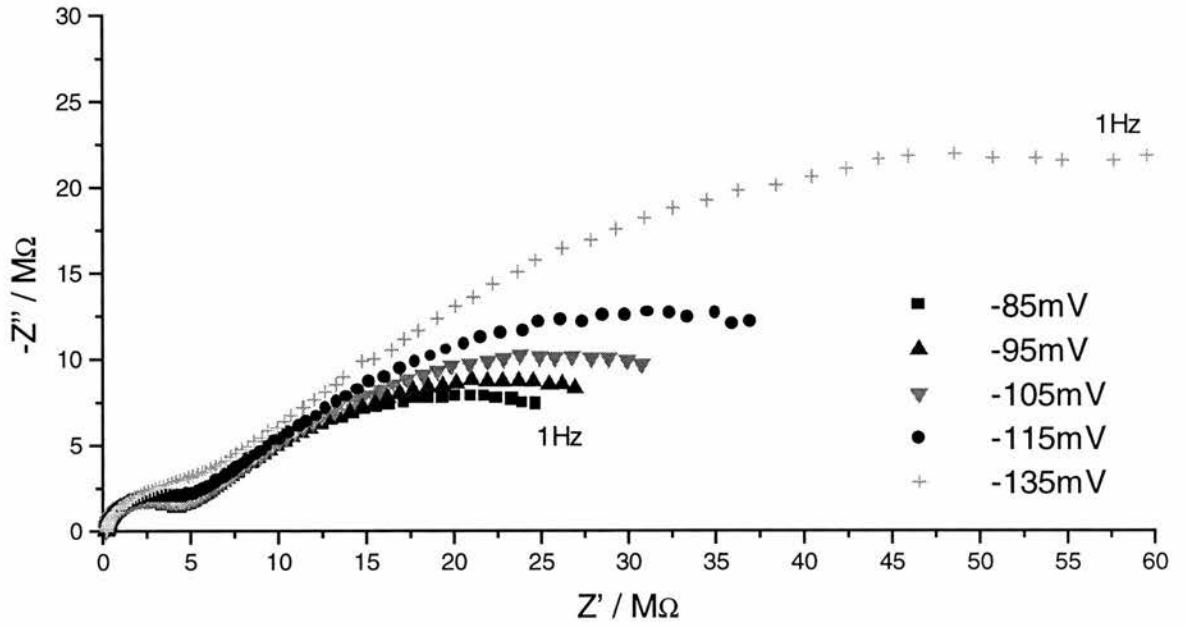


Figure 6.6

Effect of potential on impedance - high frequency region

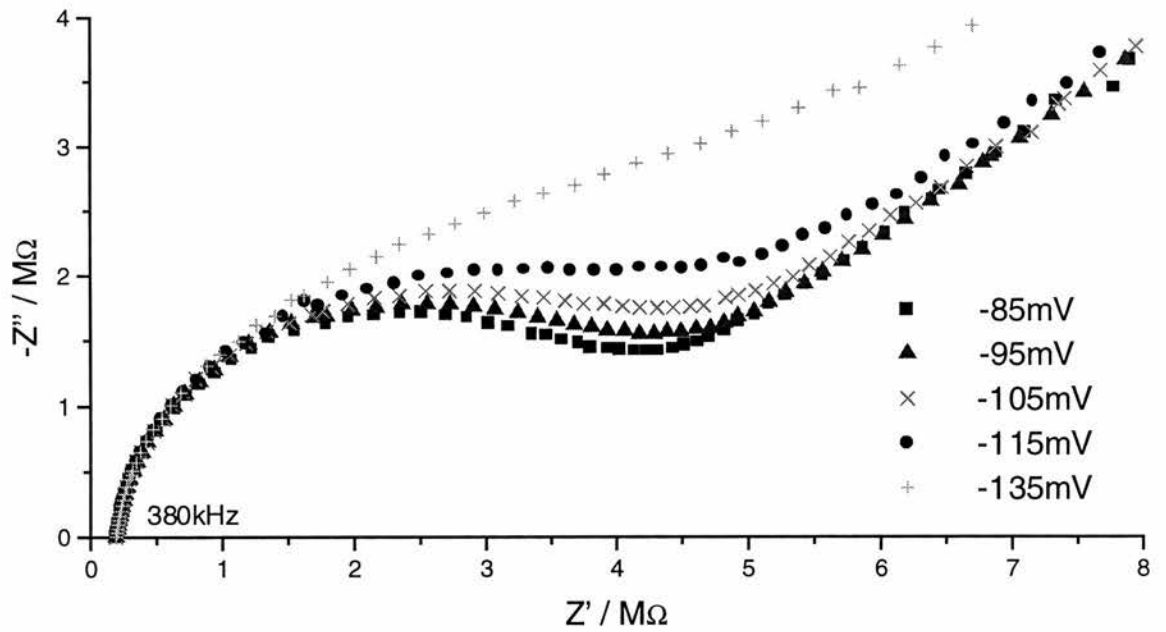


Figure 6.7

Effect of temperature on impedance - full frequency sweep

Pt ($a = 5 \mu\text{m}$) / tetraglyme, 2 mM TCNQ, 2 mM LiTCNQ, 0.1 M LiClO₄ / Pt gauze

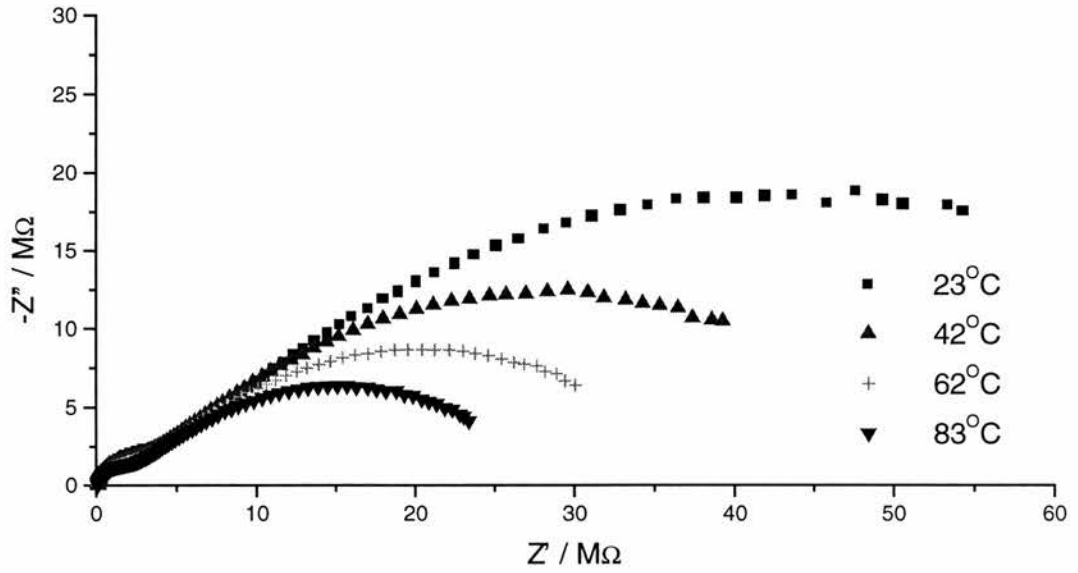
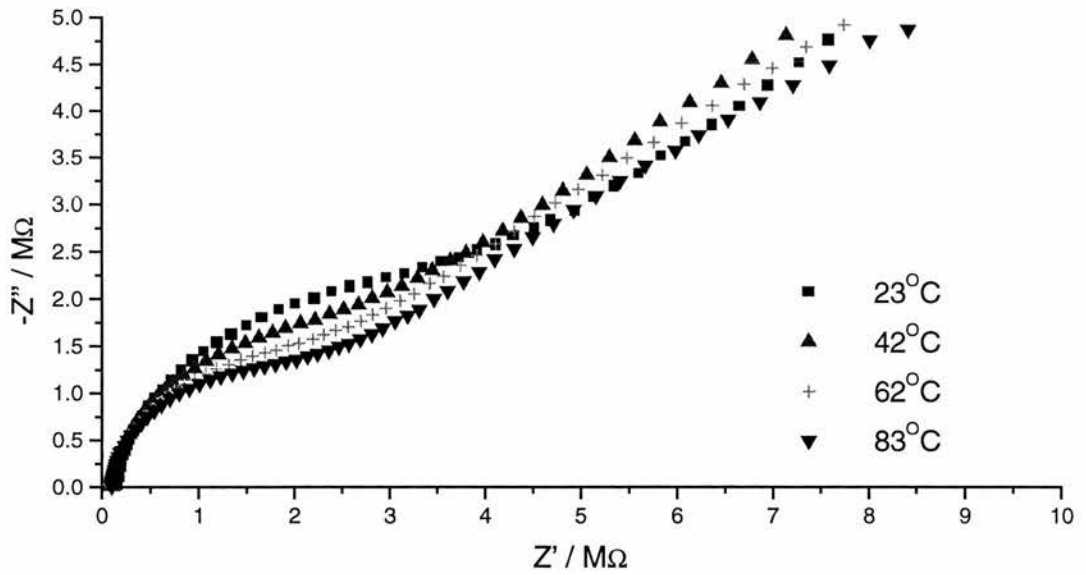


Figure 6.8

Effect of temperature on impedance - high frequency region



6.3.3 The Effect of Redox Couple Concentration on Impedance Data

Figures 6.9 and 6.10 show the effect of changing the concentration of the redox couple at constant temperature whereby the impedance increases as concentration is reduced. As with ferrocene the impedance does not rise by as much as would be expected when concentration is lowered, hinting again that the electrode reaction is more complex than a simple E mechanism.

Figure 6.9

Effect of different redox-couple concentrations on impedance - all frequencies
Pt ($a = 5 \mu\text{m}$) / tetraglyme, LiTCNQ, TCNQ, 0.1M LiClO₄ / Pt gauze at 19°C

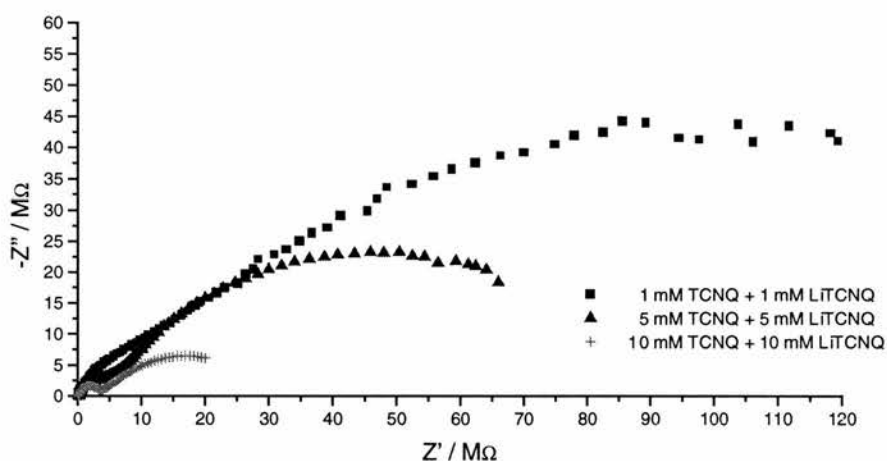
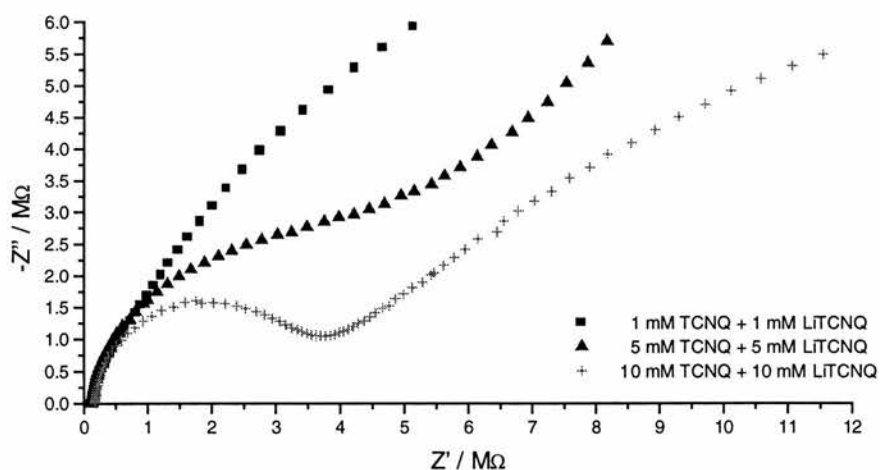


Figure 6.10

Magnified high frequency semi-circles



6.3.4 CNLS Analysis of the Impedance Data

The impedance data were analysed using the EC impedance model for coupled homogeneous reactions derived in Chapter 3. Good fits of the model to the data appeared to be obtained. Unfortunately, unreasonable values for the electrochemical parameters were obtained with errors generally of the order of 1,000%+, indicating that the model is inappropriate to the data. A different model is therefore required to analyse the TCNQ / TCNQ⁻ data. At this stage it is unclear which model is appropriate since voltammetry results are consistent with apparently similar ion-pairing phenomena for both redox couples. It was decided to use the hemispherical approximation for E mechanism electron transfer to see whether it fitted the data. This model, in fact, produced very good fits to the data at high frequencies as shown in Figures 6.11 and 6.12 and yielded sensible parameter values with low errors. The fit is somewhat poorer at lower frequencies, where the impedances are higher than the fitted model. This could be because the additional impedance associated with the homogeneous chemical reaction is not taken into account in the hemispherical approximation for simple electron transfer. It is unclear why the ion-association impedance model does not fit the data. Presumably there must be an additional but unknown complicating factor present in the electrochemistry. It was decided to carry out impedance analysis using the E model with the knowledge that the precise value obtained in any individual result should be treated with scepticism but that, as seen in Chapter 5, any trends observed should be reliable. The results from these experiments, i.e. values of C_{dl} , k_s and D are shown in Tables 6.4 to 6.7 and are plotted in Figures 6.13 to 6.15.

Figure 6.11

Impedance data and hemispherical approximation E mechanism fit

Pt ($a = 5 \mu\text{m}$) / tetraglyme, 2 mM LiTCNQ, 2 mM TCNQ, 0.1 M LiClO₄ / Pt gauze

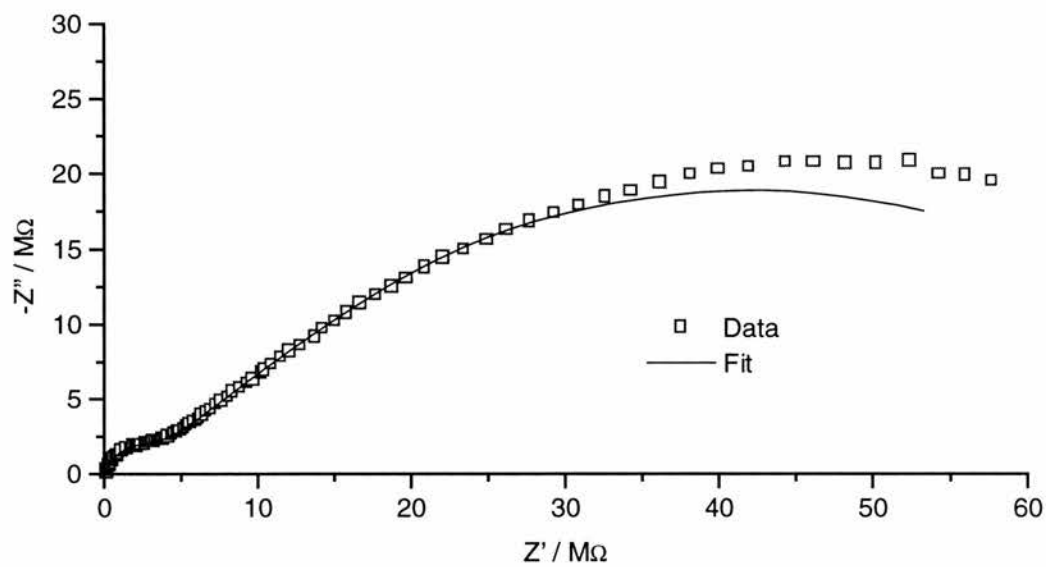


Figure 6.12

Magnified high frequency region

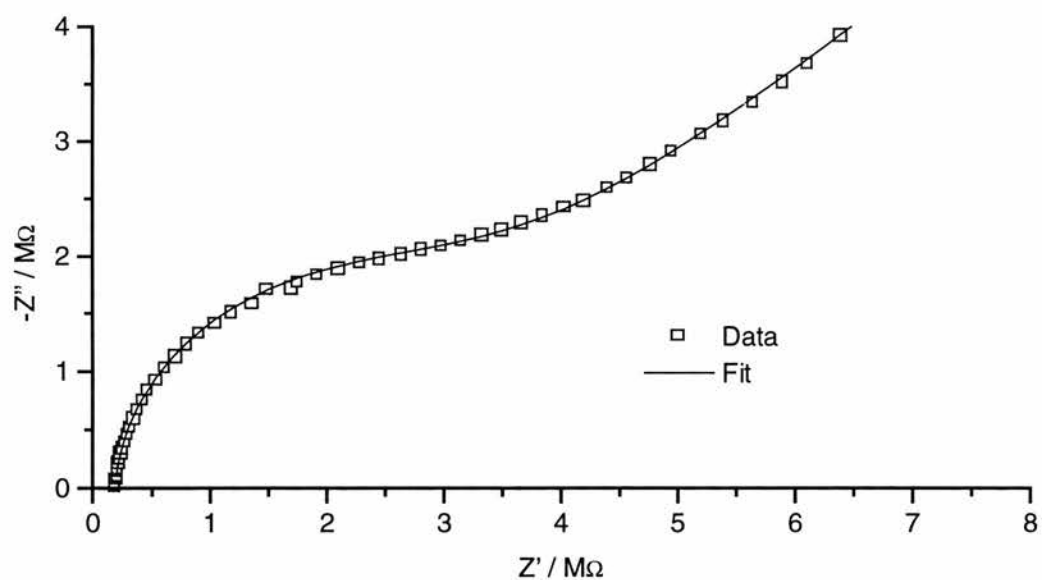


Table 6.4

Pt (a =5 μm) / tetraglyme, 1 mM LiTCNQ, 1 mM TCNQ, 0.1 M LiClO₄ / Pt gauze

Temp. / K	1/Temp K ⁻¹	k _s cm s ⁻¹	ln (k _s)	D /10 ⁶ cm ² s ⁻¹	ln (D)	a _{calc} / μm	C _{dl} / $\mu\text{F cm}^{-2}$
293	0.0034	0.147	-1.92	1.79	0.582	5.12	6.25
293	0.0034	0.144	-1.94	1.80	0.591	5.09	8.31
307	0.0033	0.243	-1.47	2.66	0.977	5.55	5.34
308	0.0033	0.261	-1.43	2.61	0.958	5.45	5.76
319	0.0031	0.288	-1.20	3.27	1.19	5.22	7.11
319	0.0031	0.290	-1.30	3.33	1.20	5.21	6.42

Table 6.5

Pt (a =5 μm) / tetraglyme, 2 mM LiTCNQ, 2 mM TCNQ, 0.1 M LiClO₄ / Pt gauze

Temp. / K	1/Temp K ⁻¹	k _s cm s ⁻¹	ln (k _s)	D /10 ⁶ cm ² s ⁻¹	ln (D)	a _{calc} / μm	C _{dl} / $\mu\text{F cm}^{-2}$
293	0.00341	0.0465	-3.07	1.78	0.574	5.75	9.0
294	0.0034	0.0440	-3.12	1.82	0.600	5.64	9.1
308	0.00325	0.0646	-2.74	2.51	0.919	5.72	11.0
309	0.00324	0.0634	-2.76	2.70	0.995	5.68	11.1
320	0.00313	0.0775	-2.56	3.28	1.19	5.81	10.6
320	0.00313	0.0865	-2.45	3.36	1.21	5.80	10.9
336	0.00298	0.118	-2.14	4.34	1.47	5.72	8.93
338	0.00296	0.120	-2.12	4.56	1.52	5.76	7.68
356	0.00281	0.215	-1.64	6.12	1.81	5.82	7.25
358	0.00279	0.238	-1.44	6.28	1.84	5.63	6.63

Table 6.6

Pt (a =5 μm) / tetraglyme, 5 mM LiTCNQ, 5 mM TCNQ, 0.1 M LiClO₄ / Pt gauze

Temp. / K	1/Temp K ⁻¹	k _s cm s ⁻¹	ln (k _s)	D /10 ⁶ cm ² s ⁻¹	ln (D)	a _{calc} / μm	C _{dl} / $\mu\text{F cm}^{-2}$
295	0.00339	0.0221	-3.81	1.91	0.649	5.65	7.83
295	0.00339	0.0209	-3.87	1.96	0.674	5.73	4.8
310	0.00323	0.0312	-3.47	2.60	0.955	5.54	5.09
311	0.00322	0.0368	-3.30	2.66	0.980	5.75	5.08
332	0.00301	0.0502	-2.99	4.22	1.44	5.32	6.11
332	0.00301	0.0581	-2.85	4.22	1.44	5.38	7.45
348	0.00287	0.0709	-2.65	5.17	1.64	5.65	7.17
348	0.00287	0.0867	-2.44	5.59	1.72	5.72	7.53
365	0.00274	0.0950	-2.35	7.30	1.99	5.48	8.04
364	0.00275	0.100	-2.30	7.21	1.97	5.66	8.70

Table 6.7

Pt (a =5 μm)/ tetraglyme, 10 mM LiTCNQ, 10 mM TCNQ, 0.1 M LiClO₄ / Pt gauze

Temp. / K	1/Temp K ⁻¹	k _s cm s ⁻¹	ln (k _s)	D /10 ⁶ cm ² s ⁻¹	ln (D)	a _{calc} / μm	C _{dl} / $\mu\text{F cm}^{-2}$
293	0.00341	0.0141	-4.26	1.97	0.676	5.81	8.96
293	0.00341	0.0146	-4.23	1.94	0.663	5.73	7.80
306	0.00327	0.0202	-3.90	2.35	0.855	5.82	6.71
306	0.00327	0.0195	-3.94	2.47	0.906	5.79	6.44
323	0.00310	0.0257	-3.66	3.54	1.26	5.60	5.79
325	0.00308	0.0243	-3.72	3.58	1.28	5.65	5.03
339	0.00295	0.0397	-3.23	4.80	1.57	5.64	5.26
340	0.00294	0.0383	-3.26	4.74	1.56	5.62	5.08
361	0.00277	0.0522	-2.75	6.79	1.91	5.49	6.41
361	0.00277	0.0561	-2.88	6.95	1.94	5.48	7.47

Figure 6.13

Dependence of C_{dl} on temperature and concentration of redox couple.

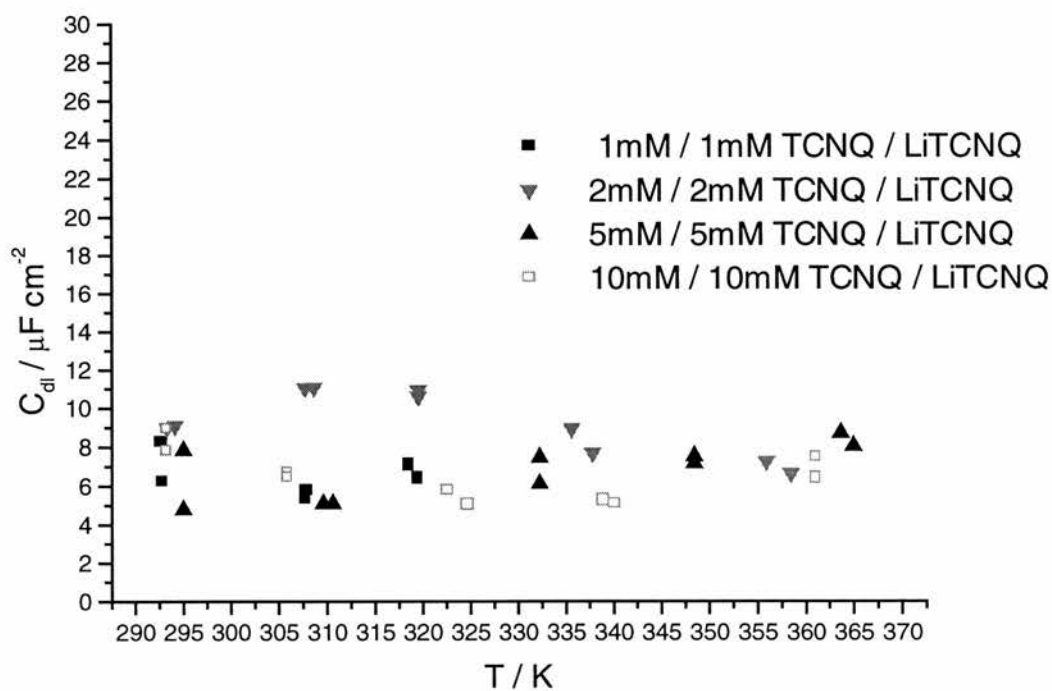


Figure 6.14

Arrhenius plots of D for different concentrations of redox couple.

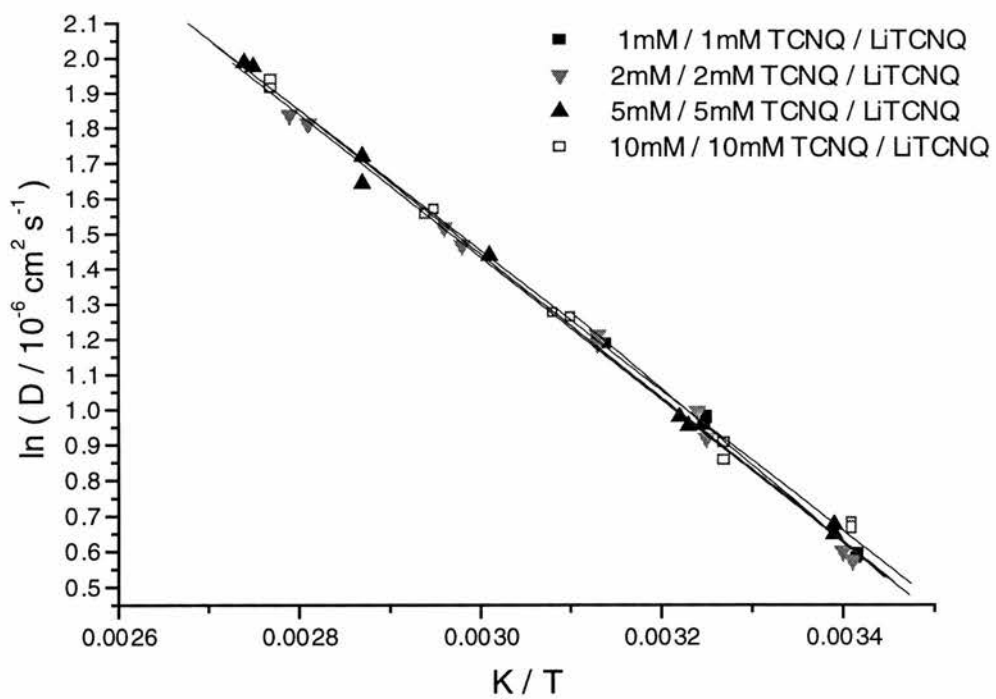


Figure 6.15

Arrhenius plots of k_s for different concentrations of redox couple.

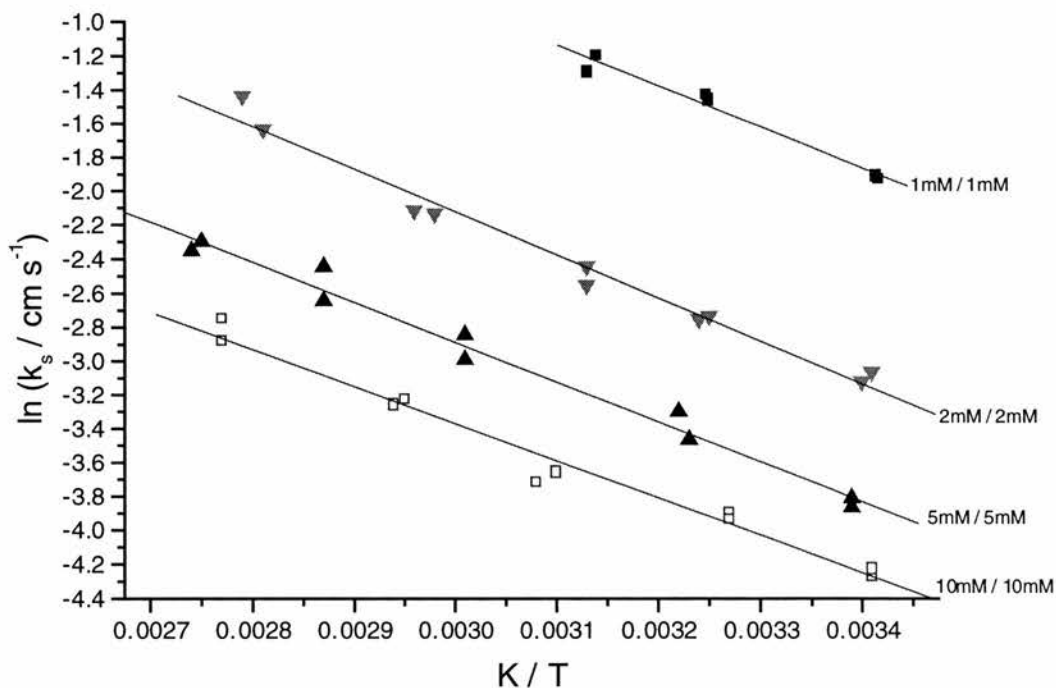


Figure 6.13 shows that, as with ferrocene, double-layer capacitance values were around 5 to $10 \mu\text{F cm}^{-2}$ and, as might be expected, were independent of redox couple concentration. There was no dependence of the double-layer capacitance on temperature.

The pre-exponential factors and activation energies for electron transfer and diffusion are shown in Table 6.8. These were obtained from the y-intercepts and gradients of the Arrhenius plots in Figures 6.14 and 6.15.

As would be expected, the activation energies for diffusion are independent of the redox couple concentration. At around 16 to 18 kJ mol^{-1} they are somewhat lower than those obtained for ferrocene - i.e. around 20 kJ mol^{-1} .

Table 6.8

Activation energies for electron transfer and diffusion for TCNQ / TCNQ⁻ in tetraglyme

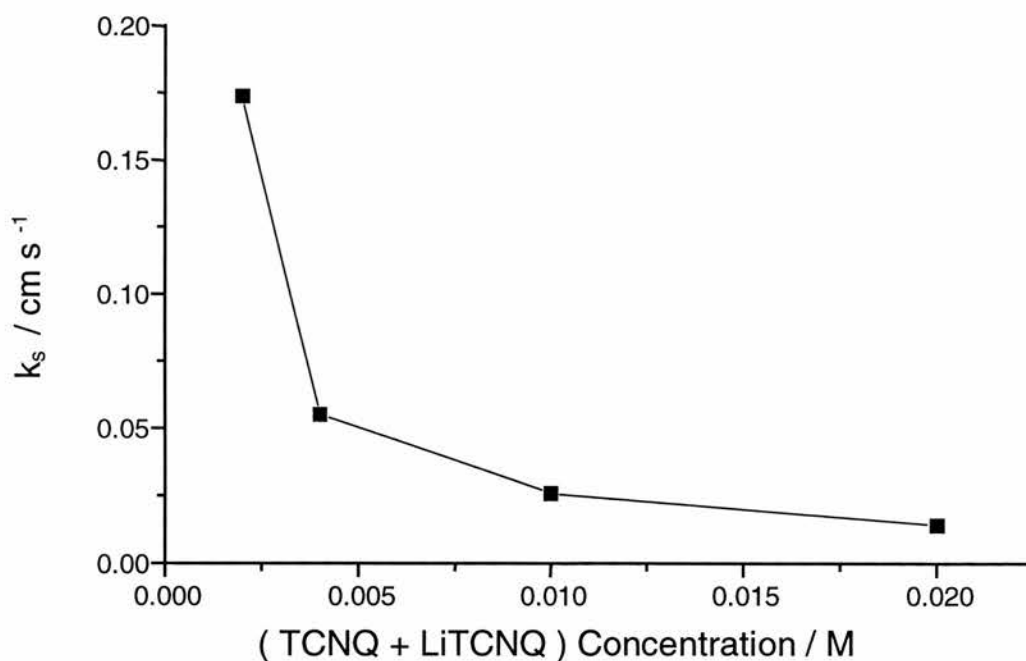
TCNQ + LiTCNQ Concentration / mM	E _a (Diffusion) / kJ mol ⁻¹	Pre-exponential factor (Diffusion) / cm ² s ⁻¹	E _a (Electron transfer) / kJ mol ⁻¹	Pre-exponential factor (Electron transfer) / cm s ⁻¹
1 + 1	18.1 ± 0.3	3100 ± 100	20.3 ± 1.2	620 ± 70
2 + 2	16.8 ± 0.4	1800 ± 100	21.0 ± 1.8	240 ± 20
5 + 5	17.0 ± 0.5	1900 ± 100	19.6 ± 1.6	65 ± 10
10 + 10	16.6 ± 0.5	1700 ± 100	18.3 ± 1.5	25 ± 5

The activation energies for electron transfer are, at 18 to 20 kJ mol⁻¹, rather similar to the values determined for diffusion.

Unlike diffusion but again similar to the observations for ferrocene, the electron transfer rates are found to be highly dependent on the concentration of the redox couple. The lower the concentration of the couple, the higher is the observed heterogeneous rate constant. Rate constant values at 25°C were read from Figure 6.15 and plotted in Figure 6.16 against the total concentration of the TCNQ/TCNQ⁻ redox couple to yield a shape very similar to that obtained with ferrocene.

Figure 6.16

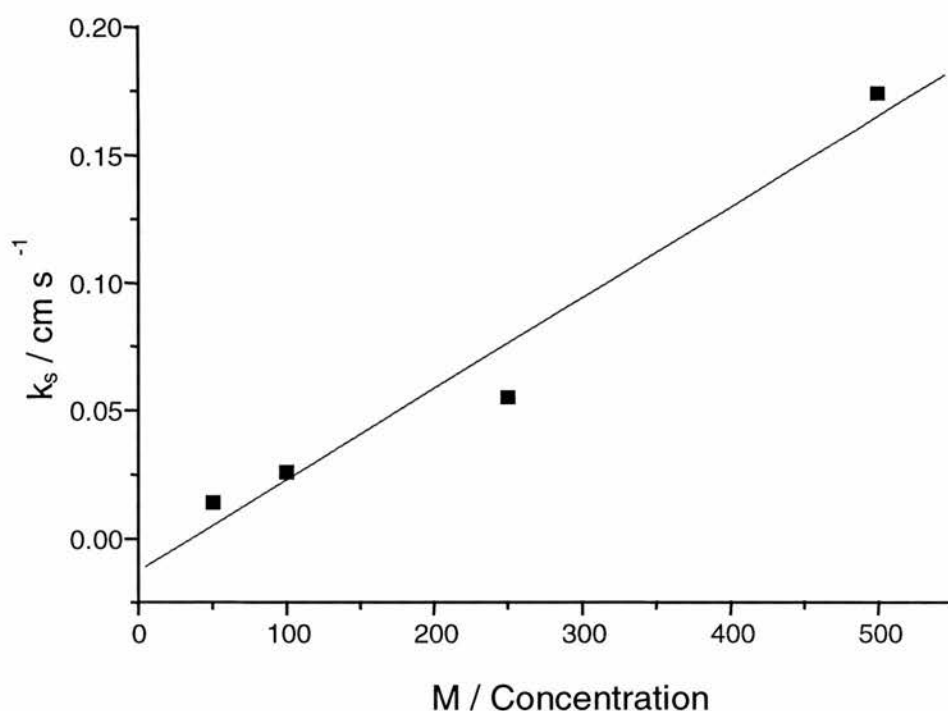
Relationship Between k_s and the concentration of the TCNQ / TCNQ⁻ redox couple at 25°C.



Again, as with ferrocene, plotting k_s against the reciprocal of concentration results in a straight line that probably passes through the origin - shown in Figure 6.17.

Figure 6.17

Relationship between k_s and reciprocal TCNQ / LiTCNQ concentration at 25 °C.

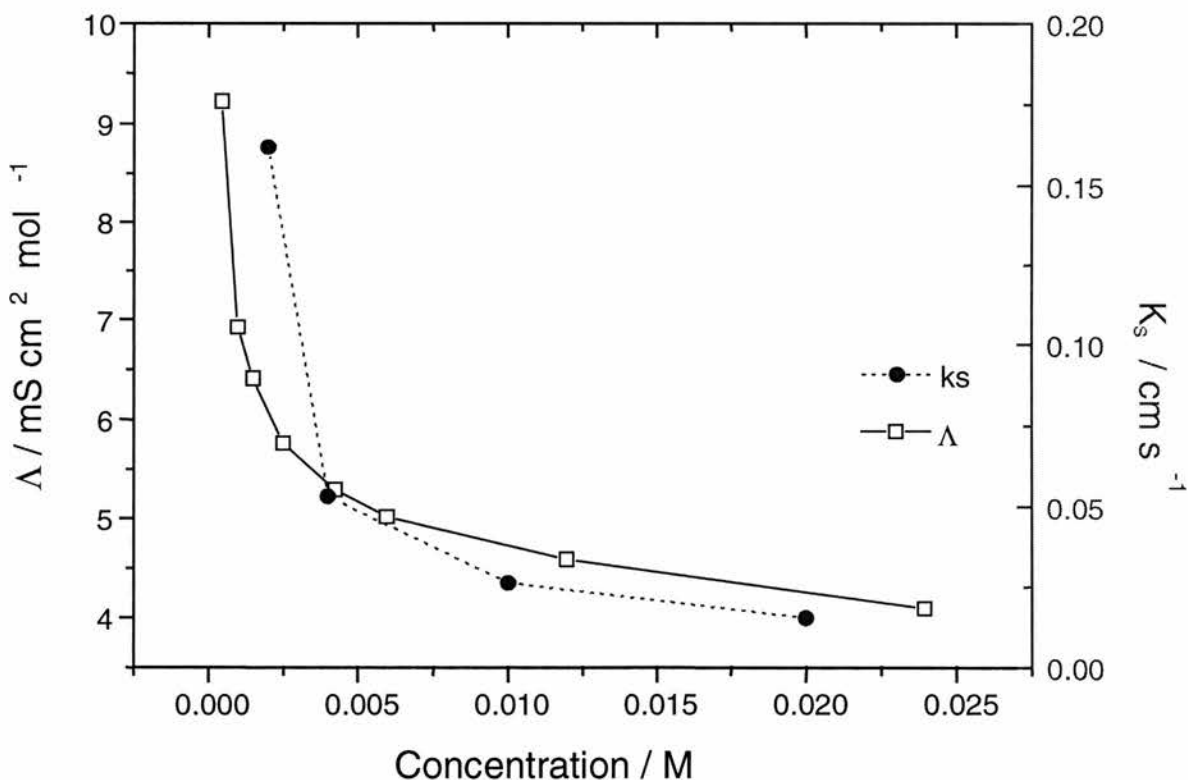


So the relationship between k_s and the redox couple concentration appears to be identical for TCNQ / TCNQ⁻ and ferrocene / ferrocenium. For the ferrocene / ferrocenium redox couple, a polymerisation mechanism was proposed to explain the trend. Could it be that there is a similar surface reaction for the TCNQ / TCNQ⁻ couple? The answer to this question is an unambiguous negative because, unlike the ferrocene system, no evidence of impedance increasing with time was found in the TCNQ system, and there is therefore no evidence of a surface reaction. The behaviour of the heterogeneous rate constants when the redox concentration is

changed is virtually identical for both ferrocene and TCNQ. It is highly unlikely that such similar rate constant trends could have entirely different causes. On the basis that polymerisation is not observed for TCNQ it is possible now to exclude it as the likely cause of the rate constant trends for ferrocene in tetraglyme.

Having excluded polymerisation, other mechanisms can be considered. Recall the shape of the molar conductivity plot in Figure 6.4. It is very similar to the plot of k_s against concentration in Figure 6.16. For convenience the molar conductivity and k_s are compared on the same graph in Figure 6.18.

Figure 6.18
Molar conductivity and k_s of LiTCNQ in tetraglyme at 25°C.

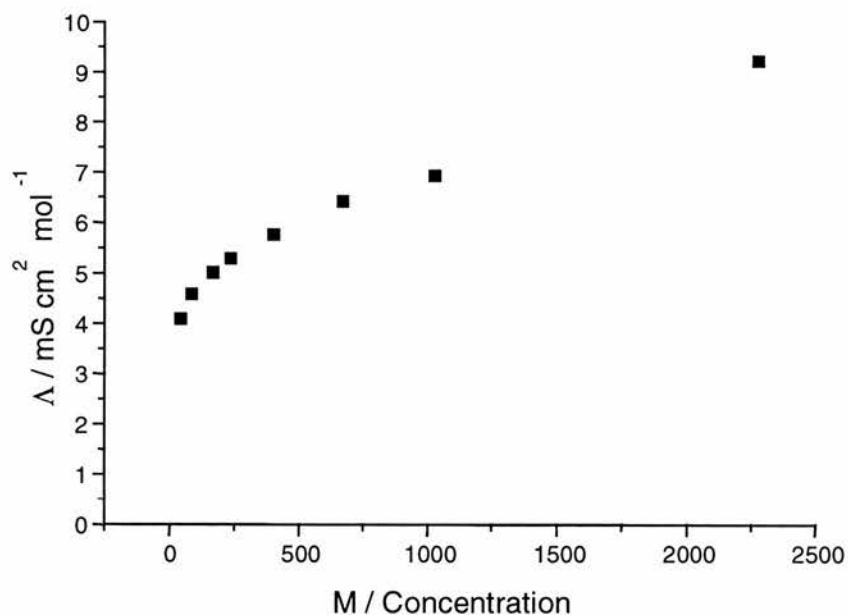


Although the graphs do not overlay one another precisely, their shapes are indeed similar enough that it might appear reasonable to propose that the same cause is

responsible for their shapes. In this context, since a plot of k_s against reciprocal concentration is linear, it is interesting to plot molar conductivity against reciprocal concentration, shown in Figure 6.19. The graph in Figure 6.19 has a curved part and a linear part. Unfortunately the concentrations at which the graph is linear are not those for which k_s varies linearly with reciprocal concentration. In fact the molar conductivity graph is curved at the concentrations at which the k_s graph is linear.

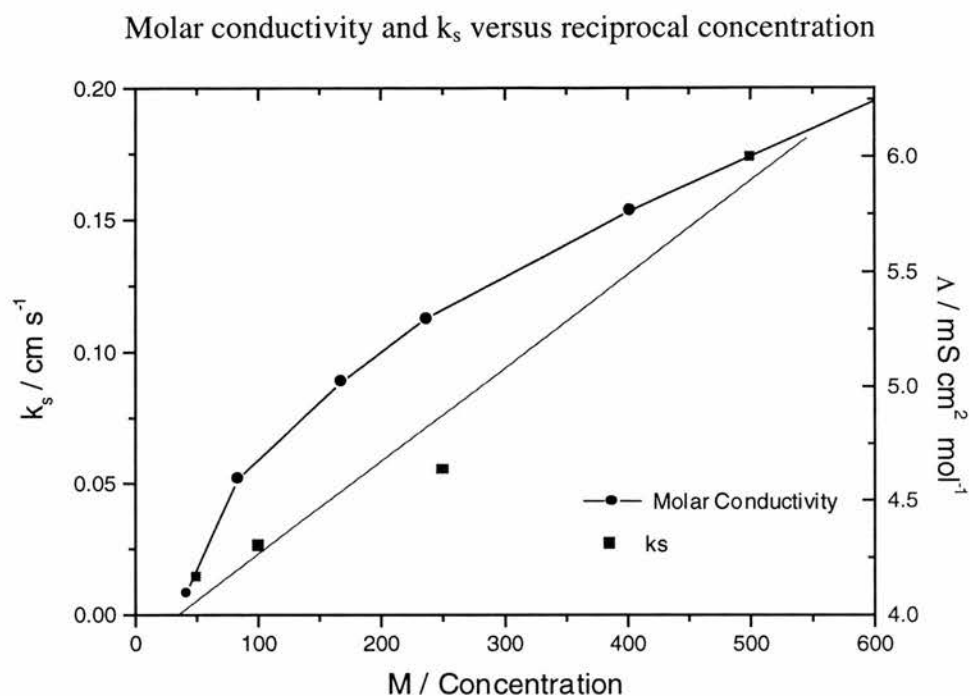
Figure 6.19

Molar conductivity versus reciprocal concentration for LiTCNQ in tetraglyme.



In Figure 6.20, both k_s and Λ are plotted against the reciprocal of redox concentration on the same graph, showing clearly the curvature in the conductivity data where rate constant data are linear.

Figure 6.20



It becomes clear that the molar conductivity changes by only about 50% on this graph but k_s increases by a factor of about 7. This implies that whatever the mechanism is withdrawing redox species from the electron transfer process it is many times more effective than ion-association *in the conductivity cell*. At first sight, this would appear to indicate that ion-association is not the cause of k_s decreasing when the electroactive species concentration increases. It is possible, however, that the degree of ion-association in the conductivity cell does not truly represent the ion-association affecting the electron transfer process. The degree of ion-association inferred from the bulk conductivity measurements obviously must correspond to the ion-association in the bulk and this is highly dependent on the relative permittivity of the bulk solution. The redox species participating in electron transfer reactions, however, are not located in the bulk solution but are located at the outer Helmholtz plane (OHP). The relative permittivity at the OHP is always lower than in the bulk solution because of the greater dipole ordering in the

vicinity of the electrode. In the case of bulk water, for example, the relative permittivity at room temperature is 78; while at the IHP ϵ is believed to be only 6; and at the OHP ϵ is believed to be intermediate between the two extremes at 40.⁽⁹⁾

Nicholas and Reich carried out experiments in which the conductance of lithium perchlorate was measured at different concentrations in solutions whose relative permittivity was altered by varying the proportion of THF ($\epsilon = 7.54$) to methanol ($\epsilon = 33$)⁽¹⁰⁾. For relatively dilute solutions (i.e. 0.1 M or less) Figure 8 in Reference 10 shows that the rate of change of molar conductivity with electrolyte concentration increases as the relative permittivity decreases. For example when the concentration is increased from 0.1 mM to 0.1 M at $\epsilon = 33$, Λ varies by a factor of about 2 but at $\epsilon = 7.54$, the factor increases to about 10. Nicholas and Reich's results, taken in isolation, are consistent with the hypothesis that measuring the rate of change of conductivity / ion-association in the bulk solution underestimates the rate of change of ion-pairing observed in the reaction layer. It must be borne in mind, however, that ion-pairing equilibria will be dominated by the lithium perchlorate supporting electrolyte and that small changes in the concentration of the redox couple should not be expected to change the ion pairing equilibrium. This is illustrated, in Table 5.12 for example where the association constant does not change when the concentration of ferrocene is increased. Furthermore, it has been shown that although low relative permittivity in the double layer may be expected to increase ion association, the effect is often overwhelmed by the dissociation field effect⁽¹¹⁾. The dissociation field effect describes the phenomenon whereby the high electric field in the double layer causes the rate at which a charged or uncharged species dissociates into two oppositely charged products to be dramatically

enhanced relative to where there is no electric field. The dissociation field effect thus predicts that there will in fact be less ion pairing in the double layer than in the bulk solution, although there are experimental exceptions where increased ion association in the double layer has been observed⁽¹²⁾.

It is also reasonable to ask whether there are any associations possible in the double layer which would be enhanced by lower permittivity but which would be unaffected by the dissociation field effect. This in fact would be the case if one or both of the dissociated species were uncharged. Therefore, although it does not seem very likely, if conditions in the double layer promoted formation of pairs of the type (Fc-Fc^+) and (TCNQ-TCNQ^-) , such pairs would be unaffected by the dissociation field effect.

It is interesting to review some of the data from the previous chapter and this chapter and the literature in the context of the dissociation field effect. First of all, Hupp has published values of ferrocenium's association constant, β , obtained by spectroscopy⁽¹³⁾. In acetonitrile with TBABF_4 , $\beta = 38$. In dichloromethane with TBAPF_6 , $\beta \approx 720,000$. Hupp verified an approximate linear relationship between $\log \beta$ and the bulk relative permittivity, ϵ . Tetraglyme and dichloromethane share the same value of $\epsilon \approx 9$ and therefore it might have been expected that a very large value of β should have been obtained for association between perchlorate and ferrocenium in Chapter 5. Yet a value of $\beta = 25.7$ was obtained for ferrocenium and perchlorate pairing by voltammetry. For TCNQ^- and Li^+ in tetraglyme comparison of voltammetry data with Chapter 5 shows that a very similar association constant, i.e. $\beta \approx 25$ is obtained. It is reasonable to ask why such

differing values are obtained by different techniques. The very high value obtained by spectroscopy clearly is related to association in the bulk solution. The value of β obtained by voltammetry is related to a shift in half-wave potential. The potential shift is brought about by changes in the relative concentrations of the redox couple at the electrode surface and hence is determined by the extent of ion association in the double layer. The potential shift should therefore be very strongly influenced by the dissociation field effect and hence it is logical that the value of β obtained by voltammetry should be lower than that obtained by spectroscopy.

Christie has carried out impedance measurements of the cobaltocene / cobaltocenium couple in tetraglyme in a three electrode cell with a normal sized platinum working electrode and has observed an extremely similar relationship between k_s and redox concentration to that observed here ⁽¹⁴⁾. Christie concluded that the reasons for the relationship were not clear but tentatively suggested that the effect could result from ion pairing and suggested that the measured rate constant may not be for electron transfer but for ion pairing. However, this suggestion may not be correct, because the high frequency semi-circle from which k_s was obtained is potential dependent and hence must fundamentally be caused by a charge-transfer resistance acting in parallel to a capacitance. Christie also found good agreement between manual analysis of the semi-circle diameter compared with k_s obtained via least squares analysis. What is important is the fact that Christie observed the same concentration dependence of k_s using a different reactant and using a different experimental procedure whereby a three electrode cell and a normal electrode were employed. The similarity of the results reported here to those reported by Christie

would seem to rule out the possibility that the results reported here are a quirk of microelectrode impedance spectroscopy.

It is concluded for both ferrocene and TCNQ in tetraglyme that a possible explanation for the very sharp decrease in the heterogeneous rate constant with increasing concentration of redox species is a double layer effect which lowers the effective concentration of reactants in the reaction layer. An example of such a double layer effect is the pairing of neutral with charged reactant in the low permittivity region of the double layer. There is, however, no firm evidence to support this suggestion.

Ion pairing is unlikely to cause the observed behaviour because the dissociation field effect would tend to suppress ion pairing in the double layer relative to the bulk but to explain the rate of variation of k_s with concentration the ion pairing in the double layer would have to be enhanced relative to the bulk. Furthermore, there is no shift in half-wave potential when the redox concentration is changed which would be a necessary indication of ion pairing.

Although the dependence of the observed value of k_s on reactant concentration has tentatively been ascribed to a double layer effect, it would be foolish to rule out the possibility that its true cause may have an entirely different explanation.

6.3.5 *The Effect of Supporting Electrolyte*

To explore further the influences which determine the observed rate constants in the TCNQ / TCNQ⁻ system a further series of impedance experiments was performed. In these experiments, in addition to varying the concentration of the redox couple and the temperature, the concentration of the supporting electrolyte was varied also. The data were analysed using the hemispherical model for simple heterogeneous electron transfer. Typical plots, highlighting the effect of supporting electrolyte on impedance with all other experimental factors constant are shown in Figures 6.21 and 6.22.

These impedance plots show that increasing the supporting electrolyte concentration has a pronounced effect on the size of the high-frequency charge-transfer semi-circle, causing it to shrink. The effect on the diffusion impedance - most easily discernible at lower frequencies - is less pronounced. Results from CNLS analysis of the impedance data are shown in Tables 6.9 to 6.12 and plotted in Figures 6.23 to 6.24.

Figure 6.21

Impedance data from 350 kHz - 1 Hz

Pt ($a = 5 \mu\text{m}$) / tetraglyme, LiTCNQ, TCNQ, LiClO₄ / Pt gauze at 19°C

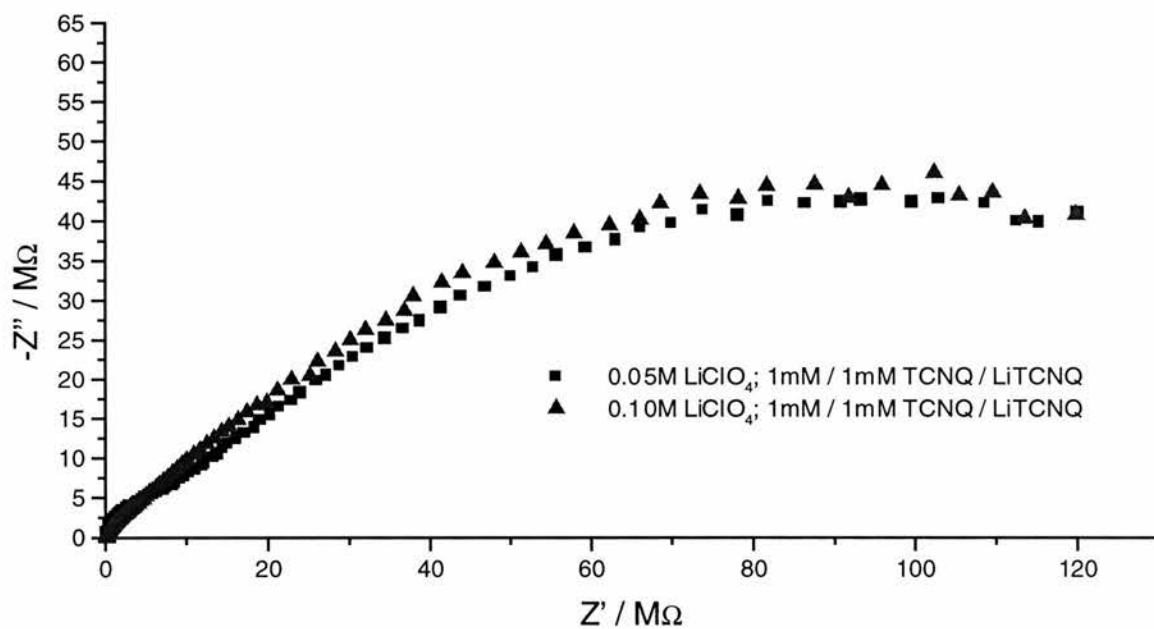


Figure 6.22

High frequency impedance data

Pt ($a = 5 \mu\text{m}$) / tetraglyme, LiTCNQ, TCNQ, LiClO₄ / Pt gauze at 19°C

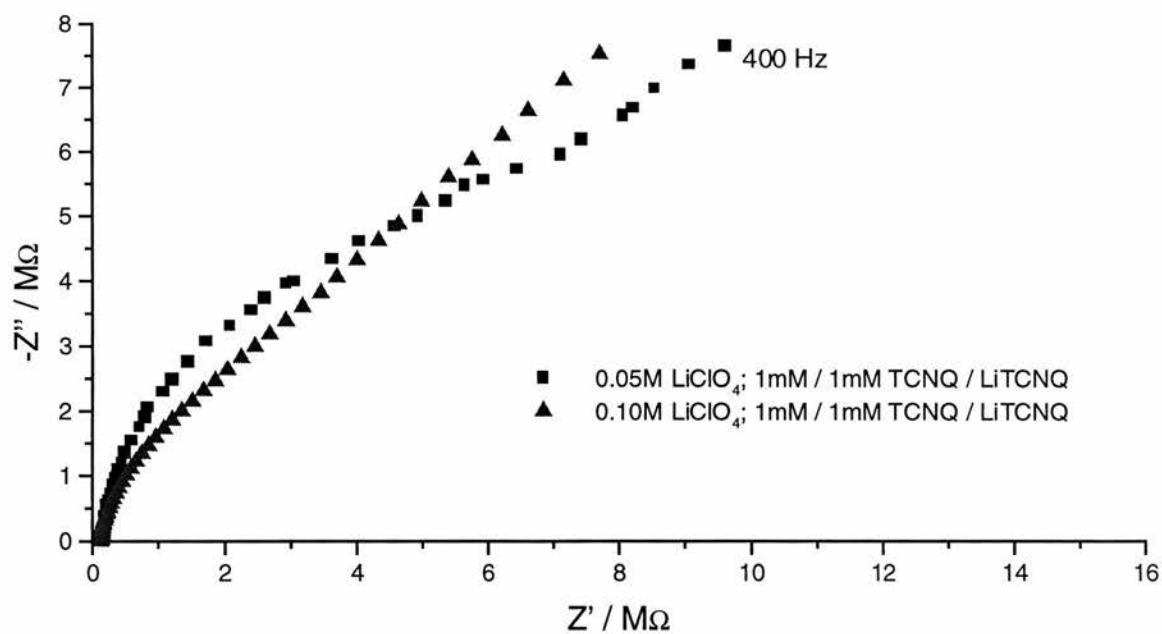


Table 6.9

Pt ($a = 5 \mu\text{m}$) / tetraglyme, 1 mM LiTCNQ, 1 mM TCNQ, 0.05 M LiClO₄ / Pt gauze

Temp. / K	1/Temp K ⁻¹	k_s cm s ⁻¹	ln (k_s)	D /10 ⁶ cm ² s ⁻¹	ln (D)	a_{calc} / μm	C_{dl} / $\mu\text{F cm}^{-2}$
293	0.00342	0.0599	-2.81	1.63	0.486	4.90	9.75
293	0.00342	0.0575	-2.86	1.75	0.560	4.69	9.82
293	0.00342	0.0505	-2.99	1.81	0.592	4.61	9.88
319	0.00314	0.0756	-2.58	3.11	1.13	4.93	7.03
319	0.00314	0.0756	-2.58	3.27	1.19	4.86	9.00
319	0.00314	0.0774	-2.56	3.25	1.18	4.87	10.4
319	0.00314	0.0731	-2.62	3.24	1.17	4.87	8.69
346	0.00289	0.0826	-2.49	5.29	1.67	4.97	8.45
346	0.00289	0.0830	-2.49	5.18	1.65	5.00	8.08

Table 6.10

Pt ($a = 5 \mu\text{m}$) / tetraglyme, 1 mM LiTCNQ, 1 mM TCNQ, 0.1 M LiClO₄ / Pt gauze

Temp. / K	1/Temp K ⁻¹	k_s cm s ⁻¹	ln (k_s)	D /10 ⁶ cm ² s ⁻¹	ln (D)	a_{calc} / μm	C_{dl} / $\mu\text{F cm}^{-2}$
292	0.00342	0.159	-1.84	1.47	0.383	5.08	10.6
292	0.00342	0.137	-1.99	1.56	0.445	4.98	12.9
292	0.00342	0.138	-1.98	1.61	0.476	4.90	13.3
308	0.00325	0.178	-1.72	2.43	0.888	4.89	8.21
308	0.00325	0.178	-1.73	2.40	0.874	4.92	7.65
307	0.00325	0.189	-1.67	2.32	0.843	4.97	6.46
326	0.00307	0.228	-1.48	3.26	1.18	5.10	5.78
325	0.00307	0.225	-1.49	3.29	1.19	5.09	5.97
340	0.00294	0.227	-1.48	4.48	1.50	4.90	7.94
340	0.00294	0.231	-1.46	4.51	1.50	4.90	8.03

Table 6.11

Pt (a=5 μm) / tetraglyme, 5 mM LiTCNQ, 5 mM TCNQ, 0.25 M LiClO₄ / Pt gauze

Temp. / K	1/Temp K ⁻¹	k _s cm s ⁻¹	ln (k _s)	D /10 ⁶ cm ² s ⁻¹	ln (D)	a _{calc} / μm	C _{dl} / $\mu\text{F cm}^{-2}$
297	0.00336	0.0568	-2.87	1.79	0.582	4.78	13.1
297	0.00336	0.0537	-2.92	1.76	0.567	4.79	12.4
335	0.00299	0.147	-1.91	3.98	1.38	4.91	10.9
335	0.00298	0.125	-2.08	3.98	1.38	4.86	13.9
336	0.00298	0.134	-2.01	4.02	1.39	4.87	12.3
356	0.00281	0.177	-1.73	5.65	1.73	4.92	10.2
347	0.00288	0.172	-1.76	4.97	1.60	4.91	10.0
347	0.00288	0.161	-1.82	4.93	1.59	4.91	10.0
347	0.00288	0.177	-1.73	4.90	1.59	4.92	10.3
315	0.00317	0.107	-2.23	2.63	0.96	4.89	13.1
315	0.00317	0.093	-2.37	2.56	0.94	4.86	14.4
315	0.00318	0.096	-2.34	2.57	0.94	4.87	14.3

Table 6.12

Pt (a =5 μm) / tetraglyme, 5 mM LiTCNQ, 5 mM TCNQ, 0.5 M LiClO₄ / Pt gauze

Temp. / K	1/Temp K ⁻¹	k _s cm s ⁻¹	ln (k _s)	D /10 ⁶ cm ² s ⁻¹	ln (D)	a _{calc} / μm	C _{dl} / $\mu\text{F cm}^{-2}$
294	0.00340	0.0882	-2.43	1.10	0.094	4.99	12.8
294	0.00340	0.0941	-2.36	1.15	0.143	4.85	15.3
294	0.00340	0.132	-2.02	1.09	0.090	4.99	13.0
313	0.00319	0.145	-1.93	1.88	0.631	5.00	11.7
313	0.00319	0.175	-1.74	1.91	0.645	5.02	11.4
313	0.00319	0.178	-1.72	1.87	0.625	5.03	10.5
330	0.00303	0.264	-1.33	2.77	1.02	5.06	12.3
355	0.00282	0.526	-0.641	4.49	1.50	5.06	12.5
355	0.00282	0.482	-0.729	4.51	1.51	5.04	13.1
350	0.00286	0.396	-0.927	4.17	1.43	5.04	11.4
343	0.00292	0.315	-1.15	3.63	1.29	5.03	13.7
337	0.00297	0.260	-1.34	3.25	1.18	5.02	12.8
321	0.00312	0.158	-1.84	2.34	0.848	5.01	11.0
321	0.00312	0.154	-1.87	2.35	0.855	4.73	13.7

Figure 6.23
 Arrhenius plots showing
 dependence of k_s on background electrolyte concentration.

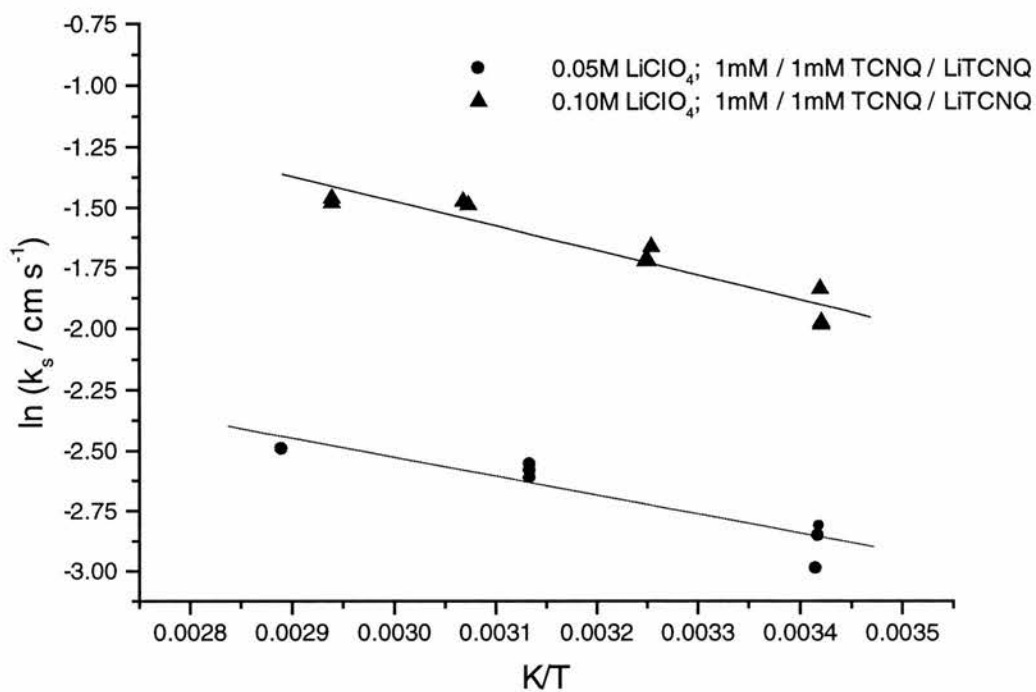


Figure 6.24
 Arrhenius plots showing
 dependence of D on background electrolyte concentration.

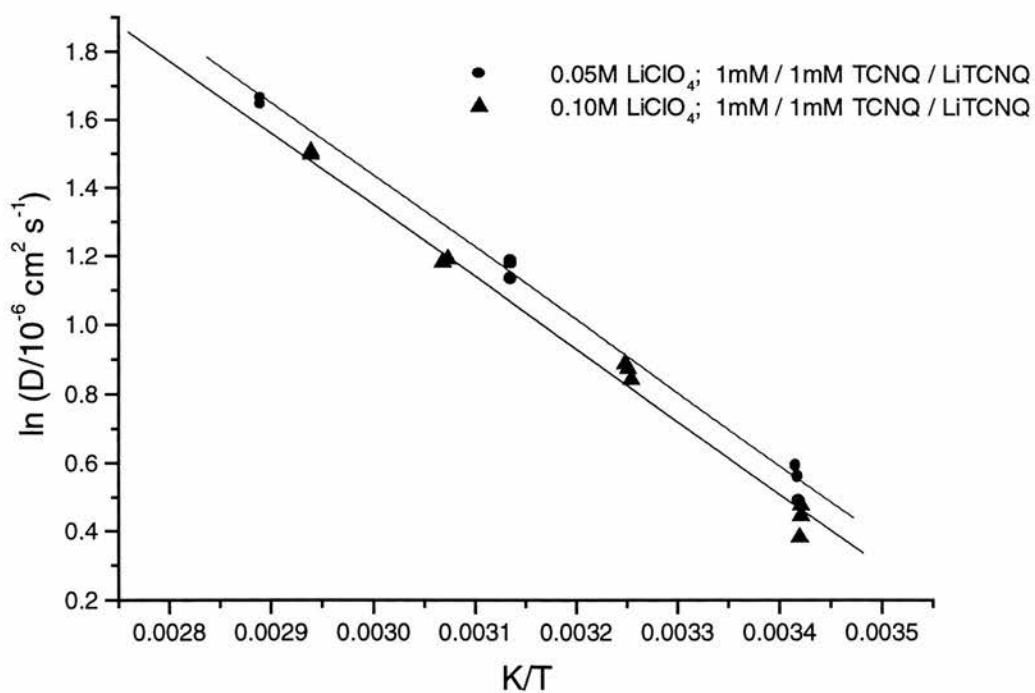


Figure 6.25

Arrhenius plots showing
dependence of k_s on background electrolyte concentration

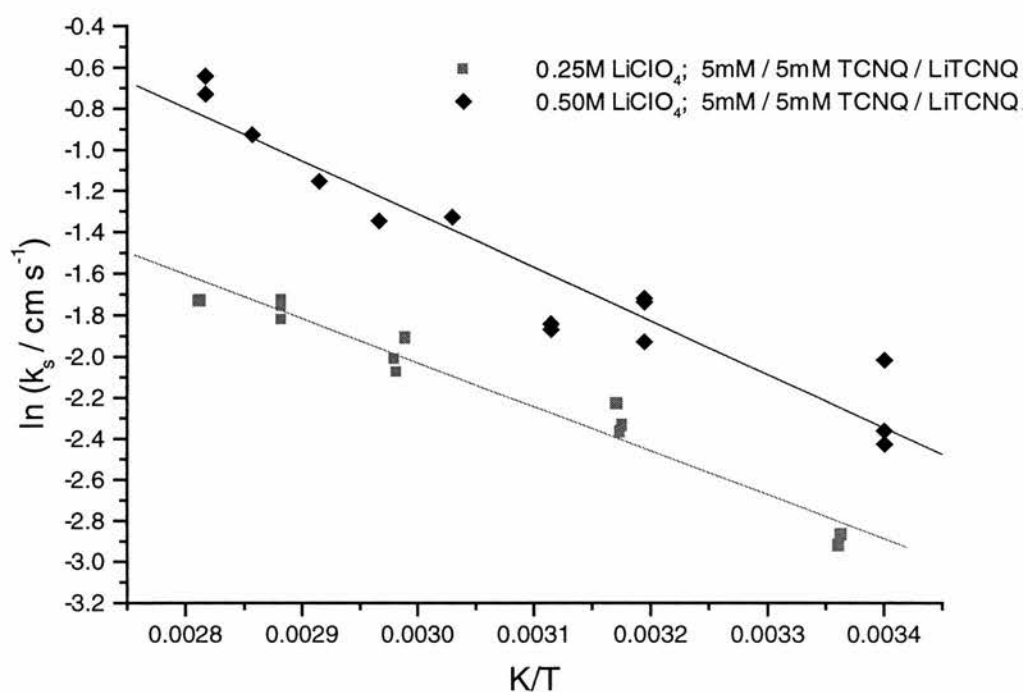
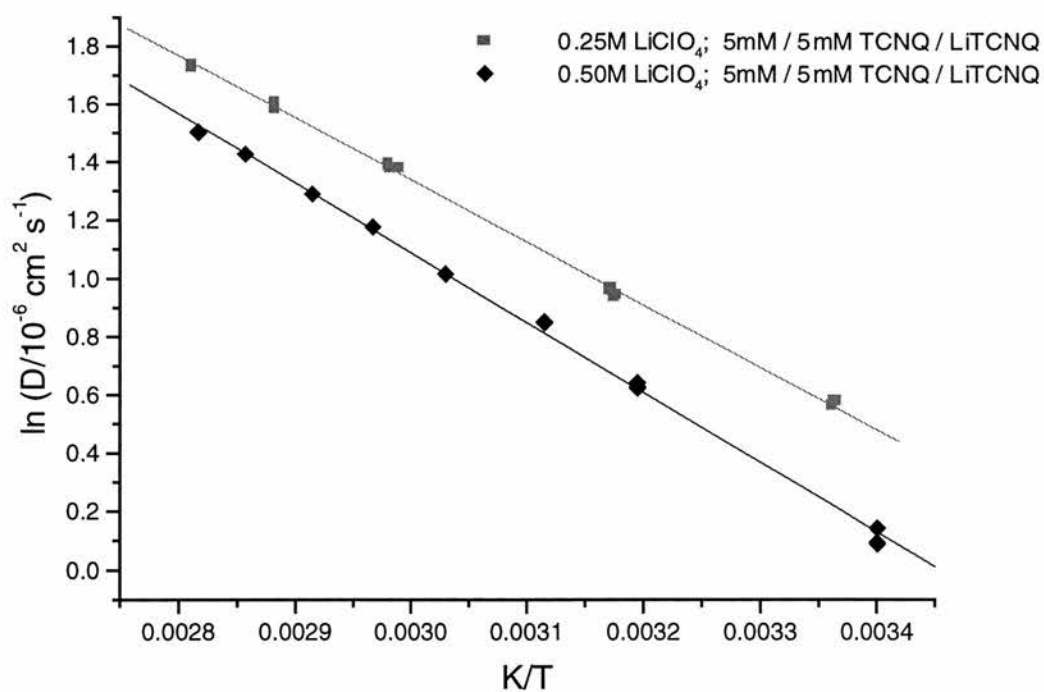


Figure 6.26

Arrhenius plots showing
dependence of D on background electrolyte concentration



Activation energies and pre-exponential factors for electron transfer and diffusion may be obtained from the Arrhenius plots and are shown in Table 6.13.

The activation energies for electron transfer rise with background electrolyte concentration. An increase would be expected from the discussion in Chapter 5 where it was noted that activation energy for electron transfer increases with the solution viscosity and supporting electrolyte concentration. Despite higher activation energies, values of k_s increase when the concentration of supporting electrolyte is increased. This is attributable to *apparent* increases in the pre-exponential factor with supporting electrolyte concentration. Compared with the unpaired ion, paired TCNQ⁻ would therefore appear to have a greatly increased probability of participating in a heterogeneous electron transfer reaction. This is, in fact, the opposite of the effect found when the redox couple concentration is increased, as is shown in Figure 6.15, in which circumstance it was an *apparent* decrease of the pre-exponential factor while activation energy remains constant that lowers k_s . To illustrate whether the redox concentration effect or the electrolyte effect is dominant it is interesting to look at the impedance data from a tetraglyme solution containing initially 0.5 M lithium perchlorate and 10 mM each of TCNQ and LiTCNQ. The solution was diluted several times so that the concentrations of both the redox couple and the background electrolyte decreased in the same proportion. Results of CNLS analysis are shown in Tables 6.14 and 6.15, and this data, combined with data from Tables 6.9 and 6.11 is used to produce Figures 6.27 and 6.28 and hence the activation energies shown in Table 6.16.

Table 6.13

Activation energies of electron transfer and diffusion for
 TCNQ / TCNQ⁻ in tetraglyme with varying background electrolyte and redox salt concentrations.

LiClO ₄ Concentration / M	TCNQ + LiTCNQ Concentration / mM	E _a (Diffusion) / kJ mol ⁻¹	Pre-exponential factor (Diffusion) / cm ² s ⁻¹	E _a (Electron transfer) / kJ mol ⁻¹	Pre-exponential factor (Electron transfer) / cm s ⁻¹
0.05	1 + 1	17.6 ± 0.6	2400 ± 100	6.6 ± 0.5	1.2 ± 3.1
0.10	1 + 1	17.5 ± 0.7	2600 ± 100	8.5 ± 0.5	4.9 ± 1.1
0.25	5 + 5	17.8 ± 0.3	2400 ± 100	17.8 ± 1.6	80 ± 8.0
0.50	5 + 5	19.9 ± 0.5	3900 ± 100	21.5 ± 1.5	630 ± 70

Table 6.14

Pt (a =5 μm) /tetraglyme, 10 mM LiTCNQ, 10 mM TCNQ, 0.5 M LiClO₄ / Pt

gauze

Temp. / K	1/Temp K ⁻¹	k _s cm s ⁻¹	ln (k _s)	D /10 ⁶ cm ² s ⁻¹	ln (D)	a _{calc} / μm	C _{dl} / $\mu\text{F cm}^{-2}$
297	0.00337	0.0597	-2.82	1.81	0.591	4.49	13.7
297	0.00337	0.0650	-2.73	1.76	0.564	4.49	12.2
297	0.00337	0.0532	-2.93	1.73	0.546	4.54	11.2
297	0.00337	0.0588	-2.83	1.71	0.534	4.52	10.4
297	0.00337	0.0591	-2.83	1.71	0.534	4.58	10.9
319	0.00313	0.116	-2.16	2.85	1.05	4.67	11.1
319	0.00314	0.101	-2.29	2.81	1.03	4.69	13.6
318	0.00314	0.101	-2.29	2.81	1.03	4.69	14.6
318	0.00314	0.128	-2.06	2.75	1.01	4.68	10.0
339	0.00295	0.221	-1.51	4.08	1.40	4.76	11.0
354	0.00282	0.262	-1.34	5.20	1.64	4.80	12.3
354	0.00282	0.277	-1.28	5.19	1.64	4.81	13.4
354	0.00282	0.225	-1.49	5.18	1.64	4.80	11.4

Table 6.15

Pt (a =5 μm) / tetraglyme, 2 mM LiTCNQ, 2 mM TCNQ, 0.1 M LiClO₄ / Pt gauze

Temp. / K	1/Temp K ⁻¹	k _s cm s ⁻¹	ln (k _s)	D /10 ⁶ cm ² s ⁻¹	ln (D)	a _{calc} / μm	C _{dl} / $\mu\text{F cm}^{-2}$
297	0.00337	0.0563	-2.88	1.94	0.662	4.87	12.2
297	0.00337	0.0587	-2.84	1.95	0.669	4.86	10.3
316	0.00316	0.0796	-2.53	3.02	1.104	4.96	14.9
316	0.00316	0.0770	-2.56	3.07	1.121	4.96	13.8
335	0.00298	0.0981	-2.32	4.57	1.520	4.93	15.1
335	0.00298	0.0938	-2.37	4.50	1.505	5.00	14.4
356	0.00281	0.1066	-2.24	6.42	1.859	5.03	13.6
356	0.00281	0.1050	-2.25	6.49	1.870	5.04	11.8

Figure 6.27

Arrhenius plots showing

dependence of k_s on redox couple and background electrolyte concentration.

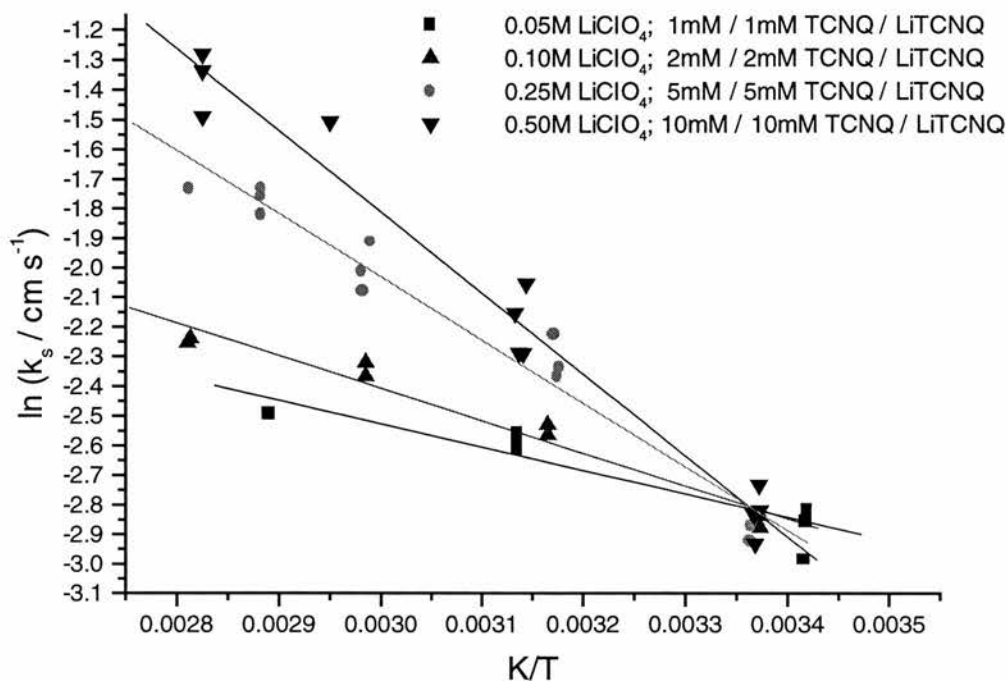


Figure 6.28

Arrhenius plots showing

dependence of D on redox couple and background electrolyte concentration

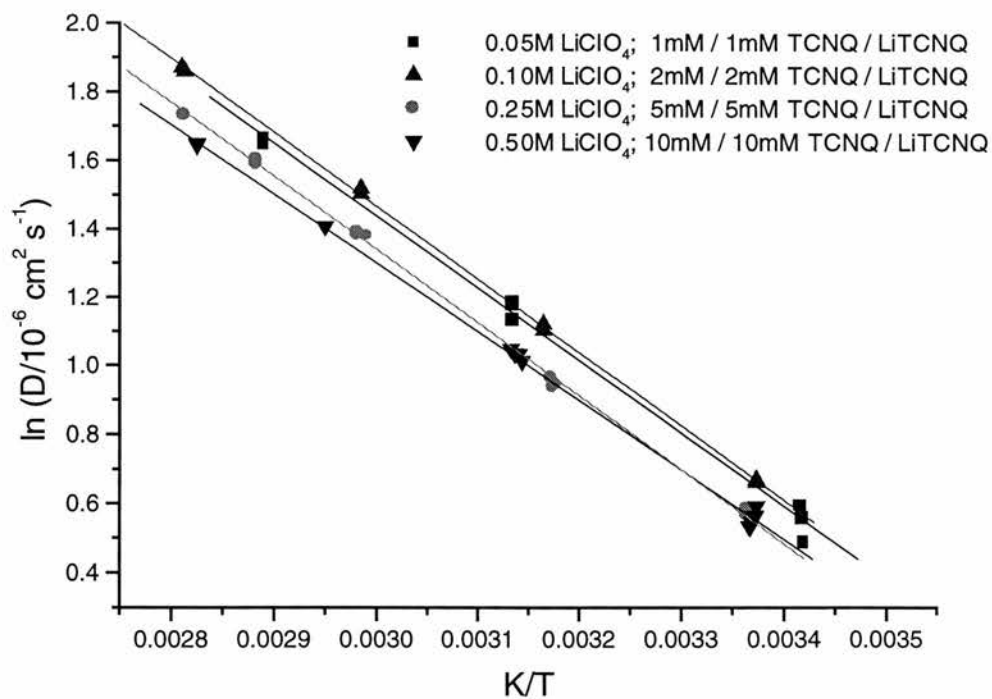


Table 6.16

Activation energies of electron transfer and diffusion for

TCNQ / TCNQ⁻ in tetraglyme with varying background electrolyte and redox salt Concentrations.

LiClO ₄ Concentration / M	TCNQ + LiTCNQ Concentration / mM	E _a (Diffusion) / kJ mol ⁻¹	Pre-exponential factor (Diffusion) / cm ² s ⁻¹	E _a (Electron transfer) / kJ mol ⁻¹	Pre-exponential factor (Electron transfer) / cm s ⁻¹
0.05	1 + 1	17.6 ± 0.6	2400 ± 100	6.6 ± 0.5	1.2 ± 3.1
0.10	2 + 2	17.6 ± 0.2	2700 ± 100	9.1 ± 0.5	2.4 ± 1.3
0.25	5 + 5	17.8 ± 0.3	2400 ± 100	17.8 ± 1.6	80 ± 8.0
0.50	10 + 10	16.7 ± 0.3	1600 ± 100	22.8 ± 2.4	610 ± 40

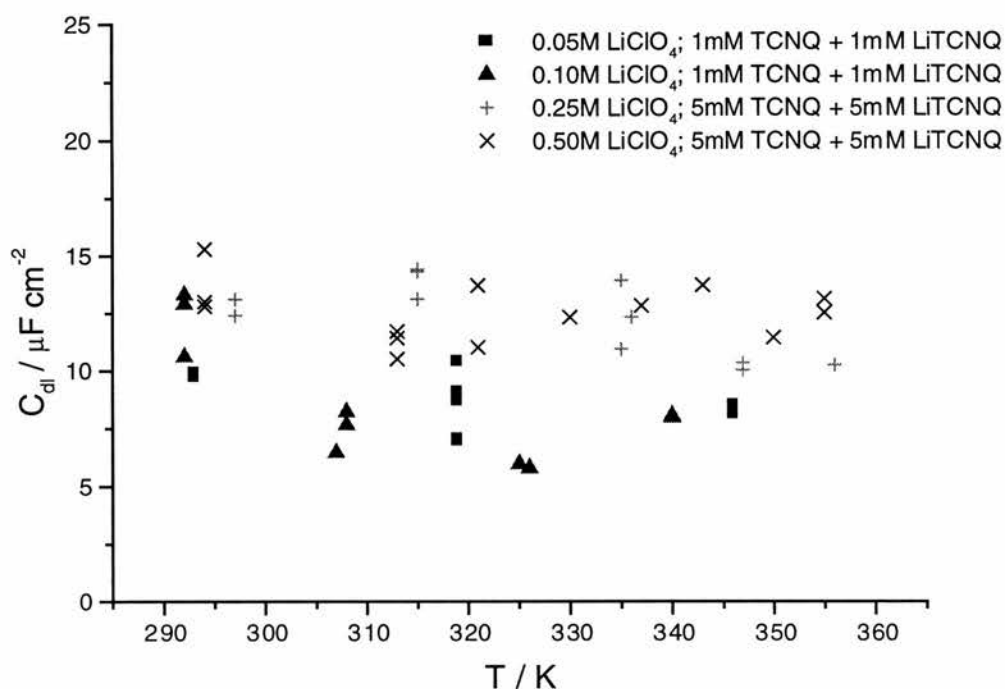
It is clear that at room- and higher temperatures the acceleration of the electron transfer caused by the addition of increasing concentrations of background electrolyte outweighs both the deceleration attributable to greater viscosity and the deceleration attributable to higher concentrations of the redox couple.

These results are not at all like those obtained by Murray and Pyati who found that increasing the concentration of supporting electrolyte (and hence viscosity) resulted in the activation energies for both diffusion and electron transfer to increase ⁽¹⁵⁾. Here Figures 6.26 and 6.28 show that although diffusion is slower when the background electrolyte concentration is increased there is little change in the activation energy for the process. Figures 6.23 and 6.25 illustrate the behaviour of k_s , increasing when more background electrolyte is added.

In order to explain these results, it is appropriate to discuss the electrochemical effects which can result from changing the supporting electrolyte concentration. When the supporting electrolyte concentration is increased the extent of ion association between the lithium cations and the TCNQ⁻ anions should follow suit. The number of ions present in the double layer should also increase slightly, resulting in an increased double layer capacitance. Although the data are a little scattered, an indication that this is indeed the case is seen in Figure 6.29 where data from Tables 6.9 to 6.12 is plotted.

Figure 6.29

Dependence of double layer capacitance on electrolyte concentration



If it were possible for the supporting electrolyte ions in the double layer to catalyse the electron transfer by some means then this might explain the increase in the heterogeneous rate constant as the supporting electrolyte concentration is increased. Catalysis, however, should result in a lowering of the activation energy and this is in fact the opposite of what is observed. Catalysis of electron transfer by ions in the double-layer is, therefore, highly improbable.

It has already been stated that changing the concentration of the supporting electrolyte can change the double layer structure. Mechanisms by which changes in the double layer structure can affect the observed value of k_s include ⁽¹⁶⁾:

1. A change in the electrolyte diameter at the double layer changing the location of the outer Helmholtz plane (OHP). In general, locating the OHP farther from the electrode surface will cause a reduction in the electron transfer rate.

2. A change in the electrolyte concentration in the diffuse layer affecting the proportion of the applied potential dropping over the diffuse layer and thus altering the potential available to drive the electron transfer.

3. Specific adsorption of species can block reaction sites on the metal surface or modify the double layer in such a way that if anions are adsorbed, the potential at the OHP is more negative than it would otherwise be, and if cations are adsorbed, more positive.

In the case of the TCNQ / TCNQ⁻ experiments in tetraglyme, there is no evidence of specific adsorption such as a significant change in double layer capacitance and the only electrolyte involved is lithium perchlorate, hence the electrolyte diameter is constant. Any double layer effects in these experiments will therefore be restricted to the second mechanism above and this can be examined by means of the Frumkin correction which, for a single electron reduction, $O + e \rightleftharpoons R$, states:

$$k_s(\text{measured}) = k_s(\text{true}) \exp\left[\frac{(\alpha - Z_o)F\phi_2}{RT}\right] \quad [6.1]$$

where Z_0 is the charge on the species being reduced, α is the transfer coefficient and ϕ_2 is the potential at the outer Helmholtz plane relative to the bulk solution. By reference to equation [6.1] it is apparent that for reduction of an uncharged reactant (TCNQ) the measured rate constant is expected to *increase* with electrolyte concentration, entirely consistent with the experimental results reported here. Conway has shown how, in keeping with the results reported here, very significant differences in the observed value of k_s can result from the Frumkin effect when the concentration of background electrolyte is varied ⁽¹⁷⁾. To discover whether double layer effects account for all of the relationship between k_s and electrolyte concentration, numerical values of ϕ_2 are required. Unfortunately, whilst ϕ_2 values are commonly available for reactions at mercury electrodes, they are less common for reactions at other electrodes. Thus it is concluded that although double layer effects are qualitatively consistent with observations, quantitative analysis is not possible.

The next logical question is, if a Frumkin type double layer effect is responsible for the increase in apparent electron transfer rates when the supporting electrolyte concentration is increased, why did Pyati and Fawcett not observe a similar effect for $[\text{Co}(\text{bpy})_3]^{2+/3+}$ in glymes when they increased the supporting electrolyte concentration but reduced the average chain length of the glymes, keeping the solutions iso-viscous ⁽¹⁵⁾? In fact Pyati and Murray found that there was no change in k_s under these conditions. The Frumkin correction for Pyati and Murray's experiment would indicate that, as with TCNQ^{0/1-}, the apparent value of k_s should grow larger at higher electrolyte concentrations. One possible answer to this puzzle was put forward by Gennet, Milner and Weaver who, working with ferrocene in a

variety of aprotic solvents were also surprised that double-layer effects were negligible ⁽¹⁸⁾. These authors suggested that this could be explained by the hypothesis that although the ferrocenium ion is positively charged and should be repelled by the positively charged electrode, the preferential approach of the cyclopentadiene rings with a relatively high electron density to the electrode surface could render the simple point-charge model upon which the Frumkin correction is based inappropriate. Such an explanation might also apply to the $[\text{Co}(\text{bpy})_3]^{2+/3+}$ employed by Pyati and Murray. It is likely that a much more pronounced Frumkin effect is observed here for TCNQ where the electrode is negatively charged and TCNQ^- is also negatively charged.

Finally, it is clear that that activation energies and pre-exponential factors for electron transfer as shown in Tables 6.8, 6.13, and 6.16 are distorted by the double-layer effects. Unless corrections can be applied at different concentrations and temperatures the data can have little meaning. The data to enable corrections to be carried out are not available. It is also clear that if this work had been carried out only at 0.1 M concentration of supporting electrolyte, a practice which is not uncommon in kinetic studies, the results for electron transfer activation energies shown in Table 6.8 could have been accepted as legitimate. Hence possibly misleading conclusions about the relationship between the activation energy for electron transfer and the activation energy for diffusion could have been reached.

6.4 Conclusions

Ion association between the TCNQ⁻ radical anion and the lithium cation was established using cyclic voltammetry and conductivity measurements.

The values of the diffusion coefficient from cyclic voltammetry were in good agreement with those from CNLS analysis of impedance data. Calculated values for the microdisc radius were similar to the geometric value and, as expected double layer capacitance values were around $10 \mu\text{F cm}^{-2}$.

Impedance measurements revealed the same dependence of k_s on redox concentration for TCNQ as had been observed for ferrocene. There was, however, no sign of any deposition on the microelectrode in the TCNQ experiments, ruling out a polymerisation mechanism that had previously been proposed to explain the observations. A single explanation was sought for the behaviour in both the TCNQ and ferrocene cells. The explanation may lie in behaviour of some complexity in the double layer with the consequence that the effective concentration of electroactive species is lowered and hence the observed value of k_s is lower than the true value. One highly speculative explanation for this is that there is association of the neutral and charged redox species in the double layer. The determination of the true value of k_s is further complicated by both ion pairing, established by voltammetry and conductivity measurements and by another double layer phenomenon, the Frumkin effect, revealed by impedance measurements of solutions containing varying concentrations of supporting electrolyte. The consequence of each of these effects will be to underestimate the true value of k_s .

These effects, individually, are difficult to quantify. Taken together, they ensure that it is almost impossible to extract a true value for the standard heterogeneous rate constant for the system studied in this chapter and to correlate k_s with D as was carried out for ferrocene in the previous chapter.

As regards ferrocene, it is likely, as stated above, that the main factor determining the observed value of k_s will not be the polymerisation proposed in Chapter 5 but may be the same double-layer association process hypothesised for TCNQ. It is likely that the values of k_s for ferrocene are not subject to the Frumkin double layer effect.

6.5 References

1. D.S. Acker, W.R. Hertler, *J. Am. Chem. Soc.*, (1962), 84, p3370.
2. P.H.H Fisher, C.A. McDowell, *J. Am. Chem. Soc.*, (1963), 85, 2694.
3. M. Sharp, *Electrochim. Acta*, (1976), 21, p973.
4. D.L. Jeanmaire, R.P. Van Duyne, *J. Am. Chem. Soc.*, (1976), 98, p4029.
5. M. Watanabe, T.T. Wooster, R.W. Murray, *J. Phys. Chem.*, (1991), 95, p4563.
6. T.T. Wooster, M. Watanabe, R.W. Murray, *J. Phys. Chem.*, (1992), 96, p5886.
7. G.N. Kamau, J.F. Rusling, *J. Electroanal. Chem.*, (1990), 292, p187.
8. P.W. Atkins, *Physical Chemistry*, Oxford University Press, (1984), p893.
9. J. O'.M. Bockris, A.K.N. Reddy, *Modern Electrochemistry*, Macdonald & Co., London, (1970), 2, p757.
10. M. Nicolas, R. Reich, *J. Phys. Chem.*, (1979), 83, p749.
11. H.W. Nurnberg, G. Wolff, *J. Electroanal. Chem.*, (1969), 21, p99
12. L. Gierst, L. Vandenberghe, E. Nicolas, A. Fraboni, *J. Electrochem. Soc.*, (1966), 113, p1025.
13. J.T. Hupp, *Inorganic Chemistry*, (1990), 29, p5010.
14. L. Christie, Ph.D. Thesis, (1995), School of Chemistry, University of St. Andrews.
15. R. Pyati, R.W. Murray, *J. Am. Chem. Soc.*, (1996), 118, p1743.
16. A.J. Bard, L.R. Faulkner, *Electrochemical Methods Fundamentals and Applications*, (1980), John Wiley and Sons Inc., p541.
17. B.E. Conway, *Theory and Principles of Electrode Processes*, (1965), Ronald, New York., p94.
18. T. Gennett, D.F. Milner, M.J. Weaver, *J. Phys. Chem.*, (1985), 89, p2787.

CHAPTER 7

A MICROELECTRODE IMPEDANCE STUDY OF THE HETEROGENEOUS KINETICS OF FERROCENE AND FERROCENE CARBOXYLIC ACID IN NEAR SOLID PEO

Introduction

In Chapter 5 a study was made of the electrochemistry of the ferrocene/ferrocenium couple in tetraglyme. A wide variation in the solvent dynamics, without varying other factors, is made possible by employing a liquid and a solid of the same chemical structure. It would be very interesting, therefore, to replace the liquid tetraglyme solvent employed in Chapter 5 with solid poly(ethylene oxide). Both of these solvents have structure $\text{CH}_3\text{-O-(CH}_2\text{CH}_2\text{O)}_n\text{CH}_3$. In the solid, movement of the solvent dipoles, rotation in particular, is very restricted compared to the liquid. Vibration within the ferrocene molecule is not expected to be altered as significantly in moving from the liquid to the solid environment. If the decrease in the value of k_s is similar to the decrease in D in moving from liquid to solid this will tend to confirm the strong influence of the solvent on the electron transfer and hence be evidence for outer sphere solvent dynamic control of the rate of electron

transfer in both phases. On the contrary, if there is strong inner sphere control of the reaction then k_s values should vary little between the phases.

Ferrocene or ferrocene carboxylic acid were introduced with lithium perchlorate supporting electrolyte into PEO of $\overline{M}_n = 100,000$ using the solvent casting method described in Chapter 2. All films were made with a ratio of lithium to polymer oxygen of 1:10, i.e. Li:O = 1:10. This corresponds to a lithium peroxide concentration of approximately 2.5 M. The resulting films were transferred into electrochemical cells and impedance measurements made with platinum microelectrodes in a two-electrode cell with a 1 cm² lithium counter electrode as described in Section 2.4.

7.1 Impedance Measurements

7.1.1 Effect of Potential on Impedance.

Typical complex plane plots showing the effect of potential on the impedance spectrum of ferrocene in *tetraglyme* were presented in Figure 5.12. It is clear from this graph that both the high frequency semi-circle and lower frequency data are strongly dependent on the applied potential. This is exactly what would be expected of a heterogeneous charge transfer process. In solid PEO, however, although the lower frequency data are strongly potential dependent, the high frequency semi-circle is not. This is illustrated in Figures 7.1 and 7.2 where the temperature was held constant at 60 °C. It is concluded that the high frequency

semi-circle in Figure 7.2 is not a part of the charge transfer process and is caused by an unrelated mechanism.

Manual analysis of the semi-circle can be carried out via the $\omega RC = 1$ relation. In Figure 7.2 the diameter of the semi-circle is approximately $1.5 \text{ M}\Omega$ and the frequency at which the semi-circle reaches its maximum height is $68,000 \text{ Hz}$. Thus,

$$C = \frac{1}{2\pi \times 68,000 \times 1.5 \times 10^6} \text{ Farads}$$

yielding a capacitance of 1.6 pF . If the capacitance and associated resistance result from phenomena related to the electrode surface, it is useful to reformulate them in terms of surface area. This results in a capacitance of $0.5 \mu\text{F cm}^{-2}$ and resistance of $5 \Omega \text{ cm}^2$.

Figure 7.1

Effect of applied potential

Pt ($a = 10 \mu\text{m}$) / ferrocene carboxylic acid, LiClO_4 , PEO100,000 / $\text{Li}_{(s)}$: $T = 60^\circ\text{C}$

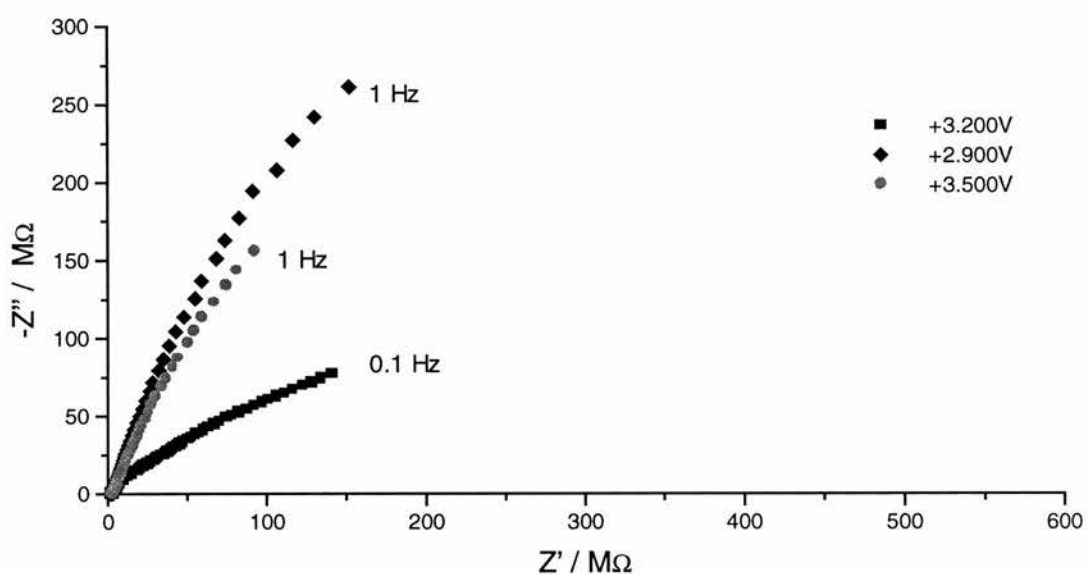
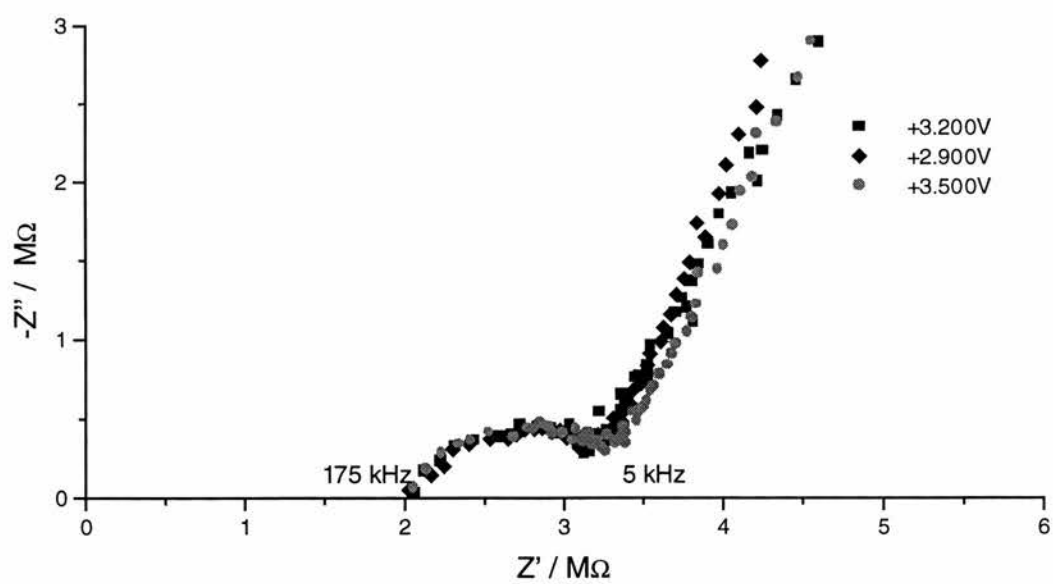


Figure 7.2

Effect of applied potential - High frequency region

Pt ($a = 10 \mu\text{m}$) / ferrocene carboxylic acid, LiClO_4 , PEO100,000 / $\text{Li}_{(s)}$: $T = 60^\circ\text{C}$



7.1.2 *Effect of Time on Impedance*

The first observation regarding impedances in the solid polymer is that they are clearly much higher than impedances measured in tetraglyme. This is indicative of slower processes in the solid. Impedance plots of ferrocene in tetraglyme had proved to be relatively stable with time - although slight increases of impedance were noted for higher ferrocene concentrations as illustrated for 22 mM ferrocene in Figure 5.46. A much more obvious dependence of impedance on time was found in solid PEO. Figures 7.3 and 7.4 show how the impedance changes fairly quickly with time for 12 mM ferrocene carboxylic acid in PEO100,000 at 60 °C. Note how the high frequency semi-circle, in addition to being independent of potential is also independent of time at 60 °C. The increase in impedance at lower frequencies appears to be characterised by the data forming an increasingly steeply angled line with respect to the real axis. The effect of surface adsorption on the shapes of impedance plots was discussed by Los and Laviron who showed, from theoretical considerations, that the phase angle of lower frequency data should be expected to increase with adsorption ⁽¹⁾. They noted Smith's explanation of the physical meaning of increasing phase angles in terms of dissipation ⁽²⁾. Thus in a heterogeneous process, energy is dissipated by the diffusion process. In a heterogeneous process involving adsorbed molecules, however, there can be no diffusion since the participating molecules are confined to the electrode surface. In a system with adsorbing redox molecules, as the dissipation owing to diffusion becomes relatively less important, the reactance becomes relatively more important and the phase angle increases. Thus the impedance plots in Figure 7.3 may indicate adsorption of ferrocene onto the microelectrode surface.

As noted in Chapter 5 there is evidence for ferrocene forming passivating layers on the microelectrode in a variety of solvents including tetraglyme. The impedance plots are found to change with time as a result of film formation. The changes noted in Chapter 5 are not, however, consistent with adsorption. There is in fact no change in the phase angle of the lower frequency data in liquid solvents such as tetraglyme and other aprotic solvents. The only change is that the charge transfer resistance increases, as demonstrated most clearly by Mahlendorf and Heinze ⁽³⁾. Why, one must ask, does ferrocene adsorb onto a platinum electrode in PEO/LiClO₄ but not in tetraglyme/LiClO₄ or other solvents such as acetonitrile? The key to answering the question probably lies in the fact that adsorption occurs in the high molecular weight, long-chain, *solid*, polymer system while passivation occurs in the *liquid* systems.

In a liquid system the solvent molecules enjoy greater freedom of movement and, as shown in Figure 3.1, the solvent will generally surround the metal electrode. Molecules of the redox couple are also surrounded by their own solvent layer and generally do not come into direct contact with the metal. In the polymer electrolyte, however, if one considers a polymer chain to be one solvent molecule, part of this molecule can be in contact with the metal electrode while in close proximity another part solvates a redox molecule. It is conceivable that thermal, segmental motions of the polymer chain can readily move a portion of the chain containing a redox molecule onto the electrode surface such that the redox molecule comes into direct contact with the metal and becomes adsorbed. Once adsorbed, charge transfer takes place in the absence of diffusion. With time more redox molecules come into contact with the metal and become adsorbed. Diffusion

becomes increasingly unimportant as a charge transport mechanism and impedance plots at lower frequencies become increasingly vertical.

Figure 7.3

Effect of time at 60 °C

Pt (a = 10 μm) / 12 mM ferrocene carboxylic acid, LiClO₄, PEO100,000 / Li(s) :

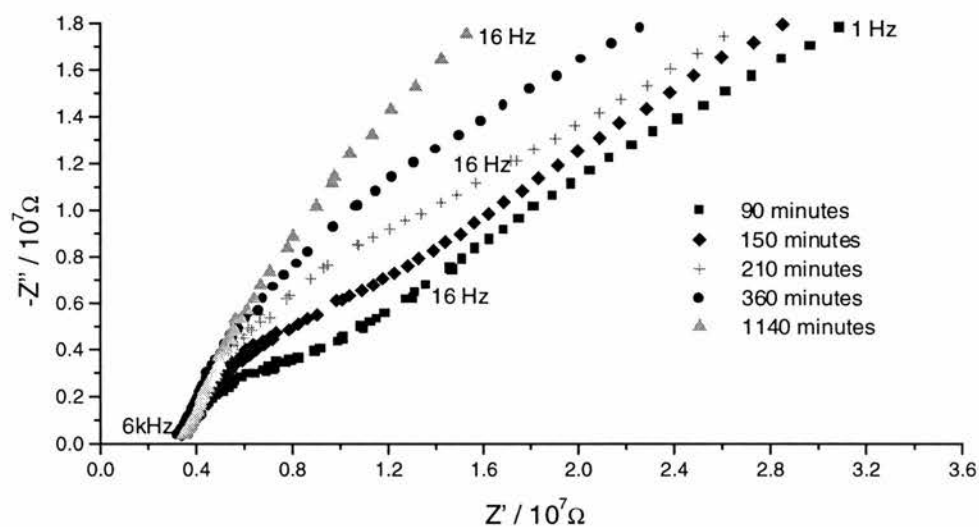
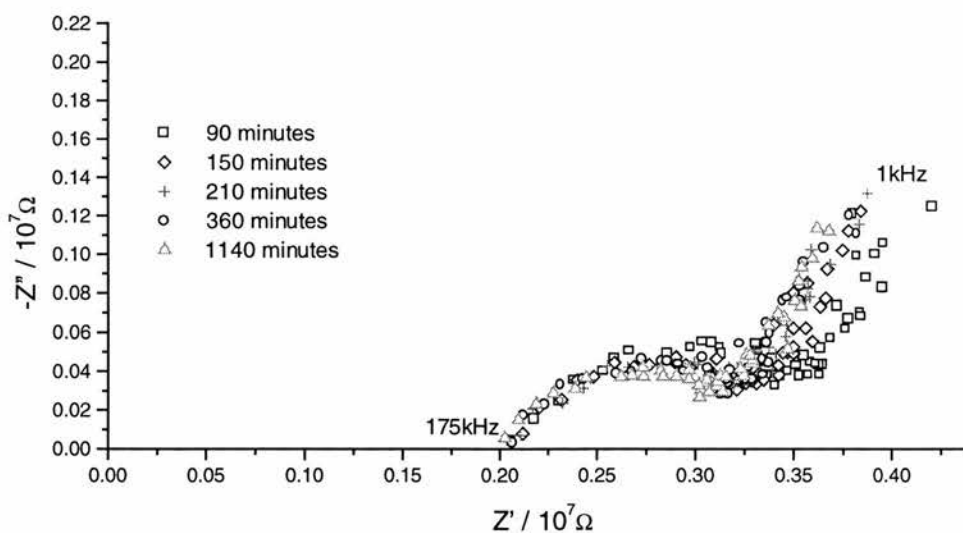


Figure 7.4

Effect of time at 60 °C - High frequency region

Pt (a = 10 μm) / 12 mM ferrocene carboxylic acid, LiClO₄, PEO100,000 / Li(s) :



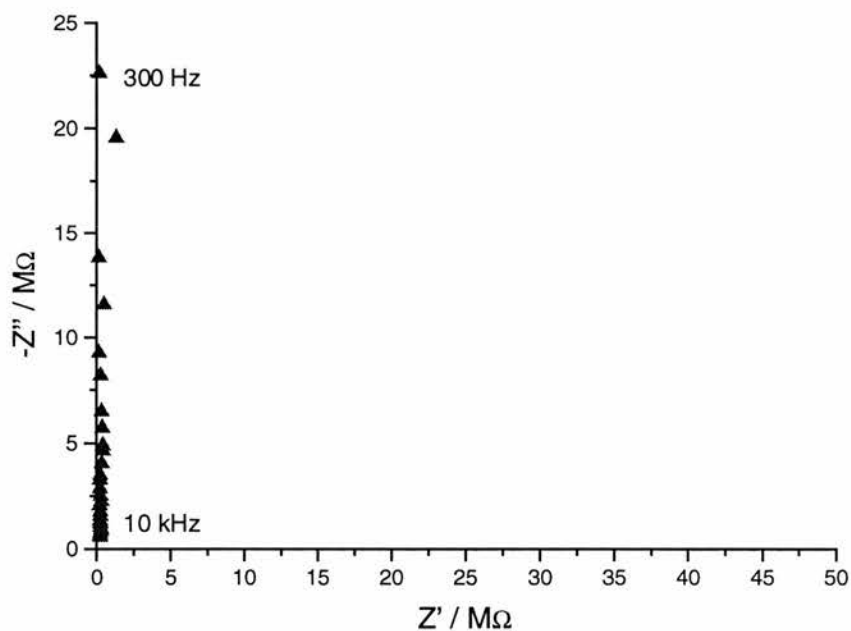
7.1.3 Effect of Temperature on Impedance

The melting point of pure PEO100,00 is 65 °C which can be lowered somewhat by the presence of LiClO₄ ⁽⁴⁾. The phase diagram for LiClO₄ in PEO in reference 4 indicates that the melting temperature for the Li:O = 1:10 electrolyte should be about 60 °C. This was borne out by experience in trying to obtain impedance data whereby it was found that impedance data at temperatures lower than 60 °C were purely capacitances, as shown in Figure 7.5, for example.

Figure 7.5

Pt (a = 10 μm) / 12 mM ferrocene, LiClO₄, PEO100,000 / Li_(s) :

Temperature = 55 °C



Clearly, below the melting temperature, there is no electrochemical contact between the microelectrode and polymer electrolyte. In order to obtain an impedance spectrum it was found that the cell had to equilibrate at a minimum temperature of somewhere in the region of 58 to 60 °C. The fact that this temperature coincides

with the melting temperature from the phase diagram is obviously not a coincidence. The objective of measuring the kinetics of ferrocene in a truly solid polymer had therefore been defeated because unless the polymer was heated to the point at which it just began to melt it would not wet the electrode. Nevertheless, the polymer, although liquid at its melting temperature is an extremely viscous liquid in which the motion of the dipoles is still very restricted compared to the freely flowing liquid tetraglyme. A comparison of the kinetics is still, therefore, of interest for the reasons outlined in the introduction to this chapter.

When the temperature is increased further, as would be expected, the impedance decreases. This can be seen in Figure 7.6 but is more clearly seen in the spectroscopic plot in Figure 7.8. Interestingly the high frequency semi-circle disappears when the temperature is increased and does not reappear when the cell is cooled. This is shown in Figure 7.7. Such behaviour might suggest that a volatile impurity, such as the acetonitrile solvent, is removed permanently when the temperature is raised. This seems unlikely, however, in light of the procedures, described in Chapter 2 including several days treatment under dynamic vacuum, used to remove the solvent prior to the film being placed in the cell. It would seem unusual that a volatile impurity could resist the deliberate attempts to remove it and then quickly evaporate in the experimental cell. A further argument against the idea of residual solvent in the films is that when the polymer is heated and then cooled, its impedance is lower than prior to heating. The removal of residual solvent, if there were any, would be expected to have the opposite effect.

An alternative explanation of the high frequency semi-circle is that even at 60 °C the polymer electrolyte might still not be in full contact with the microelectrode and that raising the temperature allows it to flow sufficiently to completely wet the metal surface of the electrode. A weakness in this explanation is that in the next chapter a very similar, potential independent, high frequency semi-circle will be shown also to have occurred in studies of buckminsterfullerene in dichloromethane, benzonitrile and 1,2 dichlorobenzene where wetting should not be a problem.

It is possible that the semi-circle may have resulted from some sort of high frequency artefact in the impedance data. An argument against this proposal, however, is that in solid PEO the semi-circle is removed by heating and cooling. The cooled polymer electrolyte has a solution resistance similar to the starting material but its impedance plot does not contain the high frequency semi-circle.

The capacitance of the potential independent semi-circle was noted in the previous section as $0.5 \mu\text{F cm}^{-2}$. Such a figure is much lower than the capacitance of the double layer. It is, however, possible for oxide layers on the electrode surface to generate potential independent capacitances smaller, often by orders of magnitude, than a normal double layer capacitance ⁽⁵⁾. An oxide layer may, therefore be the best explanation for the potential independent feature reported in this and the following chapter but it is not clear why the oxide layer would appear in all spectra in solid PEO and disappear after heating.

None of the above explanations would appear to completely account for the high frequency semi-circle. The fact that it is potential independent and therefore

unconnected with the charge transfer process means that it may be excluded from analysis for charge transfer information. It will be established in Chapter 8 that, provided the value of k_s is not too high, accurate values of electrochemical parameters including k_s can be generated by analysis of only lower frequency data. Given that this is true and that the main purpose of the experiments is to investigate the charge transfer process, the explanation of the potential independent high frequency semi-circle shall be pursued no further.

Figure 7.6

Effect of temperature

Pt ($a = 10 \mu\text{m}$) / 12 mM ferrocene carboxylic acid, LiClO_4 , PEO100,000 / $\text{Li}_{(s)}$:

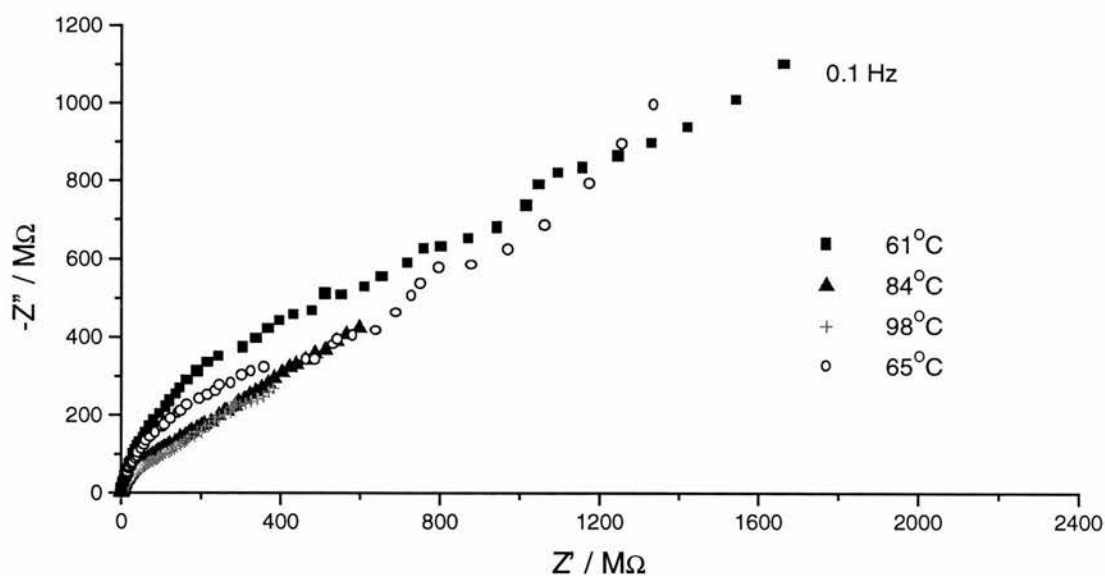


Figure 7.7

Effect of temperature - High frequency region

Pt (a = 10 μm) / 12 mM ferrocene carboxylic acid, LiClO₄, PEO100,000 / Li_(s) :

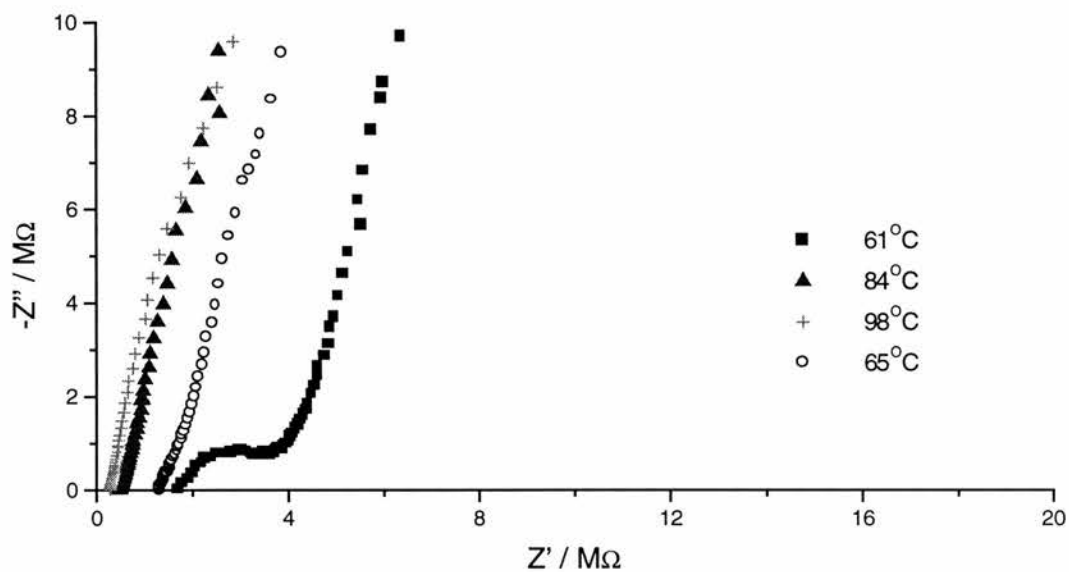
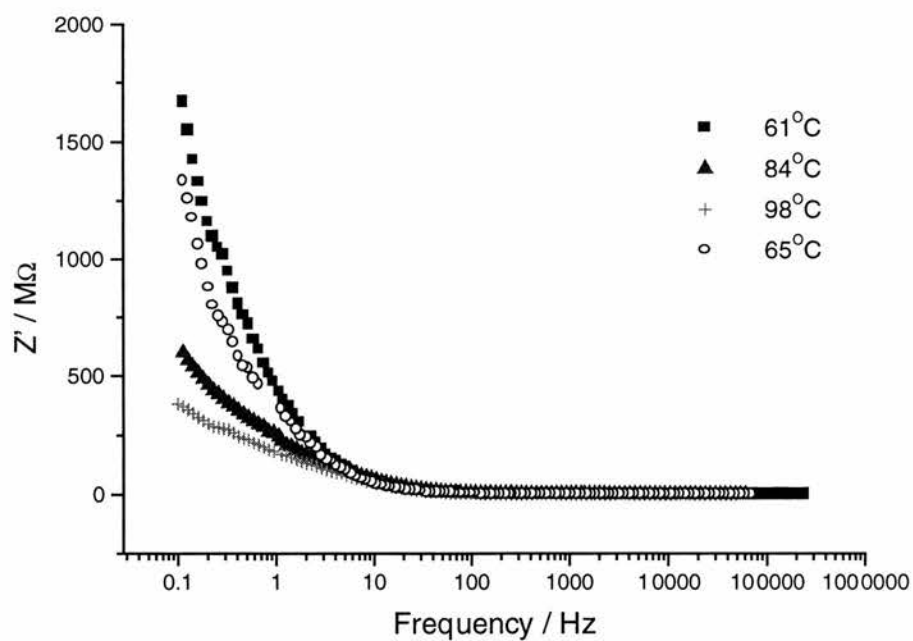


Figure 7.8

Spectroscopic plot of effect of temperature on real impedance

Pt (a = 10 μm) / 12 mM ferrocene carboxylic acid, LiClO₄, PEO100,000 / Li_(s) :



7.1.4 CNLS Fitting of Impedance Data

Of the two existing CNLS fitting models, i.e. the E and EC models, neither yielded wholly satisfactory fits to the experimental data. This was particularly true for impedance data obtained after longer contact between electrolyte and microelectrode. The deviation of data from E or EC behaviour increased with time. This deviation is related to the increasing phase angle caused, it was proposed in Section 7.1.2, by adsorption. Although adsorption, in itself, is an interesting phenomenon, it is not the principle focus of these experiments and it was decided to attempt to obtain data from electrolytes after minimum contact time with the microdiscs, say within an hour or two. This approach, it was hoped, would allow extraction of the electrochemical parameter values in near-solid PEO for legitimate comparison with those already obtained in tetraglyme. The E model was chosen in preference to the EC model because it tended to yield better fits.

Adsorption onto the microelectrode also made it impractical to carry out a quantitative study of the effect of temperature. This was because of the long contact times required in temperature studies for the heating, temperature equilibration and measurement steps.

Figures 7.9 and 7.10 show, respectively, the E mechanism fit for the complete frequency sweep and the magnified high frequency region for ferrocene carboxylic acid in PEO.

Figure 7.9

Pt ($a = 10 \mu\text{m}$) / 12 mM ferrocene carboxylic acid, LiClO_4 , PEO100,000 / Li(s) :
Time = 90 minutes, Temperature = 60°C

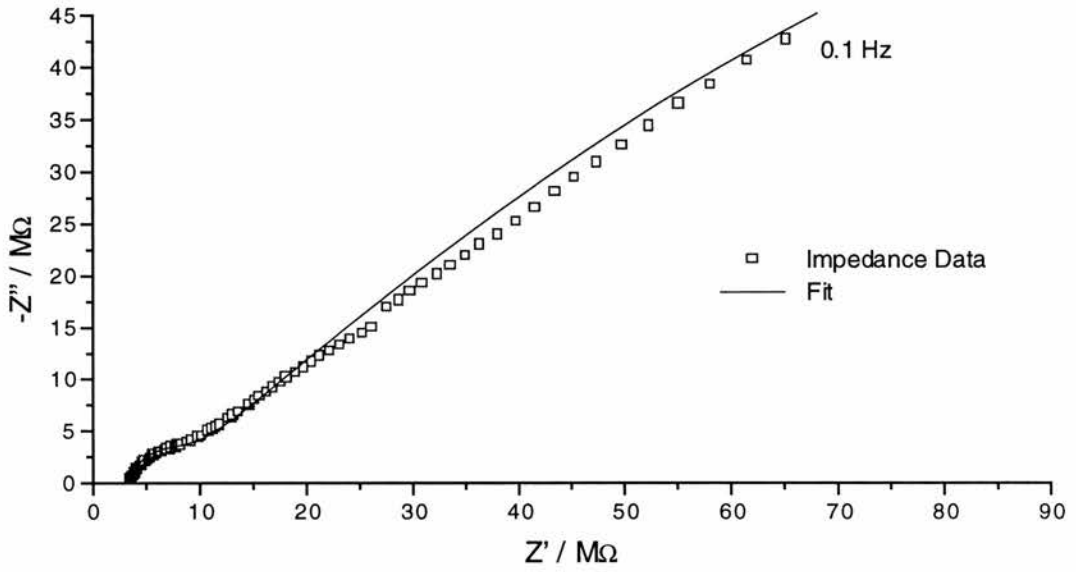
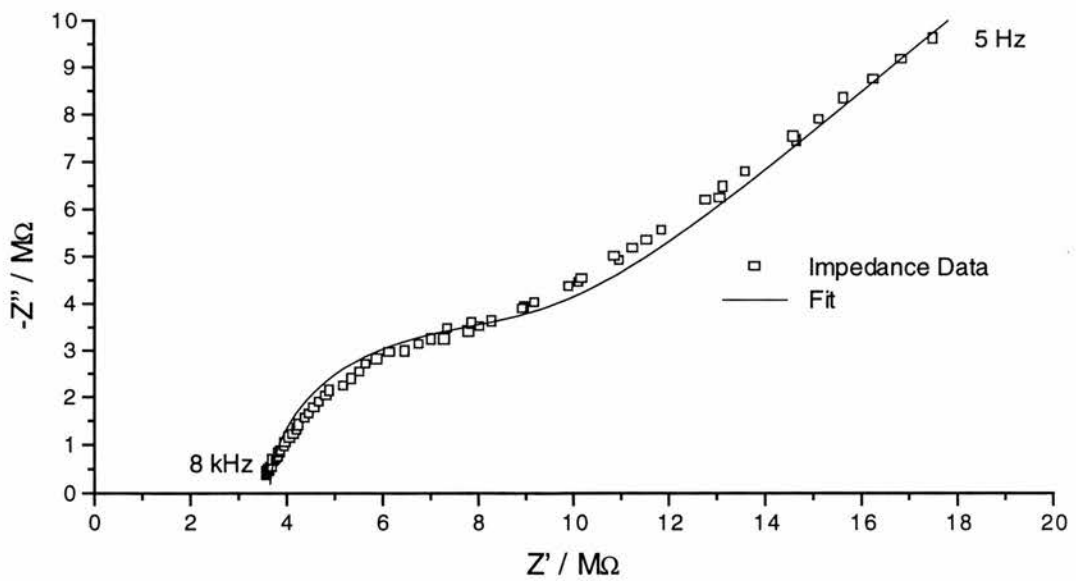


Figure 7.10

Higher frequency region magnified

Pt ($a = 10 \mu\text{m}$) / 12 mM ferrocene carboxylic acid, LiClO_4 , PEO100,000 / Li(s) :
Time = 90 minutes, Temperature = 60°C



This fit is in fact the best fit of model to data obtained for any of the data gathered in PEO and was obtained after 90 minutes contact between microdisc and PEO. After 360 minutes, however, Figures 7.11 and 7.12 show that there has been a marked deterioration in the fit.

Having devised a strategy to obtain kinetic data with minimum interference from time-dependent changes, it remained to be established that reproducible results could be obtained from two polymer films made identically. Figure 7.13 shows typical impedance plots from identically produced films. Clearly, different impedance plots were obtained from the "identical films". This may have been caused by microscopic inhomogeneities in the films or differences in the surface conditions on the microelectrodes.

From those plots which lent themselves to satisfactory analysis, by taking averages obtained from about four or five experiments on "identical" films, the results shown in Table 7.1 were obtained. The reader must be cautioned that these numbers should be regarded as accurate only to within about $\pm 40\%$.

Figure 7.11

Pt ($a = 10 \mu\text{m}$) / 12 mM ferrocene carboxylic acid, LiClO_4 , PEO100,000 / $\text{Li}_{(s)}$:
Time = 360 minutes, Temperature = 60°C

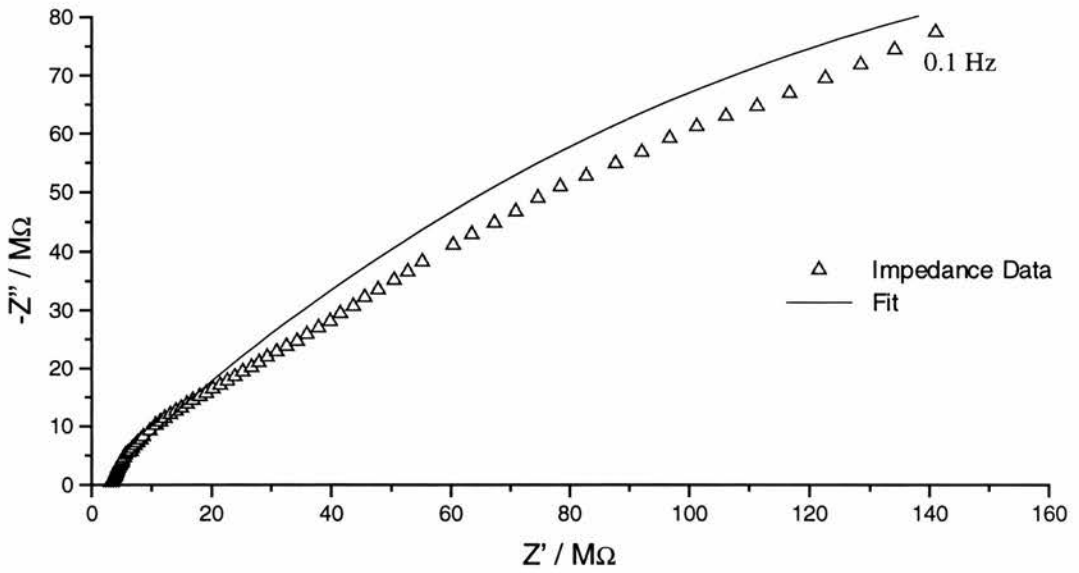


Figure 7.12

Higher Frequency Region Magnified

Pt ($a = 10 \mu\text{m}$) / 12 mM ferrocene carboxylic acid, LiClO_4 , PEO100,000 / $\text{Li}_{(s)}$:
Time = 90 minutes, Temperature = 60°C

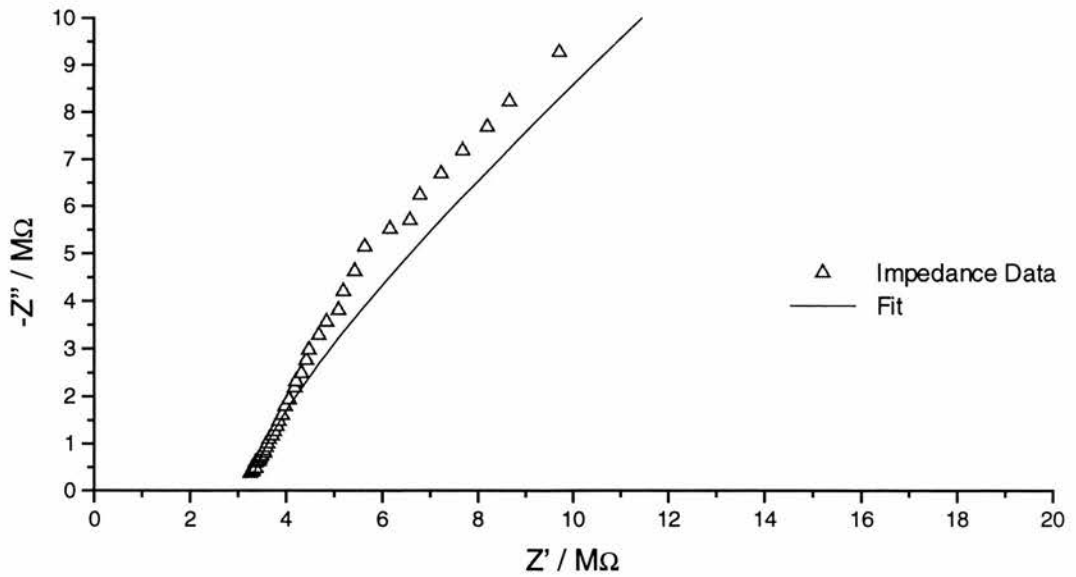


Figure 7.13

Pt (a = 5 μm) / 12 mM ferrocene, LiClO_4 , PEO100,000 / $\text{Li}_{(s)}$:

Temperature = 60 $^{\circ}\text{C}$

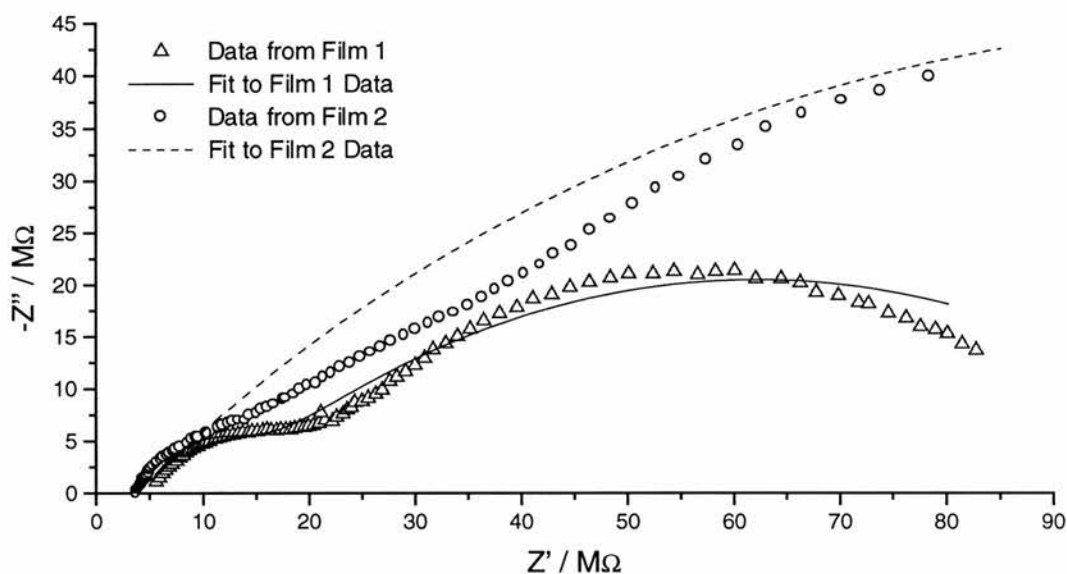


Table 7.1

Averaged results from CNLS analysis of
impedance data from polymer electrolytes at 60 $^{\circ}\text{C}$.

Redox Molecule	Concentration / mM	C_{dl} / $\mu\text{F cm}^{-2}$	D / $10^6 \text{ cm}^2 \text{ s}^{-1}$	k_s / cm s^{-1}
Ferrocene	12	60	0.3	0.01
Ferrocene	12	30	0.08	0.002
Carboxylic Acid				

The results in Table 7.1 indicate that ferrocene diffuses through the polymer electrolyte an order of magnitude more slowly than it does through tetraglyme. This order of magnitude ratio also applies to the relative rates of electron transfer, consistent with outer sphere solvent dynamic control of the electrode kinetics. It is likely, therefore, that the difference in electron transfer rates between ferrocene in liquid tetraglyme and in the near-solid polymer electrolyte is determined mainly by outer sphere effects. The slow kinetics of ferrocene carboxylic acid relative to ferrocene in PEO may be related to the diffusion being slowed by extra interactions of the carboxylic acid group with the polymer electrolyte while the electron transfer is slowed owing to increased internal reorganisation energy.

7.2 Conclusions

Complex plane impedance plots of polymer films containing ferrocene or ferrocene carboxylic acid all contained a potential independent, high frequency semi-circle. Data points comprising this feature were excluded from CNLS impedance analysis.

Unlike in the free flowing liquid phase, in near-solid PEO the redox couple appears to have been adsorbed onto the electrode surface. The difference, it is proposed, relates to the fact that segmental motion of the polymer chain in the near-solid polymer can bring the redox species into direct contact with the electrode whereas in the liquid this is prevented by the electrode's own solvation layer.

Pyati and Murray have correlated k_s with D for $[\text{Co}(\text{byp})_3]^{2+/3+}$ in liquids over a wide range of viscosities and concluded that the strong linear relationship indicates solvent dynamic control of the kinetics ⁽⁶⁾. The data presented here for ferrocene in near-solid PEO and (in Chapter 5) for ferrocene in tetraglyme are consistent with the hypothesis that this correlation can be extended from the liquid into the near-solid.

7.3 References

1. P. Los and E. Laviron, *J. Electroanal. Chem.* (1997), 432, p85.
2. D.E. Smith, in A.J. Bard (Ed.), *Electroanalytical Chemistry*, Vol. 1, Marcel Dekker, New York, (1970), p1.
3. F. Mahlendorf and J. Heinze, *J. Electroanal. Chem.*, (1993), 352, p119.
4. F.M Gray, *Solid Polymer Electrolytes; Fundamentals and Technological Applications*, (1991), VCH Publishers Inc., Cambridge, p76.
4. R. D. Armstrong, M. Todd, in P.G. Bruce (Ed.), *Solid State Electrochemistry*, Cambridge University Press, Cambridge, (1995), p264.
5. R. Pyati and R.W. Murray, *J. Am. Chem. Soc.*, (1996), 118, p1743.

CHAPTER 8

A MICROELECTRODE IMPEDANCE STUDY OF THE HETEROGENEOUS KINETICS OF BUCKMINSTERFULLERENE IN APROTIC ORGANIC SOLVENTS

Introduction

There has been considerable interest in the electrochemistry of buckminsterfullerene (C_{60}) and it has been shown that up to six separate electron transfer steps can be identified as it is successively reduced ^{(1), (2)}. The C_{60} molecule is of particular interest because its large size and spherical shape indicate that there should be strong outer-sphere solvent dynamic control of the electron transfer process.

Unfortunately, solubility considerations have limited the selection of suitable solvents to those with rather low polarity, such as 1,2-dichlorobenzene, dichloromethane or benzonitrile, and this has resulted in the electrochemical process being complicated by ion-association ^{(3), (4)}.

To date the electrochemistry of C_{60} has not been investigated by microelectrode impedance spectroscopy. Given that ion-association has been identified as a feature of C_{60} 's electrochemistry in the aforementioned solvents, there is a possibility that it may be rather similar to that of TCNQ, investigated in Chapter 6. This is because both C_{60} and TCNQ are neutral molecules which can undergo a one-electron reduction following which the resulting radical anion appears to undergo a homogeneous reaction with the supporting electrolyte. Equations were derived in Chapter 3 intended to permit analysis of microelectrode impedance data for the EC reaction. Unfortunately, it was found that the equations could not be applied with any degree of success to the TCNQ reaction. Studying the C_{60} reaction offered a further opportunity to test the equations. Finally, and somewhat surprisingly, given that its anions are known to form ion-pairs, it would appear that the dependence of the kinetics of C_{60} electron transfer have not been investigated as a function of supporting electrolyte concentration. One consequence of this is that theoretical predictions that the combined effect of using a supporting electrolyte consisting of large cations (TBA^+) combined with the large size of the C_{60} anion will cause the Frumkin effect to be negligible have not yet been tested ⁽⁵⁾. It was intended therefore to obtain data to test this prediction.

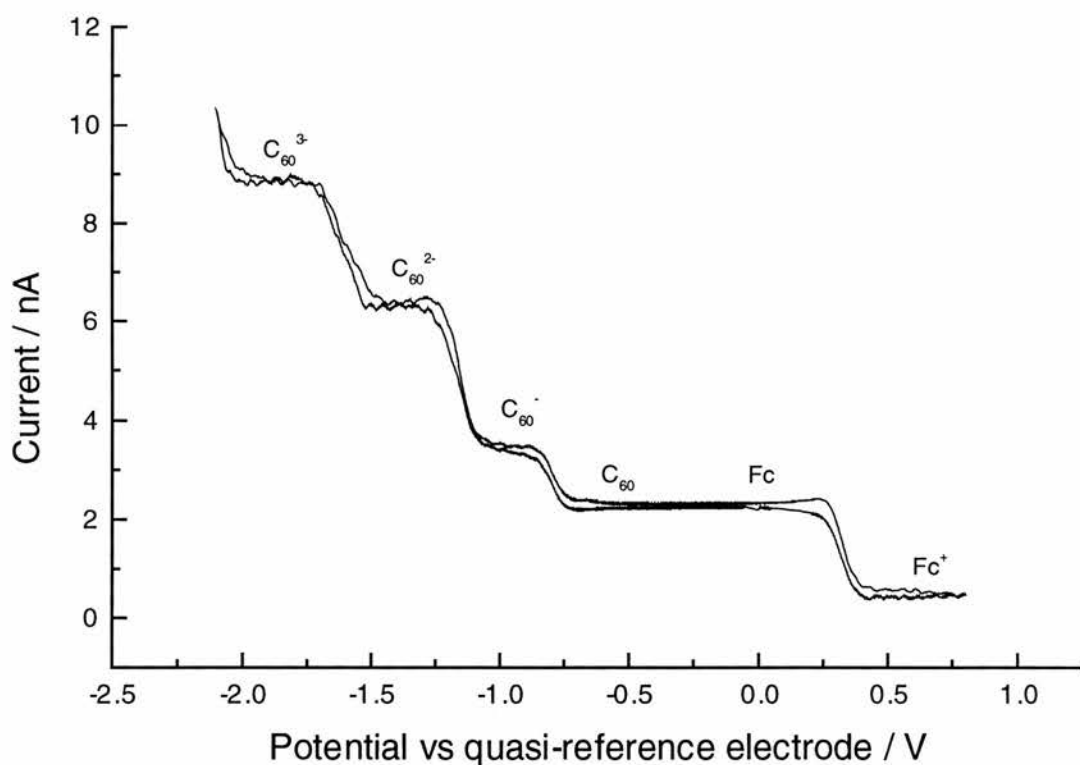
8.1 Cyclic Voltammetry

Cyclic voltammetry of C_{60} was carried out using the equipment described in Chapter 2 in benzonitrile, dichloromethane and 1,2 dichlorobenzene with TBAP and TBABF₄ as background electrolytes using two-electrode cells in which both electrodes were platinum. Lithium perchlorate was employed as the background electrolyte only in benzonitrile because it was insoluble in the other liquids. Attempts were also made to obtain cyclic voltammograms in acetonitrile and in ethylene oxide oligomers including tetraglyme but C_{60} was insufficiently soluble in these media to obtain satisfactory results. A typical voltammogram showing four successive reduction waves for C_{60} is shown in Figure 8.1.

Figure 8.1

Cyclic voltammogram of:

Pt (a = 10 μm) / CH₂Cl₂, 0.19 mM C_{60} , Fc, 0.0048 M TBAP / Pt gauze



As can be seen in Figure 8.1 ferrocene was also added to the solutions, as an internal voltammetric standard, following the example of Fawcett et al. ⁽³⁾. Given the results in Chapter 5 where the half-wave potential for ferrocene oxidation shifted consistently with changing background electrolyte concentration owing probably to ion pairing there was initial trepidation regarding use of ferrocene as an internal standard. This trepidation, however, proved unwarranted and potential shifts for ferrocene oxidation were in the range ± 10 mV and showed no trend as the background electrolyte concentration was varied over two orders of magnitude. In contrast, as will be seen, the half-wave potentials for C₆₀ reduction varied monotonically by around 100 mV over the same concentration range. These observations indicate that there is little association between the ferrocenium cation and the background electrolyte in these solvents but that there is ion-association involving the buckminsterfullerene anion. Interestingly, Dubois et al. also used ferrocene as an internal standard in voltammetry studies of C₆₀ in which the background electrolyte concentration was always held at 0.1 M but the actual salt used was varied ⁽⁴⁾. They found marked potential shifts of the ferrocene half wave potential with a range of 290 mV for different salts in THF and smaller but still significant (about 70 mV) shifts in other solvents such as benzonitrile and dichloromethane. They concluded that in these circumstances ferrocene may not be the best internal reference for the salts and solvents used. For the work reported in this chapter, where the electrolyte concentration was varied, ferrocene *was* a satisfactory internal reference. The comments of Dubois et al. support, however, the findings in Chapter 5 that the ferrocenium ion probably forms ion pairs in some low dielectric media and hence ferrocene is not suitable as a voltammetry reference in these circumstances.

Figure 8.2 shows cyclic voltammograms of the first (and, in some cases, higher) reduction steps of C_{60} in dichloromethane with varying TBAP background electrolyte concentration. (The voltammogram for the most dilute solution has already been shown in Figure 8.1.) These voltammograms are typical of those obtained using other solvents and electrolytes. The $|E_{3/4} - E_{1/4}|$ values for the C_{60} reduction steps and the ferrocene oxidation step at room temperature generally varied from 55mV to 62mV indicating that electron transfer is essentially reversible in dichloromethane, 1,2-dichlorobenzene or benzonitrile with TBAP or TBABF₄ background electrolytes. The first reduction waves for C_{60} are shown on their own in more detail in Figure 8.3.

Figure 8.2
Cyclic voltammograms of
Pt (a = 10 μ m) / CH₂Cl₂, 0.19 mM C_{60} , Fc, TBAP / Pt gauze

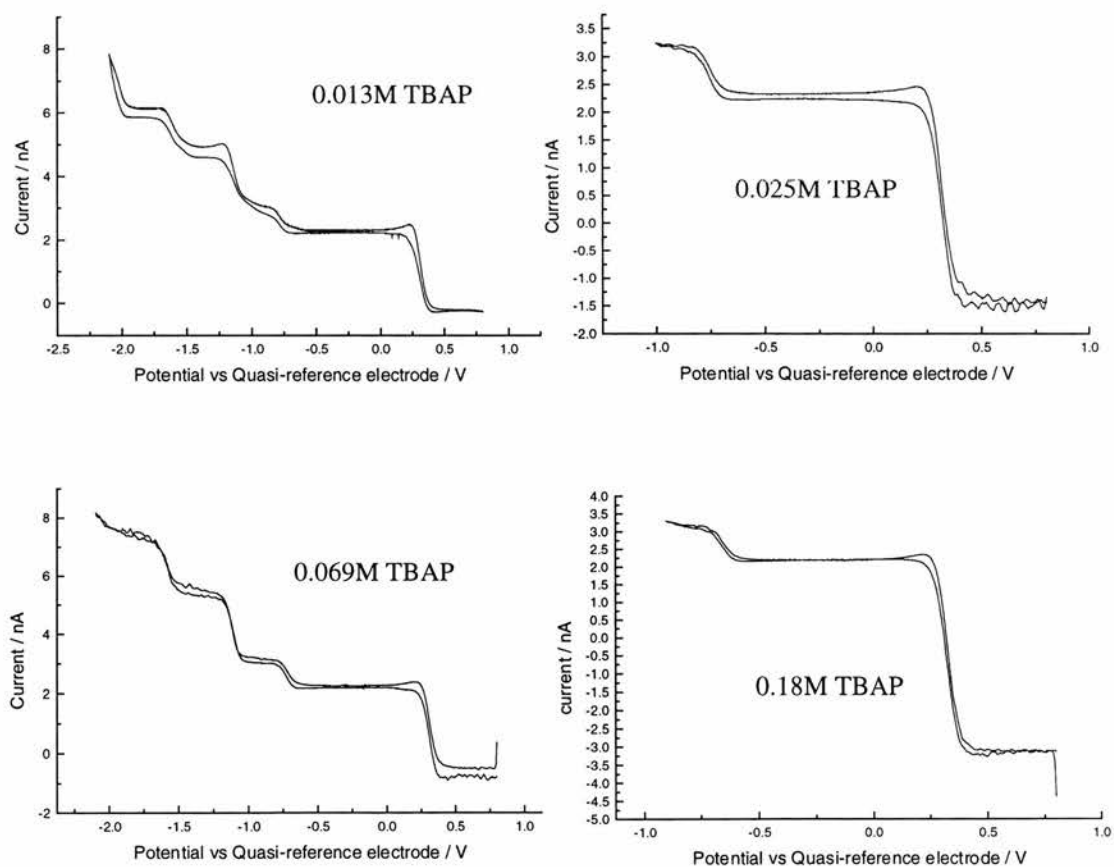
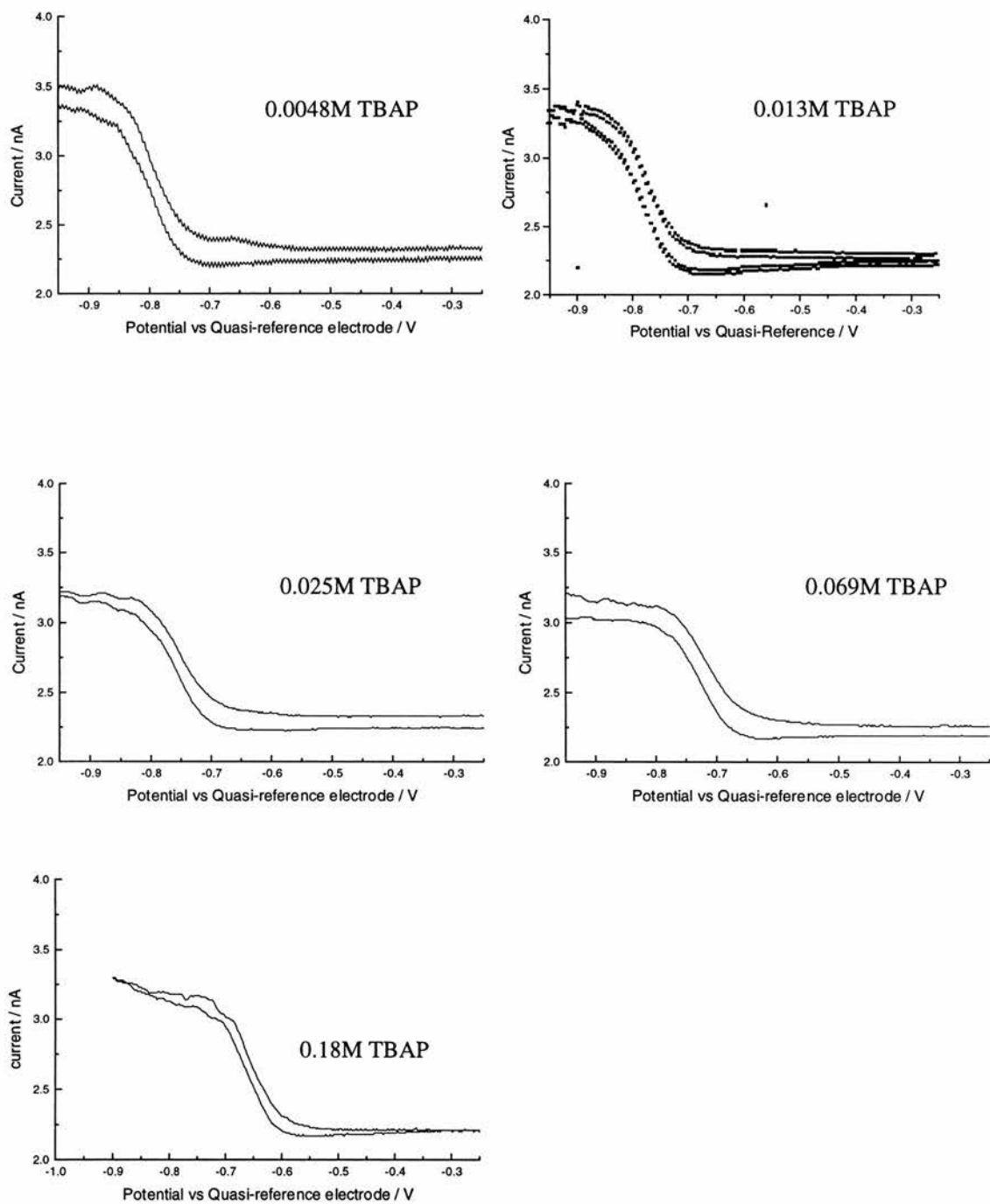


Figure 8.3

Cyclic voltammograms of the first reduction wave for C_{60}

Pt ($a = 10 \mu\text{m}$) / CH_2Cl_2 , 0.19 mM C_{60} , Fc, TBAP / Pt gauze



Sometimes, higher values of $|E_{3/4} - E_{1/4}|$ were obtained, although there appeared to be no particular pattern to this behaviour. Frequently it was noted that after making one voltammetry sweep, a much smaller wave or indeed no voltammetric wave at all was obtained if the sweep were repeated. If the microelectrode was wiped gently with tissue paper, the voltammetric wave reappeared. When a microelectrode which had failed to yield a voltammetric wave was examined under an optical microscope at 400x magnification the electrode surface, which normally had a shiny appearance, had instead a colourless but rather cloudy coating accompanied by dirty, black spots. Polishing restored the microelectrode to its normal, shiny appearance. This evidence is consistent with the occurrence of some sort of fairly rapid deposition process on the microelectrode surface under voltammetric conditions. Since the voltammetry experiments were concerned principally with obtaining half wave potentials for reversible electron transfer it was important to obtain the voltammograms before deposition interfered too much with the results. In an attempt to minimise the effects of the deposition, voltammograms were generally obtained at a scan rate of 100 mV s^{-1} rather than the rate of 10 mV s^{-1} used elsewhere in these studies.

As a result of employing more rapid scan rates the C_{60} voltammetry experiments no longer truly conformed to steady-state conditions. This is apparent from the dimensionless parameter p from Aoki et al., which was used in Chapter 5 (equation [5.7]) to assess the establishment of steady state conditions: i.e.

$$p = \left(\frac{nF}{RT} a^2 v / D \right)^{1/2}$$

Assuming a typical D value of $1 \times 10^{-5} \text{ cm}^2 \text{ s}^{-1}$ leads to a p value of 0.63 and an error of around 12% in D values obtained from cyclic voltammetry. This error, combined with the fact that one could never be certain if the size of the diffusion limited current had been altered owing to the deposition process renders values of diffusion coefficient from voltammetry unreliable. In fact the calculated diffusion coefficients, (not shown), are about 20 to 30% higher than those obtained from impedance measurements. This result is readily obtained by applying the equation $D = i_d/4nFCa$, as in previous chapters, to the voltammograms shown in Figure 8.3, for example.

Tables 8.1 to 8.7 below show how the measured half-wave potentials vary with supporting electrolyte concentration. A linear variation in half-wave potential with the logarithm of the background electrolyte concentration was found. This is graphed in Figures 8.4 and 8.5.

Table 8.1

Pt ($a = 10 \mu\text{m}$) / dichloromethane, 0.19 mM C_{60} , Fc, TBAP / Pt gauze

[TBAP] / M	$E_{1/2}$ / V
0.0048	-0.800
0.013	-0.783
0.025	-0.756
0.069	-0.722
0.18	-0.659

Table 8.2

Pt (a =10 μm) / dichloromethane, 0.19 mM C_{60} , Fc, TBABF₄ / Pt gauze

[TBABF ₄] / M	E _{1/2} / V
0.0053	-0.738
0.012	-0.715
0.022	-0.701
0.065	-0.662
0.20	-0.618

Table 8.3

Pt (a =10 μm) / 1,2-dichlorobenzene, 0.23 mM C_{60} , Fc, TBAP / Pt gauze

[TBAP] / M	E _{1/2} / V
0.0054	-0.875
0.010	-0.871
0.021	-0.854
0.067	-0.821
0.18	-0.789

Table 8.4

Pt (a =10 μm) / 1,2-dichlorobenzene, 0.23 mM C_{60} , Fc, TBABF₄ / Pt gauze

[TBABF ₄] / M	E _{1/2} / V
0.0052	-0.822
0.010	-0.810
0.021	-0.786
0.065	-0.764
0.19	-0.717

Table 8.5

Pt (a =10 μm) / benzonitrile, 0.34 mM C_{60} , Fc, TBAP / Pt gauze

[TBAP] / M	$E_{1/2}$ / V
0.0363	-0.540
0.19	-0.507

Table 8.6

Pt (a =10 μm) / benzonitrile, 0.34 mM C_{60} , Fc, TBABF₄ / Pt gauze

[TBABF ₄] / M	$E_{1/2}$ / V
0.0404	-0.485
0.0813	-0.484
0.233	-0.4621

Table 8.7

Pt (a =10 μm) / benzonitrile, 0.34 mM C_{60} , Fc, LiClO₄ / Pt gauze

[LiClO ₄] / M	$E_{1/2}$ / V
0.0951	-0.543
0.143	-0.667
0.205	-0.702
0.263	-0.737

Figure 8.4

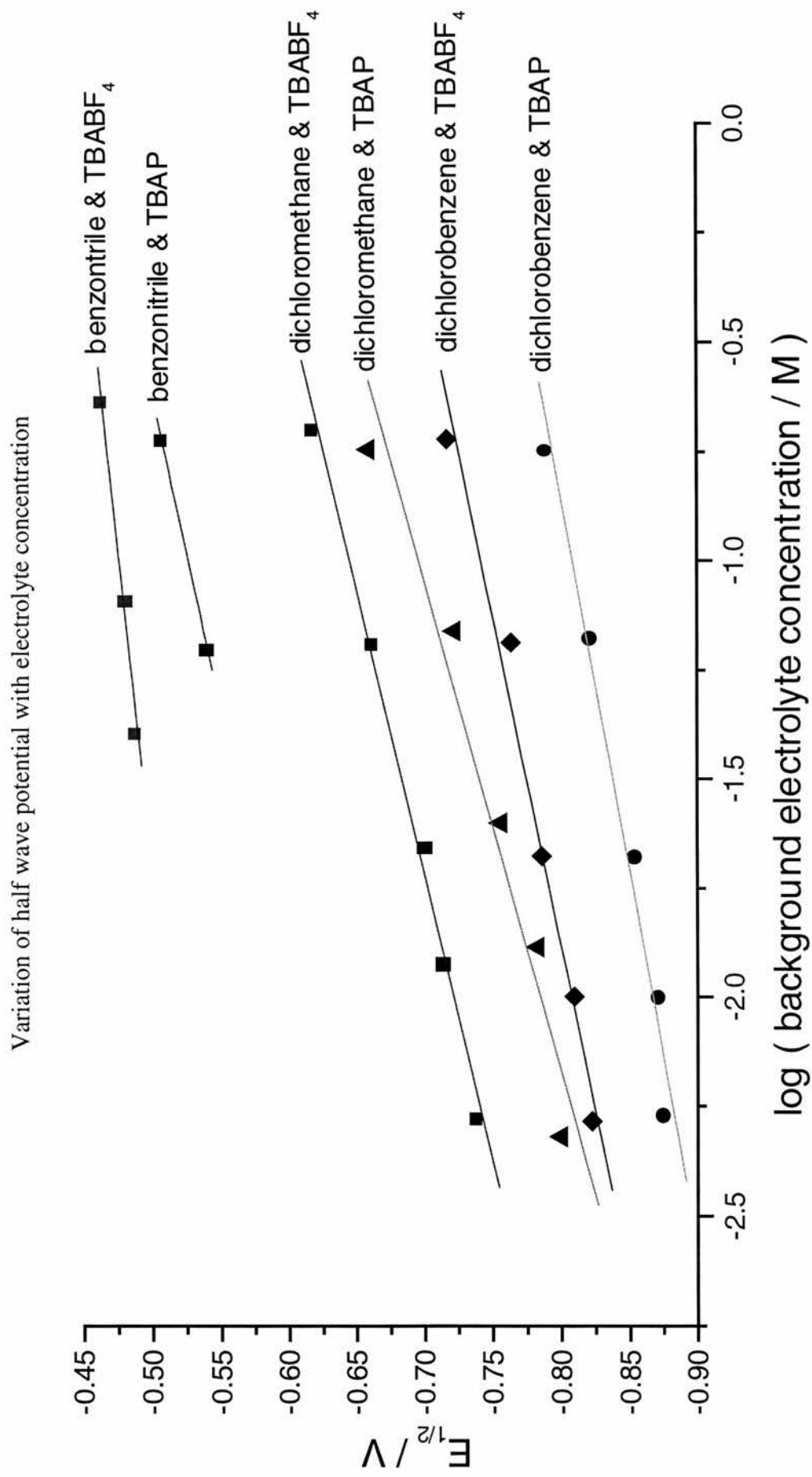
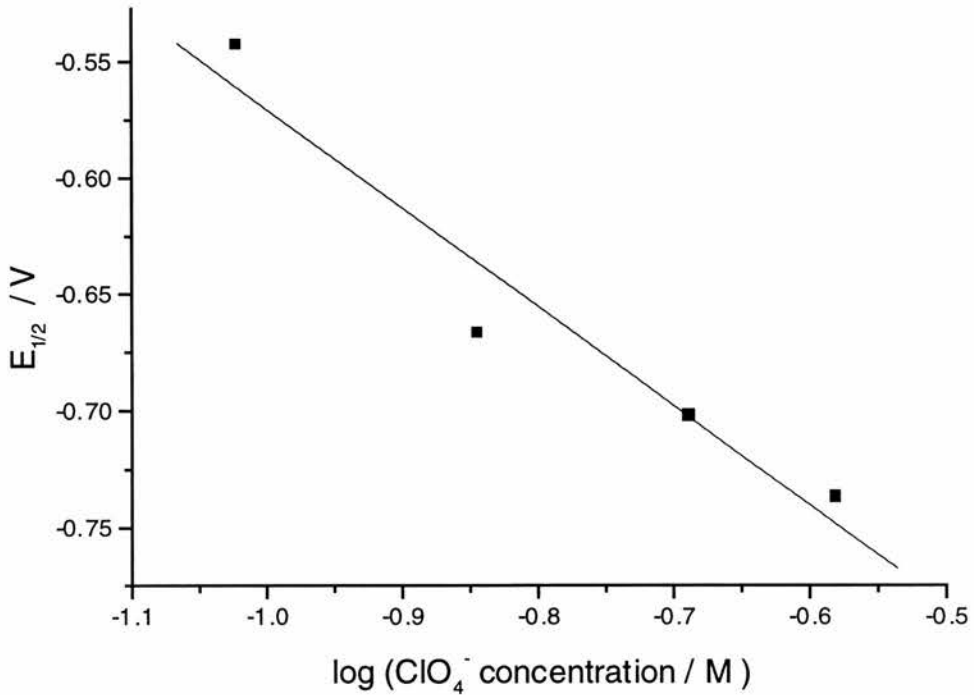


Figure 8.5

Change of half wave potential in benzonitrile with lithium perchlorate concentration



It is possible to analyse graphs of half-wave potential against logarithm of electrolyte concentration for the number of electrolyte cations associated with each C_{60}^- anion radical. This is achieved by means of the following equation used in similar circumstances by Fawcett and co-workers⁽³⁾ and also used in Chapter 5 (equation [5.3]) where the symbols used were also defined.

$$E_{1/2} - E_{1/2}^o = \frac{RT}{F} \ln(1 + \beta a_X^p)$$

$$\Rightarrow E_{1/2} - E_{1/2}^o = \frac{2.303RT}{F} \log_{10}(1 + \beta a_X^p)$$

Fawcett et al. in fact chose to use the simpler form of the equation by assuming that ion association is strong, characterised by a large association constant β and hence that $\beta a_x^p \gg 1$, and $\beta a_x^p + 1 \approx \beta a_x^p$. A little algebra yields the Lingane equation (equation [5.2]) written here in terms of base ten logarithms.

$$E_{1/2} - E_{1/2}^o = \frac{2.303pRT}{F} \log_{10} \beta + \frac{2.303pRT}{F} \log_{10} a_x$$

In Chapter 5 it was assumed that p was equal to unity and this enabled the calculation of β . Here Fawcett's method and assumption that $\beta a_x^p \gg 1$ are used to estimate the number of cations, p , associating with each C_{60}^- radical anion. By assuming that concentrations can be substituted for activities, it becomes apparent that a plot of $E_{1/2}$ against the logarithm of concentration has a slope of $2.303pRT/F$ from which p is found. If m is defined as the slope of the plot in mV, and $T = 298K$ then p is given by:

$$p = \frac{16.9m}{1000}$$

Values of p calculated from the slopes of the plots are shown in Table 8.8.

Table 8.8

Values of p from the rate of change of $E_{1/2}$ with concentration.

Solvent	Background Electrolyte	Slope / mV / log C	Fit Factor	p
Dichloromethane	TBABF ₄	76 ± 4	0.993	1.28
Dichloromethane	TBAP	89 ± 12	0.975	1.50
Dichlorobenzene	TBABF ₄	66 ± 6	0.989	1.12
Dichlorobenzene	TBAP	58 ± 5	0.987	0.98
Benzonitrile	TBABF ₄	34 ± 5	0.989	0.57
Benzonitrile	TBAP	69 *	1.000	1.17*
Benzonitrile	TBAP/LiClO ₄	-42 ± 8	0.967	-0.71 ⁺

* Analysis based on only two data points, therefore values highly uncertain.

⁺ The negative gradient and negative value of p for additions of lithium perchlorate to the solution indicate that the lithium cation is associating with the C₆₀ molecule in preference to the radical anion!

The values of p make sense physically in that taking them each to the nearest whole number indicates that each anion becomes associated with one cation. This contrasts with a value of $p = 2$ claimed by Fawcett et al. working with TBAP in benzonitrile ⁽³⁾. In Fawcett et al's paper the gradient from which p is derived is not stated but from their Figure 3, a plot of TBAP concentration squared against $\exp(fE_{1/2})$, it is possible to calculate that the gradient of half-wave potential versus log concentration in their experiments is in fact 77 mV / log C yielding a value for p of 1.23, in better agreement with the results reported here.

On the whole, the cyclic voltammetry of C_{60} solutions proved rather tricky, much more so than for the other electron transfer reactions reported in this thesis. Certainly deposition took place on the electrode surface making it difficult to obtain repeatable, reliable results. These difficulties have not been reported by other authors studying similar or identical cells. The reason for the difficulties is unknown. Despite the difficulties, clear evidence was found for ion-association of the C_{60} radical anion with the TBA^+ ions of the supporting electrolyte, consistent with an EC mechanism. Where the background electrolyte was lithium perchlorate the evidence indicated that Li^+ ions associate with C_{60} rather than C_{60}^- .

8.2 Impedance Studies of C₆₀

8.2.1 *The Effect of Time on Impedance Data*

Given the difficulties encountered in the cyclic voltammetry experiments, it was a pleasant surprise to find that the impedance experiments offered fewer difficulties. The deposition that took place within minutes in voltammetry experiments took place over a time scale of many hours or even days in impedance experiments. This indicates that the rapid deposition observed in voltammetry was probably related mainly to processes taking place at potentials removed from the equilibrium potential for the first reduction of C₆₀. Figures 8.6 to 8.9 illustrate the effect of time on impedance data. The first of these two plots, Figures 8.6 and 8.7, show an increase in impedance over a period of 24 hours for TBABF₄ in dichloromethane. This was the fastest change with time for all the salts and solvents studied in the C₆₀ experiments. Figures 8.8 and 8.9, for TBAP in 1,2 dichlorobenzene, show the slowest observed change, whereby there was little discernible change in the impedance data over a period of 48 hours. The conclusion drawn from these observations was, for the least stable solution, that provided the data for C₆₀ in dichloromethane could be gathered within a (long) working day, the results with regard to such parameters as the standard heterogeneous rate constant should be reasonably reliable. For the other solutions, the data could be gathered over a longer period of time.

Figure 8.6

Effect of time on impedance data - all frequencies

Pt ($a = 10 \mu\text{m}$) / dichloromethane, 0.19 mM C_{60} , 0.012 M TBABF₄ / Pt gauze

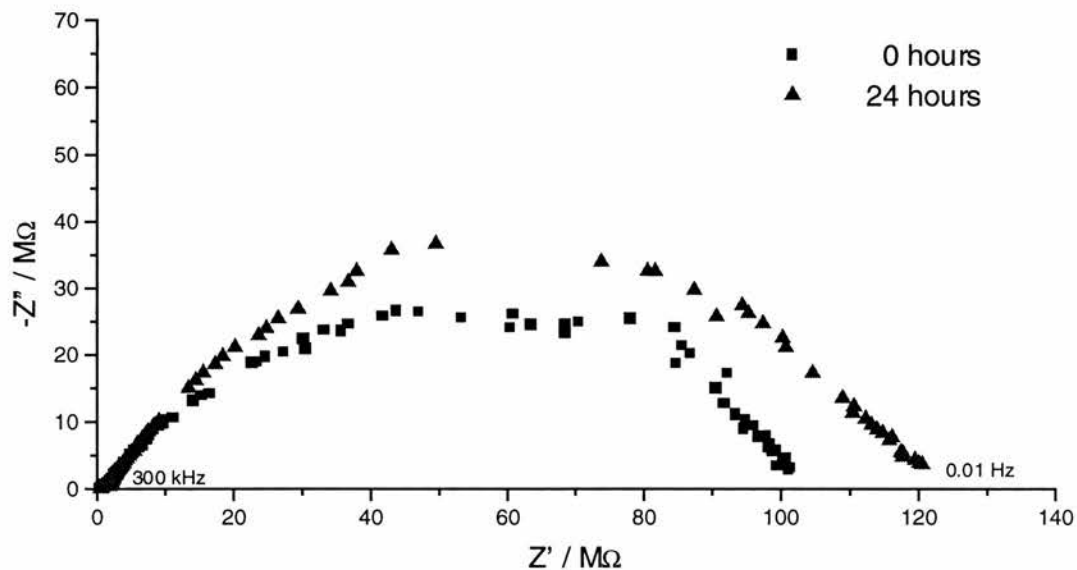


Figure 8.7

Effect of time on impedance data - high frequencies

Pt ($a = 10 \mu\text{m}$) / dichloromethane, 0.19 mM C_{60} , 0.012 M TBABF₄ / Pt gauze

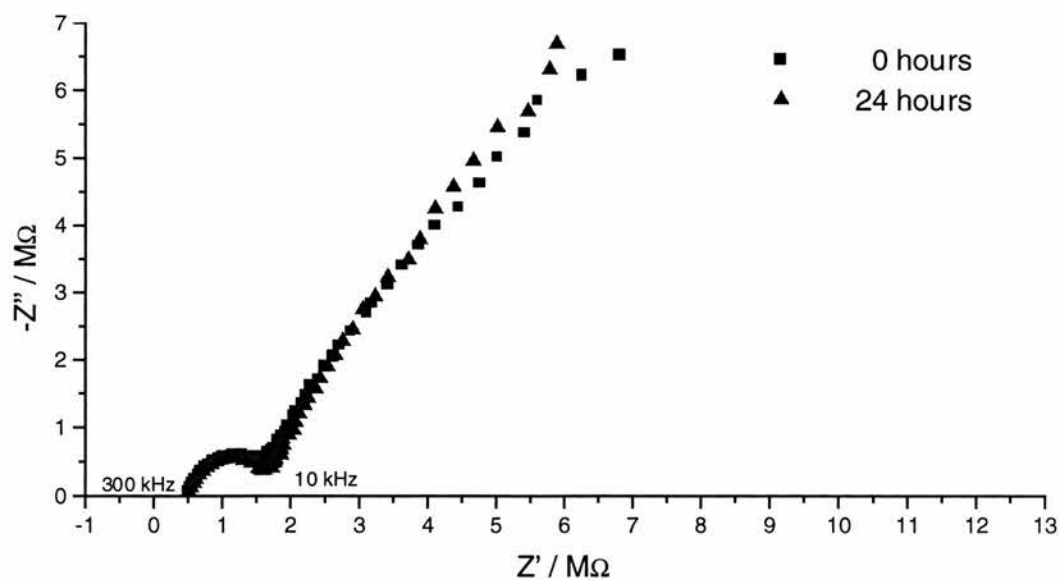


Figure 8.8

Effect of time on impedance data - all frequencies

Pt ($a = 10 \mu\text{m}$) / 1,2 dichlorobenzene, 0.22 mM C_{60} , 0.18 M TBAP / Pt gauze

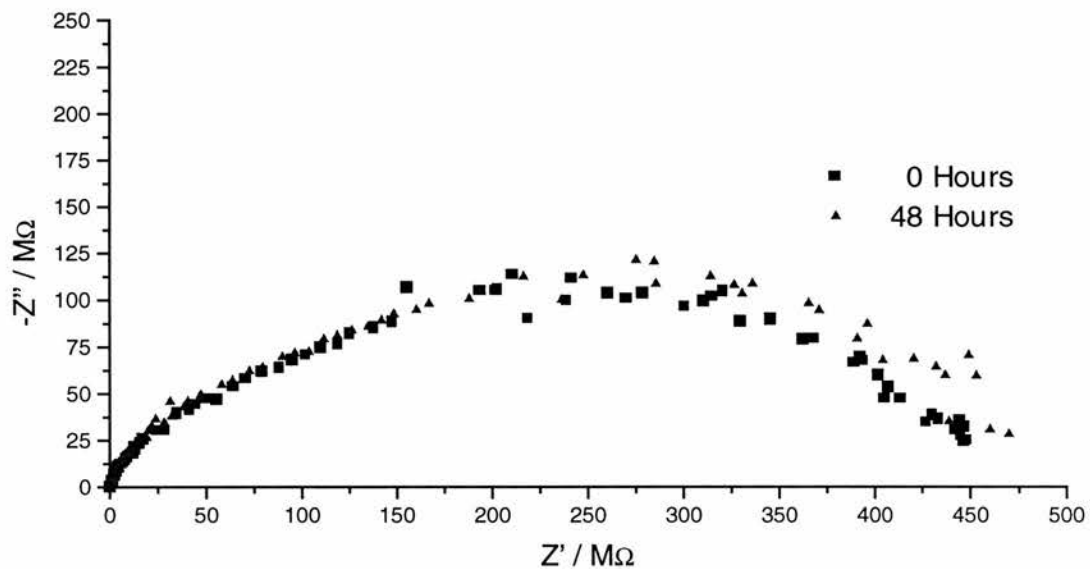
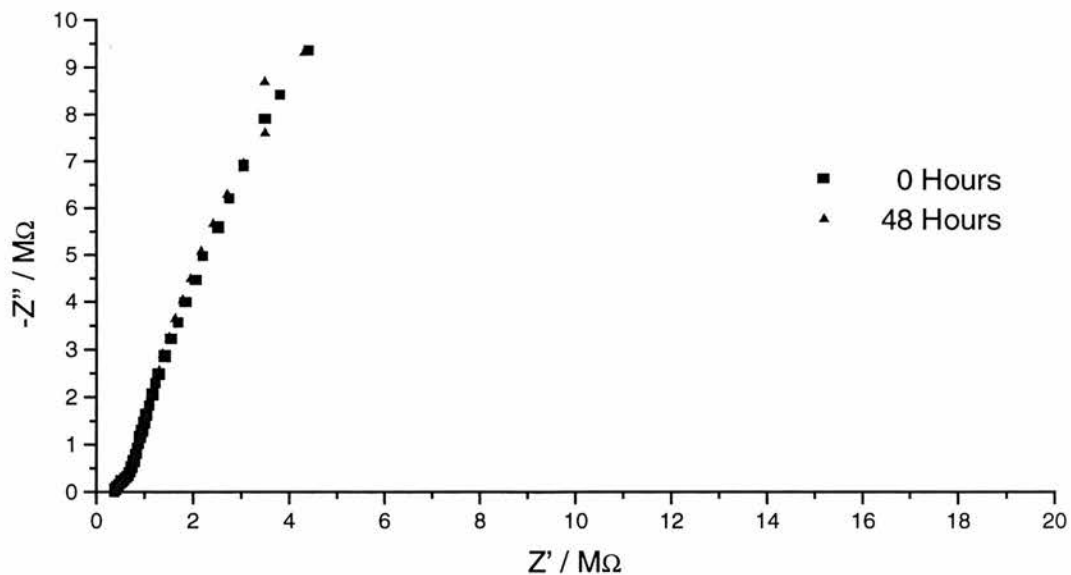


Figure 8.9

Effect of time on impedance data - high frequencies

Pt ($a = 10 \mu\text{m}$) / 1,2 dichlorobenzene, 0.22 mM C_{60} , 0.18 M TBAP / Pt gauze



8.2.2 *The Effect of Potential on Impedance Data*

An interesting aspect of the buckminsterfullerene study was the behaviour of the high frequency impedance data. In Chapter 7, impedance plots for ferrocene / ferrocenium charge transfer in near-solid PEO contained a high frequency feature which looked like a typical charge-transfer / double-layer capacitance semi-circle. This semi-circle was, however, insensitive to potential and so was concluded to be unconnected with the charge transfer process. Figures 8.10 and 8.11, for C₆₀ in dichloromethane with TBABF₄ electrolyte, illustrate how varying the potential results in increased impedances at low frequencies, but has no effect on the high frequency semi-circle.

In the case of the solid polymer the high frequency semi-circle vanished when the cell was heated and did not reappear on cooling. This suggested the possibility of incomplete wetting of the electrode surface, giving rise to additional capacitance effects. In the organic liquids the high frequency semi-circle does not change with time as can be seen, for example, in Figure 8.7. It does not seem likely that incomplete wetting of the metal by the solvent is a realistic possibility. The capacitance and resistance of the semi-circle shown in Figure 8.11 are 2.4 pF and 1 M Ω respectively. Reformulated to reflect the microdisc surface area they are 1 $\mu\text{F cm}^{-2}$ and 3 $\Omega \text{ cm}^2$. In this form, it is clear that the capacitance term is too low for it to be the capacitance of the double layer but it and the resistance are very similar in size to the values of 0.5 $\mu\text{F cm}^{-2}$ and 5 $\Omega \text{ cm}^2$ noted in the solid PEO environment where the possibility of their being caused by an oxide layer on the electrode surface was tentatively proposed.

Figure 8.10

Effect of potential on impedance data - all frequencies

Pt (a = 10 μm) / dichloromethane, 0.19 mM C_{60} , 0.12 M TBABF₄ / Pt gauze

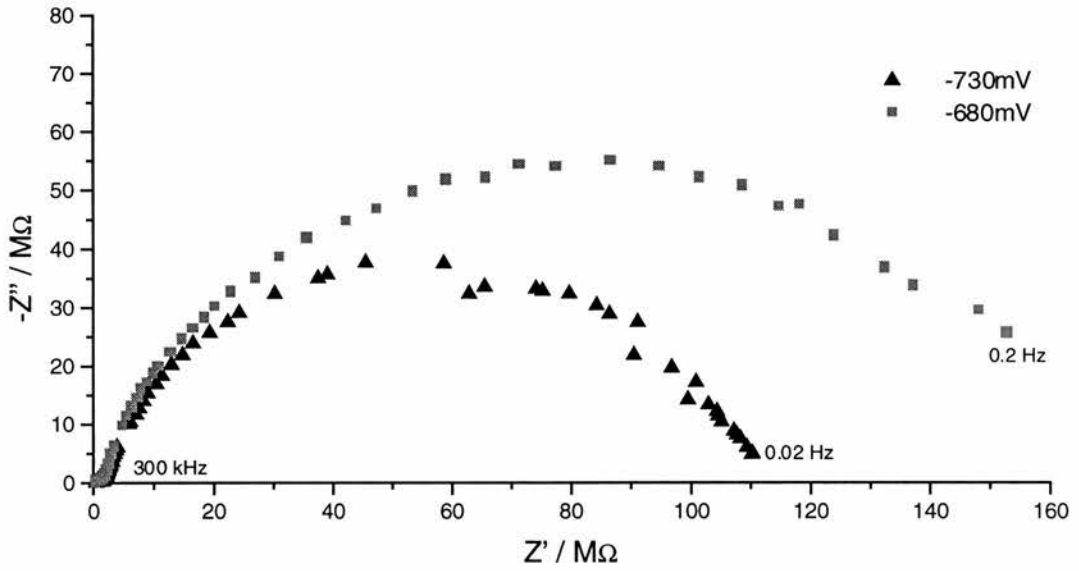
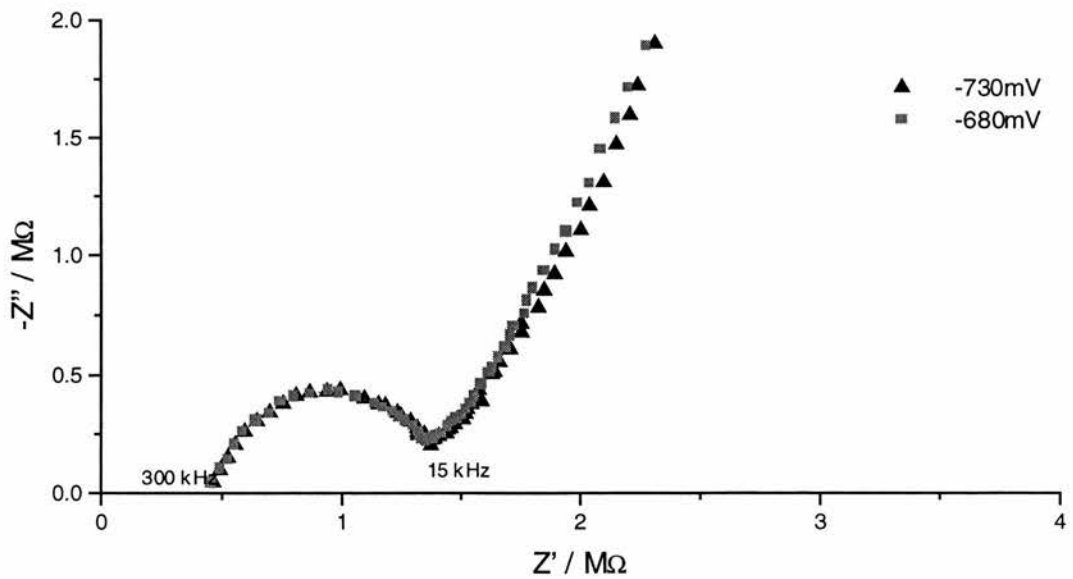


Figure 8.11

Effect of potential on impedance data - high frequencies

Pt (a = 10 μm) / dichloromethane, 0.19 mM C_{60} , 0.12 M TBABF₄ / Pt gauze



Since the high frequency data are not relevant to the charge transfer process they must be excluded from the CNLS analysis. It might be thought that exclusion of the highest frequency data would prevent extraction of k_s from the data since the majority of the charge transfer information contained in the impedance spectrum will be contained in the high frequency data. In order to see whether this is indeed the case a number of simulation calculations were carried out.

8.2.3 *Simulations of Impedance Plots*

One particularly simple means of determining the effect of parameter values on impedance plots is to run computer simulations. A number of simulations were carried out using the hemispherical approximation equations for an E mechanism. At this stage EC simulations were not run because the principle reason for making the simulations was to determine how much information about k_s could be obtained without inclusion of high frequency data. This could be ascertained more directly without additional complicating parameters. The parameter values substituted into the E equations for simulations are typical of the values likely to be encountered in the experimental work carried out for this thesis. The plots show the effect of holding other parameters constant whilst changing the value of k_s .

The first plots show simulations of parameter values typical of those encountered in the aqueous study reported in Chapter 4. Figures 8.12 and 8.13 are simulated with a microdisc of radius 5 μm while Figures 8.14 and 8.15 are for radius 10 μm . The

other parameters for the simulation calculation are: total redox couple concentration = 2 mM, $T = 295 \text{ K}$, $C_{dl} = 20 \mu\text{F cm}^{-2}$, and $D = 6 \times 10^{-6} \text{ cm}^2 \text{ s}^{-1}$.

Figure 8.12

Simulation of impedance data - parameters typical of aqueous experiments
Microdisc radius $5 \mu\text{m}$, 300 kHz to 0.015 Hz

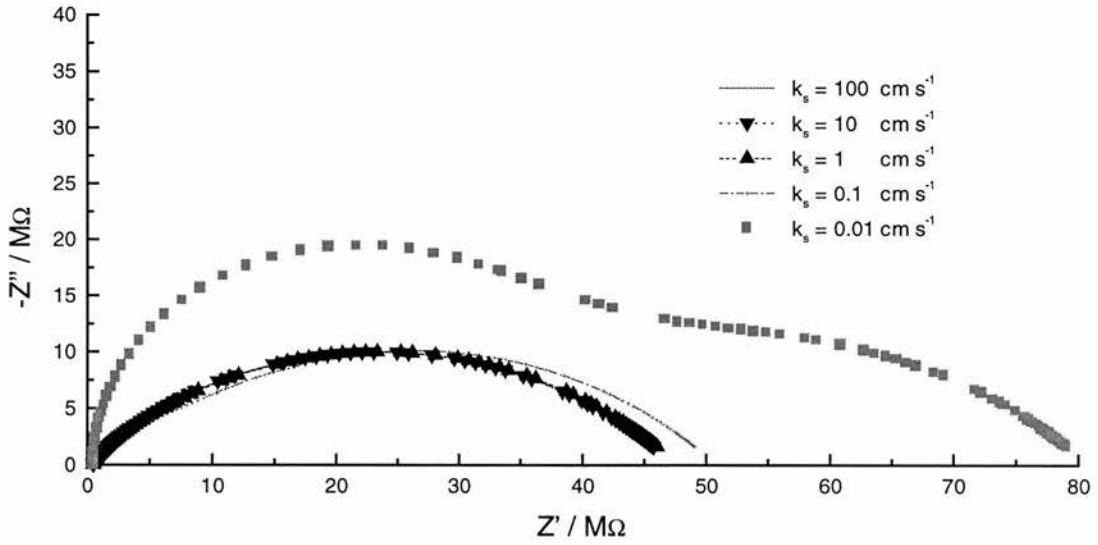


Figure 8.13

Simulation of impedance data - parameters typical of aqueous experiments
Microdisc radius $5 \mu\text{m}$ -high frequency region

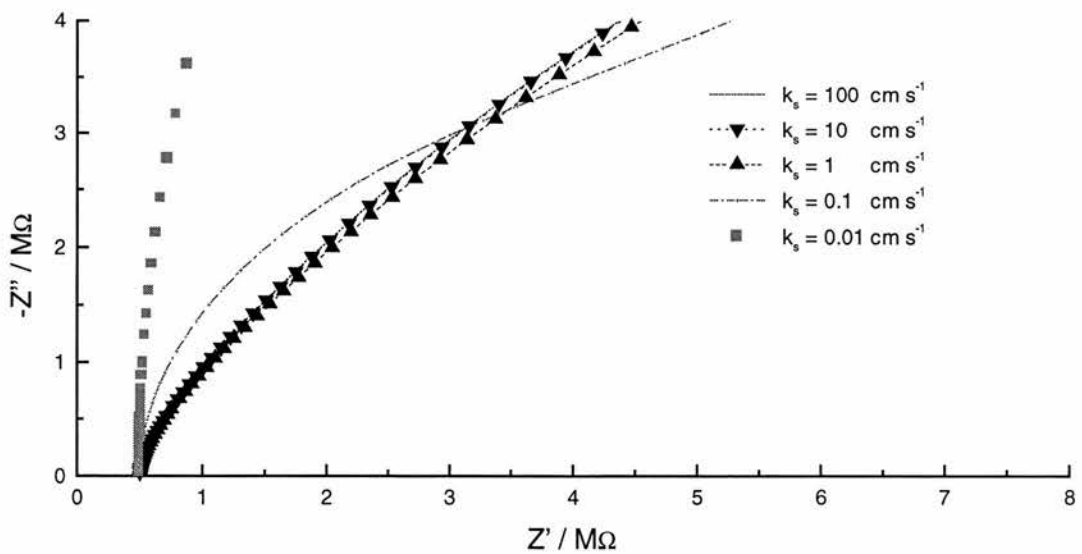


Figure 8.14

Simulation of impedance data - parameters typical of aqueous experiments
Microdisc radius $10\ \mu\text{m}$, 300 kHz to 0.015 Hz

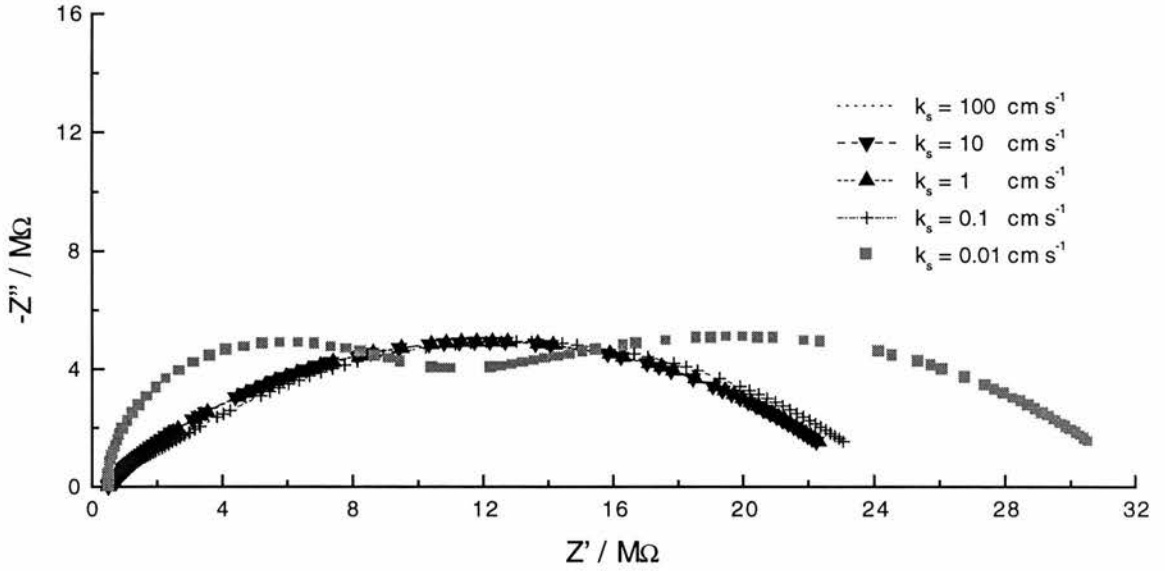
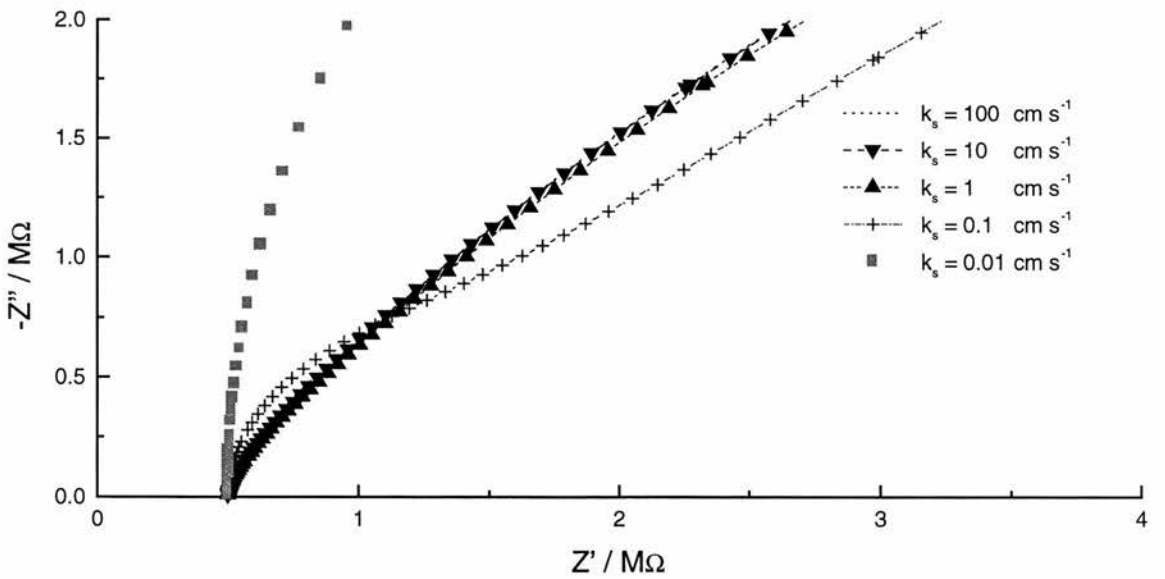


Figure 8.15

Simulation of impedance data - parameters typical of aqueous experiments
Microdisc radius $10\ \mu\text{m}$ - high frequency region



It is apparent from these plots that for reactions where k_s is of the order of 1 cm s^{-1} or slower, the plots differ in size/shape at both high and low frequencies. Since the value of k_s is the only difference between these plots it is reasonable to conclude that provided k_s is around 1 cm s^{-1} or lower there should be a very good chance of obtaining reliable values for k_s from analysis of high *or* low frequency data. This is particularly true of the smaller, $5 \mu\text{m}$, microdisc.

For faster reactions, although different values of k_s between 1 and 10 cm s^{-1} should cause slight differences in the impedance plots at high frequencies, it is unlikely that precise values of k_s will be obtained because the plots with these values are just too similar to one another.

In the context of analysis of C_{60} impedance data the important point to take from the above discussion is that provided a reaction has slow enough kinetics the value of k_s should be obtainable from analysis of only the low frequency data.

A further series of simulations were performed to look at the influence of k_s on the impedance plots when the other parameters are typical of those encountered in the ferrocene experiments reported in Chapter 5, i.e. $T = 295 \text{ K}$, total redox couple concentration = 20 mM , $C_{dl} = 10 \mu\text{F cm}^{-2}$, $D = 2 \times 10^{-6} \text{ cm}^2 \text{ s}^{-1}$ and a $5 \mu\text{m}$ radius microdisc. These simulations are shown in Figures 8.16 and 8.17.

Figure 8.16

Simulation of impedance data - parameters typical of ferrocene experiments
Microdisc radius 5 μm , 300 kHz to 0.015 Hz

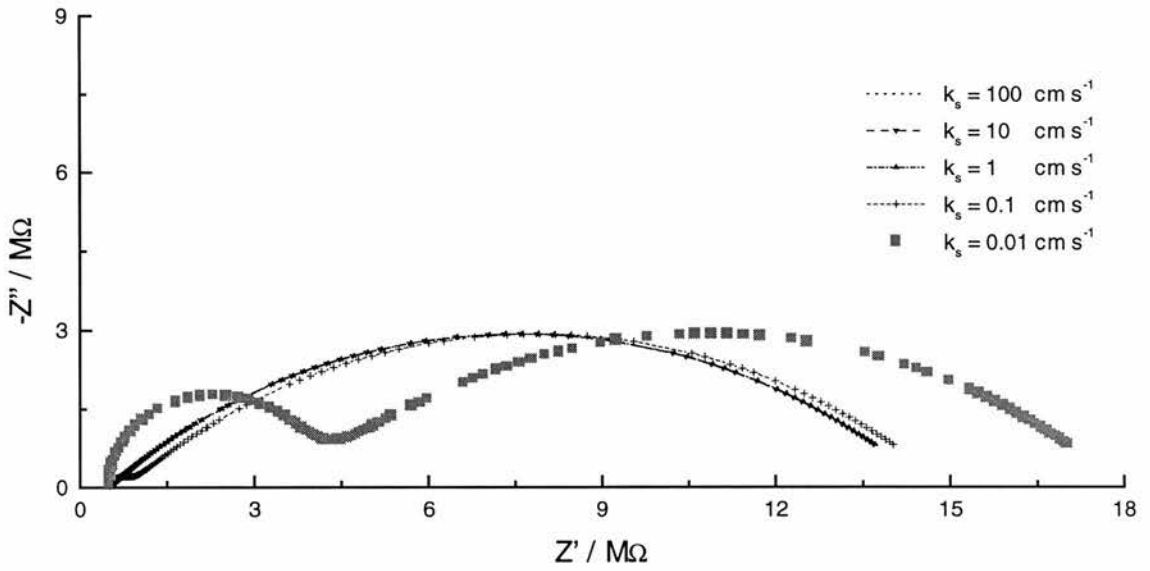
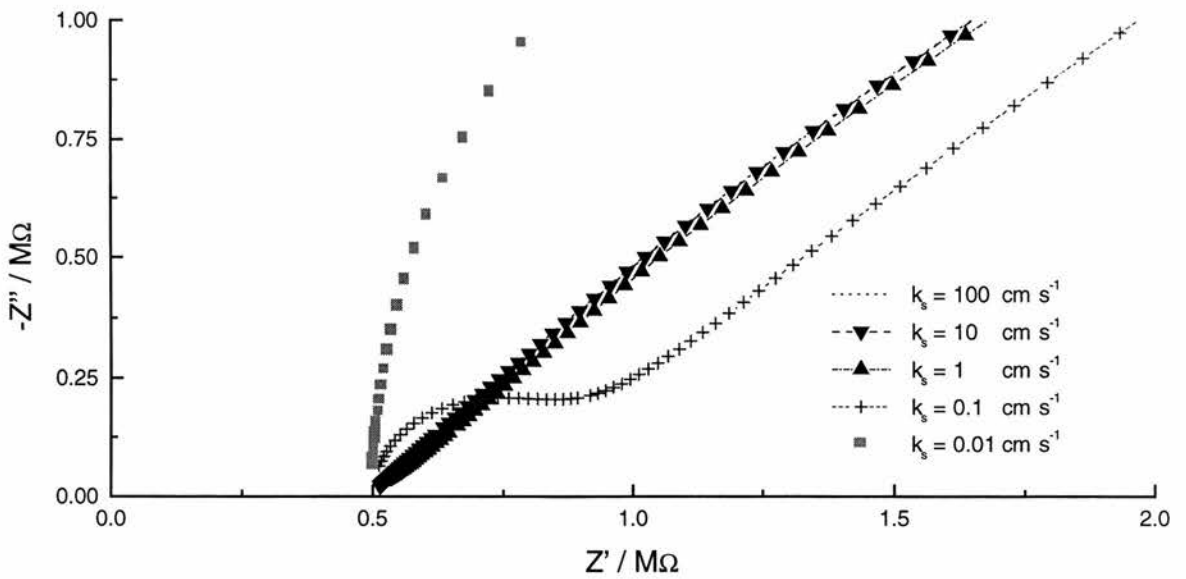


Figure 8.17

Simulation of impedance data - parameters typical of ferrocene experiments
Microdisc radius 5 μm - high frequency region



These simulations, using parameters typical of the ferrocene experiments, once again indicate that provided electron transfer kinetics are not too rapid, the value of k_s has sufficient influence on the low frequency data that its value should be calculable by CNLS analysis of the just low frequency data. To test whether this is true in practice, two of the data sets presented in Chapter 5 for ferrocene cells are reanalysed here. These are purely illustrative examples and the conclusions drawn are valid for all other concentrations of ferrocene. Results from CNLS analysis of impedance data from the cells containing 12 mM ferrocene and 60 mM ferrocene using the hemispherical model for an EC reaction are shown in Tables 8.9 and 8.10. Results from analysis of the whole frequency range are compared with results from analysis of just the low frequency data. The low frequency data were obtained by deleting sufficient high frequency points to remove the high frequencies "charge-transfer" semi-circle. The data and fits for 12 mM ferrocene are shown in Figures 8.18 to 8.21.

Figure 8.18

136 kHz to 0.3 Hz fitted

Pt ($a = 5 \mu\text{m}$) / tetraglyme, 12 mM ferrocene, 0.5 M LiClO_4 / Pt gauze

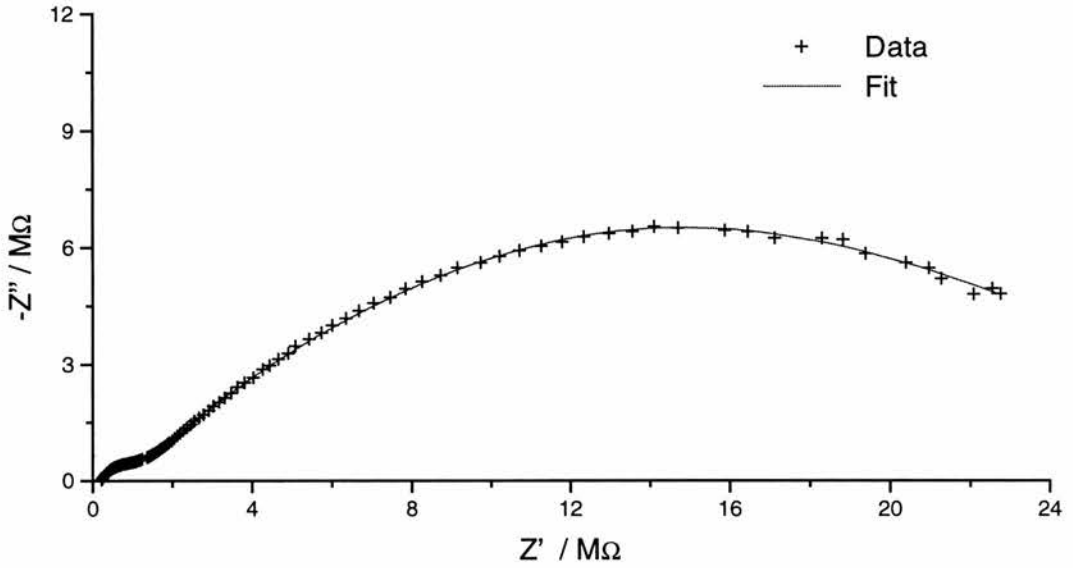


Figure 8.19

Magnified high frequency region of 136 kHz to 0.3 Hz fitted

Pt ($a = 5 \mu\text{m}$) / tetraglyme, 12 mM ferrocene, 0.5 M LiClO_4 / Pt gauze

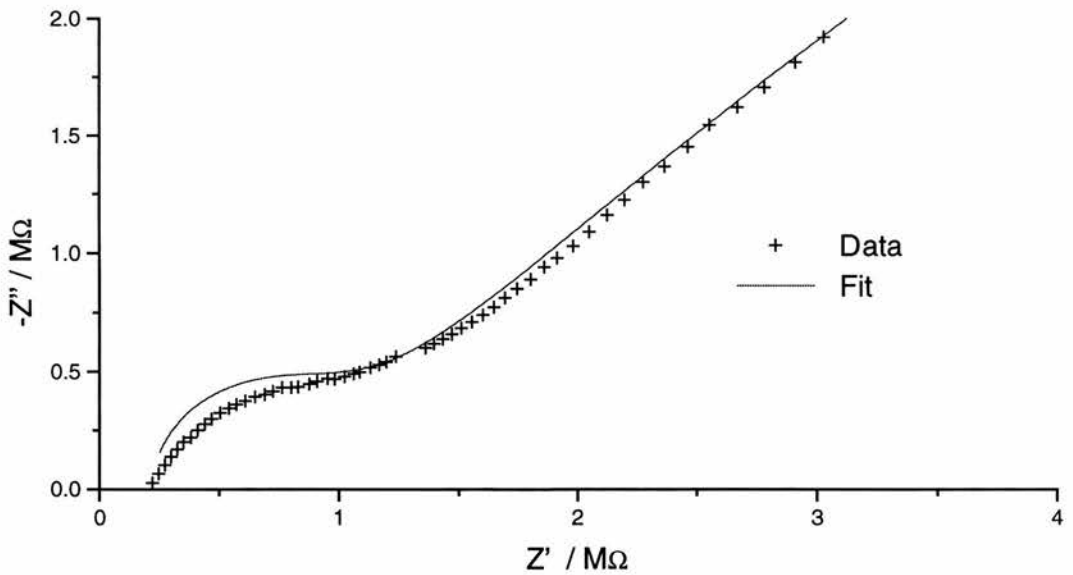


Figure 8.20

1.9 kHz to 0.3 Hz fitted

Pt ($a = 5 \mu\text{m}$) / tetraglyme, 12 mM ferrocene, 0.5 M LiClO_4 / Pt gauze

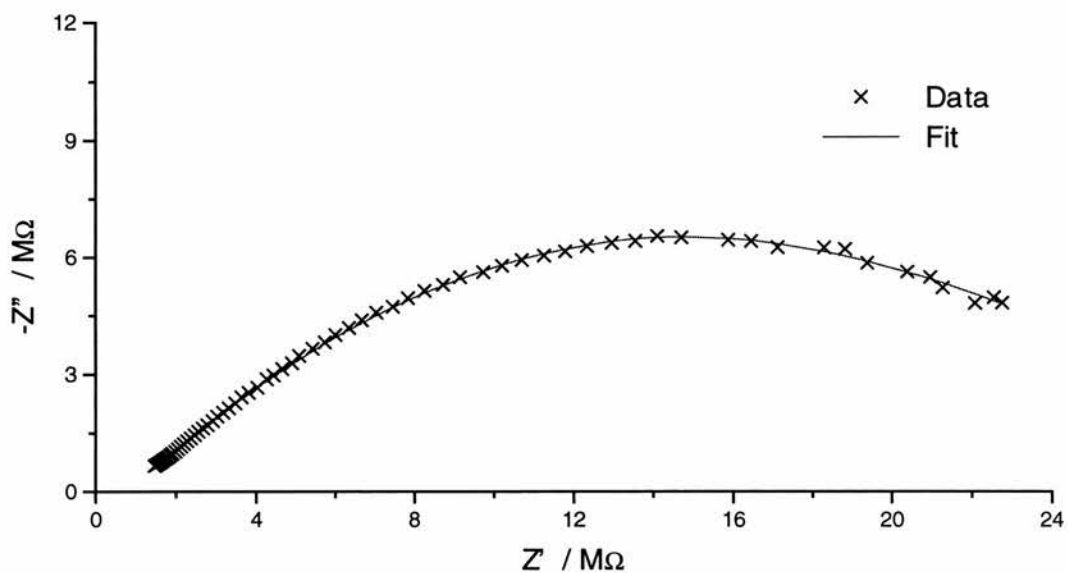


Figure 8.21

Magnified high frequency region of 1.9 kHz to 0.3 Hz fitted

Pt ($a = 5 \mu\text{m}$) / tetraglyme, 12 mM ferrocene, 0.5 M LiClO_4 / Pt gauze

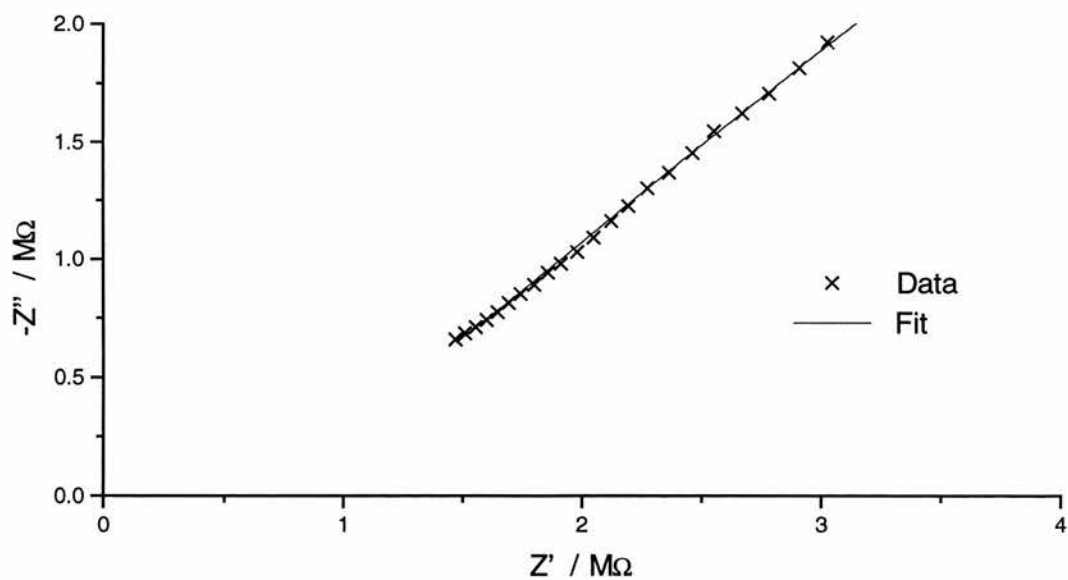


Table 8.9

Results of CNLS analysis using Hemispherical EC model for Pt ($a = 5 \mu\text{m}$) / tetraglyme, 12 mM ferrocene, 0.5 M LiClO₄ / Pt gauze

Statistical Fitting Parameter	Highest Frequency / kHz	Lowest Frequency / Hz	C _{dl} / $\mu\text{F cm}^{-2}$	D / $10^6 \text{ cm}^2 \text{ s}^{-1}$	a / μm	k _s / cm s^{-1}	k ₁ / s^{-1}	k ₂ / s^{-1}
-2	136	0.30	8.54	1.79	4.89	0.0865	2.32	5.78
+1	136	0.30	8.91	1.61	5.13	0.0753	2.38	8.42
-2	1.94	0.30	9.59	1.54	5.34	0.0643	1.67	9.95
+1	1.94	0.30	7.06	1.61	5.16	0.0744	2.28	8.57
Mean Value								
			8.52	1.64	5.13	0.0751	2.16	8.18
Largest difference from mean			17%	9.1%	4.7%	15%	23%	29%

Table 8.10

Results of CNLS analysis using Hemispherical EC model for Pt ($a = 5 \mu\text{m}$) / tetraglyme, 60 mM ferrocene, 0.5 M LiClO_4 / Pt gauze

Statistical Fitting Parameter	Highest Frequency / kHz	Lowest Frequency / Hz	C_{dl} / $\mu\text{F cm}^{-2}$	D / $10^6 \text{ cm}^2 \text{ s}^{-1}$	a / μm	k_s / cm s^{-1}	k_1 / s^{-1}	k_2 / s^{-1}
-2	136	0.30	10.0	1.60	5.81	0.0270	5.00	7.90
+1	136	0.30	9.15	1.59	5.80	0.0260	4.22	9.21
-2	2.94	0.30	9.83	1.59	5.83	0.0259	4.37	8.86
+1	2.94	0.30	8.58	1.66	5.63	0.0279	4.47	10.3
Mean Value								
			9.39	1.61	5.77	0.0267	4.51	9.07
Largest difference from mean			8.6%	3.1%	2.4%	4.5%	10.8%	14%

It is clear from the tables that whichever statistical fitting parameter is applied, the calculated values for C_{dl} , D , a , and k_s show very little dependence on whether or not the high frequency data are included in the CNLS analysis and are certainly within experimental error. The values of k_1 and k_s are more variable but this variability disappears if only the values from +1 fitting, i.e. emphasising the low frequency data, are used. This makes physical sense and it is highly probable that the values of k_1 and k_2 obtained using the +1 parameter are more reliable than those obtained using -2.

The above data indicate that it is not always necessary to work at frequencies sufficiently high that a "charge-transfer semi-circle" is seen in the impedance plot to obtain reliable values of the electrochemical parameters from CNLS analysis. For the redox couples studied here, provided k_s is lower than 1 cm s^{-1} , it should be possible to obtain k_s from the low frequency data.

Finally, simulations are presented in Figures 8.22 and 8.23 for electrochemical parameters more typical of the C_{60} impedance experiments, i.e. total redox couple concentration = 0.25 mM , $C_{dl} = 10 \text{ } \mu\text{F cm}^{-2}$, $D = 1 \times 10^{-5} \text{ cm}^2 \text{ s}^{-1}$, and a microdisc radius of $10 \text{ } \mu\text{m}$. Despite changing the parameter values, the results of these simulations are entirely consistent with those discussed on the preceding pages and indicate that provided k_s is lower than 1 cm s^{-1} its value can be obtained from CNLS analysis of low frequency impedance data. If k_s is greater than 1 cm s^{-1} , how much greater cannot be known.

Figure 8.22

Simulation of impedance data - parameters typical of C_{60} experiments
Microdisc radius $10\ \mu\text{m}$, 300 kHz to 0.015 Hz

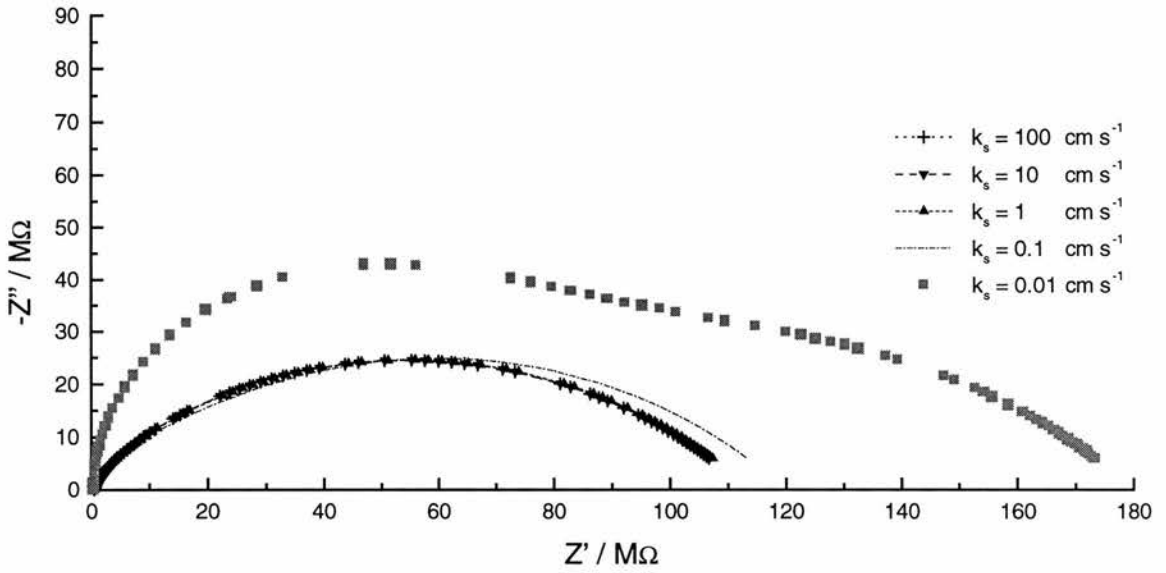
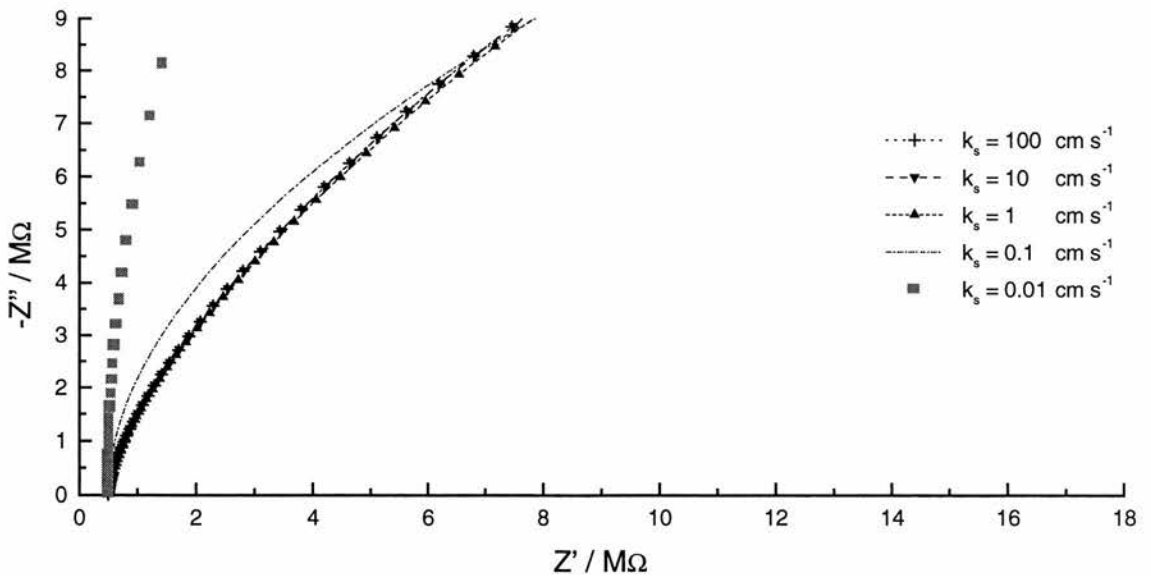


Figure 8.23

Simulation of impedance data - parameters typical of C_{60} experiments
Microdisc radius $10\ \mu\text{m}$ - high frequency region



8.2.4 CNLS Analysis of Impedance Data

In Section 8.1 evidence was presented showing that each C_{60}^- radical anion associates with (to the nearest whole number) one cation and the EC mechanism established, i.e.



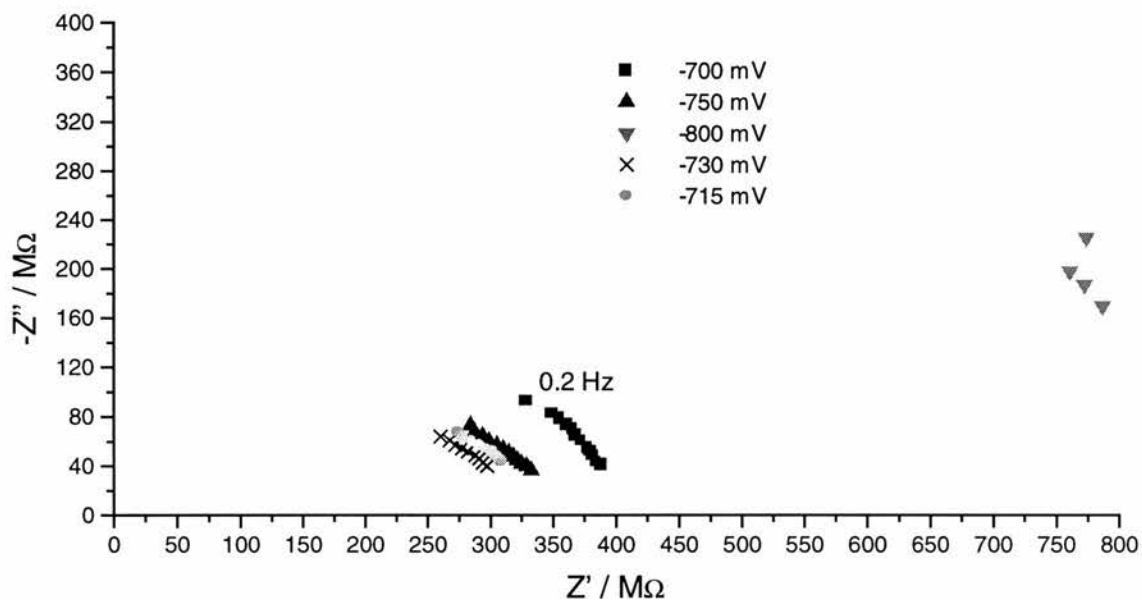
The equations necessary for analysis of microelectrode impedance data from an EC reaction were derived in Chapter 3. Comparisons of fitting impedance data from C_{60} solutions using the hemispherical approximation E or EC models indicated that superior fits were obtained with the EC model.

Impedance data were gathered in the same three solvents using the same electrolytes as had been employed in voltammetry. No internal voltammetric standard was required for the impedance experiments, however, and therefore no ferrocene was added to the solutions. Impedance data were gathered at different concentrations of background electrolyte. Since the high frequency data were insensitive to the applied potential, the potential of minimum impedance was found by gathering impedance data at low frequencies to determine which potential resulted in the lowest impedance. The effect of potential at low frequencies is shown in Figure 8.24 and in this example the potential of minimum impedance was identified as -730 mV.

Figure 8.24

Low frequency impedance data

Pt (a = 10 μm) / benzonitrile, 0.38 mM C_{60} , 0.22 M LiClO_4 / Pt gauze



Having established a satisfactory method of obtaining the potential of minimum impedance, impedance data were gathered to determine the effect of electrolyte concentration. Typical impedance plots are shown in Figures 8.25 to 8.27.

Figure 8.25

Pt (a = 10 μm) / dichloromethane, 0.12 mM C_{60} , TBABF₄ / Pt gauze

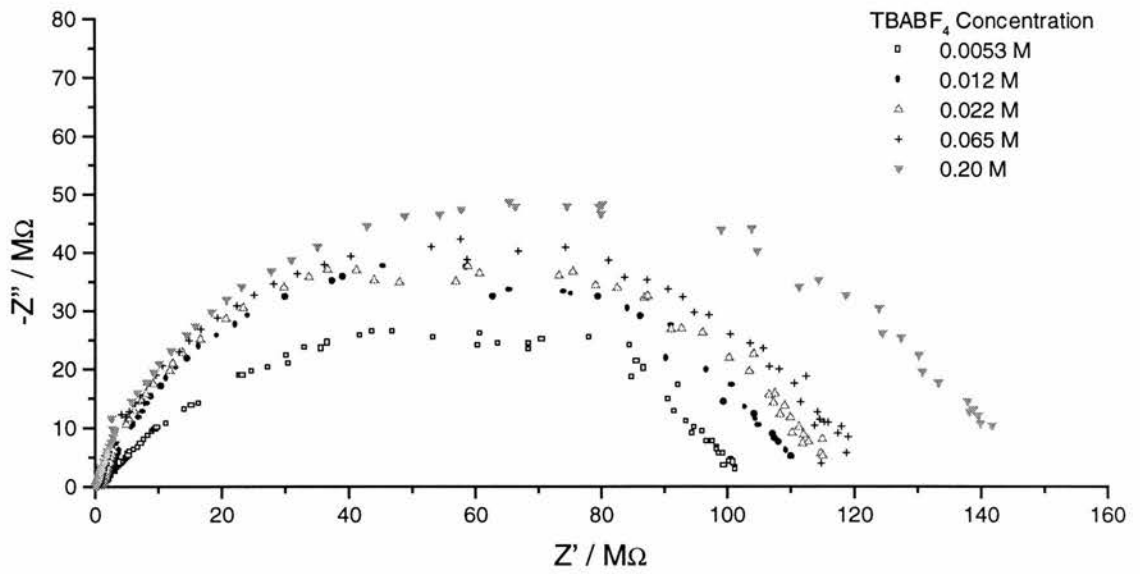


Figure 8.26

Pt (a = 10 μm) / 1,2 dichlorobenzene, 0.25 mM C_{60} , TBAP / Pt gauze

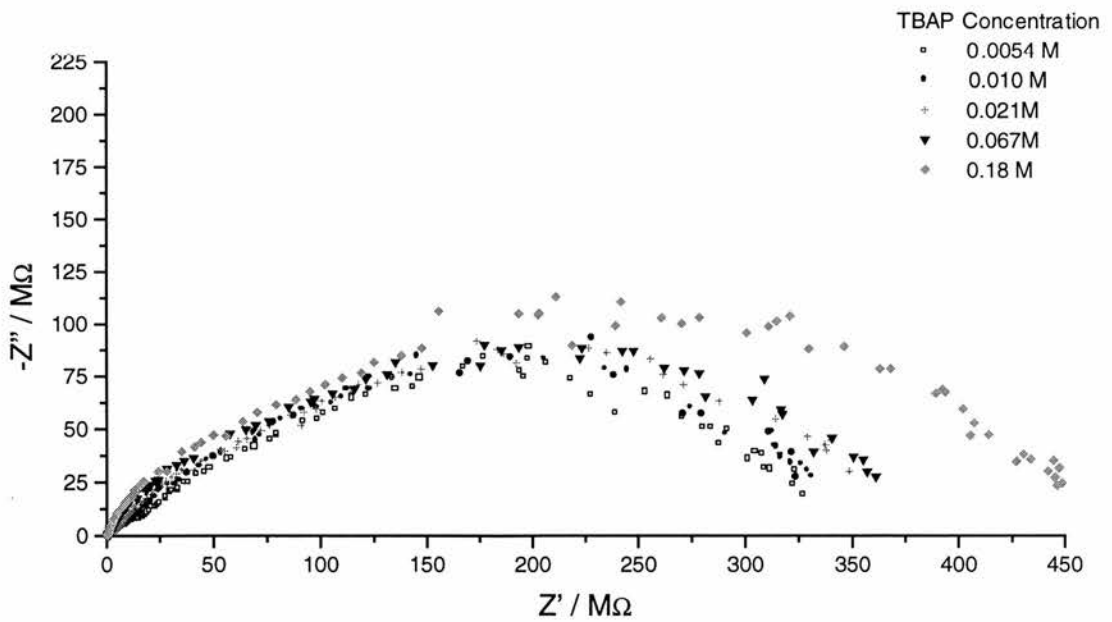
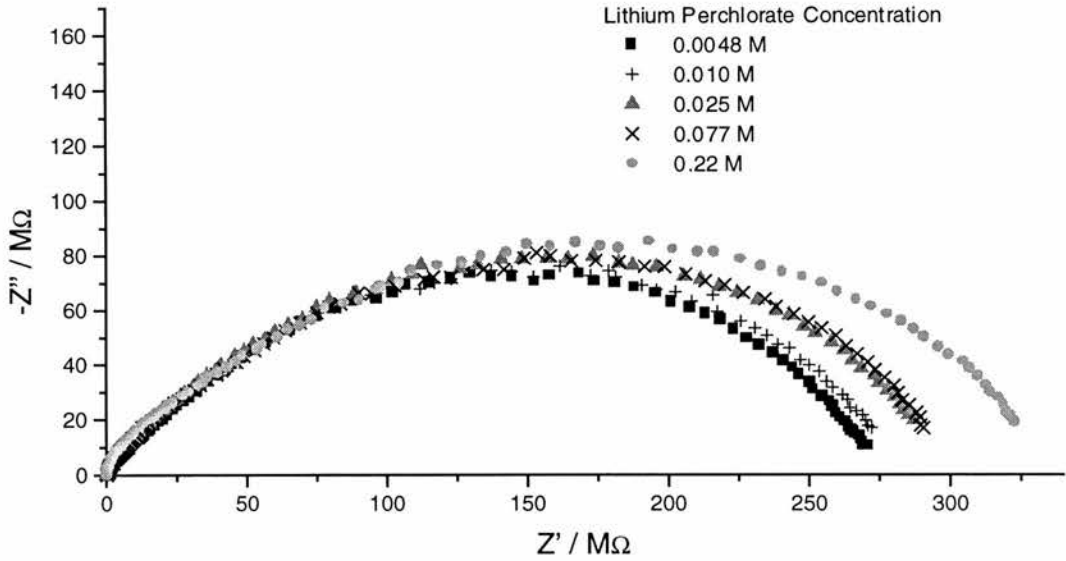


Figure 8.27

Pt (a = 10 μm) / benzonitrile, 0.38 mM C_{60} , LiClO_4 / Pt gauze



Impedance analysis of these data proved to be less straightforward than for ferrocene and TCNQ in tetraglyme. An indication of the method used to obtain values of the electrochemical parameters, for the case of dichloromethane solution containing 0.0053 M TBABF₄, is presented below.

To begin with, all data points associated with the high frequency semi-circle are deleted so that instead of beginning the analysis at about 300 kHz, it begins at 8 kHz. Results obtained from fitting this data to the EC model are shown in Table 8.11 below:

Table 8.11

Results of initial CNLS fitting of C_{60} impedance data to the EC model

Property	-2 Statistical Parameter Fit	+1 Statistical Parameter Fit
$C_{dl} / \mu\text{F cm}^{-2}$	10.6	10.8*
$D / 10^5 \text{ cm}^2 \text{ s}^{-1}$	1.39	1.49
$a / \mu\text{m}$	11.5	10.7*
$k_s / \text{cm s}^{-1}$	0.790*	96.0 ⁺
k_1	4.00	8.90*
k_2	6.60	0.0669*
K	1.65	133*

* 8% < Standard deviation error < 500%

⁺ Standard deviation error \geq 500%

Taking the above values and their errors into account, parameter values are accepted as follows: $C_{dl} = 10.6 \mu\text{F cm}^{-2}$, $D = 1.49 \times 10^5 \text{ cm}^2 \text{ s}^{-1}$ and $a = 11.5 \mu\text{m}$.

With these values accepted, and written as constant parameters in the CNLS analysis, re-analysis of the remaining parameters yields the values shown in Table 8.12.

Table 8.12

Results of second CNLS fitting of C₆₀ impedance data to the EC model

Property	-2 Statistical Parameter Fit	+1 Statistical Parameter Fit
$k_s / \text{cm s}^{-1}$	0.747	0.468*
k_1 / s^{-1}	3.49	3.76
k_2 / s^{-1}	6.11	5.62
K	0.571	0.669

* Standard deviation error = 19%

The < -2 > statistical fit value of $k_s = 0.747 \text{ cm s}^{-1}$ is now accepted in preference to the < +1 > fit value because the < -2 > fit favours high frequency data in which the majority of charge transfer information is contained. The < +1 > statistical fit values for k_1 , k_2 and K are accepted as most of the information about these parameters is carried in the lower frequency data.

Similar procedures were used to obtain electrochemical parameters for the other solutions. In the cases where k_s was found to exceed 1 cm s^{-1} simulations have already established that it is not possible to say how much higher than 1 cm s^{-1} k_s in fact is.

The results obtained are as follows:

Table 8.13

Results for Pt (a = 10 μm) / dichloromethane, 0.12 mM C_{60} , TBABF₄ / Pt gauze

TBABF ₄ Concentration / M	C _{dl} / $\mu\text{F cm}^{-2}$	D / $10^5 \text{ cm}^2 \text{ s}^{-1}$	a / μm	k _s / cm s^{-1}	k ₁ / s^{-1}	k ₂ / s^{-1}	K
0.0053	10.6	1.49	11.5	0.747	3.76	5.62	0.669
0.012	12.0	1.05	13.6	> 1	2.36	4.76	0.496
0.022	17.2	1.43	10.1	> 1	2.49	3.13	0.796
0.065	12.6	1.25	11.0	> 1	3.08	2.05	1.50
0.20	10.6	1.11	10.0	> 1	3.21	1.10	2.92

Table 8.14

Results for Pt ($a=10\ \mu\text{m}$) / dichloromethane, 0.12 mM C_{60} , TBAP / Pt gauze

TBAP Concentration / M	C_{dl} / $\mu\text{F cm}^{-2}$	D / $10^5\ \text{cm}^2\ \text{s}^{-1}$	a / μm	k_s / cm s^{-1}	k_1 / s^{-1}	k_2 / s^{-1}	K
0.0048	8.89	1.09	10.9	> 1	2.04	17.0	0.120
0.013	11.5	1.07	10.5	> 1	6.66	2.40	2.78
0.025	10.7	0.982	10.9	> 1	6.67	7.93	0.841
0.069	10.2	0.929	10.6	> 1	1.37	0.260	5.27
0.18	10.9	0.909	10.1	> 1	4.42	0.507	8.72

Table 8.15

Pt (a=10 μm) / 1,2 dichlorobenzene, 0.25 mM C_{60} , TBABF_4 / Pt gauze

TBAP Concentration / M	C_{dl} / $\mu\text{F cm}^{-2}$	D / $10^6 \text{ cm}^2 \text{ s}^{-1}$	a / μm	k_s / cm s^{-1}	k_1 / s^{-1}	k_2 / s^{-1}	K
0.0052	7.64	3.83	11.2	0.0152	2.94	4.43	0.664
0.010	7.50	3.62	11.3	0.0206	2.62	2.64	0.992
0.021	7.26	3.55	10.8	0.0387	2.38	1.58	1.51
0.065	7.35	3.56	10.1	0.115	1.67	0.394	4.24
0.18	8.76	3.33	9.55	0.278	1.21	0.112	10.8

Table 8.16

Pt (a=10 μm) / 1,2 dichlorobenzene, 0.25 mM C₆₀, TBAP / Pt gauze

TBAP Concentration / M	C _{dl} / $\mu\text{F cm}^{-2}$	D / $10^6 \text{ cm}^2 \text{ s}^{-1}$	a / μm	k _s / cm s^{-1}	k ₁ / s^{-1}	k ₂ / s^{-1}	K
0.010	6.43	3.58	11.5	0.0258	2.00	2.36	0.847
0.021	6.10	3.48	10.7	0.0440	2.83	1.51	1.87
0.067	6.37	3.80	9.40	0.109	2.45	0.457	5.36
0.18	7.65	3.69	8.29	0.125	0.889	0.105	8.47

Table 8.17

Pt (a=10 μm) / benzonitrile, 0.38 mM C_{60} , LiClO_4 / Pt gauze

LiClO_4 Concentration / M	C_{dl} / $\mu\text{F cm}^{-2}$	D / $10^6 \text{ cm}^2 \text{ s}^{-1}$	a / μm	k_s / cm s^{-1}	k_1 / s^{-1}	k_2 / s^{-1}	K
0.0048	7.53	3.58	9.19	0.399	1.65	2.03	0.813
0.010	6.84	3.30	9.00	0.191	1.47	2.21	0.665
0.025	6.64	3.10	8.45	0.369	2.05	2.01	1.02
0.077	7.81	3.04	8.55	0.139	2.03	1.14	1.78
0.22	7.12	2.73	8.45	0.0827	2.27	1.13	2.10

8.2.5 Discussion of Impedance Results for TBAP and TBABF₄ Supporting Electrolytes.

Double layer capacitances were, as expected, around 10 $\mu\text{F cm}^{-2}$.

Diffusion coefficients were, as also should be expected, highest in dichloromethane, the least viscous of the solvents. As electrolyte concentration was increased diffusion coefficients became smaller owing, as discussed in earlier chapters, to increases in viscosity. Such decreases in the diffusion coefficient of C₆₀ when the supporting electrolyte concentration was increased were also observed by Mirkin et al. ⁽⁶⁾. These authors used values of the diffusion limited current in microelectrode voltammetry to obtain $D = 3.9 \times 10^{-6} \text{ cm}^2 \text{ s}^{-1}$ in 1,2 dichlorobenzene with 0.1 M TBABF₄. This is in excellent agreement with the values obtained here by microelectrode impedance spectroscopy for C₆₀ in 1,2 dichlorobenzene with 0.065 M and 0.18 M TBABF₄ where D values were $3.8 \times 10^{-6} \text{ cm}^2 \text{ s}^{-1}$ and $3.7 \times 10^{-6} \text{ cm}^2 \text{ s}^{-1}$ respectively. Fawcett et al. obtained $D = 1.7 \times 10^{-5} \text{ cm}^2 \text{ s}^{-1}$ in dichloromethane with 0.1 M TBAP while Oyama et al. working with the same solvent but with 0.1 M TBABF₄ obtained $D = 8.4 \times 10^{-6} \text{ cm}^2 \text{ s}^{-1}$ ^{(7), (8)}. Fawcett et al's value is almost double the values obtained here of $0.929 \times 10^{-5} \text{ cm}^2 \text{ s}^{-1}$ and $0.909 \times 10^{-5} \text{ cm}^2 \text{ s}^{-1}$ respectively in 0.069 M and 0.18 M TBAP. Oyama et al's value is in better agreement with the values obtained here of $1.25 \times 10^{-5} \text{ cm}^2 \text{ s}^{-1}$ and $1.11 \times 10^{-5} \text{ cm}^2 \text{ s}^{-1}$ respectively in 0.065 M and 0.20 M

From consideration of the reorganisation dynamics, standard heterogeneous rate constants for C₆₀ were expected to be high, higher than for TCNQ for example.

This is because the large size and spherical symmetry of C_{60} will dictate that both the internal molecular reorganisation and the external, solvent reorganisation should be relatively small when an electron is added. This expectation was realised for the lowest viscosity solvent, dichloromethane, but not for the others where the values of k_s for C_{60} are similar to those found for ferrocene and TCNQ at comparable supporting electrolyte concentrations. One must bear in mind though that C_{60} was present in millimolar quantities, at which concentration all of the available evidence indicates that ferrocene and TCNQ yield k_s values greater than 1 cm s^{-1} . Furthermore the solvents in which C_{60} was studied were less viscous than tetraglyme, a fact which, assuming outer sphere control of the kinetics, should also result in C_{60} yielding higher electron transfer rates than ferrocene and TCNQ in tetraglyme. Overall, it seems that the values of k_s for C_{60} are lower than solvent dynamic effects alone would have predicted.

Other authors have measured k_s for C_{60} . Mirkin et al. determined k_s for C_{60} in 1,2 dichlorobenzene with 0.1 M TBABF₄ using scanning electrochemical microscopy in a thin layer cell to be $0.46 \pm 0.08 \text{ cm s}^{-1}$ ⁽⁶⁾. This value is somewhat higher than the values found here of 0.12 cm s^{-1} and 0.28 cm s^{-1} in 1,2 dichlorobenzene with 0.065 M and 0.18 M TBABF₄ respectively. Fawcett et al., using ac voltammetry at a 25 μm radius microdisc, found the rate constant to be 0.33 cm s^{-1} in dichloromethane with 0.1 M TBAP ⁽⁷⁾. This is in fact smaller than the value determined here of greater than 1 cm s^{-1} . Oyama et al. used fast sweep cyclic voltammetry at a microelectrode to measure k_s and found it to be $0.29 - 0.41 \text{ cm s}^{-1}$ in dichloromethane with 0.1 M TBABF₄ ⁽⁸⁾. Here it was measured to be around 0.747 to 1 cm s^{-1} . The values of k_s obtained here agree with those obtained by other

authors using different techniques to within a factor of two or three and as such, agreement is relatively good given the high variability in k_s often seen between different laboratories ^{(9), (10)}. The other authors whose work has been referenced here with regard to C_{60} kinetics have noted that the k_s they obtained is lower than they had expected and have attributed the sluggishness to ion association ^{(3), (5), (6), (7), (11)}.

Although ion association is undoubtedly significant in determining the observed rate of electron transfer in C_{60} systems, it is important also to consider other effects.

Fawcett et al. have suggested that all other factors being equal, the outer sphere contribution to the Gibbs activation energy for a reaction in which an anion is formed is larger than that for a cation leading to a significant difference in electron transfer rates ^{(7), (12)}, i.e. k_s values for anion formation will be less than for cation formation. Taking this into account, it is unsurprising that heterogeneous kinetics for C_{60} are no faster than for ferrocene.

As we saw for TCNQ, reorganisation dynamics and ion pairing are not alone in determining the observed rate of electron transfer and double-layer effects such as the Frumkin effect can also be very important. The size of the C_{60} molecule has provoked speculation that the mean distance of the centre of the C_{60} molecule from the electrode when TBA^+ is the supporting electrolyte cation could lead to slower electron transfer rates ^{(5), (8)}. Krishnan et al. also proposed that the Frumkin correction should be negligible because the reaction site is probably far from the electrode surface, and that a considerable part of the molecule may lie outside the

OHP⁽⁵⁾. Contrary to this theoretical prediction, however, the results in Tables 8.13, 8.15 and 8.16 for C₆₀ in dichloromethane with TBABF₄ electrolyte and in dichlorobenzene with TBAP and TBABF₄ electrolytes show a substantial increase in the value of k_s with increasing supporting electrolyte concentration. These data are consistent with a Frumkin effect as strong as that observed for the TCNQ molecule. No conclusion can be drawn for C₆₀ in dichloromethane with TBAP electrolyte as, for these cells, values of k_s (Table 8.14) are greater than 1 cm s⁻¹ and therefore it is not possible to tell whether it is changing or in which direction. The useable experimental data indicate that, despite its large size, there is a significant Frumkin effect for the reduction of C₆₀ when TBA⁺ is the supporting electrolyte cation. This is very strong evidence in support of the proposition C₆₀ is in fact located within the OHP and *not* outside it.

In comparing C₆₀ with TCNQ, the size of C₆₀ is probably relevant in explaining its apparent sluggishness. In the case of TCNQ the electrolyte cation was Li⁺ and for C₆₀ it was TBA⁺. The radius of the TBA⁺ is larger than Li⁺⁽¹³⁾ and this implies that the OHP in the TCNQ experiments would be located nearer the electrode surface than in the C₆₀ experiments. This factor determines that TCNQ will be able to approach the electrode more closely than C₆₀. This closeness of approach effect will be intensified when one considers that TCNQ is a much flatter molecule than C₆₀ and hence the redox centre of TCNQ can be located considerably nearer the electrode surface than can C₆₀'s. Longer distances are expected to retard the rate of electron transfer and the greater separation of C₆₀ than TCNQ from the electrode may offer an explanation for why, despite probably more favourable solvent dynamics, the heterogeneous kinetics of C₆₀ are no faster than TCNQ^{(8), (18)}.

The reactant size has played a central role in the immediately preceding discussions regarding solvent dynamic and double layer effects. The literature treatment of reactant size in this respect appears to lack consistency. Two very different means of defining reactant size have been used to analyse the kinetics of C_{60} ^{(5), (7)}. These are, on the one hand the Stokes radius, and alternatively the crystal/van der Waals radius.

Provided the diffusion coefficient of the molecule of interest and the viscosity of the solution are known the Stokes-Einstein equation may be used to estimate the effective radius of a spherical molecule in as much as the frictional force it experiences moving through the solution reflects its size. The Stokes radius, as it is known, may be larger than that of the "naked" ion owing to the ion's solvation layer. The Stokes-Einstein equation states:

$$D = \frac{kT}{6\pi r\eta} \quad [8.1]$$

where k is the Boltzmann constant, r is the Stokes radius of the diffusing molecule and η is the viscosity of the solution. From diffusion coefficients obtained in this and previous chapters we can write that for C_{60}/C_{60}^- in dichloromethane at room temperature the mean diffusion coefficient is about $1.27 \times 10^{-5} \text{ cm}^2 \text{ s}^{-1}$ and in 1,2 dichlorobenzene about $3.58 \times 10^{-6} \text{ cm}^2 \text{ s}^{-1}$. For TCNQ/TCNQ⁻ in tetraglyme the mean diffusion coefficient is about $1.6 \times 10^{-6} \text{ cm}^2 \text{ s}^{-1}$; and for ferrocene/ferrocenium in tetraglyme it is also about $1.6 \times 10^{-6} \text{ cm}^2 \text{ s}^{-1}$. The viscosity of these solutions, respectively, is about 0.44 cP, 2.6 cP, 3.25 cP and 3.25 cP^{(5), (14)}. Substituting these

values into equation [8.1] yields values for the Stokes radii shown in Table 8.18:

Table 8.18

Estimated approximate Stokes radii

<i>Molecule</i>	<i>Solvent</i>	<i>Stokes Radius / nm</i>
$C_{60}^{0/1-}$	Dichloromethane	0.39
$C_{60}^{0/1-}$	1,2 dichlorobenzene	0.24
TCNQ ^{0/1-}	Tetraglyme	1.02
Ferrocene ^{0/1+}	Tetraglyme	1.02

The Stokes radii for C_{60} look as if they could be in error. The van der Waals radius of C_{60} is 0.42 to 0.5 nm^{(5), (7)} and it does not seem likely that C_{60} and its anion in solution would behave as if their radii were equal to or smaller than this. Pyati and Murray in their study of $[Co(bpy)_3]^{2+/3+}$ in different solvents also found the Stokes radius of 0.53 nm was lower than the 0.7 nm radius in the metal complex⁽¹⁶⁾. The reasons for the results measured here are presumably either the unsuitability of the Stokes-Einstein equation for C_{60} in organic solvents or the inaccuracy of the experimentally obtained diffusion coefficients. The Stokes-Einstein equation, however, assumes the diffusion of a *spherical* species through a liquid and as such, C_{60} should be an ideal molecule to which to apply the equation. As regards possible inaccuracy of diffusion coefficients, both CNLS modelling of impedance data and the steady state current from voltammetry agree to the extent that they

both yield low values of the Stokes radius. In the light of this, the low values of Stokes radii for C_{60} are difficult to explain. Furthermore, the diffusion coefficients upon which the Stokes radii are based seem reliable in terms of agreement with Mirkin et al. and Oyama et al.^{(6), (8)}. Krishan et al. obtained higher Stokes radii for C_{60}/C_{60}^- , i.e. 1.11 nm in dichloromethane and 0.77 nm in 1,2 dichlorobenzene⁽⁵⁾. These values were based on smaller diffusion coefficients than obtained here or by Mirkin et al., Fawcett et al. or Oyama et al.^{(6), (7), (8)}. Clearly, the diffusion coefficients of C_{60} and its anion in solution have not been satisfactorily resolved. Until this is done, the Stokes radii of C_{60} will remain unknown with any certainty. It is hoped that the values of Stokes radii shown in Table 8.18 will at least be self-consistent since all were obtained in the same laboratory, by the same research worker, using the same equipment and methods of analysis. So here is one difficulty, i.e., Stokes radii differ between laboratories. There also, however, appears to be disagreement over whether it should be the Stokes or the crystal/van der Waals radius that determines the outer sphere dynamics of a system.

Frequently found in the literature is the calculation of the outer sphere Gibbs reorganisation energy from:

$$\Delta G_{os}^* = \frac{N_A e^2}{32\pi\epsilon_0 r} \left(\frac{1}{\epsilon_{op}} - \frac{1}{\epsilon} \right) \quad [8.2]$$

N_A is Avogadro's number, e the electron charge, ϵ_0 the vacuum permittivity, ϵ_{op} the optical solvent permittivity, ϵ the relative permittivity and r the radius of the reactant. Provided that r is known this calculation is straightforward. Once ΔG_{os}^*

is known its value may be substituted in the encounter pre-equilibrium equation to calculate a theoretical value of the standard heterogeneous rate constant for adiabatic electron transfer ^{(5), (7)}, i.e. into:

$$k_s = \kappa K_p \tau_L^{-1} \left(\frac{\Delta G^*}{4\pi RT} \right)^{1/2} \exp\left(\frac{-\Delta G^*}{RT} \right) \quad [8.3]$$

where κ is the electronic transmission coefficient, K_p is the stability constant of the precursor complex, τ_L is the longitudinal relaxation time and ΔG^* is the reorganisation energy. The value of k_s obtained from this, or more sophisticated models, can then be compared with the experimental value of k_s and conclusions drawn with regard to the assumptions underlying the model. It is clear that the value of r adopted is crucial to the value calculated for k_s and use of different radii by different workers cannot lead to a consistent understanding of the solvent dynamics.

C_{60} has a radius of 0.36 nm in crystalline form. Fawcett et al. employ the van der Waals radius of C_{60} of 0.43 nm in outer sphere energetics calculations based on the pre-encounter equilibrium model ⁽⁷⁾. Krishnan et al. acknowledge the van der Waals radius of C_{60} to be 0.5 nm, similar to the value employed by Fawcett et al., but do not use this figure in their pre-encounter equilibrium model calculations. They use instead the larger Stokes radius of 0.74 to 2.5 nm, depending upon the solvent ⁽⁵⁾. Elsewhere Baranski, Winkler and Fawcett assume a radius of 0.37 nm for ferrocene when in fact the radius in the crystalline form is 0.16 nm and Pyati and Murray, use the metal complex radius rather than the Stokes radius ^{(19), (20), (16)}.

Marcus defined the radius of the reactant to include any inner co-ordination shell⁽¹⁵⁾. On this basis it would appear more appropriate to use the Stokes radius in calculations involving the encounter pre-equilibrium model. For dichloromethane, $\epsilon = 8.93$ and $\epsilon_{op} = 2.02$ ⁽¹⁶⁾. Taking these values and substituting them along with C_{60} 's Stokes radius from Table 8.18, $r = 0.39$ nm, (which virtually coincides with the crystalline radius,) into equation [8.2] yields a value of $\Delta G^*_{OS} = 15.7$ kJ mol⁻¹. This figure, when substituted into [8.3] results in:

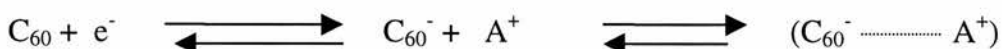
$$k_s = \frac{\kappa K_P}{10^{-12} s} \times 0.296 \text{ cm s}^{-1}$$

Clearly the value of the encounter pre-equilibrium term, i.e. κK_P is now crucial to the value of k_s that will be calculated. For adiabatic reactions, κ , the transmission coefficient is equal to unity. In the absence of steric interactions the upper limit for K_P is about 60 pm for a spherical reactant⁽¹⁰⁾. In their calculations, Krishnan et al. assumed $\kappa K_P = 4$ ps, while Fawcett et al. assumed $\kappa K_P = 20$ ps^{(5), (7)}. Here, if the example of Krishnan et al. is followed a value of $k_s = 1.18$ cm s⁻¹ is obtained. If instead the example of Fawcett et al. is followed a value of $k_s = 5.92$ cm s⁻¹ is obtained. Different choices of the pre-encounter-equilibrium term and different choices of which definition of radius is employed and different experimentally determined values of Stokes radius obviously ensure that the value of k_s determined by the encounter pre-equilibrium model encompass a fairly large range of values. The experimental values of k_s found here were generally > 1 cm s⁻¹, as shown in

Tables 8.13 and 8.14 and hence, despite the complications of ion-association reactions, are in agreement with either of the theoretically determined values.

Although apparently reasonable agreement between experimental rate constants and the encounter pre-equilibrium model was obtained here, the approach followed can certainly be regarded as an approximation, reliable perhaps to an order of magnitude. To improve the accuracy of the model, agreed accurate estimates are required for the diffusion coefficients and the encounter pre-equilibrium term. Also agreement is required on the definition of the appropriate reactant radius.

The homogenous parameters k_1 , k_2 , and K shown in Tables 8.13 to 8.16 show great qualitative self-consistency. Within any data set the rate constants for ion-association, k_1 , vary little. On the other hand, as the concentration of supporting electrolyte is increased, the rate constants for ion-dissociation decrease. The net effect of this is that K , the degree of ion association, grows larger with increasing supporting electrolyte concentration, consistent with a mechanism of the type shown proposed from voltammetry data, i.e.



The homogenous parameters indicate that at low concentrations of supporting electrolyte there are almost equal quantities of unassociated C_{60}^- and associated C_{60} or an excess of the unassociated species. When the supporting electrolyte concentration is increased, the impedance data indicate that the equilibrium shifts so that a clear majority of C_{60}^- exists as the ion pair.

8.2.6 Discussion of Results for LiClO_4 Supporting Electrolyte.

The results for C_{60} where lithium perchlorate is employed as a supporting electrolyte are discussed here separately. Although the results are in accord with previous results with regard to double layer capacitances and diffusion, they are very different to those obtained with TBAP and TBABF₄ for the other electrochemical parameters. Differences were deduced from both the voltammetry and impedance methods.

When TBA^+ was the supporting electrolyte cation a strong Frumkin double layer effect was observed and the observed value of k_s increased with supporting electrolyte concentration. When, however, Li^+ is the supporting electrolyte cation there is no Frumkin effect. This is consistent with the OHP moving closer to the electrode surface when the large TBA^+ cation is replaced by the smaller Li^+ cation. In this circumstance the redox centre of the $\text{C}_{60}^{0/1-}$ pair will be located outside the OHP and accordingly no Frumkin double layer effect is observed. These new relative positions of redox centre and OHP do not, however, necessarily mean that the redox centre is any farther from the metal surface than it was when TBA^+ was the cation. Hence we should not be surprised that, at low concentrations of supporting electrolyte, k_s is still relatively fast. Rather than growing larger with supporting electrolyte concentration, as it would if the redox centre was located at or close to the OHP, k_s becomes smaller owing to ion pairing.

Voltammetry results, shown in Figure 8.5 and Table 8.8 have already indicated that C_{60} associates with the lithium cation more so than C_{60}^- does. This is a curious observation as one would expect a negatively charged species to associate more strongly with a cation than an uncharged species does. On the other hand, if one considers larger and larger molecules, each with highly de-localised electron density there must be a hypothetical molecular size and geometry at which an additional electron charge makes a negligible contribution to the molecular electron density or polarisability. While the electrostatic interaction of this hypothetical anion with a large soft cation such as TBA^+ would still be stronger than the interaction of TBA^+ with the neutral molecule there may be little difference between the molecule and its anion's interaction with a hard cation such as Li^+ . Although this speculation does not take us to a point where we can accept that Li^+ associates more strongly with C_{60} than with C_{60}^- , it does indicate the possibility of approximately equal association. In fact the tantalising possibility that C_{60} associates more strongly than does C_{60}^- with Li^+ is supported by Dubois et al. who found experimental evidence consistent with the absence of significant electrostatic type ion pairing between Li^+ and C_{60}^- ⁽⁴⁾. They also found that solvents with acceptor properties *seem* (Dubois et al's italics) to stabilise C_{60} more than C_{60}^- . Taking Dubois et al's finding in combination with the results presented in this chapter, it seems highly probable that the lithium cation associates more strongly with neutral C_{60} than with its anion. Why this should be so is not known. One could, however, speculate that since the interaction between C_{60} and Li^+ cannot be electrostatic the difference must lie in the covalent bonding possibilities between the C_{60} molecule and Li^+ compared with the C_{60}^- anion and Li^+ . This is likely to be related to differences in the HOMO structure of the two species ⁽¹⁷⁾.

8.3 Conclusions

Half-wave potentials obtained by cyclic voltammetry shifted to less negative values as the TBA⁺ supporting electrolyte concentration was increased, consistent with an EC mechanism of electron transfer. When Li⁺ was the cation in the supporting electrolyte there was a negative shift of half-wave potentials, consistent with a CE mechanism and, surprisingly, stronger association between Li⁺ and C₆₀ than Li⁺ with C₆₀⁻. The Lingane equation was used to deduce that, on average, ion-association takes the form of pairing.

A potential independent, high-frequency semi-circle, similar to that observed in measurements of solid PEO, was observed in the complex-plane plot. Data points associated with the semi-circle were deleted prior to CNLS analysis. Computer simulations of impedance data and trials with data from ferrocene in tetraglyme experiments indicated the legitimacy of this procedure with regard to obtaining k_s from low frequency data. k_s values of 1 cm s⁻¹ or less should readily be calculated.

Although the hemispherical approximation for an EC reaction had failed to satisfactorily analyse impedance data relating to the electrode kinetics of TCNQ, it was successfully applied to the electrode kinetics of C₆₀. CNLS analysis of impedance data yielded values of the microdisc radius similar to the geometric value and double-layer capacitances around 10 μF cm⁻². Calculated diffusion

coefficients agreed with those obtained by some laboratories but agreed less well with those obtained by others. There is some inconsistency in literature diffusion coefficients for C_{60} in organic solvents. The values of D obtained here and by most laboratories yield Stokes radii lower than the van der Waals radius of a crystalline C_{60} molecule. This does not make physical sense and is currently inexplicable.

Using the Stokes radius in the encounter pre-equilibrium model yields theoretical k_s values consistent with those obtained in dichloromethane. The values of k_s were also in reasonably good agreement with those obtained by other laboratories. Measurement of k_s as a function of supporting electrolyte concentration showed that, contrary to theoretical predictions, a clear Frumkin double-layer effect is observed where the supporting electrolyte cation was TBA^+ . This indicates that the large size of TBA^+ causes the OHP configuration to be such that it permits C_{60} molecules to move into the OHP. When the position of the OHP is moved closer to the electrode by replacement of TBA^+ with Li^+ no Frumkin effect is observed, indicating that C_{60} is too large to enter this OHP.

The values of the homogeneous parameters behaved in a sensible way consistent with increased ion association when the supporting electrolyte concentration was increased.

8.4 References

1. Q. Xie, E. Perz-Cordero, L. Echegoyen, *J. Amer. Chem. Soc.*, (1992), 114, p3978.
2. T. Ohsawa, T. Saji, *J. Chem. Soc., Chem. Comm.*, (1992), p281.
3. W.R. Fawcett, M. Opallo, M. Fedurco, J.W. Lee, *J. Am. Chem. Soc.*, 1993, 115, p196.
4. D. Dubois, G. Moninot, W. Kutner, M.T. Jones, K.M. Kadish, *J. Phys. Chem*, 1992, 96, p7137.
5. V. Krishnan, G. Moninot, D. Dubois, W. Kutner, K.M. Kadish, *J. Electroanal. Chem.*, (1993), 356, p93.
6. M.V. Mirkin, L.O.S. Bulhoes. A.J. Bard, *J. Am. Chem. Soc.*, (1993), 115, p201.
7. W.R. Fawcett, M. Opallo, M. Fedurco, J.W. Lee, *J. Electroanal. Chem.*, 1993, 344, p375.
8. N. Oyama, S. Kikuyama, T. Tatsuma, *J. Electroanal. Chem.*, (1993), p367.
9. A.P. Abbott, C.L. Miaw, J.F. Rusling, *J. Electroanal. Chem.*, (1992), 327, p31 - 130.
10. W.R. Fawcett, M. Opallo, *Angew. Chem. Int. Ed. Engl.*, (1994), 33, p2131.
11. M. Opallo, *Polish J. Chem.*, (1993), 67, p2093.
12. M. Hoom, W.R. Fawcett, *J. Phys. Chem. A* (1997), 101, 3726 - 3730.
13. M.E. Peover, in A.J. Bard (Ed.) *Electroanalytical Chemistry*, (1967), Vol 2, Chapter 1, Marcell Dekker, New York.

14. D. Brouillette, G. Perron, J.E. Desnoyers, *J. Solution Chem.*, (1998), 27, p151.
15. R. A. Marcus, *J. Chem. Phys.*, (1965), 43, p679.
16. R. Pyati, R.W. Murray, *J. Am. Chem. Soc.*, (1996), 118, p1743.
17. J. Stinchcombe, A. Penicaud, P. Bhyrappa, P.D.W. Boyd, C.A. Reed, *J. Am. Chem. Soc.*, (1993), 115, P5212.
18. S.B. Khoo, J.K. Foley, S. Pons, *J. Electroanal. Chem.*, (1986), 215, p273.
19. A.S. Baranski, K. Winkler, W.R. Fawcett, *J. Electroanal. Chem.*, (1991), 313, p367.
20. N.N. Greenwood, A. Earnshaw, *Chemistry of the Elements*, (1984), Pergamon Press, Oxford, p368,

CHAPTER 9

CONCLUDING REMARKS

The hemispherical approximation for diffusion to a microdisc had been developed immediately before the research work described in this thesis began. Prior to this development, impedance studies at a microdisc were few in number. The objective of the work was to verify the technique, use it, and extend it where necessary to study electrochemical systems in the liquid and solid phases. The reactants studied were ferrocene, TCNQ and buckminsterfullerene.

Ferrocene was studied in tetraglyme and PEO whilst TCNQ was studied in tetraglyme. The kinetics of these systems had not previously been published. The kinetics of heterogeneous transfer involving ferrocene and its cation are generally supposed to be controlled by an outer-sphere mechanism. Values of the kinetic parameters were measured in both the liquid and near-solid environment by microelectrode impedance spectroscopy. In near-solid PEO there appeared to be strong adsorption of ferrocene onto the electrode restricting the scope of measurements that could be made to those that could be obtained before impedance plots data were distorted too much by the adsorption. Changes in the value of the heterogeneous electron transfer rate constant and diffusion coefficient of the same order of magnitude between tetraglyme and PEO were consistent with strong outer sphere control of the electron transfer in both liquid and near-solid environments. The kinetics in PEO were an order of magnitude slower than in tetraglyme. Surprisingly, the observed heterogeneous rate constant for electron transfer in

tetraglyme was found to be dependent on reactant concentration for both ferrocene and TCNQ. This is tentatively attributed to double layer effects causing the relative effective concentration of the redox species to be lowered. Arrhenius plots showed that the Gibbs activation energy of electron transfer for ferrocene was higher than for diffusion.

Half-wave potential shifts with background electrolyte concentration in voltammetry experiments indicated that the electron transfers in tetraglyme for both the ferrocene and TCNQ systems proceeded by an EC mechanism. New equations were derived to enable the effect of a homogeneous chemical reaction coupled with Warburg diffusion to be modelled for CNLS analysis of microdisc impedance data. These equations were applied successfully to the ferrocene system but were less successful in analysis of the TCNQ system.

Buckminsterfullerene was studied in dichloromethane, 1,2 dichlorobenzene and benzonitrile. Kinetic data had been published for buckminsterfullerene in these solvents and it was planned to compare the results obtained by microelectrode impedance spectroscopy with published kinetic data obtained using different techniques. Although reduction of buckminsterfullerene had been reported as an EC mechanism, the effect of supporting electrolyte concentration on the observed heterogeneous rate constant had not previously been reported. This meant predictions that a Frumkin type double layer effect would not be observed because the size of C_{60} molecules would place them outside the OHP had not been tested. The EC model for impedance at a microdisc was applied successfully to impedance data from C_{60} systems. Results indicated that where the supporting electrolyte

cation was $\text{TBA}^+ \text{C}_{60}$ was located at the OHP but with Li^+ it was located outside the OHP. Voltammetry data, somewhat surprisingly, indicated that Li^+ associates with neutral C_{60} in preference with anionic C_{60}^- . The values of k_s for $\text{C}_{60}^{0/1-}$ obtained by impedance spectroscopy at a microdisc agreed reasonably well with those obtained employing different techniques.

Simulations of electrochemical parameters typical of those encountered in this study, for microdiscs of radius 5 and 10 μm , indicate that provided $k_s < 1 \text{ cm s}^{-1}$ it is not necessary to obtain a high frequency semi-circle to determine k_s . Thus impedance spectra obtained at lower frequencies, less than 5 kHz, for example, can satisfactorily determine all normally required parameters. Smaller microdiscs could determine faster kinetics at low frequencies.

To sum up, the use of the hemispherical approximation to analyse microelectrode impedance data obtained in different media has been established to yield comparable results to other techniques where published data were available and thus must be regarded as proven. It has been used successfully to measure heterogeneous rate constants up to 1 cm s^{-1} in a variety of situations and could be used with smaller microelectrodes to measure faster reactions. The technique has been extended to analyse situations in which one of the redox species undergoes homogeneous reaction.

Future Work

The observation that k_s is inversely proportional to reactant concentration is puzzling and has not been fully explained here. The relationship should be verified by a different technique such as fast cyclic voltammetry, after which the tentative proposal that it results from association between the charged and uncharged redox species could be tested, by spectroscopy, perhaps.

The encounter pre-equilibrium equation for estimating standard heterogeneous rate constants relies on the use of appropriate reactant radii. There appear to be differences in the literature regarding which definition of reactant radius should be used. Some authors favour the radius of the crystalline molecule while others favour the Stokes radius. A standard agreed approach would be preferable and should be developed.

The apparent preference of the lithium cation to associate with neutral buckminsterfullerene rather than the buckminsterfullerene anion is an interesting observation worthy of complete explanation.